

Dynamics of chemically active suspensions

Thesis by
Wen Yan

In Partial Fulfillment of the Requirements for the
Degree of
Doctor of Philosophy

The logo for the California Institute of Technology (Caltech), featuring the word "Caltech" in a bold, orange, sans-serif font.

CALIFORNIA INSTITUTE OF TECHNOLOGY
Pasadena, California

2016
Defended May 24, 2016

© 2016

Wen Yan

ORCID: 0000-0002-9189-0840

All rights reserved except where otherwise noted

ACKNOWLEDGEMENTS

I would like to express my sincere gratitude to my advisor Prof. John F. Brady. His great mentoring style, continuous support, and sharp intuition regarding physics guided me through my many years as a graduate student. He also allowed me great freedom to explore the field and I benefited a lot from his style.

Besides this, my sincere thanks go to my thesis committee: Prof. Wang, Prof. Hunt, and Prof. Kochmann. Chapter VIII of this thesis is directly related to comments from Prof. Wang. Prof. Hunt and Prof. Kochmann gave great lectures about transport theories and continuum mechanics, which have become a major component of this thesis.

My sincere thanks also go to my group colleagues: Dr. Nicholas Hoh, Dr. Marco Heinen, Charles Slominski, Mikey Phan, Isaac Fees, Sho Takatori, Kevin Marshall and Mu Wang.

Last but not least, I would like to thank my parents and Yi-Fan Zhang, for their selfless and heartwarming support during my challenging times.

ABSTRACT

Active matter refers to a material that consists of individual particles or bodies capable of propelling themselves; that is, they ‘swim’. Each active particle (or swimmer) propels itself at some velocity $U_0\mathbf{q}$, where U_0 is the swim velocity and \mathbf{q} is the swim direction, which is subject to random (Brownian) reorientation on a time scale τ_R .

Despite the complex phenomena in real systems, the minimal active Brownian particle model exhibits physical behavior. In this model, the particle’s self-propulsion velocity U_0 is usually assumed to be a given constant and \mathbf{q} is subject to rotational Brownian diffusivity $D_R = 1/\tau_R$. Also, the interaction between active Brownian particles is usually assumed to be collision only (pure repulsive) (Solon *et al.*, 2015a) or a pairwise additive potential (Redner *et al.*, 2013). The behavior of this model system can be successfully explained by thermodynamic-type models, with the introduction of swim pressure as an equation of state (Takatori *et al.*, 2014; Takatori & Brady, 2015).

The swim pressure is analogous to the classic pressure in a gas, and more closely analogous to the osmotic pressure of a molecular or colloidal solute, and is defined through the swimming diffusivity D^{swim} and drag coefficient on each swimmer ζ : $\sigma^{swim} = -n\zeta D^{swim}$. It is the pressure required to confine the active particles within a fixed volume, and is the sum of all particles’ collisional forces exerted on the container walls. Therefore, the swim pressure is a well-defined *mechanical* pressure.

In this thesis, we shall see that the applicability of swim pressure extends beyond the description of a homogeneous, ‘thermodynamical equilibrium’ state. It can be used in a continuum mechanics formulation to *predict* the deformation and motion of general active matter.

Continuum mechanics is built upon the notion that the conservation of momentum arises from a balance between surface and body forces. For active matter, the surface force takes the form of the swim pressure (or a swim stress), while the body forces include an extra piece that is intrinsically due to activity – the average swim force. It is shown that the average swim force acts like a body force – an *internal* body force. With properly defined surface and body forces, a continuum description is possible when variations occur on scales much larger than the run length of the active particles. This is verified with simulations for an active Brownian particle system under gravity.

Below the continuum mechanics scale, at the level of the individual active particles, the microscopic origin of the swim pressure is analyzed. A general theory is proposed, as an extension of the theory for passive Brownian colloids, for determining the force (and torque) exerted on a boundary (or body) in active matter. The theory shows that the swim pressure is associated with the swimmer-wall collisions and the accumulation of swimmers close to a non-penetrating boundary. Further, the accumulation boundary layer is impacted by the detailed shape of the boundary. With a properly designed asymmetric shape, a passive body immersed in swimmers can achieve a net force, and that force can be calculated from the active colloidal perspective.

The notion of swim pressure (or stress) is extended to anisotropic situation. It is shown that, by manipulating the orientation \mathbf{q} , active Brownian particles with a nematic orientation field exhibit a tensorial anisotropic swimming stress $\boldsymbol{\sigma}^{swim} = -n\zeta \mathbf{D}^{swim}$, i.e., the pressure on a flat wall can be written as $\Pi^W = (\boldsymbol{\sigma}^{swim} \cdot \mathbf{n}) \cdot \mathbf{n}$. This tensorial continuum mechanics view is shown to be consistent with the microscopic theory, through the formation of the accumulation boundary layer.

The discussions for the minimal active Brownian particle model constitute the foundation of a mechanical view for general active matter. In this work, chemically

active particles are considered as an example. They may achieve self-propulsion by self-diffusiophoresis in a concentration gradient of chemical solutes they create themselves by patterned surface catalytic reactions.

The chemical solute concentration field provides both self-propulsion and particle-particle interaction. To probe the system dynamics, the particles' trajectories and the solute concentration field must be simultaneously solved. A simulation algorithm – Accelerated Laplacian Dynamics (ALD) – is developed to track the system dynamics. With simulation results, we first clarify the notion of chemical screening (Morris & Brady, 1995), which means the perturbation caused by each particle is screened to an exponentially screened short-ranged perturbation.

Simulations show that uniformly reactive particles, which do not self-propel, form clusters but no dense-dilute coexistence is observed. Janus particles with self-propulsion show coexistence of dense and dilute regions, in agreement with the experiments by Theurkauff *et al.*, (2012) and Palacci *et al.*, (2013). The steady state structure of the dense-dilute coexistence can be explained with a continuum mechanics model based on a mean-field approach to swim pressure and force balance, as established for the minimal active Brownian particles model.

The onset of the dense-dilute separation is explained by a stability theory with a detailed solution of the Smoluchowski equation. When the particle-particle attraction is strong enough, clusters spontaneously appear from a homogeneous system of chemically active particles. The instability threshold and spectrum are calculated with both the detailed Smoluchowski equations and a coarse-grained continuum approach; the two agree. Self-propulsion decreases the growth rate, but it has no impact on the stability threshold because the effect of self-propulsion enters at a higher order in wave number than the competition between attraction and translational Brownian motion.

Repulsive self-diffusiophoretic particles with homogeneous surface catalytic reac-

tion are investigated with ALD simulations. By a mapping to the classic one component plasma system, the system behavior can be described by a coupling parameter Γ_c , which compares the strength of diffusiophoretic repulsion and translational Brownian motion. When confined in a constant-volume constraint, Body-Centered Cubic crystals may form, and the ‘melting point’ is found to be $\Gamma_c^{BCC} \approx 140$.

PUBLISHED CONTENT AND CONTRIBUTIONS

1. Takatori, S. C., Yan, W. & Brady, J. F. Swim Pressure: Stress Generation in Active Matter. *Phys. Rev. Lett.* **113**, 028103 (2014).
DOI: 10.1103/PhysRevLett.113.028103. W. Yan participated in the conception of the project and the analysis of data.
2. Yan, W. & Brady, J. F. The swim force as a body force. *Soft Matter* **11**, 6235–6244 (2015).
DOI: 10.1039/C5SM01318F. W. Yan participated in the conception of the project, solved and analyzed the system dynamics, prepared the data, and participated in the writing of the manuscript.
3. Yan, W. & Brady, J. F. The force on a boundary in active matter. *J. Fluid Mech.* **785**, R1 (2015).
DOI: 10.1017/jfm.2015.621. W. Yan participated in the conception of the project, solved and analyzed the system dynamics, prepared the data, and participated in the writing of the manuscript.

TABLE OF CONTENTS

Acknowledgements	iii
Abstract	iv
Published Content and Contributions	viii
Table of Contents	ix
List of Illustrations	xi
Chapter I: Introduction	1
Chapter II: The swim force as a body force	11
2.1 Introduction	12
2.2 The swim force	15
2.3 The global force balance	18
2.4 Particle-phase momentum balance	20
2.5 The effect of internal and external body forces	21
2.6 Suspension momentum balance	28
2.7 Conclusions	29
Chapter III: The force on a boundary in active matter	32
3.1 Introduction	33
3.2 Theory	34
3.3 Examples	37
3.4 Discussion	42
Chapter IV: The curved kinetic boundary layer of active matter	46
4.1 Problem formulation	50
4.2 Analytical solution	55
4.3 Results	61
4.4 Discussion & Conclusions	69
Chapter V: Active matter with nematic orientation: enhanced anisotropy and tensorial swim stress	76
5.1 Introduction	77
5.2 Nematic orientation order: anisotropic swim diffusivity	78
5.3 Force on a boundary: the tensorial swim stress	87
5.4 Conclusions & Discussions	94
Chapter VI: A method to determine the behavior of active diffusiophoretic suspensions: Accelerated Laplacian Dynamics	98
6.1 Introduction	99
6.2 Problem formulation	102
6.3 Method for solution of Laplace's equation	107
6.4 Results	118
6.5 Conclusions	147
Chapter VII: Clustering of chemically active particles: stability analysis with the matrix perturbation method	152

7.1	Problem formulation & methodology	157
7.2	The base case: $P = 0$	168
7.3	The general case with propulsion: $P \neq 0$	173
7.4	Active flux and continuum mechanics	181
7.5	Discussion & Conclusions	188
Chapter VIII: Anti-swarming: structure and dynamics of repulsive chemically active particles		
	active particles	190
8.1	Introduction	191
8.2	Problem formulation	192
8.3	The weak repulsion regime: fluctuating interaction	195
8.4	The strong repulsion regime: ‘liquid-crystal’ phase transition	198
8.5	Conclusions & Discussion	200
Chapter IX: Conclusions and outlook		
	Appendix A: The swim force of active matter	209
	Appendix B: Anisotropic stress under \hat{H} field	214
	Appendix C: Closure of the Smoluchowski equation	216
	Appendix D: Principal curvatures	218
	Appendix E: The notation for rotational flux in 3D space	220
	Appendix F: Faxen Laws for a homogeneously reactive particle	222
	Appendix G: Faxen Laws for a Janus reactive particle	224
	Appendix H: All contributions of \mathcal{E} in the Ewald sum	226
	Appendix I: Feedback factor F_c	228
	Appendix J: Linear dynamic system	230
	Appendix K: Perturbation of eigenvalues & eigenvectors of a complex matrix: general theory.	231
	Appendix L: Perturbation series: full solution	236
	Bibliography	239
	Appendix M: Consent form	250

LIST OF ILLUSTRATIONS

<i>Number</i>	<i>Page</i>
<p>2.1 Active Brownian Particles (ABPs) in a container of height L in the z-direction and periodic in the x- and y-directions. Each active particle experiences a swim force $\mathbf{F}^{swim} = \zeta U_0 \mathbf{q}$, with $\mathbf{q}(t)$ the direction of swimming. An external gravitational ($\hat{\mathbf{G}}$) and polarization ($\hat{\mathbf{H}}$) field may also be applied. The top and bottom boundaries do not allow the particles to escape (no flux), but the flow of fluid \mathbf{u}_f is unimpeded – they are osmotic barriers. The horizontal plane $S(z)$ is the cross-section considered in global force balance (2.4).</p>	17
<p>2.2 <i>Active particles with gravity.</i> The local area fraction ϕ_A vs height z/a in 2D. The symbols are simulation results and the solid lines are solutions to the continuum description (2.7). The log plot shows the same data as the linear plot. The dashed line corresponds to Boltzmann distribution $n \propto \exp(-\Delta\rho V_p g z / (k_B T + k_s T_s))$, that is, $\exp(-0.04z/a)$; here $k_s T_s = \zeta U_0^2 \tau_R / 2$. $N = 1000$ particles are simulated in a square box of size $250a$ and $\phi_A^0 = 0.05$. The box is periodic in the x-direction but confined by two no-flux walls located at $z = 0$ and $z = L$. The inset compares the force on the bottom wall from the particle-wall interactions in simulation with the buoyant weight of the particles.</p>	22

- 2.3 *Orienting field to cancel gravity.* The wall pressure vs simulation time. Here, $\text{Pe}_R = a/(U_0\tau_R) = 0.2$, $D_T = 0$, $\chi_R = \Omega_c\tau_R = 1$ and $\Delta\rho V_P g\tau_R/(\zeta a) = 2.23 = \langle q_z \rangle U_0\tau_R/a$. The insert shows the local area fraction ϕ_A as a function of height z , sampled by Voronoi cells. $N = 1668$ particles are simulated in a square box of size $512a$ at $\phi_A^0 = 0.02$. The data are averaged over 16 realizations. The system is periodic in the x -direction but confined by two no-flux walls located at $z = 0$ and $z = L$. The theory for the dilute limit and can be found in Appendix B. 24
- 2.4 The anisotropic wall pressures compared with the dilute 2D theory (Appendix B). The circles are ABP simulations for $\text{Pe}_R = a/(U_0\tau_R) = 0.2$, $D_T = 0$, $\phi_A^0 = 0.02$ and $N = 1668$. (A) For $\hat{\sigma}_\perp$ the \hat{H} field is applied in the x -direction, whereas (B) for $\hat{\sigma}_\parallel$ the \hat{H} is applied in the z -direction and canceled by \mathbf{F}^{ext} . The square box of size $512a$ is periodic in the x direction and confined by no-flux walls located at $z = 0$ and $z = L$ 25
- 2.5 *No gravity but with an orienting field.* The local area fraction ϕ_A vs height z/a with the \hat{H} field applied downward and $\mathbf{F}^{ext} = 0$. The symbols are simulation results and the solid line is the solution to the the continuum description (2.7). The dashed line is a Boltzmann distribution $\phi_A \propto \exp\{-\langle F^{swim} \rangle z / (k_B T + k_s T_s \hat{\sigma}_\parallel)\} = \exp(-0.04z/a)$, where $k_s T_s = \zeta U_0^2 \tau_R / 2$. $N = 1000$ particles are simulated in a square box of size $250a$ at $\phi_A^0 = 0.05$. The box is periodic in x but confined by no-flux walls at $z = 0, L$. The inset compares the force on the bottom wall from the particle-wall interactions in simulation with the ‘weight’ of the particles due to the swim force. 26

- 2.6 *A depletion zone induced by polarization.* The local area fraction ϕ_A vs height z/a with the \hat{H} field applied upward in the region $z < L/4$ and $F^{ext} = 0$. The solid lines are simulation. $N = 1668$ particles are simulated in a square box of size $512a$ at $\phi_A^0 = 0.02$. The box is periodic in x but confined by no-flux walls at $z = 0, L$. $Pe_R = 0.2$, $D_T = a^2/\tau_R$. The inset checks the global force balance (2.3) and (2.4). 28
- 3.1 Π^W of ABPs confined between parallel walls in 2D. The inset shows the area fraction distribution $\phi(z)$. Here, $\ell = U_0\tau_R$ is the run length and $\delta = \sqrt{D_T\tau_R}$ is the microscopic length. The swimmer radius is a . H is the width of the channel. 39
- 3.2 Π^W of ABPs outside and inside a circle. Legends are as in Fig. 3.1. 40
- 3.3 Theoretical predictions of the force on an asymmetric body in 2D with curvatures R and $2R$ compared to ABP simulations. The symbols are simulation results and the solid lines were obtained by numerically solving for the n, m fields. The force is calculated from (3.2) with body normal \mathbf{n} and is scaled by the bulk active pressure $\Pi^\infty = n(k_B T + k_s T_s)$ 41
- 4.1 The formation of the boundary layer on the body surface. When a swimmer comes to the surface, it transmits a force to the wall of $\mathbf{F} = -\zeta \mathbf{U}_0 \cdot \mathbf{n}$. The swimmers form an accumulation boundary layer, with thickness on the order of $\delta = \sqrt{D_T\tau_R}$. The inner solution is solved in the local coordinate system q_1, q_2 , depending on the local curvature. The definition of the local curvature is shown in Fig. 4.2. 53

- 4.2 The local representation of an arbitrary curved surface. The two principal curvature directions are located in the two perpendicular planes. The local curvilinear coordinate system q_1, q_2, q_\perp is build on the surface, where locally it is orthogonal. q_\perp aligns with the normal vector \mathbf{n} pointing toward the outside of the shape at that point. The sign of principal curvatures κ_1 and κ_2 follows the convention shown here. 54
- 4.3 The number density n/n^∞ in two systems. In the left, $\lambda'\delta^2/|R| = \frac{1}{2\sqrt{6}} \approx 0.204$, and the outer solution $n_{out} = const = n^\infty$ still holds. In the right, $\lambda'\delta^2/|R| = \frac{1}{2}\sqrt{\frac{3}{2}} \approx 0.612$, and the outer solution $n_{out} = const = n^\infty$ is invalid. The left case is located at the $O(\delta/|R|)^2$ regime in Fig. 4.5, while the right case is located at the linear regime. 62
- 4.4 The scalar integration of pressure $\oint \Pi^{swim} dL$ on an asymmetric body immersed in ABPs. The dashed line is equation (4.67). The symbols are simulation results for $N = 40000$ particles equilibrated for $3000\tau_R$, and the solid lines are Finite Element solution for up to $10^4\tau_R$ to ensure a steady state is reached. 67
- 4.5 The net force \mathbf{F}^{net} on an asymmetric body immersed in ABPs. The body shape is shown in (4.3). The data is collected from the same simulations and PDE solutions in Fig. 4.4. The $O(\delta/|R|)^2$ and $O(\delta/|R|)$ asymptotic lines are for ease of view. 68
- 4.6 The origin of a non zero flux $j_{n,\perp}$. In the left, curvature is symmetric. On the right, the curvature is asymmetric. 70
- 5.1 The nematic order parameter $\tilde{Q} = \langle \mathbf{q}\mathbf{q} \rangle$ as a function of field strength $\chi_R = \epsilon/k_B T$ 80
- 5.2 \mathbf{D}^{swim} in the directions parallel and perpendicular to the field \hat{H} in 3D space. The solid lines are analytic solutions (5.12). 82

5.3	D^{swim} in the directions parallel and perpendicular to the field \hat{H} in a 2D layer. The solid lines are analytic solutions (5.26).	85
5.4	\hat{H} is the external field direction, and $U_0\mathbf{q}$ is the swim velocity of each ABP. $\mathbf{q} \cdot \hat{z} = \cos \theta$, $\hat{H} \cdot \hat{z} = \cos \varphi$. The normal vector of the bottom wall $\mathbf{n} = \hat{z}$	89
5.5	Comparison between the colloidal perspective and the continuum mechanics tensorial perspective. The solid lines are calculated analytically from (5.39), the open symbols are calculated from (5.36), solved by FEM solver with $\delta^2/\ell^2 = 0.2$ and $L = 20\ell$. The cross symbols are measured from particle-wall collisions in Brownian dynamics simulations, with $\ell = 4a$ and $\delta = 0$, in a box with $L = 128a = 32\ell$ and periodic in the horizontal direction.	90
5.6	Comparison between the colloidal perspective and the continuum mechanics tensorial perspective for the shear component, and the corresponding flux along the wall. The solid lines are calculated analytically from (5.39); the open symbols are data calculated from the same FEM solution as in Fig. 5.5.	92
5.7	The boundary layer structure for the case of $\chi_R = 1.6$ (left column) and $\chi_R = 0.4$ (right column), taken from the same data as shown in Fig. 5.5. Here n^∞ is the number density in the bulk, corresponding to the n in Fig. 5.5 and Fig. 5.6. z represents the height in this boundary layer. $m_t = \mathbf{m} \cdot \mathbf{t}$ is the tangential component of polar order m . For the \hat{H} in Fig. 5.4, m_t is towards the left on the bottom wall. For $\varphi = 0$, $m_t = 0$ everywhere as estimated by (5.42) and Fig. 5.6.	93

- 6.1 (A) The uniformly reactive sink particle and the Janus particle with orientation vector ξ . Both particles have radius a , interaction layer thickness δ and surface normal vector \mathbf{n} . A reactive surface is colored green and a non-reactive surface is blue. Motion ($\Delta \mathbf{X}$) of each Janus particle in a system is governed by the over-damped Langevin equation (6.6). (B) The concentration field c of reactive solute molecules (shown by the red dots) is solved simultaneously with the motion of the active particles. 103
- 6.2 Change of particle reactivity Δq_i in the vicinity of the removed test sink particle. Markers are simulation data and solid lines are the theoretical predictions for Brinkman screening (6.45). Simulation data are from a single configuration with $N = 625$, $\phi = 0.01$ (cubic periodic box = $64 \times 64 \times 64a^3$). Particles are randomly distributed. . 124
- 6.3 Change of particle reactivity Δq_i in the vicinity of the removed test Janus particle. Markers are simulation data and solid lines are the theoretical predictions for Brinkman screening (6.45). Simulation data are from a single configuration with $N = 625$, $\phi = 0.01$ (cubic periodic box = $64 \times 64 \times 64a^3$). Particles are randomly distributed. . 125
- 6.4 Reactivity $\langle q \rangle / q_0$ of the sink system for different values of the fuel strength: (A) $S_D = 0.3$, (B) $S_D = 0.9$, and (C) $S_D = 6.0$ for $\phi = 0.04$, and $Da = 2.0$. There are $N = 2503$ particles in the cubic periodic unit cell. All cases start from a randomly distributed particle configuration. Particles are colored by reactivity $\langle q \rangle / q_0$. (A) is a system snapshot at steady state. (B1) and (C1) are snapshots in transient states and (B2) & (C2) are at the steady states, respectively. 130

- 6.5 Probability distribution of local particle volume fraction ϕ_p at the steady state. Here $\phi = 0.04$, $Da = 2.0$, $N = 2503$ and the periodic box = $64 \times 64 \times 64a^3$. The steady state configurations are A, B2 and C2 in Fig. 6.4. 131
- 6.6 Snapshot at steady state of a monolayer of Janus particles. Blue is the non-reactive part and green is the reactive hemisphere. The Janus particles are confined within the circular wall shown in the figure. The wall has no effect on the solute concentration field. $N = 2048$, $S_D = 30$, $Da = 5$, $R_{\text{wall}} = 128a$. Only 1/4 of the simulated system is shown. 135
- 6.7 The area fraction ϕ_A measured from simulation (black symbols), ϕ_A predicted by the model (red curve), and the average osmotic force $\langle F^{osmo} \rangle$ (blue symbols) as defined in (6.30). Since the orientation distribution is still isotropic, the osmotic force is dominated by the diffusiophoretic force: $\langle F^{osmo} \rangle \approx \langle F^{\nabla c} \rangle$. A negative diffusiophoretic force means a force directed towards the center $r = 0$; the solid blue line is the reference for $n\langle F^{\nabla c} \rangle = 0$. $N = 2048$, $S_D = 60.0$, $Da = 5.0$, $r_{\text{wall}} = 256a$. Data is collected from a steady state period of $t = 5000a^2/D$ 136
- 6.8 Reactant concentration c and velocity $Pe_p = Ua/D$ along the radial direction. The boundary condition is $c/c^\infty = 1$ as $r \rightarrow \infty$. Data is collected from the same simulation as in Fig. 6.7. 137
- 6.9 The collision pressure Π^P and swim pressure Π^{swim} . Data is collected from the same simulation of Fig. 6.8. 141
- 6.10 The product $\phi_A c/c^\infty$ as a function of r . Data is collected from the same simulation as Fig. 6.8. It is clear that in the dilute region $\phi_A c/c^\infty$ is approximately a constant. The fluctuation is due to the noise in the $c(r)/c^\infty$ measurement in Fig. 6.8. 145

7.1	Motion functions of a Janus particle \hat{P} , \hat{M} , \hat{A} and a uniformly reactive particle \hat{M}_u	161
7.2	The instability dispersion relation $\sigma(q)$ for uniformly reactive particles $P = A = 0$ at $Da = 2$. The theory is given by (7.28), and the simulation is extracted from an ensemble of 1200 systems with $N = 1668$ particles in a periodic box size $L = 512a$. $\phi = 0.02$ and $M_{C0}/D_T = 2$	171
7.3	The instability dispersion relation $\sigma(q)$ for $Da = 5$ Janus particles. The theory is (7.28) with the first correction of $O(P^2)$, and the simulations are averaged over an ensemble of 1200 systems. $N = 1668$ particles are simulated with periodic box size $L = 512a$. $\phi = 0.02$. $M_C = (M + A/2)c_0/D_T = 12 \gg M_C^* = 1$ to ensure that instability is significant for quantitative measurement, but not too large to go beyond the linear instability regime.	176
7.4	The parameter space (M_C, Da) and the instability threshold $M_C^* = 1$. The threshold is the same for arbitrary D_{rot} and arbitrary number density as long as it is dilute $\mathcal{P}_0 \rightarrow 0$. The colormap is for a single particle's non-dimensionalized swim velocity $c_0P/(D_T/a)$. Faster chemical reaction (larger Da) and more 'fuel' (higher c_0) gives higher swim velocity.	179
7.5	The instability dispersion relation $\sigma(q)$ for $Da = 0.02$ and $Da = 5$ Janus particles. The symbols are numerical results for M_{ins}^∞ truncated at 15×15 . The solid lines $\sigma(q)$ and the σ_{max} are calculated with the $O(P^3)$ full solution in Appendix (L). $a^2D_{rot} = D_T$ and $\phi_0 = 0.02$ is fixed.	180

- 7.6 Comparison between the coarse-grained monolayer solution $\sigma_{cg}(q)$ with the exact solution. The symbols are calculated from the coarse-grained model and the solid lines are the analytical solutions up to $O(P^2)$ solved in §7.3, corresponding to different value of D_{rot} . $Da = 5, M_C = 10, \phi_A = \pi a^2 n = 0.02$ are fixed. 184
- 7.7 Comparison between the $\phi \propto 1/U_0$ theory and the simulation measurement. ∇U_0 is applied in the y direction. $N = 1000$ ABPs are simulated in a periodic box $L_x = L_y = 250a$. $\phi_A^0 = 0.02$. Local ϕ_A is extracted by building Voronoi cells of each particle and is averaged for 500 snapshots of the steady state. $D_T = 0$ 186
- 8.1 The distribution of particle reaction q and local volume fraction ϕ_p , and their correlation. A: The snapshot of the equilibrium structure of system in a periodic box of $42a \times 42a \times 42a$, with $\phi = 4.88\%$, $Da = 2.0, N = 864, S_D = -15.0, \Gamma_c \approx 20$. Each particle is colored by q/q_0 . B: The same system, but equilibrated with stronger repulsion $S_D = -60.0, \Gamma_c \approx 80$ 196
- 8.2 The measurement of structural change of BCC and FCC crystals, both for $Da = 2.0$. $\phi = 3.88\%$ for BCC system and $\phi = 4.88\%$ for FCC system. 198
- 8.3 The measurement Q_6 of BCC. For each combination of ϕ (shape) and Da (color), simulations of different S_D are conducted so that a range of $100 < \Gamma_c < 250$ is covered. The melting point $\Gamma_c^{BCC} \approx 140$ 200
- 8.4 The measurement Q_6 of FCC. For each combination of ϕ (shape) and Da (color), simulations of different S_D are conducted so that a range of $100 < \Gamma_c < 250$ is covered. The melting point $\Gamma_c^{FCC} \approx 140$ 201

Chapter 1

INTRODUCTION

Active matter refers to a material that consists of individual particles or bodies capable of propelling themselves, that is, they ‘swim’. The concept of activity comes from swimming micro-organisms such as *E. Coli*, and is extended to synthetic chemical swimmers (Paxton *et al.*, 2006; Ebbens *et al.*, 2010). The artificial structures are based on various different mechanisms, including electrophoresis (Paxton *et al.*, 2006), bubble-generation (Manjare *et al.*, 2012), thermophoresis (Baraban *et al.*, 2013), de-mixing (Würger, 2015; Samin & van Roij, 2015), surface tension (Kitahata *et al.*, 2013), self-diffusiophoresis (Theurkauff *et al.*, 2012), biochemical reactions (Sengupta *et al.*, 2014) and so on. The size of swimmers can be as large as cm-sized ‘camphor boats’ (Kitahata *et al.*, 2013; Soh *et al.*, 2008) moving at cm s^{-1} , and can be as small as Å-sized biomolecules (Dey *et al.*, 2016). In most cases, they are μm -sized synthetic structures or micro-organisms, moving at a velocity on the order of $\mu\text{m s}^{-1}$. Almost all mechanisms rely on the creation of some asymmetric field by the objects, which then push themselves through the fluid.

Each active particle propels itself at some velocity $U_0\mathbf{q}$, where \mathbf{q} is the propulsion direction, and is subject to random (Brownian) reorientation on a time scale τ_R . For cm-sized ‘camphor boats’ (Kitahata *et al.*, 2013), the rotational re-orientation is almost absent and therefore the swimmers show directed motion. For Å-sized biomolecules, the rotational reorientation is so fast that the swimmers are purely diffusive. Theoretically, there is a transition from directed motion below the timescale of τ_R to diffusive motion at timescale longer than τ_R . Howse *et al.*, (2007) showed that the translational diffusion of a single active particle is enhanced by the swim diffusivity $D^{swim} = U_0^2\tau_R/6$ on timescales longer than τ_R , due to the fluctuation of \mathbf{q} . The fluctuation of \mathbf{q} can be either Brownian (thermal) for synthetic Janus particles, or non-Brownian for micro-organisms that ‘choose’ to swim in a different direction.

Collectively, active matter shows a lot of interesting behaviors, roughly due to three reasons. First, they can push themselves so they keep moving even in a very crowded

environment, which can push the glass transition to the random close packing limit (Berthier & Kurchan, 2013; Ni *et al.*, 2013). Second, they swim with some direction \mathbf{q} , and that can be manipulated with either the flow field or an external force field to induce phenomena like shear-trapping (Rusconi *et al.*, 2014), rheotaxis (Uspal *et al.*, 2015; Kaya & Koser, 2012) and gyrotaxis¹(Durham *et al.*, 2011; ten Hagen *et al.*, 2014). Last, but very importantly, they interact with each other through the fluid medium, the field that causes self propulsion, and/or simply geometric from non-overlapping collisions. Due to the interactions, active matter displays very interesting phenomena, such as enhanced diffusion (Dey *et al.*, 2016; Miño *et al.*, 2011), autonomous pattern-generation (Cohen & Golestanian, 2014; Delmotte *et al.*, 2015; Saintillan & Shelley, 2011; Wioland *et al.*, 2013), Casimir effect (Ray *et al.*, 2014), and meso-scale turbulence (Wensink *et al.*, 2012; Dunkel *et al.*, 2013). Also, the interaction of active matter with passive objects can be very interesting. For example, a passive tracer body shows abnormal diffusion behavior in active matter (Patteson *et al.*, 2016; Peng *et al.*, 2016).

Alongside scientific interests, some potential applications of active matter have been investigated. They can be used for microscopic ‘cargo transportation’² (Baraban *et al.*, 2012; Burdick *et al.*, 2008; Felderhof, 2014; Popescu *et al.*, 2011; Sasaki *et al.*, 2014), especially for drug delivery (Gao & Wang, 2014). When fixed in space, they keep pushing the surrounding fluid and therefore can be used as pumps (Michelin *et al.*, 2015), ranging from Å-sized enzyme pumps (Sengupta *et al.*, 2014), to cm-sized ones (Zhang *et al.*, 2015) that are able to generate finite-Reynolds-number laminar flow. Also, their intriguing interaction with passive objects can be harnessed to generate net motion in active matter. For example, bacteria close to a no-slip wall may show rheotaxis due to the hydrodynamic interactions between the bacteria and the wall (Kaiser *et al.*, 2014).

¹The directed motion due to gravitational and viscous torques in a flow.

²The movement of small objects.

One of the most notable phenomena of active matter is that they may show coexistence of dilute and dense regions in a single system at steady state. In the experiment by Theurkauff *et al.*, (2012), Janus particles in a solute reservoir and were kept in evolution to a steady state under a tilted gravity acting as a sedimentation force. At steady state the system separated into dense and dilute regions. Similar phenomena is also observed in another experiment system by Palacci *et al.*, (2013), where the dense part forms a ‘moving-crystal’. Particles with repulsive interaction show transition between uncorrelated motion and an ordered lattice (Soh *et al.*, 2008).

To understand the intriguing phenomena of active matter, different models have been proposed. The traditional approach is to track each swimmer with the probability $P(\mathbf{x}, \mathbf{q}, t)$ of finding it at location \mathbf{x} , orientation \mathbf{q} , at time t . $P(\mathbf{x}, \mathbf{q}, t)$ can tracked with Smoluchowski or Fokker-Planck equations (Saintillan & Shelley, 2015). This approach is powerful in giving very detailed information of the system with the entire trajectory in the phase-space (\mathbf{x}, \mathbf{q}) . However, this approach is limited to a ‘mean-field’ description, since solving $P(\mathbf{x}, \mathbf{q}, t)$ with particle-particle interaction is highly challenging beyond the two-body level.

Recently, the minimum Active Brownian Particle (ABP) model exhibits profound physical implications despite its simplicity. In ABPs, the particle’s self-propulsion velocity $\mathbf{U}_0 = U_0 \mathbf{q}$, where U_0 is usually assumed to be a given constant and \mathbf{q} is subject to rotational Brownian diffusivity $D_R = 1/\tau_R$. Also, the interaction between ABPs is usually assumed to be collision only (pure repulsive) (Solon *et al.*, 2015a) or a pairwise additive potential (Redner *et al.*, 2013). Under these conditions, the interaction between ABPs are short-ranged and additive, and therefore can be successfully explained by thermodynamic-type models, such as the ϕ^4 field theory (Wittkowski *et al.*, 2014), density functional theory (Menzel & Löwen, 2013), and motility-induced-phase-separation (Stenhammar *et al.*, 2013; Cates & Tailleur, 2015). For example, the dilute-dense coexistence of active matter can be explained as a first-order gas-liquid phase transition, with the introduction of swim pressure

as the Equation of State (Takatori *et al.*, 2014; Takatori & Brady, 2015).

The swim pressure is an analogy to the classical gas pressure, and is defined through the swimming diffusivity D^{swim} and drag coefficient on each swimmer ζ : $\sigma^{swim} = -n\zeta D^{swim}$. The swim pressure is the pressure required to confine the active particles within a fixed volume, and is the sum of all particles' collisional force on the container wall. It is in essence the counterpart to the osmotic pressure $\sigma = -n\zeta D = -nk_B T$ in passive Brownian particles. Therefore, swim pressure is a well posed *mechanical* pressure, and is therefore fully compatible with classic continuum mechanics. From a thermodynamic perspective, the swim pressure can be written as $\sigma^{swim} = -nk_s T_s$, where $k_s T_s$ corresponds to $k_B T$. For swimmers subject to translational Brownian motion, swim pressure and osmotic pressure are additive, and the total pressure (stress) is $\sigma = -n(k_B T + k_s T_s)$.

The classical ideal gas pressure is defined on the macroscopic scale, i.e., the length scale larger than the molecules' mean free path, and the time scale longer than molecules' collisions. It is also true for swim pressure, but the length and time scales are different because swimmers' direction \mathbf{q} may change due to Brownian motion instead of particle-particle collisions, and \mathbf{q} keeps changing on the reorient time τ_R . On time scales longer than τ_R , the motion of swimmers become diffusive with run-length $\ell = U_0 \tau_R$. Therefore, swim pressure is only meaningful on length scales longer than the run-length ℓ and time scales longer than τ_R .

In this thesis, we shall see that the applicability of swim pressure is beyond the description of a homogeneous, 'thermodynamical equilibrium' state. It can be used in a continuum mechanics formulation to *predict* the deformation and motion of general active matter. Continuum mechanics for general active matter is further discussed in the following chapters. In Chapter 2, the net (as opposed to random) motion of active matter resulting from an average swim (or propulsive) force is discussed, as the introduction of 'swim force'. It is shown that the average swim

force acts like a body force – an *internal* body force. As a result, the particle-pressure exerted on a container wall is the sum of the swim pressure (Takatori *et al.*, 2014) and the ‘weight’ of the active particles. A continuum description is possible when variations occur on scales larger than the run length of the active particles and gives a Boltzmann-like distribution from a balance of the swim force and the swim pressure. Active particles may also display ‘action at a distance’ and accumulate adjacent to (or be depleted from) a boundary without any external forces.

In Chapter 3, the microscopic origin of the swim pressure at the sub-continuum scale is analyzed. A general theory is proposed for determining the force (and torque) exerted on a boundary (or body) in active matter. The theory extends the description of passive Brownian colloids to self-propelled active particles and applies for all ratios of the thermal energy $k_B T$ to the swimmer’s activity $k_s T_s = \zeta U_0^2 \tau_R / 6$, where ζ is the Stokes drag coefficient, U_0 is the swim speed and τ_R is the reorientation time of the active particles. The theory, which is valid on all length and time scales, has a natural microscopic length scale over which concentration and orientation distributions are confined near boundaries, but the microscopic length does not appear in the force. The swim pressure emerges naturally and dominates the behavior when the boundary size is large compared to the swimmer’s run length $\ell = U_0 \tau_R$. The theory is also used to predict the motion of bodies of all sizes immersed in active matter.

In Chapter 4, the results from Chapter 3 are extended to boundaries of arbitrary shape. In the absence of translational Brownian motion, a swimmer is trapped for a time τ_R on the wall until it reorients. When $D_T > 0$, the swimmer is able to leave the wall with a Brownian hop on a microscopic length scale $\delta = \sqrt{D_T \tau_R}$ within τ_R . On the thickness of δ near the wall, swimmers accumulate and form a concentration boundary layer. The boundary layer structure is solved to calculate the swim pressure distribution and the total force (torque) on an arbitrarily shaped body immersed in swimmers, with a general scaling of the curvature effect $\Pi^{swim} \sim \lambda \delta^2 / L$, where

$$\lambda = \sqrt{2 \left(1 + \frac{\ell^2}{6\delta^2}\right)} / \delta.$$

In Chapter 5 Active Brownian Particles (ABPs) with a nematic orientation field are shown to exhibit greatly enhanced anisotropic swimming diffusivity D^{swim} . More importantly, the anisotropic D^{swim} leads to a tensorial anisotropic swimming stress $\sigma^{swim} = -n\zeta D^{swim}$, i.e., the pressure on a flat wall can be written as $\Pi^W = (\sigma^{swim} \cdot \mathbf{n}) \cdot \mathbf{n}$. Further, this tensorial continuum mechanics view is consistent with the microscopic view of $\Pi^W = n^{wall} \zeta D_T$, through the formation of a boundary layer discussed in Chapter 3 and 4. This work extends the notion of swim pressure to a tensorial swim stress.

The discussions in these chapters are for a simple ABP model with excluded volume interactions only, but that constitutes the foundation of a mechanical view for general active matter. The mechanical view is a powerful tool to understand chemically active particles driven by diffusiophoresis.

Diffusiophoresis refers to the motion of small particles resulting from a concentration gradient of a chemical solute. It is a fundamental process that occurs in both natural and engineering settings (Anderson, 1989). Traditionally, the concentration gradient of a chemical solute is imposed externally in diffusiophoretic problems. In the context of active particles driven by self-diffusiophoresis, the particles create the concentration gradient themselves through surface catalytic reactions. Particles are usually synthesized with patterned asymmetry, i.e., patterned particle shape (Wei & Jan, 2010) and/or patterned particle surface reactivity (Ebbens & Howse, 2011). Usually they are synthesized to be reactive on one half while non-reactive on the other, and therefore are named *Janus* particles (Theurkauff *et al.*, 2012; Howse *et al.*, 2007).

On the single particle level, Córdova-Figueroa & Brady, (2008) and Brady, (2011) showed that a particle's motion can be determined by solving the solute concentration field $c(\mathbf{r})$ around the particle. To leading order, the swim velocity $U_0 \propto c$. They

swim faster with more ‘fuel’ concentration c . In the presence of many particles, the disturbance on $c(\mathbf{r})$ caused by each particle propagates, and causes not only changes of swim velocity, but also particle-particle attraction or repulsion due to diffusiophoresis $\propto \nabla c$. In fact, in a many-body system, the interaction is more complicated than a simple sum of all $1/r$ perturbations. As directed by the boundary condition of solute on the particle’s surface (1.3), the particles may *adjust* their perturbations to the field and can therefore *compensate* for the fluctuations in perturbation, as described with the chemical screening theory (Morris & Brady, 1995). This complicated ‘field-driven’ nature results in fundamentally different system behaviors from the ABPs.

In fact, such ‘field-driven’ systems are common in active matter. The swimmers may interact with each other through some fields, including the Stokes flow field \mathbf{u} (hydrodynamics) (Berke *et al.*, 2008), chemical solutes concentration field c (diffusiophoresis) (Theurkauff *et al.*, 2012; Derjaguin & Golovanov, 1984), temperature field T (thermophoresis) (Baraban *et al.*, 2013), electrostatic field Φ , and so on. Almost every field ϕ is governed by a transport-type equation (Bonnecaze & Brady, 1990):

$$\frac{\partial \phi}{\partial t} + \nabla \cdot \mathbf{j}_\phi = 0, \quad (1.1)$$

$$\mathbf{j}_\phi = \mathbf{u}\phi - D\nabla\phi, \quad (1.2)$$

where D can be diffusivity of c , conductivity of T , electrical conductivity of Φ , and so on. And it is well known that the disturbance caused by one swimmer in that field ϕ propagates as $1/r$; for example, the potential of a point charge is $\Phi = e/(4\pi\epsilon_0 r)$. More importantly, the above field is subject to the boundary condition on each swimmers’ surface, and is dependent on the local value of ϕ and the surface property:

$$\mathbf{j}_\phi(\mathbf{r} \text{ on swimmer}) \sim \phi. \quad (1.3)$$

This means, in general, that the swimmers' disturbances cannot be treated as a *prescribed* 'fixed charge' e , but should be found as a *solution* to the transport equation. Therefore, the interactions between swimmers is neither short-ranged nor pairwise-additive. Instead, the entire field ϕ must be *solved*, following the swimmers' motion.

In this thesis, diffusiophoresis in a chemical solute concentration field is chosen as an example, because self-diffusiophoresis is one of the most common experimental realizations of self-propulsion mechanisms, and because a thorough understanding of the diffusion field is portable to other physical settings. In diffusiophoresis, the field ϕ is the concentration field c , D is the diffusivity of the solutes, and the boundary condition (1.3) is assumed to be a first order reaction $\mathbf{j}_c \propto c$. To solve that field, we improve the method by Bonnetcaze & Brady, (1990, 1991a,b), with a matrix-free formulation as the Accelerated Stokesian Dynamics (Sierou & Brady, 2001). The method is implemented with GPU and is highly efficient.

The efficient simulation method allows us to investigate the most fundamental questions for active matter: the coexistence (separation, clustering) of dense and dilute regions at steady state. When does the separation start from a homogeneous state? When does the coexistence reach a steady state? What is the role of the solute concentration field c ? Is the theory applicable to generalized active matter?

To answer these questions, in Chapter 6, the simulation algorithm is introduced. It allows tracking of thousands of chemically active particles, with simultaneous solution of the chemical solute field c in a multipole expansion method. With simulation results, we first clarify the notion of chemical screening (Morris & Brady, 1995). It fundamentally changes the particle-particle interactions in chemically active suspensions. Then, the dynamics of both uniformly reactive and Janus particles are discussed. Simulations show that uniformly reactive particles, which do not self-propel, form clusters but no coexistence is observed. It indicates that an instability

threshold of the clustering process may exist. Janus particles show coexistence, and a continuum mechanics model is proposed to explain the ‘equilibrium’ condition.

In Chapter 7, the question of when chemically active particles separate into dense and dilute parts is answered with an analytic solution of a linear instability analysis. The instability threshold and the orientation order in the development are calculated for geometries of both monolayer and 3D periodic systems. We found a universal instability threshold $M_C^* = 1$ independent of geometry, self-propulsion, and particle number density in the dilute limit. The effect of self-propulsion is found to be on the order of $O(-q^3)$, a higher order of wavenumber q than the translational diffusion and down-gradient diffusiophoresis at $O(q^2)$. Coarse-grained models are also discussed, and their connections to the continuum mechanics of active matter are clarified. Theories are verified by detailed particle-tracking simulations.

In Chapter 8, the analysis is extended from attractive chemically active particles to repulsive ones. Repulsive self-diffusiophoretic particles with homogeneous surface catalytic reaction are investigated with simulations. By a mapping to the classical one component plasma (OCP) system, the system behavior can be described by a coupling parameter Γ_c , which compares the strength of diffusiophoretic repulsion and translational Brownian motion. When confined in a constant-volume constraint, Body-Centered Cubic crystals may form, and the ‘melting point’ of the ‘liquid-crystal transition’ is $\Gamma_c^{BCC} \approx 140$. The Face-Centered Cubic lattice is also stable above $\Gamma_c^{FCC} \approx 140$.

The thesis concludes with a brief summary of the key results and a discussion of future directions of this work.

Chapter 2

THE SWIM FORCE AS A BODY FORCE

1. Yan, W. & Brady, J. F. The swim force as a body force. *Soft Matter* **11**, 6235–6244 (2015).

2.1 Introduction

The soft matter community has proposed several theoretical approaches to investigate the behavior of active matter systems. Thermodynamic-type models, such as the ϕ^4 field theory (Wittkowski *et al.*, 2014), motility-induced-phase-separation (MIPS) (Stenhammar *et al.*, 2013; Cates & Tailleur, 2015), and density functional theory (Menzel & Löwen, 2013), treat active matter as a single substance and try to fit it into the classical framework of the states of matter. For example, the dilute-dense coexistence of active matter can be formulated as a first-order gas-liquid phase transition (Takatori *et al.*, 2014; Takatori & Brady, 2015).

Despite their success in explaining some states of active soft matter, thermodynamic models are not sufficient when the detailed dynamics, structure and deformation are of interest, especially when external perturbations are applied. In these situations, Fokker-Planck or Smoluchowski equations are often used as they directly relate the individual swimmer's Langevin equation to the position-orientation (\mathbf{x}, \mathbf{q}) phase space probability density $P(\mathbf{x}, \mathbf{q}, t)$, which gives all the detailed information of interest. Active matter under an external force (Hennes *et al.*, 2014), polarization (Takatori & Brady, 2014), and rectification (Tailleur & Cates, 2009) have been investigated with this approach. When the detailed chemical propulsion mechanism or hydrodynamic interaction are considered, $P(\mathbf{x}, \mathbf{q}, t)$ can be solved together with the conservation equation for chemical species concentration $c(\mathbf{x}, t)$ or the flow field $\mathbf{u}(\mathbf{x}, t)$, allowing detailed knowledge of the dynamics, such as the system's stability (Lushi *et al.*, 2012).

The Smoluchowski approach, however, is not able to treat concentrated systems where particle-particle interactions are important, even for the simplest excluded volume interactions. For dense active matter, simulation is the standard approach. Active Brownian dynamics simulations of as many as 10^7 particles have been reported in order to investigate phase behavior (Stenhammar *et al.*, 2014). A few

simulations of active matter with hydrodynamic interactions have also been reported (Lefauve & Saintillan, 2014; Li *et al.*, 2015).

Even with a wealth of simulation data, some fundamental questions remain. For example, how does one *predict* the force exerted on a boundary by (dense) active matter? Simulations give an *a posteriori* determination of the force (Yang *et al.*, 2014; Mallory *et al.*, 2014), while the Smoluchowski approach can be used but only for dilute systems when particle-particle interactions are ignored (Fily *et al.*, 2014a).

For conventional atomic or molecular matter, at the particle level there are Newton's laws of motion and their phase-space equivalent the Liouville equation. For active colloids, the corresponding particle-level equations are the Langevin equation and the Smoluchowski equation. Thermodynamics, whether for conventional or active matter, does not permit any spatial or temporal variation in properties and thus, while powerful, has its limitations. To bridge the gap between the detailed particle and the thermodynamic levels, conventional matter employs continuum mechanics which applies out of equilibrium for slow spatial and temporal variations. The purpose of this work is to investigate and develop an analogous continuum mechanics description for active matter.

In conventional matter, forces at the particle level do not manifest themselves in the continuum momentum balance unless they are *external* body forces. Interparticle forces contribute to the continuum stress, but do not act as net forces at the continuum level. For active matter the situation is more complex and more interesting. As we show, the propulsive swim force acting at the particle level that causes particles to move is part of the hydrodynamic force the particles exert on the fluid, and thus when considering the momentum balance for the suspension – the mixture of particles plus fluid – there is no net hydrodynamic force and thus no net swim force acting on the mixture; only *external* body forces appear. However, the suspension is a two-phase mixture of active particles and fluid and in the continuum momentum

balance for the *particle phase* we show that a net swim force appears directly and acts as an *internal* body force. This net swim force is crucial for describing the dynamics of active matter and for computing forces exerted on boundaries.

The swim force plays a pivotal role in the swim pressure (Takatori *et al.*, 2014), the introduction of which provided a new approach to understanding the behavior of active matter. Active Brownian Particles (ABPs) that separate into dilute and dense regions are now understood as a ‘gas-liquid’ coexistence. The decrease in the swim pressure with concentration destabilizes the system resulting in phase separation (Takatori *et al.*, 2014; Takatori & Brady, 2015). The swim pressure is analogous to the osmotic pressure of a chemical solute or of passive Brownian particles and is the pressure needed to confine the active particles. In the dilute limit the “ideal gas” swim pressure is $\Pi^{swim} = n\zeta U_0^2 \tau_R / 6$ (in 3D), where n is the number density of active particles, ζ is their drag coefficient, U_0 is the swim speed, and τ_R is their reorientation time (Takatori *et al.*, 2014).

While the swim pressure can be understood solely in terms of this entropic confinement pressure and is independent of the size of the swimmers (Takatori *et al.*, 2014), micromechanically, the swim stress is given by the moment of the swim force $\langle \boldsymbol{\sigma}^{swim} \rangle = -n \langle \boldsymbol{x} \boldsymbol{F}^{swim} \rangle$, where $\boldsymbol{F}^{swim} = \zeta U_0 \boldsymbol{q}$, with \boldsymbol{q} the orientation vector of the swimmer and \boldsymbol{x} its position. The position is simply $\boldsymbol{x}(t) = \int^t U_0 \boldsymbol{q}(t') dt'$, and thus, $\boldsymbol{\sigma}^{swim} = -n\zeta U_0^2 \int^t \langle \boldsymbol{q}(t) \boldsymbol{q}(t') \rangle dt' = -n\zeta U_0^2 \tau_R / 6 \boldsymbol{I}$ (for times $t \gg \tau_R$), arising from the random reorientation of the swimmer: $\langle \boldsymbol{q}(t) \boldsymbol{q}(t') \rangle = (\boldsymbol{I}/3) \exp\{-2(t-t')/\tau_R\}$. The ‘moment arm’ for the swim stress is the swimmer’s run length, $\ell = U_0 \tau_R$.

The micromechanical definition of the swim stress thus involves the swim force, which leads to questions about the ‘force-free’ nature of low-Reynolds number swimming. Furthermore, the swim stress sparked some recent discussion (Solon *et al.*, 2015a) about whether it is a true stress – is it equal to the force per unit area on the bounding walls? – especially when the dynamics give rise to polar order: a

non-zero average orientation of the particles, $\langle \mathbf{q} \rangle \neq 0$.

In this chapter we first show the origin and definition of the swim force that is consistent with the notion of ‘force-free’ motion. We then establish the global force (or momentum) balance for active matter, focusing on the case when there is net polar order $\langle \mathbf{q} \rangle$, which corresponds to an average swim force $\langle \mathbf{F}^{swim} \rangle$. We show that in the momentum balance for the active particles the average swim force acts just like a body force, with the result that the force/area exerted by active matter on a bounding wall is the sum of the swim pressure and the ‘weight’ of the active particles. Thus, the questions raised in Solon et al (Solon *et al.*, 2015b) are straightforwardly resolved and in a manner completely consistent with one’s intuition about forces and pressures.

Further, we show that a sedimentation-like system is achieved for $\langle \mathbf{F}^{swim} \rangle \neq 0$ without any external body force and a continuum Boltzmann distribution holds just as for passive Brownian particles in a gravitational field. Active particles may also accumulate adjacent to (or be depleted from) a boundary, for example in response to an external stimulus (chemical, light, etc.). The interesting aspect is that this accumulation (depletion) occurs without there being any external force acting on the particles; it is a true ‘action at a distance’.

Although an average swim force acting like a body force arises naturally from the particle-level dynamics, it is nevertheless surprising since, as mentioned before, it does *not* appear in the macroscopic momentum balance for the entire suspension, or mixture, of particles plus fluid.

2.2 The swim force

In self-propulsion at low Reynolds number by ‘force-free’ one means that there is no *external* force causing the body to move. The ‘*internal*’ forces that cause it to move arise from deformation of the body surface and are part of the total hydrodynamic

force (and torque), which, from the linearity of Stokes flow, can be written as

$$\begin{aligned}\mathcal{F}^H &= \underbrace{-\mathbf{R}_{\mathcal{F}\mathcal{U}} \cdot \mathcal{U}}_{\mathcal{F}^{drag}} - \underbrace{\mathbf{R}_{\mathcal{F}E} : \mathbf{E}^s - \mathbf{R}_{\mathcal{F}B} \odot \mathbf{B}^s - \dots}_{\mathcal{F}^{swim}}, \\ &= \mathcal{F}^{drag} + \mathcal{F}^{swim},\end{aligned}\quad (2.1)$$

where we have grouped the force/torque together as a single vector, $\mathcal{F}^H = (\mathbf{F}^H, \mathbf{L}^H)$, and similarly for the translational/rotational velocities: $\mathcal{U} = (\mathbf{U}, \mathbf{\Omega})$. The hydrodynamic tensors $\mathbf{R}_{\mathcal{F}\mathcal{U}}$, $\mathbf{R}_{\mathcal{F}E}$, etc. are functions of the body geometry only and couple the force to the velocity, to the ‘squirming set’ $\mathbf{E}^s(t)$, $\mathbf{B}^s(t)$, etc., which characterize the ‘slip’ velocity at the body surface. A derivation of (2.1) can be found in Appendix A.

In (2.1) the hydrodynamic force/torque is written as a sum of two terms: (i) the hydrodynamic drag \mathcal{F}^{drag} and (ii) the propulsive or ‘swim’ force \mathcal{F}^{swim} . Equation (2.1) provides the *definition* of the swim force. That it is a real measurable force can be appreciated by recognizing that if one wanted to keep the swimmer from moving, say by trapping it with optical tweezers, the force/torque the trap would exert is precisely \mathcal{F}^{swim} .

In addition to the hydrodynamic drag and swim force, active particles can also be subject to thermal Brownian motion ($\mathcal{F}^B = 2k_B T \mathbf{R}_{\mathcal{F}\mathcal{U}} \delta(t)$), external forces such as buoyancy (\mathcal{F}^{ext}), and interparticle forces, for example repulsive interactions to prevent overlap at finite concentrations (\mathcal{F}^P)¹.

In the simplest model of active particles the hydrodynamic resistance tensor is an isotropic drag tensor $\mathbf{R}_{FU} = \zeta \mathbf{I}$ and the swim force is $\mathbf{F}^{swim} = \zeta U_0 \mathbf{q}$. This is the ‘Active Brownian Particle’ (ABP) model:

$$0 = -\zeta \mathbf{U} + \mathbf{F}^{swim} + \mathbf{F}^B + \mathbf{F}^{ext} + \mathbf{F}^P. \quad (2.2)$$

The orientation vector \mathbf{q} is subject to run-and-tumble or rotational Brownian diffusion ($D_R = 1/\tau_R$), which are equivalent (Cates & Tailleur, 2013), and follows

¹Hydrodynamic shear forces can also be present, but are not considered here; they enter in Eq. (2.1).

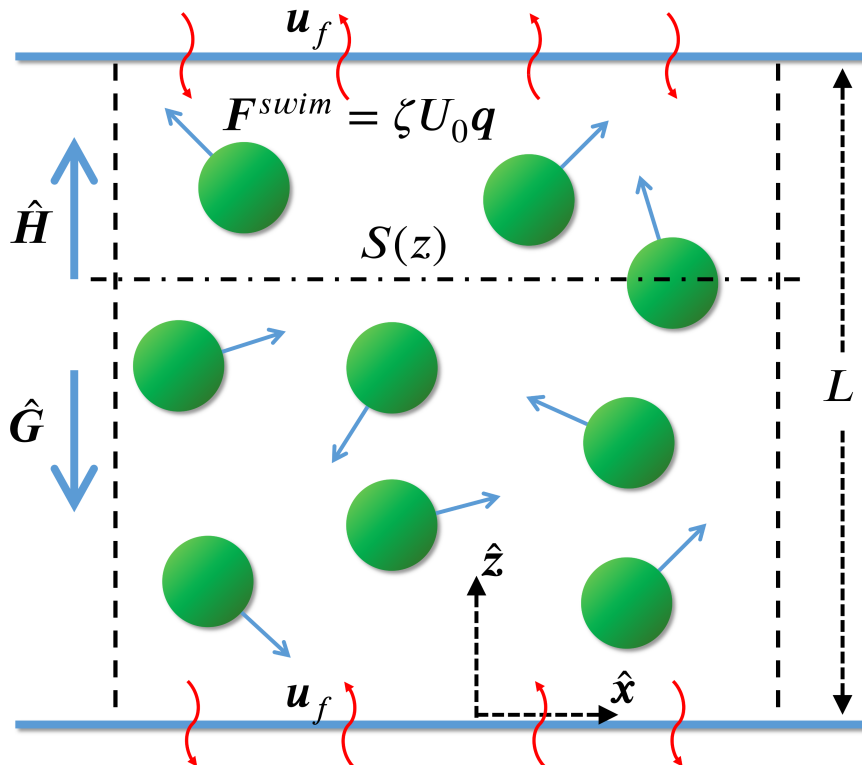


Figure 2.1: Active Brownian Particles (ABPs) in a container of height L in the z -direction and periodic in the x - and y -directions. Each active particle experiences a swim force $\mathbf{F}^{swim} = \zeta U_0 \mathbf{q}$, with $\mathbf{q}(t)$ the direction of swimming. An external gravitational ($\hat{\mathbf{G}}$) and polarization ($\hat{\mathbf{H}}$) field may also be applied. The top and bottom boundaries do not allow the particles to escape (no flux), but the flow of fluid \mathbf{u}_f is unimpeded – they are osmotic barriers. The horizontal plane $S(z)$ is the cross-section considered in global force balance (2.4).

directly from the torque balance. For a spherical swimmer, $\zeta = 6\pi\eta a$, where a is the particle size and η the viscosity of the suspending Newtonian fluid. A more detailed derivation of (2.2) can be found in Appendix B.

In this chapter we focus on the ABP (Active Brownian Particle) model (Eq. (2.2)), with both translational and rotational diffusion: D_T, D_R . The reorientation time is $\tau_R = 1/D_R$. The relative importance of advection by swimming to translational swim diffusion is given by the reorientation Péclet number (Takatori *et al.*, 2014) $Pe_R = U_0 a / (6D^{swim}) = a / U_0 \tau_R$, and is also the ratio of the particle size to the swimmer's run length.

2.3 The global force balance

Consider a very simple geometry where N swimmers are placed between two parallel walls separated by a distance L whose normals are along the z -direction as illustrated in Fig. 2.1. The walls are of large extent (infinite) and system can be taken to be periodic in the x - and y -directions. The walls are non-penetrating to swimmers but allow the solvent to pass through unimpeded – they are osmotic barriers. Each swimmer i experiences a wall force \mathbf{F}_i^W when it “collides” with a wall. The separation L between the walls is sufficiently large so that the swimmers are able to execute their random swim motion before colliding with the walls – the swimmer’s size a and run length ℓ are both small compared to L .

The *global* force balance is the sum over all swimmers of each individual Langevin equation (2.2). At steady state $\sum_i \mathbf{U}_i = 0$ and

$$0 = N\zeta U_0 \langle \mathbf{q} \rangle + N \langle \mathbf{F}^{ext} \rangle + \mathbf{F}_{Top}^W + \mathbf{F}_{Bot}^W, \quad (2.3)$$

where $\langle \mathbf{q} \rangle = \frac{1}{N} \sum_i \mathbf{q}_i$, $\langle \mathbf{F}^{ext} \rangle = \frac{1}{N} \sum_i \mathbf{F}_i^{ext}$, and $\mathbf{F}_{Top}^W = \sum_{i \in T} \mathbf{F}_i^W$ is the force on the top wall and involves only those particles interacting with that wall; a similar expression applies to the bottom wall. The Brownian and interparticle forces in (2.2) make no contribution to the global balance. Brownian forces, by definition, have zero average, while the interparticle forces are equal and opposite when two particles interact.

The net force on the walls is balanced by the total external body force acting on the particles within the volume plus the total average swim force. As far as the particles are concerned, an average swim force, $\langle \mathbf{F}^{swim} \rangle = \zeta U_0 \langle \mathbf{q} \rangle$, acts like just like a body force – an *internal* body force.

Now consider a control volume composed of the bottom wall and a horizontal plane at an arbitrary location z above the wall (cf. Fig. 2.1). The global force balance is

$$0 = \int_{V(z)} (\mathbf{F}^{swim} + \mathbf{F}^{ext}) dV + \mathbf{F}_{Bot}^W + \int_{S(z)} \boldsymbol{\sigma}^{(p)} \cdot \mathbf{n} dS, \quad (2.4)$$

where $S(z)$ is the horizontal surface at z and $\sigma^{(p)}$ is the force per unit area or stress exerted on the material (i.e. particles) within the control volume. (There is no contribution from the surfaces in the x - and y -directions because of the assumed periodicity.)

The surface $S(z)$ is of large horizontal extent and therefore forms an average. If the variation in properties in the z -direction is slow on the scale of the particle size and/or run length, we may replace the surface stress with the particle-phase stress (at z) found by standard averaging of the microscale dynamics (2.2) viz:

$$\langle \sigma^{(p)} \rangle = -nk_B T \mathbf{I} - n \langle \mathbf{x} (\mathbf{F}^{swim})' \rangle - n \langle \mathbf{x} \mathbf{F}^P \rangle, \quad (2.5)$$

where the first term on the RHS is the ideal gas Brownian osmotic pressure and the last term is the collisional pressure from the interactive forces. For the swim stress, the average swim force must be removed when computing the stress: $(\mathbf{F}^{swim})' = \mathbf{F}^{swim} - \langle \mathbf{F}^{swim} \rangle$.

The z -component of the force balance in (2.4) is

$$\Pi_{Bot}^W = \Pi^{(p)}(z) - \int_0^z (n \langle F_z^{ext} \rangle + n \langle F_z^{swim} \rangle) dz, \quad (2.6)$$

where $\Pi_{Bot}^W = F_z^W / A$ is the pressure on the bottom wall of area A , $\Pi^{(p)}$ is the pressure of the active suspension at z , and the averages under the integral sign are number averages in the horizontal plane. The force balance (2.6) requires no knowledge of the distribution of active particles $n(z)$, nor how or why there may be an average swim force. The pressure on the wall differs from the pressure of the active particles if there is a body force – external or internal – acting on the particles. Indeed, in general, if the pressure differs between two horizontal planes, then either (i) the material between the planes must be accelerating, or (ii) the pressure difference must be balanced by shear stresses at the boundaries as in flow in a tube, or (iii) there must be body forces acting throughout the volume.

The effect of an external body force is well-known, and our derivation shows that an average swim force has the same effect. An average swim force could exist throughout the volume if the swimmers had a biased swimming, say due to a gradient in a stimulant (chemical, light, etc.), or it can arise from the boundary if the boundary were to promote a local orientational order.

Recently, Solon *et al.*, (2015a) derived the dilute limit expression for the wall pressure when an external torque is applied to each ABP that collides with the wall and found that Π^W depends on the form of the torque and therefore concluded that the swim pressure was ill-defined because, according to them, it depended on the nature of the wall and therefore was not a ‘true’ pressure. A nonzero torque induces a local $\langle \mathbf{q} \rangle$ and therefore a nonzero swim force that must be included in the momentum balance.

When this internal body force is included the global force balance (2.6) is satisfied and the swim pressure is indeed well-defined and independent of the boundaries².

2.4 Particle-phase momentum balance

Straightforward averaging of the microscale dynamics (2.2) results in the momentum balance for the particle phase:

$$0 = -\zeta \langle \mathbf{j}^{rel} \rangle + n \langle \mathbf{F}^{swim} \rangle + n \langle \mathbf{F}^{ext} \rangle + \nabla \cdot \langle \boldsymbol{\sigma}^{(p)} \rangle. \quad (2.7)$$

In (2.7) $\langle \mathbf{j}^{rel} \rangle = n(\langle \mathbf{u}_p \rangle - \langle \mathbf{u} \rangle)$ is the particle flux relative to the suspension average velocity. Here, $\langle \mathbf{u}_p \rangle = \frac{1}{N} \sum_i \mathbf{U}_i$, and $\langle \mathbf{u} \rangle = \phi \langle \mathbf{u}_p \rangle + (1 - \phi) \langle \mathbf{u}_f \rangle$, with ϕ the volume fraction of particles and $\langle \mathbf{u}_f \rangle$ the average fluid velocity. Equation (2.7) should apply locally at each ‘continuum point,’ provided, as is standard in any continuum description, that there is a separation in scales with the macroscopic variations occurring on scales large compared to the microstructural length scales, importantly the run length $\ell = U_0 \tau_R$.

²The body force contribution is identical to the second term in Eq. (7) of Solon *et al.*, (2015b).

The momentum balance is used with the conservation of particle number density:

$$\frac{\partial n}{\partial t} + \nabla \cdot \langle \mathbf{u} \rangle n + \nabla \cdot \langle \mathbf{j}^{rel} \rangle = 0, \quad (2.8)$$

to determine the spatial distribution of active particles. In general, an equation for the orientation distribution $\langle \mathbf{q} \rangle$ is needed, which can be found from the Smoluchowski equation equivalent to the microscale dynamics (2.2). In the problems discussed here it is not needed.

The global force balance, (2.3) or (2.4), applies quite generally. In contrast, the continuum mechanics description, (2.7)-(2.8), requires a separation of scales between the microscale and the macroscale. While this separation is almost always true for passive Brownian particles, it requires careful examination for active matter, and is discussed in a future work.

This completes the general discussion of the balance laws for active particles. We now demonstrate by a few illustrative examples that the average swim force acts as an internal body force and that the particle-phase momentum balance can accurately predict the concentration distributions and the forces on the walls.

2.5 The effect of internal and external body forces

Passive particles with gravity

We first consider a suspension of passive Brownian particles in a container as illustrated in Fig. 2.1. The swim force is zero, $\mathbf{F}^{swim} = 0$, and, when dilute, the particle phase stress is simply the Brownian osmotic pressure $\langle \boldsymbol{\sigma}^{(p)} \rangle = -nk_B T \mathbf{I}$; the collisional stress is $O(n^2)$. In the absence of gravity, the number density is uniform with height $n(z) = n_0$ and the pressure on walls from (2.6) is the osmotic pressure $\Pi_{Bot}^W = \Pi_{Top}^W = n_0 k_B T$. With gravity, $\mathbf{F}^{ext} = \Delta \rho V_p \mathbf{g}$; the buoyant force is given by the density difference $\Delta \rho = \rho_p - \rho_f$ times the volume of a particle V_p and the acceleration of gravity \mathbf{g} . The passive Brownian particles behave like an isothermal ideal gas in an external potential. At steady state there

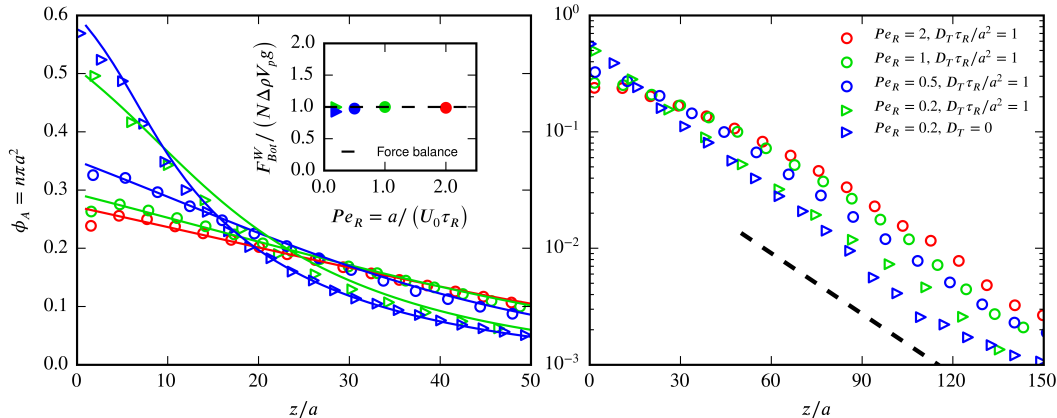


Figure 2.2: *Active particles with gravity.* The local area fraction ϕ_A vs height z/a in 2D. The symbols are simulation results and the solid lines are solutions to the continuum description (2.7). The log plot shows the same data as the linear plot. The dashed line corresponds to Boltzmann distribution $n \propto \exp(-\Delta\rho V_p g z / (k_B T + k_s T_s))$, that is, $\exp(-0.04 z/a)$; here $k_s T_s = \zeta U_0^2 \tau_R / 2$. $N = 1000$ particles are simulated in a square box of size $250a$ and $\phi_A^0 = 0.05$. The box is periodic in the x -direction but confined by two no-flux walls located at $z = 0$ and $z = L$. The inset compares the force on the bottom wall from the particle-wall interactions in simulation with the buoyant weight of the particles.

is no suspension velocity, $\langle \mathbf{u} \rangle = 0$, and the particles cannot escape the container, $\langle \mathbf{j}^{rel} \rangle = 0$. From (2.7) in the dilute limit, $n(z)$ has a Boltzmann distribution: $n(z) = n_0(L/L_G) \exp(-z/L_G) / (1 - \exp(-L/L_G))$, where $L_G = k_B T / \Delta\rho V_p g$ is the sedimentation length. The pressures at the walls are $\Pi_{Bot}^W = n(z=0)k_B T$ and $\Pi_{Top}^W = n(z=L)k_B T$, and their difference, $\Pi_{Bot}^W - \Pi_{Top}^W = n_0 \Delta\rho V_p g L$, is the total buoyant weight of the particles in the container, in agreement with the global force balance (2.6).

Active particles with gravity

We now examine a similar system of swimmers (ABPs) under gravity. Provided the gravitational forcing is not too strong no polar order will be induced by the no flux boundary at the bottom (Hennes *et al.*, 2014; Tailleur & Cates, 2009; Enculescu & Stark, 2011). In 2D for a dilute system the swim stress $\langle \boldsymbol{\sigma}^{swim} \rangle = -n\zeta U_0^2 \tau_R / 2 \mathbf{I}$, and the total particle-phase stress is $\langle \boldsymbol{\sigma}^{(p)} \rangle = -n(k_B T + k_s T_s) \mathbf{I}$,

where we define the swimmer ‘activity’ $k_s T_s \equiv \zeta U_0^2 \tau_R / 2$. We perform active Brownian dynamics simulations in 2D with periodic boundary conditions in x and with a hard-particle potential when particles collide with each other or with either the top or bottom walls. Equation (2.7) predicts a Boltzmann distribution: $n(z) \propto \exp(-\Delta\rho V_p g z / (k_B T + k_s T_s))$ in the dilute limit, which is verified by simulation over a wide range of (dilute) area fractions $\phi_A^0 = n_0 \pi a^2$, reorientation Péclet numbers $Pe_R = a / (U_0 \tau_R) \in (0.2, 5.0)$, with or without translational diffusion, D_T , and not too large gravity ($\Delta\rho V_p g / (\zeta U_0) < 0.2$) as shown in Fig. 2.2. The global force balance (2.3) (and (2.6)) is verified by measurement of the force on the bottom wall in the simulations.

Orienting field to cancel gravity

From the global force balance (2.3), if $\langle \mathbf{F}^{ext} \rangle$ and $\langle \mathbf{F}^{swim} \rangle$ cancel each other, then $\Pi_{Bot}^W = \Pi_{Top}^W$ and the continuum theory (2.7) predicts a uniform distribution of active particles. To test this, a non-zero $\langle \mathbf{q} \rangle$ can be induced by an external polarization field as discussed by Takatori & Brady, (2014). An external field $\hat{\mathbf{H}}$ applies a torque $\Omega_c \mathbf{q} \times \hat{\mathbf{H}}$ to each swimmer and therefore the orientation vector \mathbf{q} aligns in the field direction and diffuses around it through $D_R = 1/\tau_R$. The strength of the applied field is governed by the nondimensional field strength $\chi_R = \Omega_c \tau_R$. When $\chi_R \rightarrow 0$ the structure is isotropic, whereas when $\chi_R \rightarrow \infty$ all particles align and move in the direction $\hat{\mathbf{H}}$. Each swimmer has a net average velocity $U_0 \langle \mathbf{q} \rangle (\chi_R)$ due to the field, which can be canceled by \mathbf{F}^{ext} / ζ . With an orienting field the swim stress is anisotropic and given in the work of Takatori & Brady, (2014) in 3D and in Appendix B for 2D.

Simulations were conducted in the same bounded geometry with $\hat{\mathbf{H}}$ and gravity both perpendicular to the walls for a wide range of χ_R and \mathbf{F}^{ext} . The systems are homogeneous at steady state when gravity cancels the field (Fig. 2.3), and the wall pressures are equal as the global force balance (2.3) requires.

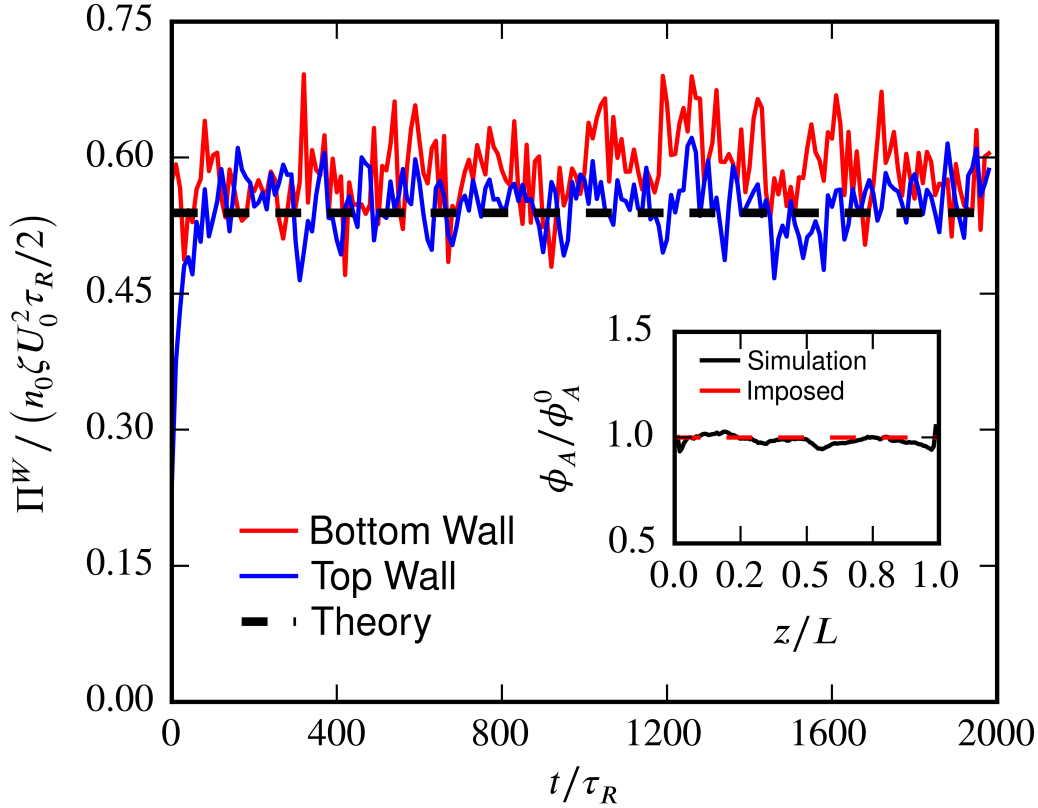


Figure 2.3: *Orienting field to cancel gravity.* The wall pressure vs simulation time. Here, $\text{Pe}_R = a/(U_0\tau_R) = 0.2$, $D_T = 0$, $\chi_R = \Omega_c\tau_R = 1$ and $\Delta\rho V_{Pg}\tau_R/(\zeta a) = 2.23 = \langle q_z \rangle U_0\tau_R/a$. The insert shows the local area fraction ϕ_A as a function of height z , sampled by Voronoi cells. $N = 1668$ particles are simulated in a square box of size $512a$ at $\phi_A^0 = 0.02$. The data are averaged over 16 realizations. The system is periodic in the x -direction but confined by two no-flux walls located at $z = 0$ and $z = L$. The theory for the dilute limit and can be found in Appendix B.

Theory (Takatori & Brady, 2014) predicts anisotropic stresses, and simulations were conducted at low area fraction ($\phi_A \approx 0.02$) without translational Brownian motion so that $\langle \sigma^{(p)} \rangle = nk_s T_s (\hat{\sigma}_{\parallel}^{swim} \hat{\mathbf{H}} \hat{\mathbf{H}} + \hat{\sigma}_{\perp}^{swim} (\mathbf{I} - \hat{\mathbf{H}} \hat{\mathbf{H}}))$, where $\hat{\sigma}_{\parallel}^{swim}$ and $\hat{\sigma}_{\perp}^{swim}$ are nondimensional functions of χ_R . To measure $\hat{\sigma}_{\perp}^{swim}$, the $\hat{\mathbf{H}}$ field is applied parallel to the walls (Case A in Fig. 2.4); and for $\hat{\sigma}_{\parallel}^{swim}$, $\hat{\mathbf{H}}$ and the gravity field are perpendicular to the walls and cancel each other (Case B in Fig. 2.4). Figure 2.4 shows that the pressures on the walls determined in simulation agree with the theory.

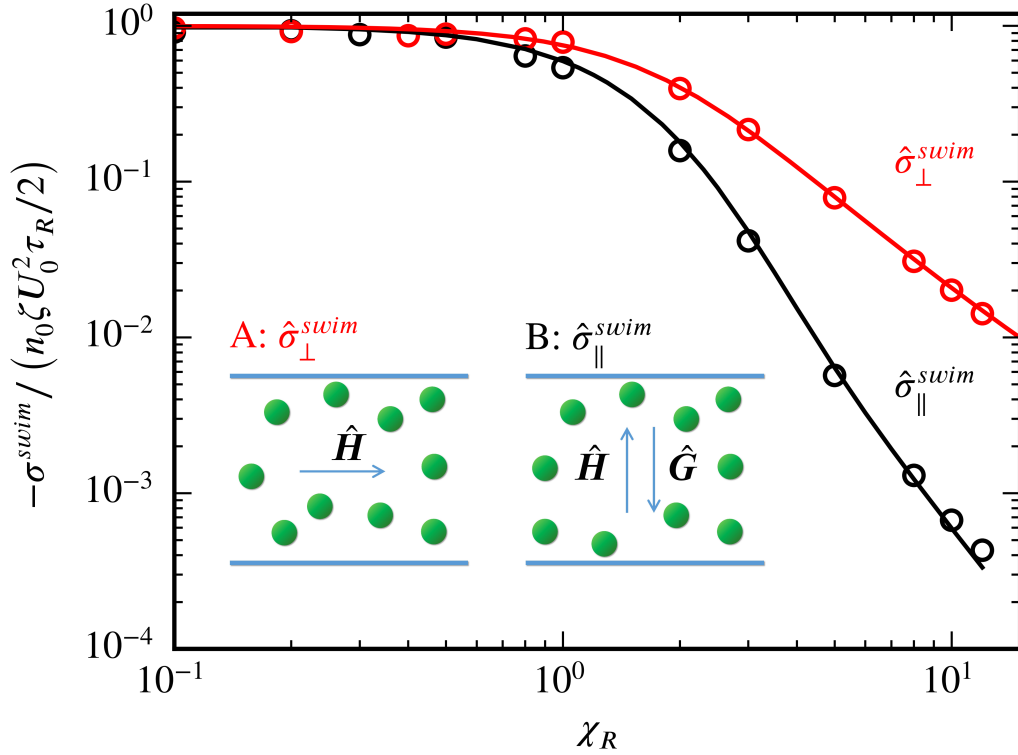


Figure 2.4: The anisotropic wall pressures compared with the dilute 2D theory (Appendix B). The circles are ABP simulations for $\text{Pe}_R = a/(U_0\tau_R) = 0.2$, $D_T = 0$, $\phi_A^0 = 0.02$ and $N = 1668$. (A) For $\hat{\sigma}_\perp$ the \hat{H} field is applied in the x -direction, whereas (B) for $\hat{\sigma}_\parallel$ the \hat{H} is applied in the z -direction and canceled by \mathbf{F}^{ext} . The square box of size $512a$ is periodic in the x direction and confined by no-flux walls located at $z = 0$ and $z = L$.

No gravity but with an orienting field

The resemblance of a swim force to an external body force is further illustrated by a system under a polarization field but no gravity. A constant downward \hat{H} field gives a ‘sedimentation-like’ system with swimmers accumulating near the bottom wall as shown in Fig. 2.5. The measured bottom wall pressure is equal to the total ‘weight’ of the particles (divided by length L_x in 2D): $N\langle F^{swim} \rangle / L_x$, as the global force balance (2.3) requires. Solving (2.7) with $\langle \mathbf{F}^{swim} \rangle = \zeta U_0 \langle \mathbf{q} \rangle (\chi_R)$ gives a Boltzmann distribution where the concentration is dilute with the ‘sedimentation length’ $L_\parallel = (k_B T + k_s T_s \hat{\sigma}_\parallel^{swim}) / \langle F^{swim} \rangle$. The only difference compared to normal gravity is the anisotropic swim stress manifested by $\hat{\sigma}_\parallel^{swim}$. As shown in Fig. 2.5 the

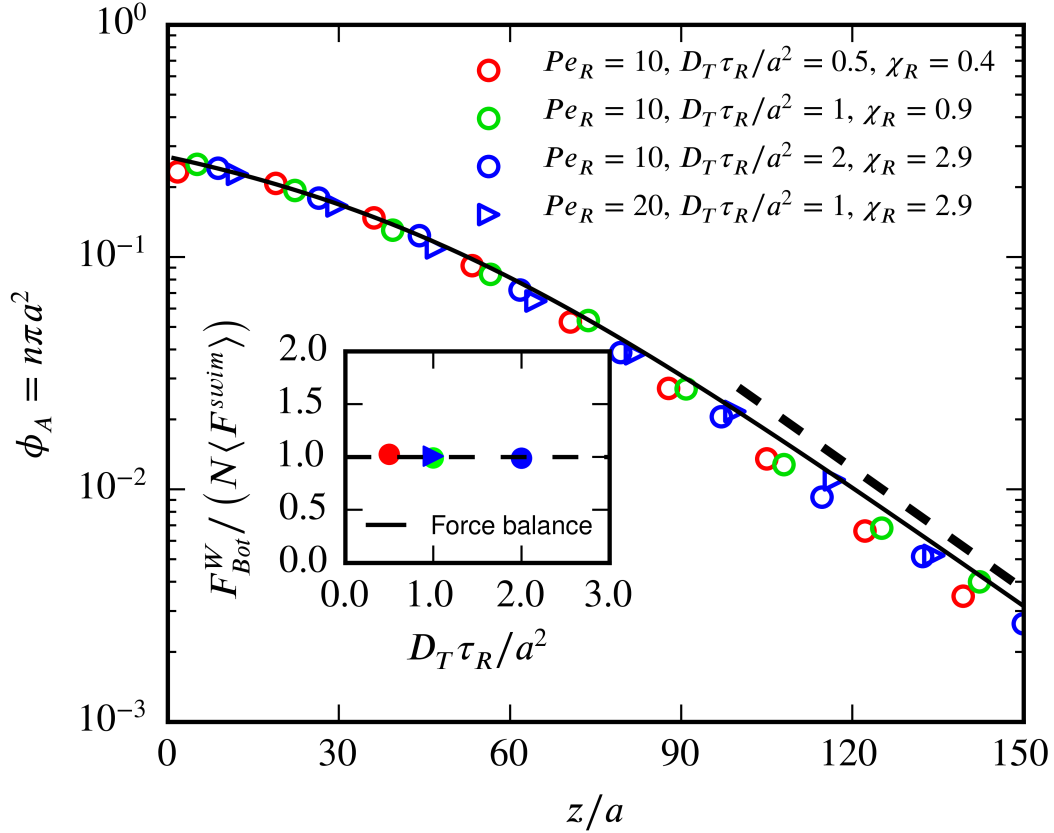


Figure 2.5: *No gravity but with an orienting field.* The local area fraction ϕ_A vs height z/a with the \hat{H} field applied downward and $\mathbf{F}^{ext} = 0$. The symbols are simulation results and the solid line is the solution to the the continuum description (2.7). The dashed line is a Boltzmann distribution $\phi_A \propto \exp\{-\langle F^{swim} \rangle z / (k_B T + k_s T_s \hat{\sigma}_{\parallel})\} = \exp(-0.04z/a)$, where $k_s T_s = \zeta U_0^2 \tau_R / 2$. $N = 1000$ particles are simulated in a square box of size $250a$ at $\phi_A^0 = 0.05$. The box is periodic in x but confined by no-flux walls at $z = 0, L$. The inset compares the force on the bottom wall from the particle-wall interactions in simulation with the ‘weight’ of the particles due to the swim force.

calculated Boltzmann distribution $n \propto \exp(-z/L_{\parallel})$ agrees with the simulations. In the simulations shown in Fig. 2.5, χ_R is adjusted according to (B.7), covering the range $\chi_R \in (0, 3)$.

Comparing the $n(z)$ distributions and the Π_{Bot}^W of passive Brownian particles (Fig. 2.2) with swimmers under gravity (Fig. 2.5), one sees clearly that with a non-zero $\langle \mathbf{q} \rangle$ swimmers behave as if acted upon by a body force. An *internal* body force $\mathbf{F}^{int} = \zeta U_0 \langle \mathbf{q} \rangle = \langle \mathbf{F}^{swim} \rangle$ acts on each particle.

Depletion zone

Up to now we have considered the simplest cases in which polar order was induced by an orienting field homogeneously throughout the region between the two bounding walls. But this is not necessary. Suppose that the orienting field only acts only over a length $\Delta < L$. The effect of this field will lead to a depletion (or an accumulation) of active particles near the boundary depending on whether the field causes the particles to swim away from or towards the boundary. If the swimming is strong enough, there will be *no* particles contacting the wall and thus Π_{Bot}^W in (2.6) will be zero. For $z > \Delta$ there is no field and $\langle F_z^{swim} \rangle = 0$, while for $z < \Delta$, $n \approx 0$, and since the swim pressure far from the wall is $\Pi^{(p)} = n\zeta U_0^2 \tau_R / 6$, the global force balance (2.6) shows that there must be a transition region of thickness $O(\ell = U_0 \tau_R)$ of high concentration of active particles near Δ . A particle swimming into the exclusion region $z < \Delta$ will, for a reorientation time, be unaware of the field and continue traveling at the swim speed. Fig. 2.6 demonstrates this behavior where a polarization field \hat{H} is applied only in the region $z < L/4$. If the field is strong enough, $\chi_R > 1$, there are no particles adjacent to the wall.

This is a very interesting result in that there are no external forces acting on the particles, yet they move away from from the wall. Passive particles cannot do this. By sensing their environment (light, chemical, etc. stimuli) active particles can adjust their internal swimming mechanisms and behave as if they experienced an

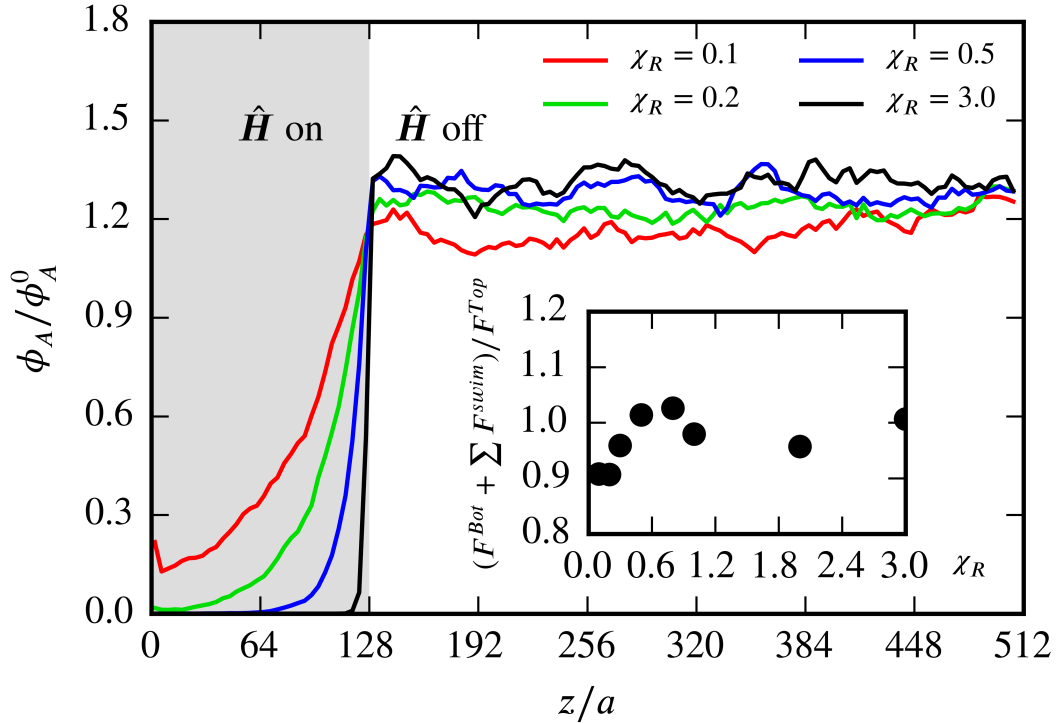


Figure 2.6: A depletion zone induced by polarization. The local area fraction ϕ_A vs height z/a with the \hat{H} field applied upward in the region $z < L/4$ and $\mathbf{F}^{ext} = 0$. The solid lines are simulation. $N = 1668$ particles are simulated in a square box of size $512a$ at $\phi_A^0 = 0.02$. The box is periodic in x but confined by no-flux walls at $z = 0, L$. $Pe_R = 0.2$, $D_T = a^2/\tau_R$. The inset checks the global force balance (2.3) and (2.4).

actual repulsive (or attractive) force. Note that we modeled the orientation process as resulting from an external torque due to the field, but this is not necessary. All that is necessary is that the active particles adjust their swimming in response to their environment and they can do this completely *internally* by simply ‘choosing’ to swim towards or away from the stimulus. No external torque (or force) is needed. It is truly an ‘action at a distance.’

2.6 Suspension momentum balance

We have discussed the global force balance for the particle phase, but have not yet addressed the macroscopic momentum balance for the entire suspension, or mixture, – the particles plus the fluid. For the mixture it must be appreciated that \mathbf{F}^{drag} and

\mathbf{F}^{swim} at the particle level are both parts of the hydrodynamic force \mathbf{F}^H exerted by the fluid on the particles (Eq. (2.1)). The particles in turn exert the same force on the fluid, and thus only the *external* body force appears in the macroscopic momentum balance for the suspension:

$$0 = n\langle \mathbf{F}^{ext} \rangle + \nabla \cdot \langle \boldsymbol{\sigma} \rangle. \quad (2.9)$$

The average suspension stress is given by

$$\langle \boldsymbol{\sigma} \rangle = -\langle p_f \rangle \mathbf{I} + 2\eta \langle \mathbf{e} \rangle + \langle \boldsymbol{\sigma}^{(p)} \rangle, \quad (2.10)$$

where $\langle \mathbf{e} \rangle = 1/2(\nabla \langle \mathbf{u} \rangle + (\nabla \langle \mathbf{u} \rangle)^\dagger)$ is the average rate of strain tensor and $\langle p_f \rangle$ is the average pressure in the fluid³. The fluid pressure distribution does whatever is necessary to ensure the incompressibility of the suspension average velocity, $\nabla \cdot \langle \mathbf{u} \rangle = 0$. For example, when polar order exactly balances gravity (Fig. 2.3), $\langle \boldsymbol{\sigma}^{(p)} \rangle$ is spatially constant, there is no flux of suspension ($\langle \mathbf{u} \rangle = 0$) or particles ($\langle \mathbf{j}^{rel} \rangle = 0$) and the fluid pressure gradient is equal to the external body force, $\nabla \langle p_f \rangle = n\langle \mathbf{F}^{ext} \rangle$.

In the case where the orienting field gave rise to a depletion zone adjacent to the bottom wall, the suspension momentum balance shows that there will be a jump in the fluid pressure across the transition region from no particles to bulk behavior of magnitude $\Delta \langle p_f \rangle = -\int^{O(\ell)} n\langle \mathbf{F}^{swim} \rangle dz$.

Computational continuum-scale studies of active suspensions (Lushi *et al.*, 2012) employ the momentum balance (2.9).

2.7 Conclusions

Interpreting an average swim force as a body force was done at two levels of description: (i) the global force balance (2.3), and (ii) the continuum description (2.7). The global force balance looks trivial because it involves only a simple sum

³There may also be a hydrodynamic stresslet contribution that takes the form: $n\langle \mathbf{S}^H \rangle \propto n\zeta U_0 a \langle \mathbf{q}\mathbf{q} \rangle$.

of each swimmer's translational Langevin equation (2.2). The sum is performed without any knowledge of how swimmers interact with the boundary, how they orient in \mathbf{q} -space, or how they are distributed in physical space. Also, no assumption of a 'continuum' is necessary and therefore (2.3) is quite general.

With the continuum approach, however, the difficult problem of determining the deformation and stress of active matter is greatly simplified to solving (2.7) along with the conservation equation for the particle number density (2.8). Further, the constitutive equation for the active stress, $\langle \boldsymbol{\sigma}^{(p)} \rangle(\phi, Pe_R, \dots)$, is determined from *homogeneous* active matter systems (Takatori & Brady, 2015) and can then be used to *predict* the behavior in *inhomogeneous* situations, just as is done, for example, for the Navier-Stokes equations – the viscosity is measured in a uniform simple shear flow and then used in *any* flow geometry no matter how complex. When $\langle \mathbf{F}^{swim} \rangle, \langle \mathbf{F}^{ext} \rangle$ are specified, the continuum equations are closed and the concentration and stress, $\phi(\mathbf{x}, t)$ and $\langle \boldsymbol{\sigma}^{(p)} \rangle(\mathbf{x}, t)$, can be determined everywhere. The force on a boundary then follows from the standard continuum expression $\int_S \langle \boldsymbol{\sigma}^{(p)} \rangle \cdot \mathbf{n} dS$.

The continuum description, which predicted the Boltzmann distributions for dilute systems, requires a separation of scales between the variation in macroscopic properties, such as $n(z)$, etc., and the microscale, which for active matter is set by the swimmer's run length, $\ell = U_0 \tau_R$ (and/or particle size a). In very dilute systems the run length can become large and if significant polar order is induced at a boundary, a continuum description may not be possible.

As a final remark, we have considered average swim forces that are the result of polar order, $\langle \mathbf{q} \rangle \neq 0$, as this is the most obvious case. However, what is important is that there is average swim force, $\langle \mathbf{F}^{swim} \rangle \neq 0$, not that there is polar order. Recently it was shown (Takatori & Brady, 2015) that if there is a spatial variation in the intrinsic swim speed $U_0(\mathbf{x})$ or reorientation time $\tau_R(\mathbf{x})$, as might happen if the local fuel concentration varies, to leading order there is an average swim force:

$n\langle \mathbf{F}^{swim} \rangle = -\langle \boldsymbol{\sigma}^{swim} \rangle \cdot \nabla \ln(U_0 \tau_R)$. This average swim force must then appear in the global force balance (2.3) or (2.6) and in the continuum description (2.7).

Chapter 3

THE FORCE ON A BOUNDARY IN ACTIVE MATTER

1. Yan, W. & Brady, J. F. The force on a boundary in active matter. *J. Fluid Mech.* **785**, R1 (2015).

3.1 Introduction

The behavior of self-propelled objects such as bacteria, algae, and synthetic Janus particles has become a dynamic field of research, both for the ‘swimming’ of individual particles (Lauga & Powers, 2009), and for the collective behavior of active suspensions (Toner *et al.*, 2005). Owing to the particles’ self motion, active matter can spontaneously phase separate into dense and dilute regions (Takatori *et al.*, 2014; Takatori & Brady, 2015; Palacci *et al.*, 2013; Stenhammar *et al.*, 2013, 2014; Cates *et al.*, 2010; Bialké *et al.*, 2013; Buttinoni *et al.*, 2013; Wysocki *et al.*, 2014; Fily & Marchetti, 2012; Fily *et al.*, 2014b) and can move collectively under an orienting field (Takatori & Brady, 2014).

Recently, the swim pressure (Takatori *et al.*, 2014; Fily *et al.*, 2014b) was introduced as a new perspective on the behavior of active matter. The swim pressure is the pressure needed to confine active particles and is analogous to the osmotic pressure of Brownian colloids. The dilute limit ‘ideal gas’ swim pressure $\Pi^{swim} = n\zeta U_0^2 \tau_R / 6$ (in 3D), where n is the number density of active particles, ζ is their drag coefficient, U_0 is the swim speed, and τ_R is their reorientation time. The swim pressure, or stress, is defined as the moment of the swim force $\langle \boldsymbol{\sigma}^{swim} \rangle = -n \langle \boldsymbol{x} \boldsymbol{F}^{swim} \rangle$, where $\boldsymbol{F}^{swim} = \zeta U_0 \boldsymbol{q}$, with \boldsymbol{q} the orientation vector of the swimmer and \boldsymbol{x} its position. The ‘moment arm’ for the swim stress is the swimmer’s run length, $\ell = U_0 \tau_R$.

The swim pressure is an average over the reorientation time τ_R , which implies an average over the run length ℓ . The swim pressure is only defined on, and applies for, lengths greater than the run length. And its use to compute forces on boundaries necessitates that the boundary or macroscopic length scale, L , be much larger than the run length (Yan & Brady, 2015a). What happens when the length scale of interest is not large compared to the run length? Can we extend the notion of the swim pressure to such situations? Or more generally, how does the swim pressure emerge from a more microscopic description?

In this paper we provide such a microscopic theory and show how the swim pressure arises naturally as the characteristic macroscopic length scale becomes large compared to the run length. The theory is an extension of the well-known dynamics of passive colloidal particles to active colloidal particles, and will allow us to compute forces and torques on bodies and thus predict their motion in response to the swimmers' activity.

3.2 Theory

For active colloidal particles there are three characteristic lengths: (i) the macroscopic length scale L , (ii) the run length $\ell = U_0\tau_R$ and (iii) a microscopic length $\delta = \sqrt{D_T\tau_R}$, where D_T is the translational diffusivity of the active particles. Although in a typical application we expect $L > \ell \gg \delta$, the theory we present is valid for any ratio of length scales.

Active Brownian particles (ABP) are governed by the Smoluchowski equation for the probability density for finding a swimmer of radius a at \mathbf{x} with orientation \mathbf{q} :

$$\frac{\partial P(\mathbf{x}, \mathbf{q}, t)}{\partial t} + \nabla \cdot \mathbf{j}^T + \nabla_R \cdot \mathbf{j}^R = 0. \quad (3.1)$$

The translational and rotational fluxes are: $\mathbf{j}^T = (U_0\mathbf{q} + \mathbf{F}^P/\zeta - D_T\nabla \ln P)P$, and $\mathbf{j}^R = -D_R\nabla_R P$, where $\nabla_R = \mathbf{q} \times \nabla_{\mathbf{q}}$ is the orientational gradient operator. For a spherical swimmer of radius a in a Newtonian solvent of viscosity η , $\zeta = 6\pi\eta a$, $D_T = k_B T/\zeta = k_B T/6\pi\eta a$, $D_R (= 1/\tau_R) = k_B T/8\pi\eta a^3$ and $\delta = \sqrt{D_T/D_R} = \sqrt{4/3}a$.

At a boundary surface the normal component of the translational flux must vanish, $\mathbf{n} \cdot \mathbf{j}^T = 0$. If there were no translational Brownian motion or boundary force ($\mathbf{F}^P = 0$), then $U_0(\mathbf{n} \cdot \mathbf{q})P = 0$, which means that either (i) $U_0 = 0$ or (ii) $\mathbf{n} \cdot \mathbf{q} = 0$ or (iii) $P = 0$ at the surface; none of which is true in general. It is essential to have a strong enough boundary force or translational Brownian diffusion (or both, or hydrodynamics) to prevent particle crossing. As is well known in colloidal dynamics, a hard-particle repulsive force is infinite and nonzero only at the boundary

surface and the no flux condition is satisfied via the Brownian flux.

Rather than having a finite range and amplitude boundary force or hydrodynamic lubrication interactions to prevent particle flux, we choose to use D_T as this is the simplest to implement theoretically and most easily reveals the underlying physics. It is important to note that whatever means are used to prevent active particles from crossing a boundary it will introduce a microscopic length scale δ . As we shall see, for pressures and forces, δ will not appear in the final results. Any of the mechanisms would produce the same behavior.

Indeed, (Ezhilan *et al.*, 2015) recently examined active particles in 2D confined between two walls without translational Brownian motion ($D_T \equiv 0$) and showed that the problem could be modeled with two regions: freely swimming bulk behavior connected to a singular surface layer of particles in contact with the walls. The action of translational Brownian motion is to spread this singular surface layer over the microscopic thickness δ adjacent to the walls, as is standard in boundary-layer theory. Our planar 2D results are in agreement with their findings.

Although we speak in terms of translational Brownian motion and forces proportional to $k_B T$, this is not necessary. One can simply replace $k_B T$ with ζD_T and the results are unchanged; the translational diffusion, like the rotary diffusion D_R , need not be thermal in origin. The Smoluchowski equation only requires that the random ‘Brownian’ displacements be small compared to any other length scale (e.g. the swimmer size).

The Smoluchowski equation applies for all length and time scales but its solution in any but the simplest situations is challenging. We need a simplified description that captures the essential physics, and, more importantly, provides insight into the general behavior and can explain phenomena without detailed calculations.

Consider a body immersed in a dilute suspension of ABPs. With $F^P = 0$, the force the active colloidal particles exert on the body is given exactly by (Brady, 1993;

Squires & Brady, 2005) $\mathbf{F} = -k_B T \int_{S_B} P(\mathbf{x}, \mathbf{q}, t) \mathbf{n} dS$, where \mathbf{n} is the outer normal to the body surface as shown in Fig. 3.3. The force averaged over the orientation of the active particles is

$$\langle \mathbf{F} \rangle_{\mathbf{q}} = -k_B T \int_{S_B} n(\mathbf{x}, t) \mathbf{n} dS, \quad (3.2)$$

where $n(\mathbf{x}, t) \equiv \int P(\mathbf{x}, \mathbf{q}, t) d\mathbf{q}$ is the number density of swimmers.

The conservation equations for the zeroth and first moments of the Smoluchowski equation are (Saintillan & Shelley, 2015):

$$\frac{\partial n}{\partial t} + \nabla \cdot \mathbf{j}_n = 0 \quad , \quad \mathbf{j}_n = U_0 \mathbf{m} - D_T \nabla n, \quad (3.3)$$

$$\frac{\partial \mathbf{m}}{\partial t} + \nabla \cdot \mathbf{j}_m + 2D_R \mathbf{m} = 0 \quad , \quad \mathbf{j}_m = U_0 \mathbf{Q} + \frac{1}{3} U_0 n \mathbf{I} - D_T \nabla \mathbf{m}, \quad (3.4)$$

where $\mathbf{m}(\mathbf{x}, t) = \int \mathbf{q} P(\mathbf{x}, \mathbf{q}, t) d\mathbf{q}$ is the polar order field, and $\mathbf{Q}(\mathbf{x}, t) = \int (\mathbf{q}\mathbf{q} - \frac{1}{3} \mathbf{I}) P(\mathbf{x}, \mathbf{q}, t) d\mathbf{q}$ is the nematic order field. Since the force on a body only involves the number density at the surface, we can use the simplest closure of the hierarchy $\mathbf{Q} = 0$. We show below (and discuss in Appendix C) that this closure is sufficient to achieve good accuracy and reveals the essential physics.

Two remarks will help understand the structure of the moment equations. First, when departures from uniformity vary slowly, the \mathbf{m} -field equation has a balance between the ‘sink’ term and the gradient in the concentration, $2D_R \mathbf{m} \approx -\frac{1}{3} U_0 \nabla n$, which gives a diffusive flux in the concentration field that incorporates the swim diffusivity: $\mathbf{j}_n \approx -(D_T + \frac{1}{6} U_0^2 \tau_R) \nabla n$. Second, at the other extreme when variations are rapid, the \mathbf{m} -field has a natural screening length where diffusion balances the sink: $D_T \nabla^2 \mathbf{m} \approx 2D_R \mathbf{m}$. This screening length is proportional to the microscopic length $\delta = \sqrt{D_T/D_R}$. The screening length plays a fundamental, but unusual, role in active matter—it is essential in order to have a well-posed problem and there will be rapid variations in properties on the scale of δ , but in the limit where $\delta \ll \ell, L$, the microscopic length does not appear in the active pressure or in the forces and torques on boundaries. The athermal limit ($D_T \rightarrow 0$) is singular and D_T (or $k_B T$)

can only be set to zero *after* the limit is taken; the force from (3.2) will then be independent of $k_B T$.

3.3 Examples

First, we consider an infinite flat plate with normal along the z -direction; there is no macroscopic length scale. The n - and m -fields are subject to no flux at $z = 0$: $\mathbf{n} \cdot \mathbf{j}_{n,m} = 0$ and a uniform concentration and no polar order as $z \rightarrow \infty$: $n \sim n^\infty$ and $\mathbf{m} \sim 0$. The concentration and polar order fields are simple exponentials decaying on the screening length

$$n = n^\infty \left(1 + \frac{1}{6}(\ell/\delta)^2 e^{-\lambda z} \right), \quad m_z = -n^\infty \frac{1}{6}(\lambda \ell) e^{-\lambda z}, \quad (3.5)$$

where $\lambda = \sqrt{2(1 + \frac{1}{6}(\ell/\delta)^2)}/\delta$ is the inverse screening length.

The concentration at the wall, $n(0) = n^\infty(1 + \frac{1}{6}(\ell/\delta)^2)$, is independent of the closure (which follows directly from (3.1) in 1D), always exceeds that far away, and can become very large as $(\ell/\delta) \rightarrow \infty$. This ‘infinite’ concentration applies for a *dilute* suspension. It is not a build-up associated with a finite concentration of active particles. Rather, it is the singularity alluded to earlier that results if translational Brownian motion (or a microscopic length) is not considered.¹

Even though the concentration can become arbitrarily large, the force per unit area or pressure on the wall from the microscopic force definition (3.2) is finite and *independent* of δ : $\Pi^W = n(0)k_B T = n^\infty(k_B T + k_s T_s)$, where we have defined the swimmer’s ‘activity’ $k_s T_s = \zeta U_0^2 \tau_R / 6 = k_B T (\ell/\delta)^2 / 6$. We recognize the pressure on the wall as the *active pressure*—the sum of the osmotic pressure of Brownian particles plus the swim pressure. And note that this is true regardless of the relative magnitudes of $k_B T$ and $k_s T_s$ (including the singular athermal limit $k_B T = 0$).² Also, the ratio $(\ell/\delta)^2 = 6D^{swim}/D_T = U_0 \ell / D_T = \text{Pe}_\ell$ is a Péclet number based on the run length measuring the relative importance of swimming to Brownian diffusion.

¹The active particle size a must be taken into account in defining the no flux surface $z = 0$.

²This same independence of $k_B T$ occurs in the analogous hard-sphere rheology problem at high Péclet numbers (Squires & Brady, 2005; Brady & Morris, 1997).

The second problem is active Brownian particles confined between two parallel plates separated by a distance H . The concentration distribution is

$$\frac{n(z)}{n_0} = 1 + \frac{1}{6} \left(\frac{\ell}{\delta} \right)^2 \frac{\sinh(\lambda z) + \sinh(\lambda(H-z))}{\sinh(\lambda H)}, \quad (3.6)$$

where the constant n_0 is related to the average number density of ABPs in the channel $\langle n \rangle = \int_0^H n(z) dz / H$. The concentration is identical at both walls and is the same as for a single wall with n_0 replacing n^∞ . In the limit of large λH , corresponding to $\delta \ll H$, and when $\delta \ll \ell$, $n_0 \sim \langle n \rangle [1 + (\ell/H)/\sqrt{3}]^{-1}$ and the pressure at the walls becomes

$$\Pi^W = \langle n \rangle \left(k_B T + \frac{k_s T_s}{1 + (\ell/H)/\sqrt{3}} \right). \quad (3.7)$$

As for a single wall the pressure is independent of the microscopic length scale δ but now depends on the ratio of the run length to the macroscopic scale ℓ/H . We shall see that this behavior is generic—the influence of the run length enters as ℓ/L . In a simulation study by Ray *et al.*, (2014) observed that the pressure in a channel depends on the gap spacing as predicted by (3.7). (In 2D the coefficient is $1/\sqrt{2}$.)

Figure 3.1 compares the concentration profile and pressure for a channel from the theory with results from ABP dynamic simulations. When a swimmer hits a boundary, it experiences a hard-particle force \mathbf{F}^P to prevent it from penetrating the boundary. (Following Foss & Brady, (2000) a potential-free hard particle force is implemented.) Also shown are the theoretical predictions from closing the hierarchy at the next level including the nematic order field \mathbf{Q} as described in Appendix C. The \mathbf{m} -field closure is sufficient, both qualitatively and quantitatively.

The next problems are the concentration and pressure distribution in 3D outside and inside a sphere, and in 2D outside and inside a circle, of radius R . Symmetry dictates that $n(\mathbf{x}) = n^\infty f(r)$ and $\mathbf{m}(\mathbf{x}) = n^\infty \mathbf{x} g(r)$, where $f(r)$ and $g(r)$ are scalar functions of r . The exterior solution in 3D has the form of an exponentially screened

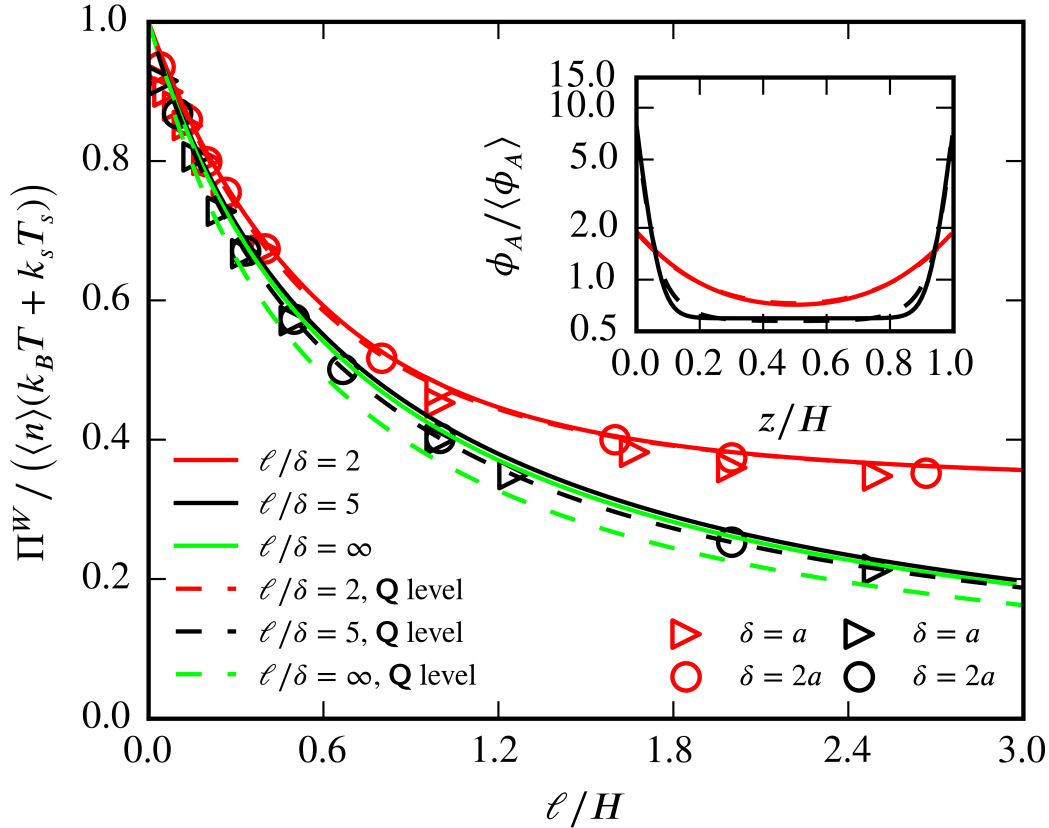


Figure 3.1: Π^W of ABPs confined between parallel walls in 2D. The inset shows the area fraction distribution $\phi(z)$. Here, $\ell = U_0 \tau_R$ is the run length and $\delta = \sqrt{D_T \tau_R}$ is the microscopic length. The swimmer radius is a . H is the width of the channel.

concentration reminiscent of Debye screening

$$\frac{n(r)}{n^\infty} = 1 + \frac{1}{6} \left(\frac{\ell}{\delta} \right)^2 \frac{1}{1 + (1 + \lambda R)(\delta/R)^2} \frac{R}{r} e^{-\lambda(r-R)}, \quad (3.8)$$

and similarly for the m -field. In 2D Bessel functions replace the exponential:

$$\frac{n(r)}{n_A^\infty} = 1 + \frac{2(\ell/\delta)^2 K_0(\lambda' r)}{K_0(\lambda' R)[2 - (\ell/\delta)^2] + K_2(\lambda' R)[2 + (\ell/\delta)^2]}, \quad (3.9)$$

where the 2D inverse screening length $\lambda' = \sqrt{1 + \frac{1}{2}(\ell/\delta)^2}/\delta$, $K_{0,2}$ are the modified Bessel functions and n_A^∞ is the area number density at infinity. For large $\lambda' r$ the concentration disturbance decays as $\sim e^{-\lambda' r}/\sqrt{r}$.

The pressure at the sphere surface in the dual limits $\delta \ll \ell$ and $\delta \ll R$, but for

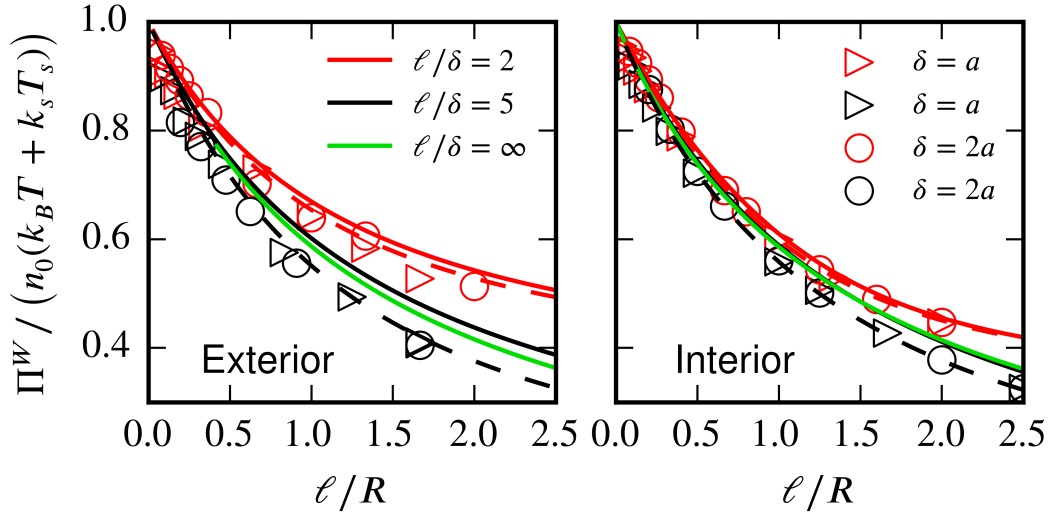


Figure 3.2: Π^W of ABPs outside and inside a circle. Legends are as in Fig. 3.1.

arbitrary ℓ/R , is

$$\Pi^{ext}(R) = n^\infty \left(k_B T + \frac{k_s T_s}{1 + (\ell/R)/\sqrt{3}} \right), \quad (3.10)$$

while for the circle

$$\Pi_{2D}^{ext}(R) = n_A^\infty \left(k_B T + \frac{k_s T'_s}{1 + (\ell/R)/\sqrt{2}} \right), \quad (3.11)$$

where $k_s T'_s = \zeta U_0^2 \tau_R / 2$ is the activity in 2D. We again see the effect of the finite run length entering as ℓ/R .

For the spherical interior problem the concentration field is given by

$$\frac{n(r)}{n(0)} = 1 + \frac{\frac{1}{6}(\ell/\delta)^2 (\sinh(\lambda r)/(\lambda r) - 1)}{\frac{1}{6}(\ell/\delta)^2 + (1 + (\delta/R)^2) \sinh(\lambda R)/(\lambda R) - (\delta/R)^2 \cosh(\lambda R)}, \quad (3.12)$$

while for the interior problem in 2D

$$\frac{n(r)}{n_A(0)} = 1 + \frac{2(\ell/\delta)^2 (I_0(\lambda' r) - 1)}{2(\ell/\delta)^2 + (2 - (\ell/\delta)^2) I_0(\lambda' R) + (2 + (\ell/\delta)^2) I_2(\lambda' R)}, \quad (3.13)$$

with $I_{0,2}$ modified Bessel functions. In the dual limits $\delta \ll \ell$, $\delta \ll R$, the interior pressure in 2D is identical to (3.11) with $\langle n_A \rangle$ replacing n_A^∞ .

Fig. 3.2 compares the predicted results in 2D for the exterior and interior problems with ABP simulations and the next level Q theory. (By symmetry $Q = h(r)I +$

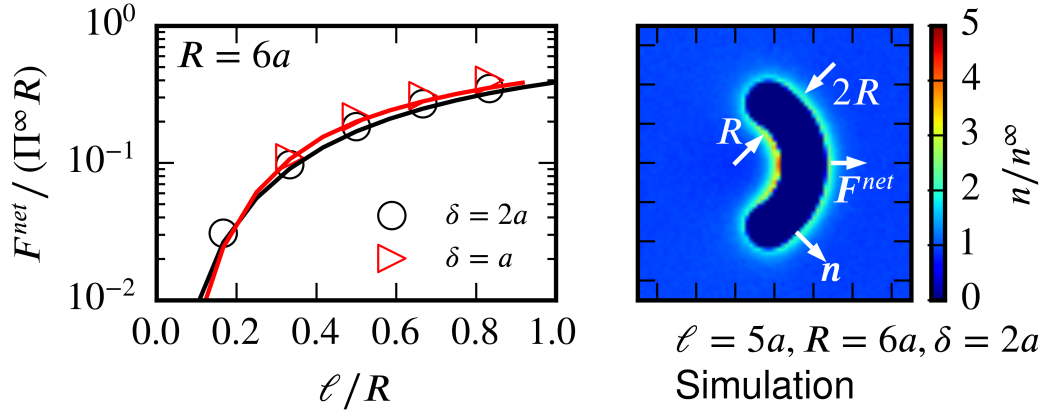


Figure 3.3: Theoretical predictions of the force on an asymmetric body in 2D with curvatures R and $2R$ compared to ABP simulations. The symbols are simulation results and the solid lines were obtained by numerically solving for the n, m fields. The force is calculated from (3.2) with body normal \mathbf{n} and is scaled by the bulk active pressure $\Pi^\infty = n(k_B T + k_s T_s)$.

$s(r)\mathbf{x}\mathbf{x}$.) Again, the m -level theory is quantitatively accurate unless $R/\delta < 5$, which is not unexpected.

By symmetry there is no net force on a sphere or a circle in an active suspension. The Brownian osmotic pressure is independent of both δ and ℓ (as it must be) and thus the integral of the constant Brownian osmotic pressure over the surface of *any* body will be zero.

From the examples the swim pressure has a correction due to the finite run length, $\Pi^{swim} \sim k_s T_s / [1 + \alpha(\ell/R)]$, where α is a constant and R is the curvature of the body. Thus, in the limit $\ell/R \ll 1$ the swim pressure is a constant at each point on the body surface and there will again be no force no matter what its shape. This is as one would expect from the pressure for a *macroscopic* object. Only when the run length is comparable to the local radius of curvature of a body is it possible to have a net force from the swimmers' activity.

Equation (3.2) for the force applies to any body shape and for any size body. Fig. 3.3 compares the force on an axisymmetric body in 2D determined by solving the

n , m fields numerically³ with ABP simulations. The agreement is excellent. If the body were free to move, its speed would result from the balance of its Stokes drag, $-\mathbf{R}_{FU} \cdot \mathbf{U}$, with the active force, where \mathbf{R}_{FU} is the hydrodynamic resistance tensor for the body. A body may also rotate if the active pressure exerts a net torque on the body, which is given by $\langle L \rangle_q = -k_B T \oint_{S_B} (\mathbf{x} - \mathbf{x}_0) \times n n dS$, where \mathbf{x}_0 is the point about which the torque is taken. The angular velocity then follows from the hydrodynamic resistance tensor coupling torque and rotation, $-\mathbf{R}_{L\Omega} \cdot \boldsymbol{\Omega}$.

3.4 Discussion

From the structure of the concentration distribution and its dependence on the ratios ℓ/δ and ℓ/L we can readily predict if a given body will experience a net force. For example, a long thin rectangle will experience no net force or torque as the active pressures are equal on both faces. If, however, we add a side arm to create a ‘T’-shaped particle, there will be a force in the direction to the top of the ‘T’. To a first approximation at each point of the surface there will be a concentration boundary layer as in (3.5) for a flat wall and thus the active pressure will be the same at all points on the body surface. However, where the top meets the side arm, the two solutions will superimpose giving an increased concentration in the ‘corners’ and thus a net force (and torque if the side arm is not at the midpoint). Similarly, a wedge-shaped particle will experience a force towards the point of the wedge from the overlapping of the concentration boundary layers on the inside corners. This reasoning can be continued for bodies composed of straight segments joined at angles (Fily *et al.*, 2014a). The precise magnitude of the force, of course, requires a solution of (3.3)-(3.4) for the given body geometry as done in Fig. 3.3, but the fact that there should be a force can be simply reasoned.

We can also reason about the interaction between two bodies through their dis-

³The unsteady equations (3.3)-(3.4) were solved numerically with a standard Galerkin P2-FEM method with adaptive mesh refinement. Implicit time-stepping was used to ensure solution stability, and the solution is tracked long enough ($\sim 150\tau_R$) to reach a steady state.

turbance to the concentration and polar-order fields. Two bodies will experience a depletion-like attraction due to the exclusion of active particles between them.⁴ When bodies are far apart the attractive force is very weak and decays exponentially with separation according to (3.8); this exponential dependence was seen in the simulations of (Ray *et al.*, 2014). Outside the screening length the concentration is undisturbed and the depletion interaction will be the same as for passive colloidal particles where the exclusion zone is geometric (Asakura & Ooswa, 1954); the Brownian osmotic pressure on the exposed surfaces is replaced by the active pressure that includes the run length (3.10). Note that the exclusion occurs on the microscopic scale δ (or swimmer size a), not on the scale of the run length. Even when the gap between two particles is less than ℓ the active particles can still access this space and exert their swim pressure.

In the examples we have considered there was no polar order far from the boundary, nor a gradient in the concentration of swimmers, and thus force or motion can only arise if the run length is on the order of the body size, $\ell/L \sim O(1)$, and if the symmetry is broken by the body shape. With macroscopic polar order, which can result from an orienting field applied to the swimmers (Takatori & Brady, 2014), even a spherical particle will experience a net force and move due to the imbalanced active pressure. We also used the simplest no-flux boundary condition on the polar order field at the body surface, but this condition can be modified. For example, a portion of the body surface may be treated such that the active particles achieve a preferred orientation or experience a localized orienting field. Such a ‘Janus’ particle may have a net force due to a spatially varying polar order boundary condition.

Indeed, a localized boundary orienting field was used by (Solon *et al.*, 2015b) to argue that the pressure of active matter is not a ‘state’ function, as the force per unit area on a wall is no longer equal to the swim pressure far from the surface. As our

⁴The force can be estimated from (3.8): $F \sim -k_B T V \nabla n$, where V is the volume of particle i and the concentration gradient due to particle j is evaluated at the center of i .

microscopic theory shows, this is to be expected in general: boundary curvature, the detailed flux conditions at the surface, etc. can all affect the value of the concentration at the surface and thus the force on the boundary. We showed recently (Yan & Brady, 2015a) that the polar order induced by an orienting field acts like a body force on the active material, and when this ‘internal’ body force is included in the momentum balance, the force per unit area on the wall plus the integral of the internal body force is equal to the active pressure far from the surface, thus restoring the active pressure as a state function.

With an external field that tends to align the swimmers and biases their motion, for example, an external torque or hydrodynamic shearing flows, the conservation equation for \mathbf{m} now has an additional ‘sink’ term, which can be written as $2D_R[\mathbf{m} - \mathbf{m}^\infty]$ where \mathbf{m}^∞ is the polar order far from the boundary induced by the field. The equation for \mathbf{Q} will have a similar \mathbf{Q}^∞ term. One now writes conservation equations for the departures of the polar order and nematic fields from their undisturbed values, $\mathbf{m}' = \mathbf{m} - \mathbf{m}^\infty$ and $\mathbf{Q}' = \mathbf{Q} - \mathbf{Q}^\infty$, and then closes the disturbance equations along the lines done here. It is not known if this simple closure proves as accurate when there is net bulk polar order.

Since the behavior is dominated by the rapid variations that occur on the screening length adjacent to the body surface, the situation has features in common with phoretic-like problems where a thin layer near the surface dominates the motion and hydrodynamic fluid motion can be incorporated in a manner similar to diffusio-phoresis (Anderson, 1989; Brady, 2011; Shklyaev *et al.*, 2014).

The theory we have developed and applied for dilute active matter can be extended to higher concentrations of swimmers. The N -particle Smoluchowski equation for passive Brownian particles including excluded volume and full hydrodynamic interactions is well known, as is the form of the many-body hydrodynamic swim force (Yan & Brady, 2015a). Reduction to the lowest moments, n and \mathbf{m} , is certain

to give rise to new phenomena since the swim diffusivity, which enters the flux expressions, can be a decreasing function of the swimmer concentration (Takatori *et al.*, 2014).

*Chapter 4***THE CURVED KINETIC BOUNDARY LAYER OF ACTIVE
MATTER**

Swimming micro-organisms may accumulate near a non-penetrating boundary due to hydrodynamic interactions (Berke *et al.*, 2008). The accumulation may also arise from ‘kinematic’ origins, e.g., elongated bacteria cannot freely swim on a surface due to a geometric constraint with the wall (Li & Tang, 2009; Li *et al.*, 2011). The accumulation due to wall-swimmer interaction gives rise to interesting behaviors; e.g., rheotaxis (Uspal *et al.*, 2015; Kaya & Koser, 2012) and circular motion (Lauga *et al.*, 2006). Also, an asymmetric macroscopic body can harvest energy from the bacteria solution and achieve net motion simply due to its shape (Kaiser *et al.*, 2014). In fact, the swimmers need not be elongated to exhibit the kinetic accumulation (Yan & Brady, 2015a; Ezhilan *et al.*, 2015). It may be simply due to the fact that when a swimmer hits a wall, it may persist with its swim orientation \mathbf{q} for a finite reorient time τ_R . In this case, the interaction with a non-penetrating boundary can be modeled by an Active Brownian Particle (ABP). Each ABP propels itself at a fixed swim velocity $U_0\mathbf{q}$, where \mathbf{q} is subject to rotational Brownian diffusivity $D_R = 1/\tau_R$. ABPs may also be subject to translational Brownian motion D_T , with $\zeta = k_B T/D_T$ the (isotropic) drag coefficient.

When an ABP is stuck on the wall, it transmits to the wall a force $-\zeta U_0\mathbf{q} \cdot \mathbf{n}$ because it cannot cross the wall, where \mathbf{n} is the wall surface normal vector. That force accumulates over time and space, and the net effect constitutes a pressure on the wall higher than the ‘passive’ osmotic pressure $n^\infty \zeta D_T = n^\infty k_B T$. That simple process is exactly the microscopic origin of the ‘swim pressure’ (Takatori *et al.*, 2014). In the absence of hydrodynamic interactions, Yan & Brady, (2015b) showed that the pressure of ABPs follow a natural extension of the Passive Brownian Particles (PBP): $\Pi^{wall} = n^{wall} \zeta D_T = n^{wall} k_B T$, where n^{wall} is the number density of particles on the wall, and it decreases to the bulk n^∞ on the microscopic length scale $\delta = \sqrt{D_T \tau_R}$. n^{wall} for various geometries can be simply calculated with the moment expansion method (Saintillan & Shelley, 2015), and including high order moments is usually not necessary (Yan & Brady, 2015b). The general result naturally extends

to the singular limit $\delta \rightarrow 0$ in the absence of translational Brownian motion $D_T \rightarrow 0$ (Fily *et al.*, 2014a; Ezhilan *et al.*, 2015).

It has been shown (Fily *et al.*, 2014a; Yan & Brady, 2015b; Smallenburg & Löwen, 2015) that the accumulation at the boundary is significantly impacted by the boundary curvature. Therefore, an asymmetric macroscopic body immersed in ABPs can achieve a net force (Yan & Brady, 2015b), simply due to its asymmetric shape. In general, n^{wall} is higher in dent regions on a shape and the higher $\Pi^{wall} = n^{wall} \zeta D_T$ in this region pushes the shape. Since ABPs are assumed to convey no friction on a boundary, the net force due to asymmetric shape can be calculated by an integration of the pressure distribution $\Pi^W = n^W \zeta D_T$ around the shape, and n^W can be numerically solved with Smoluchowski equations.

Although the above numerical approach works well case by case, an analytical prediction of the net force is missing. In general, three length scales appear in this problem: the macroscopic length scale of the body L , the microscopic length scale δ , and the particles' run-length $\ell = U_0 \tau_R$. Usually δ is on the order of the ABP's size, and $\delta \ll L$, but ℓ can be arbitrary, and it leads to various scenarios. Therefore, a general analytical theory covering all scenarios is favorable.

When $\ell \ll \delta$, the particles are simply passive Brownian particles and the net force should vanish. When $\delta \ll \ell \ll L$, the particles show significant activity, and numerical results (Yan & Brady, 2015b) show significant net forces, but the swimmer number density is only perturbed in a small region close to the body. When the run-length ℓ is further increased to be comparable with L , the net force is greatly increased and the perturbation on swimmer number density propagates far away from the body (Yan & Brady, 2015b).

Physically, when $\ell \ll L$, the particles may spend many τ_R without leaving a local region on the shape, and therefore they may establish a 'local equilibrium' of number density distribution governed by the local curvature. Therefore, following

the moment expansion approach (Yan & Brady, 2015b), the local solution of n^{wall} may be solved everywhere around the arbitrarily shaped body, and all local solutions can be matched to the global Smoluchowski equation of ABPs. This constitutes a standard boundary-layer approach, where the inner (local) and outer (global) solution should be matched to give the distribution of Π^{wall} everywhere, and the net force can be calculated with a surface integral. Since the moment expansion approach is general for arbitrary δ and ℓ , the solution is expected to cover both the limits $\delta \ll \ell$ and $\delta \gg \ell$ with a universal scaling. The scaling will be shown to be related to the inverse screening length of the number density $\lambda = \sqrt{2 \left(1 + \frac{1}{6} (\ell/\delta)^2\right)}/\delta$.

When ℓ is comparable to L , the ABPs ‘sample’ the shape of the entire shape in a single run-length $U_0\tau_R$. In this case n^W is no longer determined only by the local curvature – the variation of the curvature must be considered. Therefore the above local boundary layer solution for $\ell \ll L$ is no longer true. However, we shall see that the universal scaling based upon λ is still valid.

In this chapter, we shall start from the Smoluchowski equation for ABPs with its moment-hierarchy expansion. Then we discuss the separation of scales in the governing equation. That is, the emergence of the boundary layer of accumulation and its connection to the outer solution. By building a local curvilinear coordinate system with the principal curvature, we seek a leading order analytical solution to the boundary layer equation. Further, we match the local boundary-layer equation to the outer solution to calculate the net force on an arbitrarily shaped body. The analytical solutions are then compared to simulations. Finally, we discuss the effect of different length scales, the connection to a continuum mechanics point of view (Yan & Brady, 2015a) in an analogy to rarefied gas dynamics, and the formulation to include full hydrodynamics into this pure kinetic boundary layer analysis.

4.1 Problem formulation

From a kinetic point of view, there are three characteristic lengths for ABPs: (i) the macroscopic length scale L for the body, (ii) the run length $\ell = U_0\tau_R$ and (iii) a microscopic length $\delta = \sqrt{D_T\tau_R}$, where D_T is the translational diffusivity of the active particles. For a typical swimming micro-organism or a synthesized Janus particle, $\tau_R \sim 1$ s, $\delta \sim 1$ μm , and $\ell \sim 1 - 10$ μm .

ABPs are governed by the Smoluchowski equation for the probability density for finding a swimmer at \mathbf{x} with orientation \mathbf{q} , at time t :

$$\frac{\partial P(\mathbf{x}, \mathbf{q}, t)}{\partial t} + \nabla \cdot \mathbf{j}^T + \nabla_R \cdot \mathbf{j}^R = 0. \quad (4.1)$$

Consider a single particle without particle-particle collisions in the dilute limit. The translational and rotational fluxes are:

$$\mathbf{j}^T = (U_0\mathbf{q} - D_T\nabla \ln P)P, \quad (4.2)$$

$$\mathbf{j}^R = -D_R\nabla_R P, \quad (4.3)$$

where $\nabla_R = \mathbf{q} \times \nabla_{\mathbf{q}}$ is the orientational gradient operator (Brenner & Condiff, 1972).

For a spherical swimmer of radius a in a Newtonian solvent of viscosity η , $\zeta = 6\pi\eta a$, $D_T = k_B T / \zeta = k_B T / 6\pi\eta a$, $D_R = 1/\tau_R = k_B T / 8\pi\eta a^3$ and $\delta = \sqrt{D_T/D_R} = \sqrt{4/3}a$. In this chapter we develop a general theory for arbitrary D_T and D_R .

At a boundary, the normal component of the translational flux must vanish:

$$\mathbf{n} \cdot \mathbf{j}^T = 0. \quad (4.4)$$

At infinity, we assume the swimmers are unperturbed at n^∞ , with an unbiased orientation distribution. The conservation equations for the zeroth and first moments of the Smoluchowski equation are (Saintillan & Shelley, 2015):

$$\frac{\partial n}{\partial t} + \nabla \cdot \mathbf{j}_n = 0, \quad \mathbf{j}_n = U_0\mathbf{m} - D_T\nabla n, \quad (4.5)$$

$$\frac{\partial \mathbf{m}}{\partial t} + \nabla \cdot \mathbf{j}_m + 2D_R\mathbf{m} = 0, \quad \mathbf{j}_m = U_0\mathbf{Q} + \frac{1}{3}U_0n\mathbf{I} - D_T\nabla\mathbf{m}, \quad (4.6)$$

where $\mathbf{m}(\mathbf{x}, t) = \int \mathbf{q}P(\mathbf{x}, \mathbf{q}, t)d\mathbf{q}$ is the polar order field, and $\mathbf{Q}(\mathbf{x}, t) = \int (\mathbf{q}\mathbf{q} - \frac{1}{3}\mathbf{I})P(\mathbf{x}, \mathbf{q}, t)d\mathbf{q}$ is the (zero-traced) nematic order field. The hierarchy can be continued to include an extra equation for \mathbf{j}_Q , allowing the variation of the nematic order \mathbf{Q} in space. It has been shown (Yan & Brady, 2015b) that including a nematic order does not significantly improve the accuracy of the boundary-layer solution, assuming no nematic order appears. One can appreciate that truncation by thinking about the asymmetry induced by a wall on the ABPs' motion. The wall introduces an asymmetry that is either towards the wall or directed away from the wall. Therefore, the polar order is naturally the most effective one. Including higher moments only slightly improves the solution in the limit of $\ell \gg \delta$ and $\ell \sim L$.

We then non-dimensionalize the equations with length scale L and timescale τ_R . Consider the steady state only:

$$\hat{\nabla} \cdot \mathbf{j}_n = 0, \quad (4.7)$$

$$\hat{\nabla} \cdot \mathbf{j}_m + 2\mathbf{m} = 0, \quad (4.8)$$

with flux:

$$\mathbf{j}_n = \frac{\ell}{L}\mathbf{m} - \frac{\delta^2}{L^2}\hat{\nabla}n, \quad (4.9)$$

$$\mathbf{j}_m = \frac{\ell}{3L}n\mathbf{I} - \frac{\delta^2}{L^2}\hat{\nabla}\mathbf{m}. \quad (4.10)$$

The truncation $\mathbf{Q} = 0$ allows a simple mathematical manipulation of the equations. Set $f = \hat{\nabla} \cdot \mathbf{m}$. Take the divergence of (4.8) and eliminate $\hat{\nabla}^2 n$ with (4.7). We have

$$(\hat{\nabla}^2 - \lambda^2 L^2) f = 0, \quad (4.11)$$

$$\hat{\nabla}^2 n = \frac{L\ell}{\delta^2} f, \quad (4.12)$$

where

$$\lambda = \sqrt{2 \left(1 + \frac{1}{6} (\ell/\delta)^2\right)}/\delta \quad (4.13)$$

is the inverse screening length (Yan & Brady, 2015b).

Equation (4.11) is a homogeneous Helmholtz equation, which has a ‘screened’ solution. Since we know in free space $n = n^\infty = \text{const}$ and $\mathbf{m} = 0$, $f^\infty = 0$ and f must decay exponentially on the length scale λL away from the boundary.

Equation (4.12) is an inhomogeneous Laplace equation, and the solution can be decomposed into a homogeneous general solution n_H and an inhomogeneous particular solution n_P :

$$n = n_H + n_P, \quad (4.14)$$

$$\hat{\nabla}^2 n_H = 0, \quad \hat{\nabla}^2 n_P = \frac{L\ell}{\delta^2} f. \quad (4.15)$$

Therefore, we know that n_H decays as $1/r$ governed by the Laplace’s equation, and n_P decays at the same rate as $f = \hat{\nabla} \cdot \mathbf{m}$.

Once we know $n = n_H + n_P$, we can put it back into the equation to solve for \mathbf{m} :

$$\frac{\delta^2}{L} \hat{\nabla}^2 \mathbf{m} - 2\mathbf{m} = \frac{l}{3L} \nabla n. \quad (4.16)$$

Again, due to the structure of this inhomogeneous Helmholtz equation, \mathbf{m} can be decomposed into a homogeneous general solution and a particular solution depending on ∇n : $\mathbf{m} = \mathbf{m}_H + \mathbf{m}_P$.

$$\frac{\delta^2}{L^2} \hat{\nabla}^2 \mathbf{m}_P - 2\mathbf{m}_P = \frac{l}{3L} \hat{\nabla} n, \quad (4.17)$$

$$\frac{\delta^2}{L^2} \hat{\nabla}^2 \mathbf{m}_H - 2\mathbf{m}_H = 0. \quad (4.18)$$

With some mathematical construction, we can explicitly calculate the particular solutions n_P and \mathbf{m}_P :

$$n_P = \frac{\ell}{\delta^2 \lambda^2 L} \hat{\nabla} \cdot \mathbf{m}, \quad (4.19)$$

$$\mathbf{m}_P = \frac{1}{\lambda^2 L^2} \hat{\nabla} (\hat{\nabla} \cdot \mathbf{m}) - \frac{l}{6L} \hat{\nabla} n_H, \quad (4.20)$$

where \mathbf{m}_P contains the long-ranged, or unscreened part proportional to $\hat{\nabla} n_H$.

In sum:

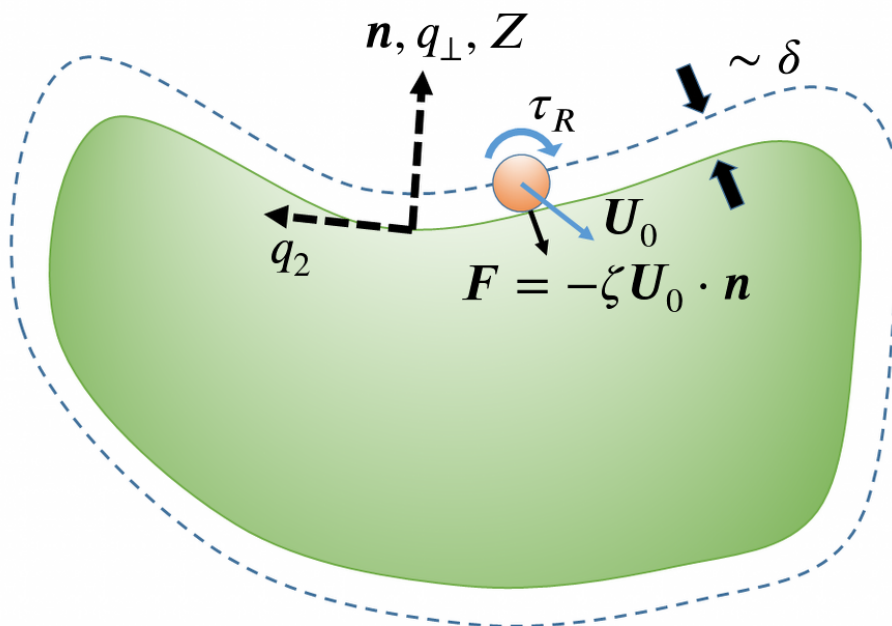


Figure 4.1: The formation of the boundary layer on the body surface. When a swimmer comes to the surface, it transmits a force to the wall of $F = -\zeta U_0 \cdot n$. The swimmers form an accumulation boundary layer, with thickness on the order of $\delta = \sqrt{D_T \tau_R}$. The inner solution is solved in the local coordinate system q_\perp, q_2 , depending on the local curvature. The definition of the local curvature is shown in Fig. 4.2.

- $f = \hat{\nabla} \cdot \mathbf{m}$ exponentially decays as $\exp(-\lambda L \hat{r})$.
- n_H is long ranged as $n^\infty + O(1/\hat{r})$.
- $n_P \sim f$ exponentially decays as $\exp(-\lambda L \hat{r})$.
- \mathbf{m}_H exponentially decays as $\exp(-L \hat{r}/\delta)$.
- \mathbf{m}_P contains both an exponential $\exp(-\lambda L \hat{r})$ and a long ranged $O(1/\hat{r}^2)$ component.

Physically, the exponentially decaying components will be ‘screened’ to the body surface. When $\delta \ll L$, the solutions can be split in the (exponential) inner region and the $O(1/\hat{r})$ outer region. The boundary layer is illustrated in Fig. 4.1. Only

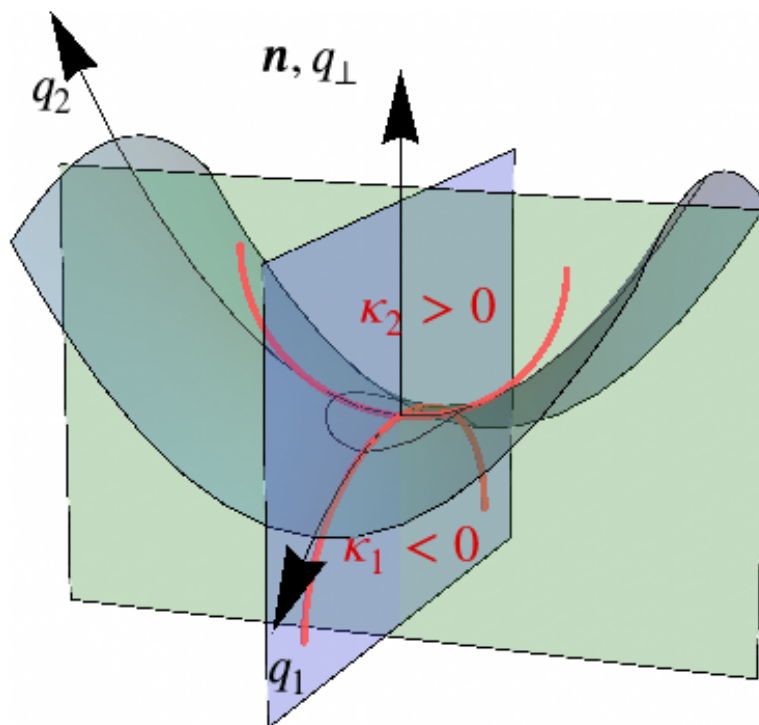


Figure 4.2: The local representation of an arbitrary curved surface. The two principal curvature directions are located in the two perpendicular planes. The local curvilinear coordinate system q_1, q_2, q_\perp is built on the surface, where locally it is orthogonal. q_\perp aligns with the normal vector n pointing toward the outside of the shape at that point. The sign of principal curvatures κ_1 and κ_2 follows the convention shown here.

n_H and the corresponding component in m_P extend to the outer region, and are governed by a simple Laplace's equation (4.12). Inside the boundary layer, due to the separation of scales, the outer solution n_H can be considered as linear or even a constant. Therefore, in this case we can split the problem into an inner region and an outer region. The inner region is attached to the body surface and can be considered as a 1D (curved) boundary layer. After the boundary layer is solved, the solution can be used as the boundary condition for the Laplace equation in the outer region. The final solution can be determined by matching the flux j_n, j_m between these two regions, which is a standard boundary-layer approach.

Recall that $\lambda = \sqrt{2 \left(1 + \frac{1}{6} (\ell/\delta)^2\right)}/\delta$. When $\ell \sim \delta$, $\lambda \sim 1/\delta$, and n_P and m_H decay at comparable rate. When $\ell \gg \delta$, $\lambda \sim \ell/\delta^2 \gg 1/\delta$, and n_P decays much faster than

m_H . In this case, the inner region of thickness δ further splits into two regions of different scales, and form ‘a boundary layer inside a boundary layer’. Our analysis in the following section, however, is a general approach and applies to both cases. In sum, we shall solve the boundary layer structure with the assumption that $\delta \ll L$, $\ell \ll L$, but we do not specify the relation between δ and ℓ .

4.2 Analytical solution

Inside the boundary layer, the solution is exponential and depends on the local geometry only. We can split the solution into the inner region n_{in}, m_{in} and outer n_{out}, m_{out} . We shall scale all lengths with the macroscopic length scale L . As discussed in the last section, the outer region is governed by a Laplace’s equation:

$$\hat{\nabla}^2 n_{out} = 0, \quad (4.21)$$

while in the inner region we shall solve the full equations, starting with (4.11). In the simplest case for a flat plate $\hat{\kappa}_1 = \hat{\kappa}_2 = 0$, the boundary layer has been solved (Yan & Brady, 2015b). Inside the boundary layer, we rescale $Z = q_{\perp}/(\delta/L) = q_{\perp}/\epsilon$, where $\epsilon = \delta/L \rightarrow 0$:

$$\frac{f_0}{n^{\infty}} = \frac{\ell L}{\delta^2} \frac{6\delta^2 + \ell^2}{18\delta^2} e^{-\lambda\delta Z}, \quad (4.22a)$$

$$\frac{n_0}{n^{\infty}} = 1 + \frac{\ell^2}{6\delta^2} e^{-\lambda\delta Z}, \quad (4.22b)$$

$$\frac{m_{\perp,0}}{n^{\infty}} = -\frac{\ell\lambda}{6} e^{-\lambda\delta Z}, \quad m_{\parallel,0} = 0, \quad (4.22c)$$

where the subscript 0 means zero curvature of the wall. For a flat wall geometry, above that boundary layer the outside solution is simply $n_{out} = n^{\infty} = const$. Now we consider an arbitrary shaped macroscopic body. To zeroth order, the flat boundary layer solution gives the pressure on the wall:

$$\begin{aligned} \Pi^{wall} &= n^{wall} \zeta D_T = \left(1 + \frac{\ell^2}{6\delta^2}\right) n^{\infty} \zeta D_T, \\ &= \zeta n^{\infty} (D_T + D^{swim}) = n^{\infty} (k_B T + k_s T_s). \end{aligned} \quad (4.23)$$

Therefore to zeroth order of curvature, the pressure on a macroscopic body is the same everywhere on the surface regardless of the body shape. The net force on any shape given by this homogeneous pressure is zero, just as a macroscopic body submersed in the atmosphere does not get any net force from the homogeneous isotropic atmospheric pressure. For a classical ideal gas, the pressure on a boundary would deviate from the ideal gas limit when the mean free path is comparable to the macroscopic body length. For ABPs, the pressure is applied to the body surface through the formation of the kinetic boundary layer, so the pressure may deviate from the isotropic swim pressure $n^\infty (k_B T + k_s T_s)$ when the boundary layer thickness is comparable to the body's lengthscale.

The boundary-layer thickness is governed by the microscopic length $\delta = \sqrt{D_T \tau_R}$; therefore we shall improve the zero-curvature solution to the leading order curvature. We locally build a curvilinear coordinate system as shown in (4.2). The local arbitrary curved surface is represented by a second order curvature (mathematically, the second fundamental form). Coordinate axes q_1, q_2 are attached to the curvature surface and q_\perp is perpendicular to it. q_1, q_2 are along the two principal curvature directions. q_\perp is aligned with the normal vector \mathbf{n} . Mathematically, we can assume that locally q_1, q_2, q_\perp are orthogonal.

In the curvilinear coordinate system, the Cartesian nabla operator $\hat{\nabla}$ in (4.11) should be replaced by the curvilinear operator $\hat{\nabla}_*$. The details can be found in Appendix D, and to the leading order of $O(\delta/|R|)$ we need only consider a constant $J_S = 2H$, where $H = \frac{1}{2}(\hat{\kappa}_1 + \hat{\kappa}_2)$ is the mean curvature. Also, the first order effects give only a correction to the normal direction. The tangential direction solution appears at second order.

Here we consider a smooth body, and we assume the curvature radii $\hat{R} = 1/\hat{\kappa} \sim O(1)$, also non-dimensionalized by L everywhere. If there is a sharp corner on the body, the curvature radii $|R_{corner}| \ll L$, and the boundary-layer assumption might no longer

be valid there, so a leading order curvature solution is not sufficient. Physically, swimmers with orientation $\mathbf{q} \neq -\mathbf{n}$ have a tangential swim velocity and are about to leave that sharp corner easily. This is also true for a passive particle with significant translational diffusivity D_T . Therefore, the kinetic accumulation on a sharp corner or tip is very weak, and the pressure there significantly decreases with increasing $\ell/|R|$ and $\delta/|R|$ (Yan & Brady, 2015b).

Inner solution

In the boundary layer, we shall use n_{top} to denote the number density at the top of the boundary layer, and n_{top} is a local value of the outer solution, which is not necessarily a constant as n^∞ :

$$\left(\hat{\nabla}_*^2 - \lambda^2 L^2\right) f = 0, \quad (4.24)$$

$$\left(-J_S \frac{\partial}{\partial q_\perp} + \frac{\partial^2}{\partial q_\perp^2} - \lambda^2 L^2\right) f = 0, \quad (4.25)$$

where $J_S \sim O(1/(R/L)) \sim O(1)$. Inside the boundary layer we rescale $Z = q_\perp/\epsilon$. Here $\epsilon \sim \delta/L \ll 1$ and $Z \sim O(1)$:

$$\left(-J_S \epsilon \frac{\partial}{\partial Z} + \frac{\partial^2}{\partial Z^2} - 2 \left(1 + \frac{\ell^2}{6\delta^2}\right)\right) f = 0. \quad (4.26)$$

The leading order effects of the curvature are captured by this asymptotic expansion:

$$f = f_0 + \epsilon f_1 + \dots, \quad (4.27)$$

$$n = n_0 + \epsilon n_1 + \dots, \quad (4.28)$$

$$m_\perp = m_{\perp,0} + \epsilon m_{\perp,1} + \dots, \quad (4.29)$$

where the leading order $f_0, n_0, m_{\perp,0}$ are just the flat surface solution (4.22).

If $\ell/\delta \sim O(1)$, then $f_0/n_{top} \sim L/\delta$, $n_0/n_{top} \sim O(1)$, $m_{\perp,0}/n_{top} \sim O(1)$. If $\ell \gg \delta$, then $f_0/n_{top} \sim \ell^3 L/\delta^4$, $n_0/n_{top} \sim \ell^2/\delta^2$, and $m_{\perp,0}/n_{top} \sim \ell^2/\delta^2$ are not on the same order, due to the different prefactors in (4.22). So we should be very careful when going to the next order without losing the scalings. Also, due to geometry (D.3),

the divergence operator at the first order includes a contribution from the curvature J_S :

$$f_0 = \frac{L}{\delta} \frac{\partial m_{\perp,0}}{\partial Z}, \quad (4.30a)$$

$$f_1 = \frac{L}{\delta} \left(-J_S m_{\perp,0} + \frac{\partial m_{\perp,1}}{\partial Z} \right). \quad (4.30b)$$

Therefore we can solve at first order:

$$\left(\frac{\partial^2 f_1}{\partial Z^2} - \lambda^2 \delta^2 \right) f_1 = J_S \frac{\partial f_0}{\partial Z}. \quad (4.31)$$

The solution is:

$$\begin{aligned} \frac{f_1}{n_{top}} &= C_1 e^{\delta \lambda Z} + C_2 e^{\delta \lambda (-Z)} \\ &+ \frac{1}{12} \ell J_S \lambda^2 L Z e^{\delta \lambda (-Z)} + \frac{\ell J_S \lambda L}{24 \delta} e^{\delta \lambda (-Z)}, \end{aligned} \quad (4.32)$$

where C_1 and C_2 are constants to be determined. As discussed in the last section, f is screened so all components of f_1 are exponential. We can determine that $C_1 = 0$ because in the final step the solution, the limit $Z \rightarrow \infty$ will be applied to attach the inner and the outer solution.

Then we can solve the first curvature correction n_1 in the normal direction:

$$\frac{\partial^2 n_1}{\partial Z^2} = \frac{\ell}{L} f_1 + J_S \frac{\partial n_0}{\partial Z}, \quad (4.33)$$

giving:

$$\begin{aligned} \frac{n_1}{n_{top}} &= \frac{C_1 \ell e^{\delta \lambda Z}}{\delta^2 \lambda^2 L} + \frac{C_2 \ell e^{\delta \lambda (-Z)}}{\delta^2 \lambda^2 L} + C_3 + C_4 Z \\ &+ \frac{\ell^2 J_S e^{\delta \lambda (-Z)}}{24 \delta^3 \lambda} + \frac{\ell^2 J_S Z e^{\delta \lambda (-Z)}}{12 \delta^2}. \end{aligned} \quad (4.34)$$

The last step is to solve for m_{\perp} :

$$-J_S \frac{\partial m_{\perp,0}}{\partial Z} + \frac{\partial^2 m_{\perp,1}}{\partial Z^2} - 2m_{\perp,1} = \frac{\ell}{3L} \frac{L}{\delta} \frac{\partial n_1}{\partial Z}. \quad (4.35)$$

The solution is:

$$\begin{aligned} \frac{m_{\perp,1}}{n_{top}} &= \frac{C_1 e^{\delta\lambda Z}}{\lambda L} - \frac{C_2 e^{\delta\lambda(-Z)}}{\lambda L} - \frac{1}{12} \ell J_S \lambda Z e^{\delta\lambda(-Z)} \\ &+ \frac{\ell J_S e^{\delta\lambda(-Z)}}{24\delta} - \frac{\ell}{6\delta} C_4. \end{aligned} \quad (4.36)$$

By definition $f = \hat{\nabla}_* \cdot \mathbf{m}$, and the solution $m_{\perp,1}$ is compatible with (4.30).

The structure of $f_1, n_1, m_{\perp,1}$ follows exactly the separation of scales as discussed in the last section. Particularly, the $C_3 + C_4 Z$ part in n_1 represents the long-range solution n_H . The $-\ell C_4/(6\delta)$ part in $m_{\perp,1}$ is also the long-ranged part $-\ell \hat{\nabla} n_H/(6\delta)$ in \mathbf{m}_P . Inside the very thin boundary layer, the variation of n_H is very slow, and is simplified to a linear function of Z in the first order solution n_1 .

Matching the boundary condition & the flux

First, the exponentially growing part C_1 must be zero. On the surface $Z = 0$, the boundary condition is simply non-penetrating:

$$\mathbf{j}_n \cdot \mathbf{n}_Z = \ell m_{\perp} - \frac{\delta^2 L}{L\delta} \frac{\partial n}{\partial Z} = 0, \quad (4.37)$$

$$\mathbf{j}_m \cdot \mathbf{n}_Z = \frac{n}{3} \ell - \frac{\delta^2 L}{L\delta} \frac{\partial m_{\perp}}{\partial Z} = 0. \quad (4.38)$$

Part 1, \mathbf{j}_n :

$$\begin{aligned} \mathbf{j}_n \cdot \mathbf{n}_Z &= \ell \left(m_{\perp,0} + \frac{\delta}{L} m_{\perp,1} \right) - \frac{\delta^2 L}{L\delta} \frac{\partial}{\partial Z} \left(n_0 + \frac{\delta}{L} n_1 \right), \\ &= -\frac{C_4 \delta^2}{L} n_{top}. \end{aligned} \quad (4.39)$$

It is a constant, and to satisfy the boundary condition $\mathbf{j}_n \cdot \mathbf{n}_Z = 0$, C_4 must be zero. So the perpendicular component of flux $j_{n,\perp} = \mathbf{j}_n \cdot \mathbf{n}_Z = 0$ throughout the boundary layer. Therefore by the continuity of flux from the outer solution to the inner solution, this zero-flux boundary condition is also the boundary condition for the outer solution $\hat{\nabla}^2 n_{out} = 0$.

Part 2, j_m :

By setting $\mathbf{j}_m \cdot \mathbf{n}_Z = 0$ at $Z = 0$ in (4.36), we can find:

$$C_2 = C_3 \frac{\ell L (6\delta^2 + \ell^2)}{18\delta^4} + \frac{\ell J_S L (9\delta^2 + 2\ell^2) \sqrt{\frac{\ell^2}{\delta^2} + 6}}{72\sqrt{3}\delta^4}, \quad (4.40)$$

where C_3 should be matched by the outer solution: as $Z \rightarrow \infty$,

$$\frac{n}{n_{top}} \rightarrow n_0(Z \rightarrow \infty) + \frac{\delta}{L} n_1(Z \rightarrow \infty) = 1 + \frac{\delta}{L} C_3. \quad (4.41)$$

Part 3, $\nabla \cdot \mathbf{j}_n$:

$\nabla \cdot \mathbf{j}_n$ does not work as a boundary condition, but we demonstrate that at steady state it is zero, as required by the governing equation (4.5). The two leading orders to the flux \mathbf{j}_n are:

$$\begin{aligned} \nabla \cdot \mathbf{j}_n &= \ell \frac{L}{\delta} \frac{\partial m_{\perp,0}}{\partial Z} - L \frac{\partial^2 n_0}{\partial Z^2} \\ &+ \ell \left(-J_S m_{\perp,0} + \frac{\partial m_{\perp,1}}{\partial Z} \right) - \delta \left(\frac{\partial^2 n_1}{\partial Z^2} - J_S \frac{\partial n_0}{\partial Z} \right), \end{aligned} \quad (4.42)$$

and we know that $m_{\perp,0} = \frac{\delta}{\ell} \frac{\partial n_0}{\partial Z}$; therefore,

$$\nabla \cdot \mathbf{j}_n = \ell \left(\frac{\partial m_{\perp,1}}{\partial Z} \right) - \delta \left(\frac{\partial^2 n_1}{\partial Z^2} \right). \quad (4.43)$$

So by the solution (4.34) and (4.36), $\nabla \cdot \mathbf{j}_n = 0$ everywhere inside the boundary layer, as required by the governing equations.

From inner to outer: continuity of $j_{n,\perp}$

Remember that, as discussed in the last section, the solution to n can be decomposed to a homogeneous solution n_H and a particular solution n_P . From an inner-outer boundary layer point of view, n_H satisfies the Laplace's equation and is just the outer solution n_{out} . In the outer region,

$$\nabla^2 n_{out} = 0, \quad (4.44)$$

$$n_{out}(\hat{r} \rightarrow \infty) = n^\infty, \quad (4.45)$$

$$\text{boundary condition (4.39): } j_{n,\perp} = \mathbf{j}_n \cdot \mathbf{n} = 0. \quad (4.46)$$

According to (4.9) and (4.19), in the outer region $\mathbf{m} = -\ell \hat{\nabla} n_H / (6L)$, therefore:

$$\begin{aligned} \mathbf{j}_n &= \frac{\ell}{L} \mathbf{m}_P - \frac{\delta^2}{L^2} \hat{\nabla} n_{out} = -\frac{\ell}{L} \frac{\ell}{6L} \hat{\nabla} n_{out} - \frac{\delta^2}{L^2} \hat{\nabla} n_{out}, \\ &\sim - (D^{swim} + D_T) \nabla n_{out} = 0. \end{aligned} \quad (4.47)$$

Then on the boundary of the outer region $\hat{\nabla} n_{out} \cdot \mathbf{n} = 0$. Therefore, by the uniqueness theorem of the Laplace's equation subject to Neumann boundary condition, the unique solution to n_{out} is simply:

$$n_{out} = const = n^\infty. \quad (4.48)$$

It gives a very simple boundary-layer solution structure. The outer solution n_{out} is simply a constant everywhere, and so at the top of the boundary layer everywhere, n_{top} is a universal constant: $n_{top} = n^\infty$. The inner solutions are given as (4.34) and (4.36), which decay exponentially from the surface and scale as n^∞ .

As shown in Fig. 4.3, when $\lambda' \delta^2 / |R| = \frac{1}{2\sqrt{6}} \rightarrow 0$, the swimmers form an accumulation boundary layer, and the solution $n^{out} = const$ is valid. When ℓ is increased so that $\lambda' \delta^2 / |R| = \frac{1}{2\sqrt{6}} \sim 1$, the boundary layer still exists but the solution n_{out} is no longer a constant.

4.3 Results

Analytical results

With the solution $n_{top} = n^\infty$ and (4.34) & (4.36), we can calculate the swim pressure exerted by the kinetic boundary layer everywhere on an arbitrary shaped body with $\Pi_{wall} = \zeta D_T n_{wall}$:

$$\begin{aligned} \frac{n_{wall}}{n^\infty} &= n_0(Z=0) + \frac{\delta}{L} n_1(Z=0), \\ &= 1 + \frac{\ell^2}{6\delta^2} + \frac{\ell^2 \lambda}{12L} J_S. \end{aligned} \quad (4.49)$$

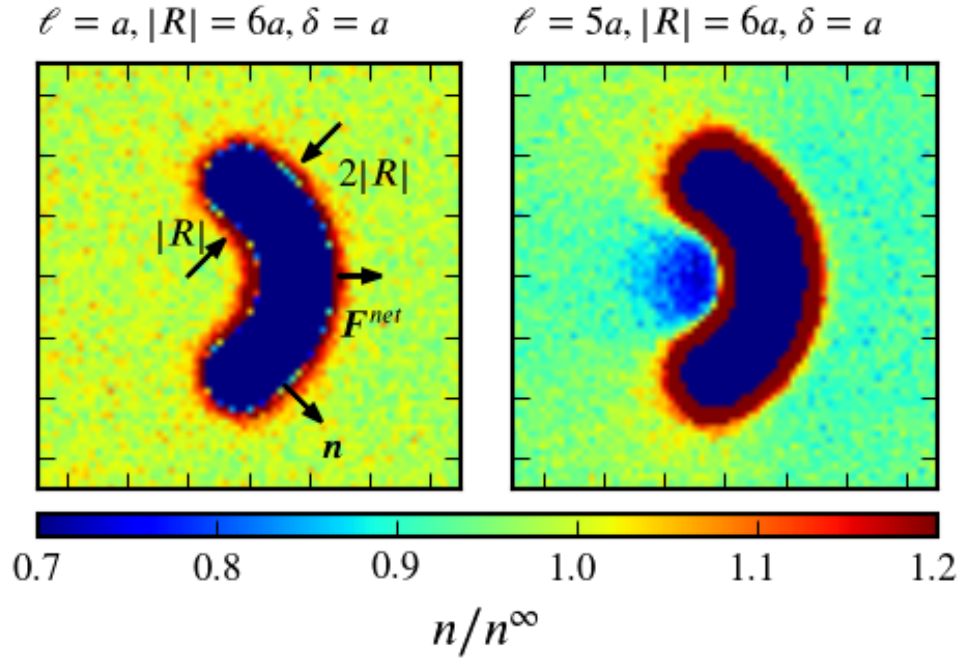


Figure 4.3: The number density n/n^∞ in two systems. In the left, $\lambda'\delta^2/|R| = \frac{1}{2\sqrt{6}} \approx 0.204$, and the outer solution $n_{out} = const = n^\infty$ still holds. In the right, $\lambda'\delta^2/|R| = \frac{1}{2}\sqrt{\frac{3}{2}} \approx 0.612$, and the outer solution $n_{out} = const = n^\infty$ is invalid. The left case is located at the $O(\delta/|R|)^2$ regime in Fig. 4.5, while the right case is located at the linear regime.

So to the first order of curvature J_S :

$$\begin{aligned}\Pi_{wall} &= n^\infty \zeta D_T + n^\infty \zeta D^{swim} \left(1 + \frac{\lambda\delta^2}{2L} J_S \right), \\ &= n^\infty k_B T + n^\infty k_s T_s \left(1 + \frac{\lambda\delta^2}{2L} J_S \right).\end{aligned}\quad (4.50)$$

Obviously, for passive Brownian particles $D^{swim} = 0$ and Π^{wall} is not impacted by the curvature J_S . For swimmers, the swim pressure is impacted by the curvature scaled as $J_S \lambda \delta^2 / (2L)$.

In the limit of very fast swimmers $\ell \gg \delta$, $\lambda \rightarrow \frac{\ell}{\sqrt{3}\delta^2}$:

$$n_{wall} \rightarrow 1 + \frac{\ell^2}{6\delta^2} \left(1 + \frac{1}{2\sqrt{3}} \left[\frac{\ell}{R_1} + \frac{\ell}{\hat{R}_2} \right] \right), \quad (4.51)$$

and the pressure:

$$\Pi_{wall} \rightarrow n^\infty k_B T + n^\infty k_s T_s \left(1 + \frac{1}{2\sqrt{3}} \left[\frac{\ell}{R_1} + \frac{\ell}{R_2} \right] \right). \quad (4.52)$$

For swimmers outside a sphere with radius $|R|$, the signed curvature radii $R_1 = R_2 = -|R|$ following the sign convention in Fig. 4.2, therefore the pressure on the wall *decreases* as the sphere decreases in size. This is consistent with the exact solution for the swim pressure inside and outside a spherical & cylindrical container, presented in a Padé form (Yan & Brady, 2015b): $1 / \left[1 + (\ell/|R|)/\sqrt{3} \right]$. It is also consistent with the results for the singular limit of no translational Brownian motion $D_T \rightarrow 0$ (Fily *et al.*, 2014a; Smallenburg & Löwen, 2015), where the result depends only on the ratio of run length to curvature radii $\ell/|R|$. The above analytical solutions are for the first order where the microscopic length δ and the run length ℓ are both much smaller than the macroscopic body length L , and therefore they are accurate only to the $O(\ell/L)$ and $O(\delta/L)$. The derivation gave us a universal scaling $\lambda\delta^2/L$:

$$\ell \sim \delta : \lambda\delta^2/|R| \sim \delta/L, \quad (4.53a)$$

$$\ell \gg \delta : \lambda\delta^2/|R| \sim \ell/L, \quad (4.53b)$$

therefore our theory works in the limit where $\lambda\delta^2/|R| \rightarrow 0$. In the following, we shall use this universal scaling.

Equation (4.50) gives the pressure distribution everywhere on an arbitrary shaped body. With surface integration, we can get the net force and torque applied on a body. Trivially, the integration of the constant part of pressure $n^\infty k_B T + n^\infty k_s T_s$ does not give a net force. To leading order:

$$\oint \Pi^{swim} dS = n^\infty k_s T_s L^2 \oint \left(1 + \frac{\lambda\delta^2}{2L} J_S \right) d\hat{S}, \quad (4.54a)$$

$$\mathbf{F}^{net} = n^\infty k_s T_s L^2 \oint -\frac{\lambda\delta^2}{2L} J_S \mathbf{n} d\hat{S}, \quad (4.54b)$$

$$\mathbf{L}^{net} = n^\infty k_s T_s L^2 \oint -\frac{\lambda\delta^2}{2L} J_S \mathbf{r} \times \mathbf{n} d\hat{S}. \quad (4.54c)$$

Here, $\oint \Pi^{swim} dS$ is a scalar ‘total’ integration of the swim pressure on the body. It is of no dynamic importance, but can be easily measured from a particle-tracking Brownian dynamics simulation to verify the boundary-layer solution. \mathbf{F}^{net} and \mathbf{L}^{net} are the first order net force and torque applied on a macroscopic body solely due to its asymmetric shape.

Equation (4.54) involves the pure geometric integral of $J_S \mathbf{n}$ on the surface. By definition:

$$J_S = 2H = (\hat{\kappa}_1 + \hat{\kappa}_2) = \hat{\nabla} \cdot \mathbf{n}. \quad (4.55)$$

It is well-known that for a smooth closed simply-connected surface:

$$\oint (\nabla \cdot \mathbf{n}) \mathbf{n} dS = 0. \quad (4.56)$$

Therefore, we conclude that to first order $O(\lambda\delta^2/L)$:

$$\mathbf{F}^{net} = 0, \quad (4.57)$$

for a smoothed body of arbitrary shape. A net force would appear to the second order $O(\lambda\delta^2/L)^2$.

Physically, to first order, $\mathbf{F}^{net} = 0$ also means that the \mathbf{L}^{net} is actually a force couple, which does not depend on the choice of the center of the torque. In fact, if we shift the torque moment center by \mathbf{r}_0 in (4.54c):

$$\begin{aligned} \mathbf{L}_0^{net} &= n^\infty k_s T_s L^2 \oint -\frac{\lambda\delta^2}{2L} J_S (\mathbf{r} + \mathbf{r}_0) \times \mathbf{n} d\hat{S}, \\ &= \mathbf{r}_0 \times \mathbf{F}^{net} + \mathbf{L}^{net} = \mathbf{L}^{net}. \end{aligned} \quad (4.58)$$

The equality holds at leading order $O(\lambda\delta^2/L)$. In fact due to the special form of the geometric integral $\oint J_S \mathbf{r} \times \mathbf{n} d\hat{S}$, there is some mathematical evidence (Sullivan, 2007) that $\mathbf{L}^{net} = 0$ to leading order, too.

Verification

To verify our analytical solution, especially the surprising result that to leading order the net force is zero, we perform Brownian dynamics simulations with ABPs and numerically solve the equations (4.7) and (4.8) with a Finite Element solver. The simulations require as many as 40,000 particles and as long as $3000\tau_R$ to capture the very weak signal of \mathbf{F}^{net} in the tremendous amount of Brownian noise. Also the Finite Element solver is expensive to solve due to the very thin boundary layer on the small scale δ . Limited by computing resources, we perform simulations and numerical solutions on a 2D geometry, for ABPs with 2D in-plane rotations.

In this case, we can repeat the solution and find the same result:

$$\frac{n_{wall}^{2D}}{n^\infty} = 1 + \frac{\ell^2}{2\delta^2} + \frac{\ell^2 \lambda'}{L} J'_S, \quad (4.59)$$

where $J'_S = \hat{\kappa}$ is simply the (non-dimensionalized) curvature of the 2D curved boundary. For a curved boundary in 2D, there is only one curvature and there is no need to define a ‘mean curvature’ H . The inverse screening length in 2D (Yan & Brady, 2015b): $\lambda' = \sqrt{(1 + \frac{1}{2}(\ell/\delta)^2)}/\delta$. So to leading order $O(\lambda\delta^2/L)$:

$$\begin{aligned} \Pi_{wall}^{2D} &= n^\infty \zeta D_T + n^\infty \zeta D^{swim} \left(1 + \frac{\lambda' \delta^2}{L} J'_S \right), \\ &= n^\infty k_B T + n^\infty k_s T'_s \left(1 + \frac{\lambda' \delta^2}{L} J'_S \right), \end{aligned} \quad (4.60)$$

where $k_s T'_s = \zeta U_0^2 / (2D_R)$. Also in the limit of $\ell \gg \delta$, similar to (4.52) the perturbation on swim pressure scales as ℓ/L :

$$\Pi_{wall}^{2D} \rightarrow n^\infty k_B T + n^\infty k_s T'_s \left(1 + \frac{\ell}{\sqrt{2}L} J'_S \right). \quad (4.61)$$

Again we take the surface integrals to get the net force:

$$\oint \Pi^{swim} dL = n^\infty k_s T'_s L \oint \left(1 + \frac{\lambda' \delta^2}{L} J'_S \right) d\hat{L}, \quad (4.62a)$$

$$\mathbf{F}^{net} = n^\infty k_s T'_s L \oint -\frac{\lambda' \delta^2}{2L} J'_S n d\hat{L}, \quad (4.62b)$$

$$\mathbf{L}^{net} = n^\infty k_s T'_s L \oint -\frac{\lambda' \delta^2}{2L} J'_S \mathbf{r} \times n d\hat{L}. \quad (4.62c)$$

Similarly, we get $\mathbf{F}^{net} = 0$ and \mathbf{L}^{net} is a force couple in the first order.

In this case, we can further simplify (4.62a), with a special case of Gauss-Bonnet theorem for a smooth 2D simple curve:

$$\oint \kappa d\hat{L} = -2\pi. \quad (4.63)$$

Here the negative sign appears due to our convention of sign as illustrated in Fig. 4.2. Mathematically speaking, the ‘total curvature’ is -2π for a closed immersed plane curve. As a result:

$$\oint \Pi^{swim} dL = n^\infty k_s T'_s C \left(1 - 2\pi \frac{\lambda' \delta^2}{C} \right), \quad (4.64)$$

where C is the circumference of that 2D shape, on the scale of the macroscopic length L . Remember that $\lambda' \delta$ has dimension 1, so the factor $\lambda' \delta^2 / L$ is on the order $O(\lambda' \delta^2 / L)$, not a second order correction.

The 2D Brownian dynamics simulation is done with the discretized Langevin equation of ABPs, with its orientation $\mathbf{q} = (\cos \theta, \sin \theta)$:

$$\Delta \mathbf{X} = U_0 \mathbf{q} \Delta t + \Delta X^B + \mathbf{F}^C / \zeta \Delta t, \quad (4.65)$$

$$\Delta \theta = \Delta \theta^B. \quad (4.66)$$

$\langle \Delta X^B \rangle = 0$, $\langle \Delta X^B \Delta X^B \rangle = 2D_T \Delta t$, and $\langle \Delta \theta^B \rangle = 0$, $\langle \Delta \theta^B \Delta \theta^B \rangle = 2D_R \Delta t$. Particle-particle collision is ignored as that effect is not included in the kinetic boundary layer solution. The ABPs have radius a , and the swimmer-body collision force \mathbf{F}^C is applied through the excluded volume interaction which occurs at the contact line calculated with the potential-free algorithm (Foss & Brady, 2000; Yan & Brady, 2015b). Due to the finite ABP radius a , the effective body shape is the original body shape plus a excluded volume layer of distance a . We use the effective body shape in all data we present.

The body shape is shown in Fig. 4.3. We purposely constructed the body shape with four circular arcs, to simplify the algorithm and to minimize the numerical error in

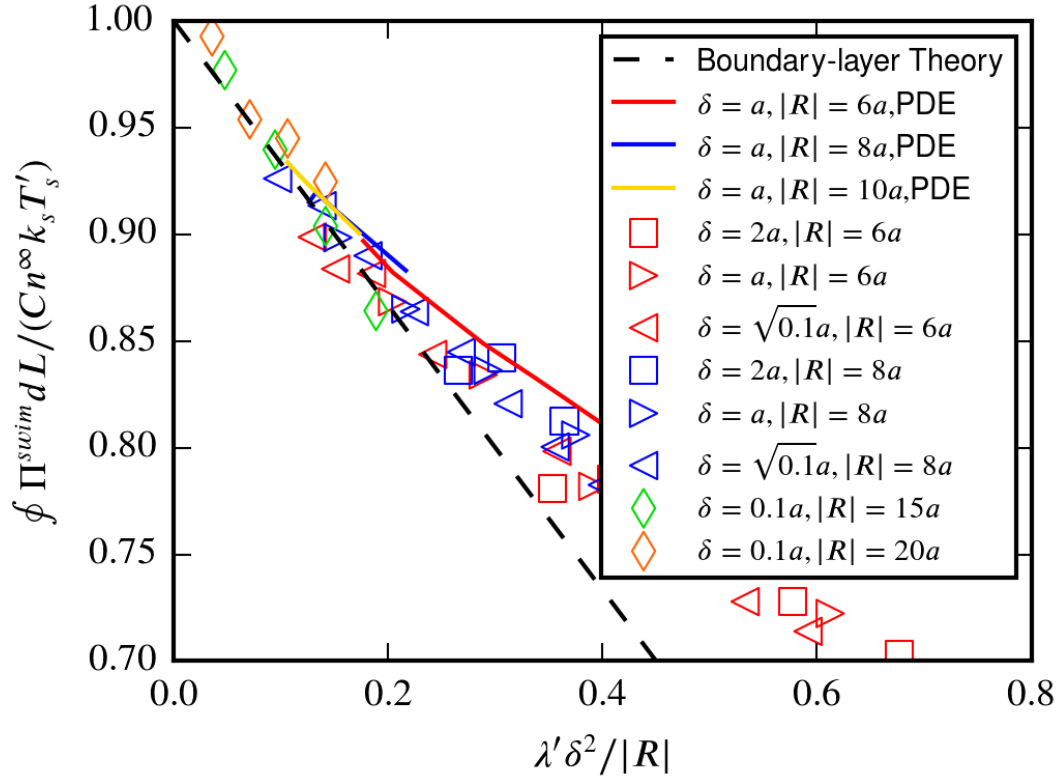


Figure 4.4: The scalar integration of pressure $\oint \Pi^{swim} dL$ on an asymmetric body immersed in ABPs. The dashed line is equation (4.67). The symbols are simulation results for $N = 40000$ particles equilibrated for $3000\tau_R$, and the solid lines are Finite Element solution for up to $10^4\tau_R$ to ensure a steady state is reached.

the contact detection process in simulations. For each combination of δ and $|R|$, we vary $\ell/\delta \in (1, 10)$ to cover both cases $\delta \approx \ell$ and $\delta \ll \ell$.

Here we choose the inner radius $|R|$ of the shape as the macroscopic length scale L , and for the shape we used the circumference $C = 3\pi|R|$. So (4.64) becomes a simple straight line for this particular shape:

$$\frac{\oint \Pi^{swim} dL}{n^\infty k_s T'_s C} = 1 - \frac{2}{3} \lambda' \delta^2 / |R|. \quad (4.67)$$

Fig. 4.4 compares (4.67) with simulation results and PDE solutions. The dashed line is calculated with (4.67). The theoretical solution applies for $\delta \ll |R|$ and $\ell \ll |R|$, and it works well in the limit $\lambda' \delta^2 / |R| \rightarrow 0$ as illustrated by Fig. 4.4.

Next, we compare the theoretical estimation of net force with the simulation results

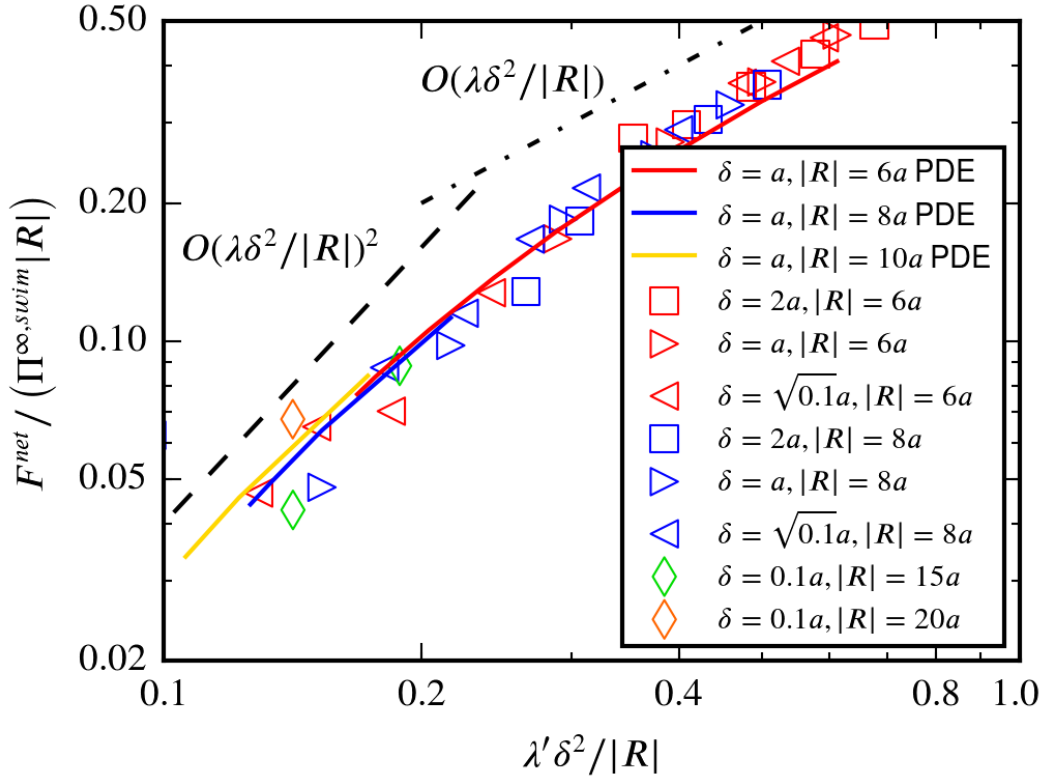


Figure 4.5: The net force \mathbf{F}^{net} on an asymmetric body immersed in ABPs. The body shape is shown in (4.3). The data is collected from the same simulations and PDE solutions in Fig. 4.4. The $O(\delta/|R|)^2$ and $O(\delta/|R|)$ asymptotic lines are for ease of view.

in Fig. 4.5. As shown in (4.60) and the definition of curvature sign in Fig. 4.2, a dent in the body means positive curvature $J'_s > 0$ and increases the swim pressure on the wall by $n^\infty k_s T'_s (\lambda' \delta^2 / L) J'_s$. Therefore the shape shown in Fig. 4.3 experience a net force towards the right. Also, because $\mathbf{F}^{net} = 0$ to the order $\lambda' \delta^2 / |R|$, asymptotically $\mathbf{F}^{net} \sim O(\lambda' \delta^2 / |R|)^2$, which is verified by the results shown in Fig. 4.5.

The simulations and numerical solutions in Fig. 4.5 show that all data and theoretic predictions of \mathbf{F}^{net} collapse on a single line, for a wide range of δ , $|R|$, and ℓ :

$$\frac{\mathbf{F}^{net}}{n^\infty k_s T'_s |R|} = f\left(\frac{\lambda \delta^2}{|R|}\right), \quad (4.68)$$

where $f(x)$ is a function determined by the shape, satisfying $f(x \rightarrow 0) \rightarrow x^2$, because we have shown with the analytic solution that for small $\lambda \delta^2 / |R|$, asymptotically $\mathbf{F}^{net} \sim O(\lambda' \delta^2 / |R|)^2$. Also, when $\lambda \delta^2 / |R|$ is large, $f(x)$ transits to a linear

function. We have shown in (4.53) that our boundary solution is no longer valid in the limit where $\lambda\delta^2/|R| \sim 1$, this may happen when $\ell \sim |R|$.

In Fig. 4.3, the different cases where $\lambda'\delta^2/|R| \rightarrow 0$ and $\lambda'\delta^2/|R| \rightarrow 1$ are compared. It is clear that in the limit of $\lambda'\delta^2/|R| \sim O(1)$, our boundary layer solution is valid. Meanwhile in the other limit, the number density n still shows a boundary layer at the microscopic length δ close to the boundary, but the outer solution $n_{out} = const$ is no longer valid. There is a clear wake (low density region) close to the concave portion of the body.

In the limit of $\lambda'\delta^2/|R| \rightarrow 1$, one can still take the surface integral of $\Pi_{wall} = n_{wall}\zeta D_T$ over the surface to get the net force, but it is no longer correct to use the constant outer solution $n_{out} = const = n^\infty$. In that case, the global transport equations (4.5) must be solved to get the correct number density field to calculate the net force, as we did in Fig. 4.4 and Fig. 4.5 with the PDE solver. Physically, when $\ell \sim |R|$, in a single run-length a swimmer does not only sample a local geometry, but actually experiences the global shape. Therefore, our solution of a completely localized boundary layer is invalid.

4.4 Discussion & Conclusions

In this chapter, we solved for the general case where δ/L and ℓ/L are both small, but the relation between δ and ℓ can be arbitrary. With the solution, we found a universal scaling emerges as $\lambda\delta^2/L$, and our analytical solution for the boundary layer is valid for $\lambda\delta^2/L \ll 1$. When $\lambda\delta^2/L$ is not small, we showed by simulations and PDE solutions that the scaling and the boundary layer structure still holds, but the outer solution n_{out} is no longer a constant n^∞ . Also, in analytical and PDE solutions the moment expansion is truncated at m level with an assumption of isotropic Q , and the solution matches the Brownian simulations well. It has been discussed and quantitatively compared by Yan & Brady, (2015b), and we shall not repeat the discussion here. The details can be found in Chapter 3.

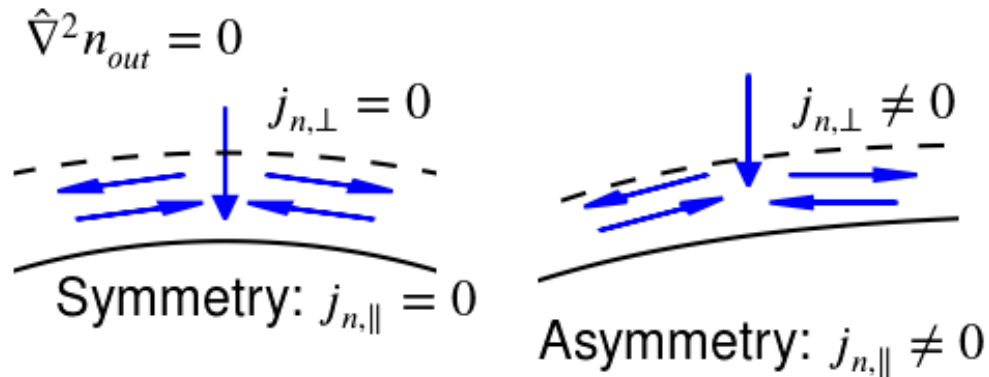


Figure 4.6: The origin of a non zero flux $j_{n,\perp}$. In the left, curvature is symmetric. On the right, the curvature is asymmetric.

Our solution is not limited to an exterior problem, it is also applicable to an interior problem where swimmers are confined in an arbitrarily shaped container and form a boundary layer on the walls.

Practically, $\delta \ll L$ is almost always satisfied in experiments, and most interest in swimmers concerns the fast swimming case where $\ell \gg \delta$. In the following, we shall discuss ℓ relative to the macroscopic length L .

Case 1, $\ell \ll L$: $F^{net} \sim O(\lambda\delta^2/L)^2$.

In this case, the disappearance of a net force at first order in $\lambda\delta^2/L$ is due to the fact that the outer solution is constant: $n = n^\infty = const$. Since the outer solution is governed by the Laplace equation, the constant solution is determined by the no flux boundary condition: $j_{n,\perp} = 0$. This is due to the continuity of the flux across the boundary layer.

The leading order expansion in the body shape is the curvature constant J_S . We expanded the boundary-layer solution on the surface with a geometric constant J_S , but J_S is only the mean curvature, and it does not take into consideration any variation of that curvature. That means, physically, in the leading order we approximated the surface with a curvature with *constant* curvature, which means the local solution

is the same at that point, and at its neighbor points. As a result, it includes no tangential flux of the swimmers. Then by the continuity of flux across the boundary layer, there is no flux coming or leaving this boundary-layer region, and $j_{\perp} = 0$.

When we allow the curvature to vary, a non-zero tangential flux is allowed. By continuity, a normal flux of outer solution can come into the boundary layer and flow tangentially somewhere. A non-zero normal flux $j_{n,\perp}$ therefore gives a non-constant outer solution n_{out} . However, when the boundary layer assumption holds, the variation of curvature appears at second order in the expansion of the curvilinear operator $\hat{\nabla}_*$, as discussed in Appendix D. That is, the deviation of n from a constant outer solution n^{∞} occurs at the second order $O(\lambda\delta^2/L)^2$. Therefore, we observe a second order net force as shown in (4.68) and Fig. (4.5). An analytical theory for the second order boundary condition would require all 21 geometric constants for curvature and curvature variations to be included, and is unnecessarily complicated (Panaras, 1987).

When $\delta \ll \ell$, we have $\lambda\delta^2/L \sim \ell/L$, as shown in (4.53), (4.52) and (4.61). This corresponds to the singular limit of no translational Brownian diffusion D_T , and it explains the appearance of the $\ell/|R|$ scaling in literature (Fily *et al.*, 2014a; Smallenburg & Löwen, 2015). However, it is important that in this case the boundary-layer thickness goes to zero, and one should not simply put the Smoluchowski equation into a PDE solver with a finite minimum mesh size l_m . In fact, in this case the number density n behaves as a δ_{dirac} function on the wall, and it cannot be appropriately captured by any finite mesh size. The proper solution for zero δ between a parallel wall configuration (Ezhilan *et al.*, 2015) must mathematically split the particles ‘on the wall’ from the bulk to appropriately capture the number density n solution. If one blindly chooses some l_m it is equivalent to specifying a finite microscopic length δ , and may lead to a mysterious constant in front of the scaling ℓ/L . Also, it is not legitimate to attach a numerically fitted high order inner solution with a leading order constant outer solution to calculate the net force. The inner and the outer

solutions must be resolved to the same order.

Case 2, $\ell \sim L$: $F^{net} \sim O(\lambda\delta^2/L) \sim O(\ell/L)$

In this case, since we assumed $\delta \ll L$, effectively we have $F^{net} \sim O(\ell/L)$. As shown in Fig. 4.3, there is also a boundary layer governed by the microscopic length δ , but on large scales the outer solution shows a clear convection-like wake structure. The physics is very similar to the $\ell \ll L$ limit. When $\ell \ll L$, swimmers explore the local curvature variations to induce a second order perturbation to n_{out} . However, when $\ell \sim L$, the swimmers experience the variation of curvature over the entire body within a single run-length and cause the deviation of n_{out} from a constant n^∞ . More specifically, in this case only a few swimmers with preferred orientation \mathbf{q} can enter the concave portion of the macroscopic body, and therefore a long range orientation field $\mathbf{m}_{out} = -\frac{\ell}{6L}\hat{\mathbf{V}}n_{out}$ appears together with a non constant n_{out} . In this case, the swimmers still show an accumulation boundary layer as shown in Fig. 4.3, and simulations with full PDE solutions all collapse on a universal scaling (4.68) $F^{net} / (n^\infty k_s T_s |R|) = f(\lambda\delta^2/|R|)$, and the function $f(x)$ is determined by the shape. Also in this limit, for a regular shaped circle or sphere the exact full solution (Yan & Brady, 2015b) shows that the Padé form:

$$\Pi_{wall} \rightarrow n^\infty k_B T + n^\infty k_s T_s \frac{1}{1 - \frac{1}{2\sqrt{3}} \left[\frac{\ell}{R_1} + \frac{\ell}{R_2} \right]}, \quad (4.69)$$

is the exact analytic solution and it works well even when $\ell/L \sim 5$. The linear expansion of this Padé form is the first order boundary layer solution (4.52). However, we cannot write (4.50) into this Padé form and attach it to the constant outer solution $n_{out} = n^\infty$ to calculate the force, because it inherently requires a second order outer solution.

The difference between the limits $\ell \ll L$ and $\ell \sim L$ can also be appreciated from a continuum mechanics point of view. We have shown that, for swimmers with no orientation bias or body force, on large scales where $L \gg \ell$ continuum mechanics

describes the number density flux very well (Yan & Brady, 2015a):

$$\mathbf{j}_n = -\frac{1}{\zeta} \nabla \cdot \boldsymbol{\sigma}^{tot}, \quad (4.70)$$

where if the swimmer-swimmer interaction is ignored (the dilute limit):

$$\boldsymbol{\sigma}^{tot} = n\zeta (D_T + D^{swim}) \mathbf{I}. \quad (4.71)$$

In this formulation, any non-continuum effects are only important on a very thin layer attached to the body surface. The thin layer is the boundary layer we analyzed in this chapter. The continuum mechanics flux (4.70) is exactly the outer flux (4.47). Also, the non-dimensionalized parameter $\lambda\delta^2/L$ is the counterpart to the Knudsen number mean free path to body size ratio $Kn = \lambda_{MFP}/L$ in rarefied gas dynamics. When $Kn \lesssim 0.1$ the Navier-Stokes equation is still applicable in the bulk, with its boundary condition modified by the Knudsen layer close to the wall. In our solution, Fig. 4.4 and Fig. 4.5, we also observed that the first order boundary layer solution is valid when $\lambda\delta^2/L \lesssim 0.2$.

However when $\ell \sim L$, the continuum mechanics transport equation can only be used in regions very far away from the body, and we need to solve for the detailed Smoluchowski equations in the vicinity. It is similar to the transition regime $Kn \approx 1$ in rarefied gas dynamics, where detailed dynamics must be solved.

General solution: spherical harmonics

The decoupled structure (4.11) allows us to construct the general solution for $f = \hat{\nabla} \cdot \mathbf{m}$, first by spherical harmonics (similar in 2D), and then by matching the boundary conditions to get the general solution without going to the details of the curvature expansion. However, in the case where $\lambda\delta^2/L \ll 1$, numerically the series constants are highly sensitive to numerical errors, and for a body of complex shape the general solution is effectively useless. Here we just present the general structure for an axisymmetric body to complete our mathematical discussion.

For a general body in 3D axisymmetric about the z -axis:

$$\hat{\mathbf{v}} \cdot \mathbf{m} = \sum_{l=0}^{\infty} B_l \sqrt{\frac{2}{\pi \lambda L r}} K_{l+\frac{1}{2}}(\lambda L r) P_l(\cos \theta), \quad (4.72)$$

$$\begin{aligned} n &= n_H + n_P \\ &= n^\infty + \sum_{l=0}^{\infty} g_l r^{-(l+1)} P_l(\cos \theta) + \frac{\ell}{\delta^2 \lambda^2 L} \hat{\mathbf{v}} \cdot \mathbf{m}, \end{aligned} \quad (4.73)$$

$$\begin{aligned} \mathbf{m} &= \mathbf{m}_H + \mathbf{m}_P \\ &= \sum_{l=0}^{\infty} C_l(\theta) \sqrt{\frac{2}{\pi \alpha r}} K_{l+\frac{1}{2}}(\alpha r) \\ &\quad + \frac{1}{\lambda^2 L^2} \hat{\mathbf{v}} (\hat{\mathbf{v}} \cdot \mathbf{m}) - \frac{l}{6L} \hat{\mathbf{v}} n_H, \end{aligned} \quad (4.74)$$

where $K_{l+\frac{1}{2}}(z)$ are the *cylindrical* modified Bessel functions. For interior problems, $K_{l+\frac{1}{2}}(z)$ should be replaced by $I_l(z)$. $P_l(x)$ is the Legendre polynomial. B_l, g_l, C_l should be matched by the no-flux boundary condition.

For a general shape in 2D, similarly we can just replace the Legendre polynomials by a Fourier mode $\cos n\theta + \sin n\theta$, and replace the $K_{l+\frac{1}{2}}(z)$ with its integer order version $K_l(z)$, to construct the general solution. The constants should also be adjusted accordingly.

Formula for hydrodynamics

In this chapter we discussed the kinetic limit, where the boundary layer emerges solely due to the run length $\ell = U_0 \tau_R$ and the microscopic length $\delta = \sqrt{D_T \tau_R}$. In this case, we showed that the interaction is completely determined by the distribution of swimmers around the body: the distribution function $P(\mathbf{x}, \mathbf{q}, t)$.

It is also true for swimmers with full hydrodynamics in Stokes flow. As shown by the equation (4.19) in Brady, (2011), the hydrodynamic force applied on the body is completely determined by the distribution function $p_{ij}(\mathbf{r})$ of a swimmer j relative to a macroscopic body i , and the full mobility matrix $\mathbf{M}_{ij}(\mathbf{r})$. In Brady, (2011), i is termed as the ‘particle’ and j is termed as the ‘solute’.

In the limit where the excluded volume interaction is effective on a range much longer than hydrodynamic interactions, the hydrodynamic mobility is simplified to the isotropic Stokes drag, and the interaction is simplified to the sum of individual Brownian collisions discussed in this chapter.

When hydrodynamic interaction is effective, the distribution function $p_{ij}(\mathbf{r})$ must be solved case by case to find the correct interaction and boundary layer form. Due to the complicated general form of $M_{ij}(\mathbf{r})$, we do not know whether a simple general solution for the boundary layer structure exists. We shall leave it for future studies.

Wen Yan thanks Eric W. Burkholder for the mathematical construction (4.11). This work is supported by NSF-CBET 1437570.

*Chapter 5***ACTIVE MATTER WITH NEMATIC ORIENTATION:
ENHANCED ANISOTROPY AND TENSORIAL SWIM STRESS**

5.1 Introduction

Each individual particle in active matter propels itself with some orientation \mathbf{q} , and therefore by manipulating \mathbf{q} interesting phenomena happen, such as shear trapping (Rusconi *et al.*, 2014), rheotaxis (Kaya & Koser, 2012), action-at-distance (Yan & Brady, 2015a), and so on. Those phenomena can mostly be explained by solving the Smoluchowski equations for the Active Brownian Particles (ABPs) model, and continuum mechanics naturally arises as a large-scale limit of the detailed Smoluchowski mechanics.

From a continuum perspective, the continuum mechanics relies on the balance of surface and body forces. The surface force of active matter has been defined as the swim pressure (Takatori *et al.*, 2014), which is the pressure required to confine the swimmers within some fixed volume, and is therefore dependent on the swim diffusivity $\sigma^{swim} = -n\zeta \mathbf{D}^{swim}$, where n is the number density and ζ is the drag. If the orientation \mathbf{q} is governed by unbiased rotational Brownian diffusivity $D_R = 1/\tau_R$, $\mathbf{D}^{swim} = U_0^2 \tau_R / 6 \mathbf{I}$ and remains isotropic. With polarization in some particular direction $\hat{\mathbf{H}}$, the stress is in general anisotropic as $\sigma^{swim} = -n\zeta U_0^2 \tau_R / 6 (\hat{\sigma}_{\parallel}^{swim} \hat{\mathbf{H}} \hat{\mathbf{H}} + \hat{\sigma}_{\perp}^{swim} \hat{\mathbf{H}}_{\perp} \hat{\mathbf{H}}_{\perp})$, where $\hat{\sigma}_{\parallel}^{swim}$ and $\hat{\sigma}_{\perp}^{swim}$ are both functions of the field strength, and are equal to 1 without the field (Takatori & Brady, 2014).

An anisotropic swim stress is unusual, but one must think of active matter in an external field. With polarization, it is clear that the ‘equilibrium’ stress is anisotropic. In this work, we consider a fundamental problem, that is, the force on a flat wall applied by anisotropic swimmers. We show that the anisotropic swim stress on a wall may actually be a real tensorial stress, based on a microscopic understanding of how the swim pressure in the bulk is transmitted to the wall (Yan & Brady, 2015b).

We would first discuss the anisotropic swim stress σ^{swim} for ABPs with a nematic order, showing that the anisotropy $\hat{\sigma}_{\parallel}^{swim} / \hat{\sigma}_{\perp}^{swim}$ can be greatly enhanced by the

orientation field. Then, we examine the force on a wall, with its normal vector \mathbf{n} in an arbitrary angle to the field direction $\hat{\mathbf{H}}$. With that model, we show that the (normal) pressure on the wall can be calculated simply as $(\boldsymbol{\sigma}^{swim} \cdot \mathbf{n}) \cdot \mathbf{n}$, in agreement with classical continuum mechanics. That is, the swim stress is *tensorial*.

5.2 Nematic orientation order: anisotropic swim diffusivity

We consider ABPs with a bi-stable orientational potential energy:

$$V(\mathbf{q}) = -\epsilon (\mathbf{q} \cdot \hat{\mathbf{H}})^2, \quad (5.1)$$

where ϵ is an energy scale, \mathbf{q} is the orientation vector and $\hat{\mathbf{H}}$ is the direction of the field. Energy is minimized for both $\mathbf{q} = \pm \hat{\mathbf{H}}$. Such a potential is often seen in magnetic nanoparticles (Coffey & Kalmykov, 2012). With $V(\mathbf{q})$, the swimmers tend to swim in the directions of $\pm \hat{\mathbf{H}}$ and show different swim diffusivity in $\hat{\mathbf{H}}$ and $\hat{\mathbf{H}}_{\perp}$ directions. The swim diffusivity comes from the fluctuations in orientation \mathbf{q} , propagated to the translational space \mathbf{x} through the self-propulsion $U_0 \mathbf{q}$ on a time scale longer than the reorientation time $\tau_R = 1/D_R$.

ϵ in (5.1) controls the strength of the field. When $\epsilon \ll k_B T$, the orientation field is weak in comparison to the Brownian reorient, and the equilibrium distribution of \mathbf{q} just slightly deviates from the isotropic distribution. When $\epsilon \gg k_B T$, the orientation field significantly deviates the equilibrium distribution of \mathbf{q} . However, the potential (5.1) is a bi-stable potential, and during the Brownian reorient events the particles occasionally get enough energy to climb over the energy barrier between the two directions with lowest energy. This behavior will later be analyzed by Kramers' hopping theory, and we shall see that it is the hopping that induces the greatly enhanced diffusivity in the direction of $\hat{\mathbf{H}}$.

This enhancement of diffusivity is different from the polarization discussed by Takatori & Brady, (2014), where the orientation potential energy shows a single minimum. In that case, under a strong polarization field all particles align with the

field, and net motion of particles at the velocity of $\langle \mathbf{q} \rangle U_0$ is induced, and $\langle \mathbf{q} \rangle$ is in the same direction of the field. The particles still show some diffusivity superposed to the average directed motion, but the diffusivity is greatly decreased because the fluctuation in \mathbf{q} is limited to only the vicinity of $\hat{\mathbf{H}}$.

Case 1. Swimmers in 3D space

The orientation is analyzed in the spherical coordinate system (r, θ, ϕ) , assuming the $\theta = 0$ axis is aligned with $\hat{\mathbf{H}}$. \mathbf{q} is confined in the angles $(0 < \theta < \pi, 0 < \phi < 2\pi)$. The orientational distribution of \mathbf{q} obeys the Boltzmann distribution, no matter the location \mathbf{x} of the swimmer:

$$P_0^\infty(d\Omega(\theta, \phi)) \propto \exp(-V(\mathbf{q})/k_B T) d\Omega, \quad (5.2)$$

where $d\Omega$ is the solid angle. Therefore the equilibrium distribution is:

$$P_0^\infty = \frac{\sqrt{\chi_R} e^{\chi_R}}{2\pi^{3/2} \operatorname{Erfi}(\sqrt{\chi_R})} \exp(-\chi_R \sin^2 \theta). \quad (5.3)$$

Here Erfi is the ‘imaginary error function’, and $\chi_R = \frac{\epsilon}{k_B T}$ is the dimensionless field strength. When $\chi_R = 0$, the orientational potential V disappears and $P_0^\infty = \frac{1}{4\pi}$.

The effect of the polarization can be quantified by the nematic order parameter $\tilde{\mathbf{Q}} = \langle \mathbf{q}\mathbf{q} \rangle$, as shown in Fig. 5.1. When $\chi_R = 0$, $\tilde{Q}_\perp = \tilde{Q}_\parallel = 1/3$. When $\chi_R \rightarrow \infty$, all particles with $\mathbf{q} = \pm \hat{\mathbf{H}}$, and therefore $\tilde{Q}_\parallel = 1$ and $\tilde{Q}_\perp = 0$:

$$\langle \mathbf{q}_\parallel \mathbf{q}_\parallel \rangle = \frac{\exp(\chi_R)}{\sqrt{\pi} \sqrt{\chi_R} \operatorname{Erfi}(\sqrt{\chi_R})} - \frac{1}{2\chi_R}, \quad (5.4a)$$

$$\langle \mathbf{q}_\perp \mathbf{q}_\perp \rangle = \frac{1}{2} (1 - \langle \mathbf{q}_\parallel \mathbf{q}_\parallel \rangle). \quad (5.4b)$$

Here by definition $\operatorname{Tr} \tilde{\mathbf{Q}} = 1$. By definition, the zero-traced nematic order parameter $\mathbf{Q} = \tilde{\mathbf{Q}} - \frac{1}{3} \mathbf{I}$, and $\tilde{Q}_\parallel = \langle \mathbf{q}_\parallel \mathbf{q}_\parallel \rangle - 1/3$, $\tilde{Q}_\perp = \langle \mathbf{q}_\perp \mathbf{q}_\perp \rangle - 1/3$.

For ABPs with nematic order, their motion is governed by the translational velocity $U_0 \mathbf{q}$, related by the orientational order of \mathbf{q} . The orientational fluctuation around the

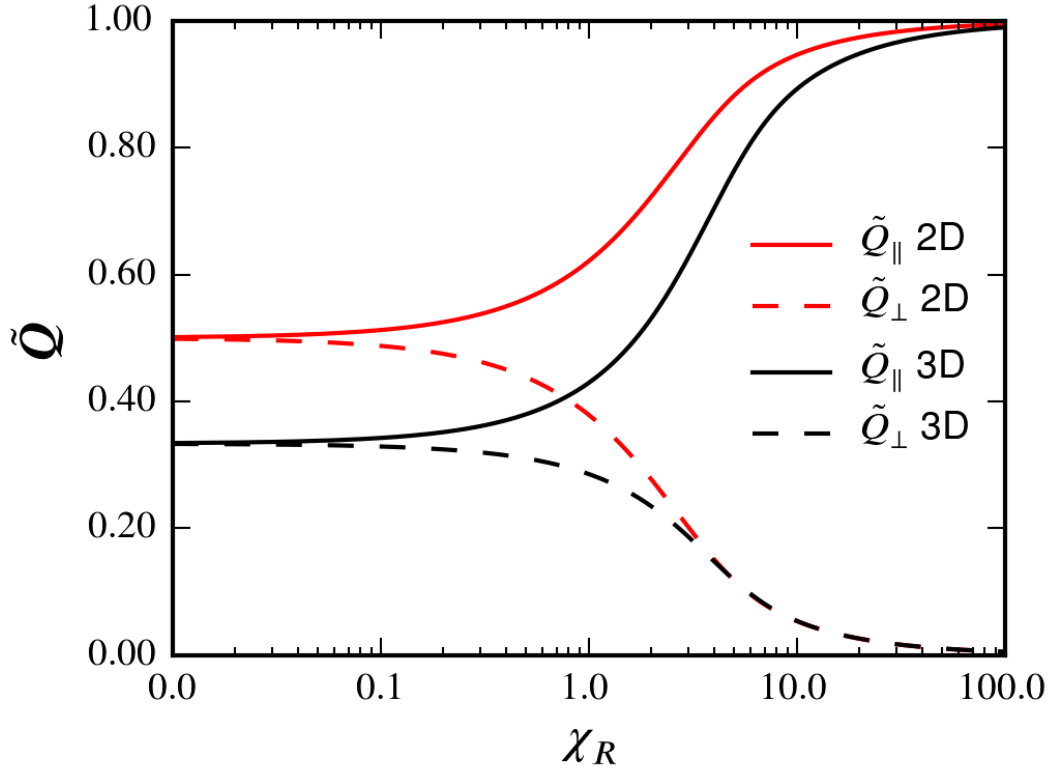


Figure 5.1: The nematic order parameter $\tilde{Q} = \langle \mathbf{q}\mathbf{q} \rangle$ as a function of field strength $\chi_R = \epsilon/k_B T$.

equilibrium P_0^∞ leads to the diffusivity D^{swim} in translational space. To calculate this, we can either use Brenner's B -field theory (Frankel & Brenner, 1989) or Brady's k -field theory (Takatori & Brady, 2014). The detailed calculation procedure has been reported before (Yan & Brady, 2015a) and the process is briefly derived here.

With the notation introduced in the Appendix B, the steady state Smoluchowski equation can be written as

$$\nabla \cdot \mathbf{j} + \nabla_R \cdot \mathbf{j}_R = 0, \quad (5.5)$$

$$\mathbf{j} = U_0 \mathbf{q} P - D_T \nabla P, \quad \mathbf{j}_R = \boldsymbol{\omega}(\mathbf{q}) P - D_R \nabla_R P. \quad (5.6)$$

$$\boldsymbol{\omega} = \frac{1}{\zeta_R} (-\nabla_R V) = -\frac{\epsilon}{\zeta_R} \mathbf{e}_\phi \sin 2\theta. \quad (5.7)$$

Here $D_R = 1/\tau_R = k_B T/\zeta_R$.

Following the \mathbf{B} -field route, we have:

$$B_{\parallel}(\theta) = \int_0^{\cos\theta} \frac{1 - e^{\chi_R - \chi_R k^2}}{2\chi_R (k^2 - 1)} dk, \quad (5.8a)$$

$$B_{\perp}(\theta) = \cos\phi \sin\theta g(\cos\theta), \quad (5.8b)$$

where the function $g(x)$ is the solution of the ODE:

$$\begin{aligned} (x^2 - 1) g''(x) + 2x (\chi_R (x^2 - 1) + 2) g'(x) \\ + 2 (\chi_R x^2 + 1) g(x) - 1 = 0, \end{aligned} \quad (5.9)$$

$g(x) = g(\cos\theta)$ satisfies (i) no singularities at $x = \cos\theta \rightarrow \pm 1$, and (ii) well-defined as $\chi_R \rightarrow 0$. Here the \mathbf{B} -field is quantitatively the orientational fluctuation of \mathbf{q} around the equilibrium P_0^{∞} . The fluctuation in \mathbf{q} induces the diffusivity in translational space. The velocity of net motion is defined as:

$$\langle \mathbf{U} \rangle = \int_{\mathbf{q}} P_0^{\infty}(\mathbf{q}) \mathbf{U}(\mathbf{q}) d\mathbf{q}. \quad (5.10)$$

For the bistable potential (5.1) discussed here, the distribution $P_0^{\infty}(\mathbf{q})$ is symmetric. As a result, $\langle \mathbf{U} \rangle = 0$, and there is no net motion.

By decomposing $\Delta \mathbf{U}(\mathbf{q}) = \mathbf{U}(\mathbf{q}) - \langle \mathbf{U} \rangle$, the effective diffusivity on top of the averaged directed motion $\langle \mathbf{U} \rangle$ is given by

$$\mathbf{D}^{swim} = \int_{\mathbf{q}} P_0^{\infty}(\mathbf{q}) \mathbf{B}(\mathbf{q}) \Delta \mathbf{U}(\mathbf{q}) d\mathbf{q}. \quad (5.11)$$

More details about the \mathbf{B} -field route can be found in Appendix B. The results for \mathbf{D}^{swim} :

$$\hat{D}_{\parallel}^{swim} = \frac{D_{\parallel}^{swim}}{U_0^2 \tau_R / 6} = 12\pi \int_0^{\pi} P_0^{\infty} \cos\theta \sin\theta \int_0^{\cos\theta} \frac{1 - e^{\chi_R - \chi_R k^2}}{2\chi_R (k^2 - 1)} dk d\theta, \quad (5.12a)$$

$$\hat{D}_{\perp}^{swim} = \frac{D_{\perp}^{swim}}{U_0^2 \tau_R / 6} = 6 \int_0^{2\pi} \int_0^{\pi} P_0^{\infty} \sin^3\theta g(\cos\theta) \cos^2\phi d\theta d\phi. \quad (5.12b)$$

The results for \hat{D}_{\parallel} and \hat{D}_{\perp} are shown in Fig. 5.2.

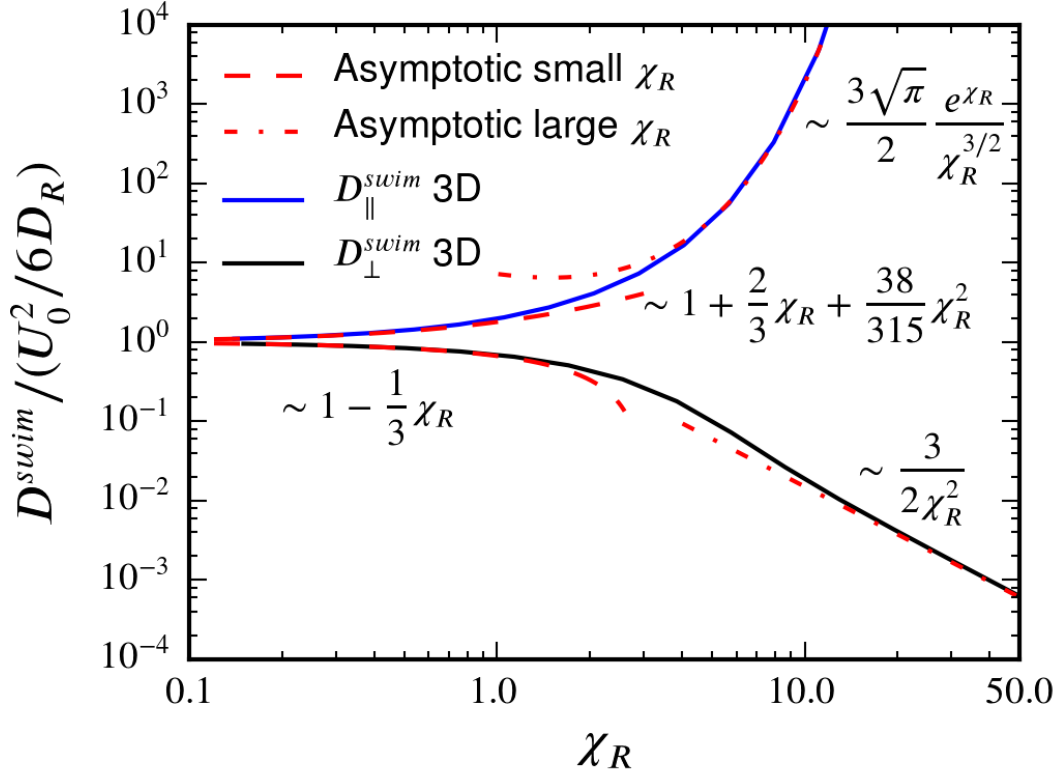


Figure 5.2: D^{swim} in the directions parallel and perpendicular to the field \hat{H} in 3D space. The solid lines are analytic solutions (5.12).

Then, $\hat{\sigma}_{||}^{swim}$ and $\hat{\sigma}_{\perp}^{swim}$ can be calculated from $\sigma^{swim} = -n\zeta D^{swim}$:

$$\hat{\sigma}_{||}^{swim} = \frac{\sigma_{||}}{-n\zeta U_0^2/6} = \hat{D}_{||}^{swim}, \quad (5.13)$$

$$\hat{\sigma}_{\perp}^{swim} = \frac{\sigma_{\perp}}{-n\zeta U_0^2/6} = \hat{D}_{\perp}^{swim}. \quad (5.14)$$

The weak-field limit

When the field is weak, the system just shows a small polarization, and by a simple series expansion of (5.12), we find easily:

$$\hat{\sigma}_{||}^{swim} \approx 1 + \frac{2\chi_R}{3} + O(\chi_R^2), \quad (5.15a)$$

$$\hat{\sigma}_{\perp}^{swim} \approx 1 - \frac{\chi_R}{3} + O(\chi_R^2). \quad (5.15b)$$

As was the case for polar order aligned with \hat{H} induced by a potential with a single position of minimum energy (Takatori & Brady, 2014), the swim pressure is

decreased in the \hat{H}_\perp direction, because the energy barrier decreases the fluctuation of \mathbf{q} in that direction. The difference is, here the stress in the \hat{H} direction is enhanced by the field. This is due to the bistable structure of the orient potential (5.1), and we shall see a more significant effect in the strong-field limit.

The strong-field limit

The strong-field limit is very interesting. In this case, the swimmers may all align with either \hat{H} or $-\hat{H}$, and only occasionally ‘jump’ between these two states. It is physically the same as the famous Kramers’ escaping rate process (Kramers, 1940), where a Brownian particle may jump out of a potential well slowly due to diffusion. As \mathbf{q} is diffusive in the rotation space, the jumping probability is modified from Kramers’ original 1D estimation. The average jumping time between the two directions are estimated to be (Coffey *et al.*, 2001):

$$\tau_j = \frac{\sqrt{\pi} \exp(\chi_R)}{2\chi_R^{3/2}} \tau_R. \quad (5.16)$$

Physically, the swimmer may move in a direction with U_0 for τ_j and then jump to the other direction and move again with U_0 for τ_j on average. Therefore on the long diffusion timescale, the diffusivity is simple a 1D random-walk:

$$\hat{\sigma}_\parallel^{swim} = \frac{D_\parallel^{swim}}{U_0^2 \tau_R / 6} \rightarrow \frac{3\sqrt{\pi} \exp(\chi_R)}{2\chi_R^{3/2}}. \quad (5.17)$$

Besides moving in $\pm\hat{H}$ directions, the swimmers also move in the perpendicular to the \hat{H} direction, due to small fluctuations around $\pm\hat{H}$ driven by D_R . Following this route, the distribution of the fluctuation field B_\perp can be approximated with a singular ‘boundary layer’ around the parallel direction. After the tedious mathematics is properly handled, the result is very simple:

$$\hat{\sigma}_\perp^{swim} = \frac{D_\perp^{swim}}{U_0^2 \tau_R / 6} \rightarrow \frac{3}{2\chi_R^2}, \quad (5.18)$$

as $\chi_R \rightarrow \infty$. The asymptotic predictions are shown in Fig. 5.2.

Case 2. Swimmers in a 2D layer: in-plane rotation

For 2D in-plane rotation, the rotational space is greatly simplified to a single angle θ . We define $\cos \theta = \mathbf{q} \cdot \hat{\mathbf{H}}$, as in the 3D case. At steady state, the equilibrium orientation distribution is:

$$P_0^\infty(\theta) = \frac{1}{2\pi I_0\left(\frac{\chi_R}{2}\right)} e^{\frac{1}{2}\chi_R \cos(2\theta)}. \quad (5.19)$$

Here, I_0 is the Bessel function, normalized so that $\int_{-\pi}^{\pi} P_0^\infty d\theta = 1$. Similar to the 3D case, the nematic order parameter $\tilde{\mathbf{Q}}$ is:

$$\langle \mathbf{q}_{\parallel} \mathbf{q}_{\parallel} \rangle = \frac{1}{2} \left(\frac{I_1\left(\frac{\chi_R}{2}\right)}{I_0\left(\frac{\chi_R}{2}\right)} + 1 \right), \quad (5.20a)$$

$$\langle \mathbf{q}_{\perp} \mathbf{q}_{\perp} \rangle = \frac{1}{2} \left(-\frac{I_1\left(\frac{\chi_R}{2}\right)}{I_0\left(\frac{\chi_R}{2}\right)} + 1 \right). \quad (5.20b)$$

Here we also have $\text{Tr } \tilde{\mathbf{Q}} = 1$, similar to the 3D case. The zero-traced nematic order parameter \mathbf{Q} is defined as $\mathbf{Q} = \tilde{\mathbf{Q}} - \frac{1}{2}\mathbf{I}$ for the 2D case. The order parameter $\tilde{\mathbf{Q}}$ is shown in Fig. 5.1.

The \mathbf{B} field route in the 2D case is:

$$B_{\parallel}(\theta) = C_1 - \int_0^\theta \frac{\sqrt{\pi} e^{\chi_R \sin^2 \kappa} \text{Erf}\left(\sqrt{\chi_R} \sin \kappa\right)}{2\sqrt{\chi_R}} d\kappa, \quad (5.21a)$$

$$B_{\perp}(\theta) = \int_0^\theta \frac{F_D\left(\sqrt{\chi_R} \cos \kappa\right)}{\sqrt{\chi_R}} d\kappa, \quad (5.21b)$$

where $F_D(z)$ is the Dawson- F integral function:

$$F_D(z) = e^{-z^2} \int_0^z e^{y^2} dy. \quad (5.22)$$

Similar to the 3D case, the swim diffusivity comes from the orientational fluctuation

\mathbf{B} :

$$\hat{D}_{\parallel}^{swim} = \frac{D_{\parallel}^{swim}}{U_0^2/2} = -2 \int_{-\pi}^{\pi} \int_0^\theta \frac{\sqrt{\pi} e^{\chi_R \sin^2 \kappa} \text{Erf}\left(\sqrt{\chi_R} \sin \kappa\right)}{2\sqrt{\chi_R}} d\kappa P_0^\infty(\theta) \cos \theta d\theta, \quad (5.23a)$$

$$\hat{D}_{\perp}^{swim} = \frac{D_{\perp}^{swim}}{U_0^2/2} = 2 \int_{-\pi}^{\pi} \int_0^\theta \frac{F\left(\sqrt{\chi_R} \cos \kappa\right)}{\sqrt{\chi_R}} d\kappa P_0^\infty(\theta) \sin \theta d\theta, \quad (5.23b)$$

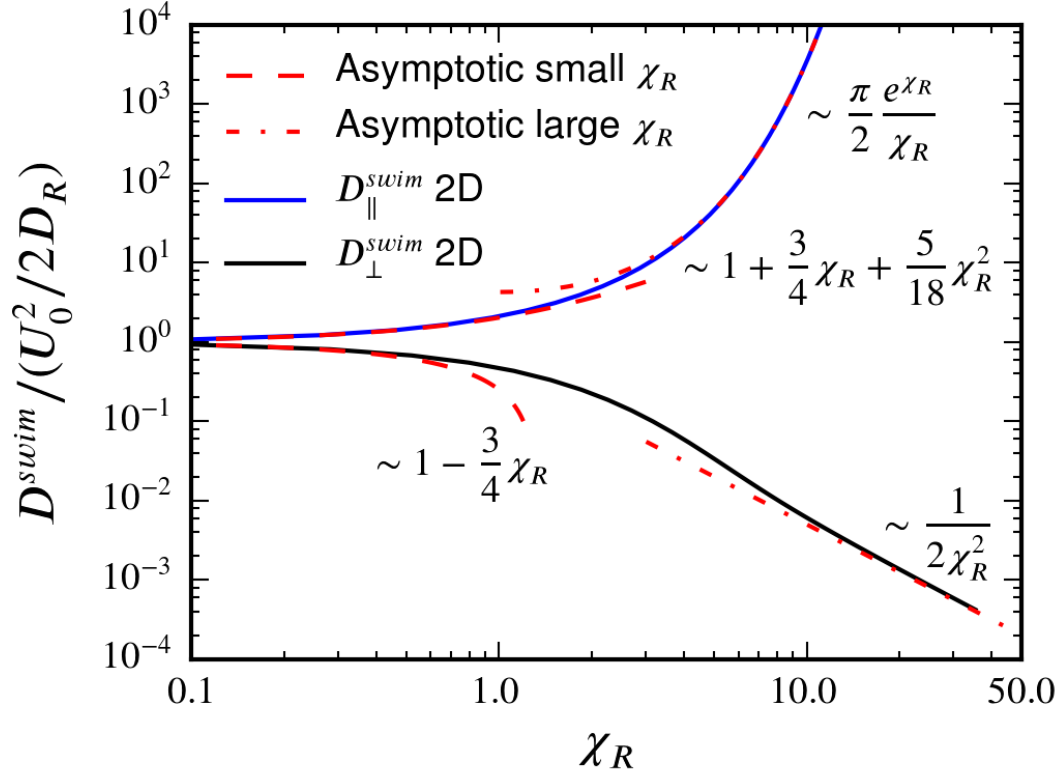


Figure 5.3: D^{swim} in the directions parallel and perpendicular to the field \hat{H} in a 2D layer. The solid lines are analytic solutions (5.26).

which are shown in Fig. 5.3.

Then, $\hat{\sigma}_{||}^{swim}$ and $\hat{\sigma}_{\perp}^{swim}$ can be calculated similar to the previous 3D case.

$$\hat{\sigma}_{||}^{swim} = \frac{\sigma_{||}}{-n\zeta U_0^2/2} = \hat{D}_{||}^{swim}, \quad (5.24)$$

$$\hat{\sigma}_{\perp}^{swim} = \frac{\sigma_{\perp}}{-n\zeta U_0^2/2} = \hat{D}_{\perp}^{swim}. \quad (5.25)$$

The difference is that, for 2D in plane rotations the isotropic swim pressure is $n\zeta U_0^2/2$, in stead of $n\zeta U_0^2/6$.

The weak field limit

In this limit, by direct expansion of (5.23):

$$\hat{\sigma}_{\parallel}^{swim} \approx 1 + \frac{3\chi_R}{4} + O(\chi_R^2), \quad (5.26a)$$

$$\hat{\sigma}_{\perp}^{swim} \approx 1 - \frac{3\chi_R}{4} + O(\chi_R^2). \quad (5.26b)$$

The strong field limit

In this case, Kramers' escaping rate theory can be directly used since the orientation space involving θ is a 1D space,

For a potential $V(\theta)$, the escape rate out of its minimum is

$$\begin{aligned} r_K &= \frac{1}{2\pi} \sqrt{V''(\theta_{min})|V''(\theta_{max})|} e^{-\frac{V(\theta_{max})-V(\theta_{min})}{\zeta D}} \\ &= \frac{\chi_R D_R}{\pi} e^{-\chi_R}, \end{aligned} \quad (5.27)$$

where $V(\theta_{min})$ and $V(\theta_{max})$ are minimum and maximum of the potential V , respectively. D_{\parallel} is the result of the 'flipping 1D' random walk in the direction of \hat{H} .

$$\hat{\sigma}_{\parallel}^{swim} = \frac{D_{\perp}^{swim}}{U_0^2 \tau_R / 2} \rightarrow \frac{\pi}{2} \frac{e^{\chi_R}}{\chi_R}. \quad (5.28)$$

D_{\perp} also forms a 'boundary layer' around the equilibrium position $\mathbf{q} \cdot \hat{H} = 0$. For 2D rotation, it can be directly calculated from the integral. We can make the 'boundary layer' approximation: $\theta \approx \sin \theta$, $\cos \theta \approx 1 - \theta^2/2$.

Therefore, the integral is explicitly integrable:

$$\frac{D_{\perp}^{swim}}{U_0^2 \tau_R / 2} \approx 8 \int_0^{\frac{\pi}{2}} \frac{e^{\frac{1}{2}\chi_R \cos(2\theta)} \sin^2 \theta}{4\pi \chi_R I_0\left(\frac{\chi_R}{2}\right)} d\theta, \quad (5.29)$$

$$= \frac{1 - \frac{I_1\left(\frac{\chi_R}{2}\right)}{I_0\left(\frac{\chi_R}{2}\right)}}{2\chi_R} \rightarrow \frac{1}{2\chi_R^2}. \quad (5.30)$$

Finally:

$$\hat{\sigma}_{\perp}^{swim} = \frac{D_{\perp}^{swim}}{U_0^2 \tau_R / 2} \rightarrow \frac{1}{2\chi_R^2}. \quad (5.31)$$

5.3 Force on a boundary: the tensorial swim stress

The pressure of isotropic swimmers on a flat wall is the swim pressure (Yan & Brady, 2015b), $\Pi^{W,swim} = n^{\infty} \zeta U_0^2 \tau_R / 6$. Throughout this section, n^{∞} is used to stress that it is the number density in the *homogeneous bulk* system. From a tensorial stress point of view, we can simply write $\mathbf{F}^W = -(\boldsymbol{\sigma} \cdot \mathbf{n})dS$, following the convention of continuum mechanics where \mathbf{n} is the wall normal vector and dS is unit wall area. For swimmers with an unbiased orientation distribution, \mathbf{F}^W contains no tangential or shear component, and we can write it as:

$$\Pi^W = -(\boldsymbol{\sigma}^{swim} \cdot \mathbf{n}) \cdot \mathbf{n}. \quad (5.32)$$

For swimmers with anisotropic orientational order, does this apply to *arbitrary* directions?

A true tensorial stress $\boldsymbol{\sigma}^{swim}$ must satisfy (5.32) for any surface with normal vector \mathbf{n} :

$$\begin{aligned} \Pi^{W,swim} &= -(\boldsymbol{\sigma}^{swim} \cdot \mathbf{n}) \cdot \mathbf{n} \\ &= n^{\infty} k_s T_s \left(\hat{\sigma}_{\parallel}^{swim} \hat{\mathbf{H}} \hat{\mathbf{H}} + \hat{\sigma}_{\perp}^{swim} \hat{\mathbf{H}}_{\perp} \hat{\mathbf{H}}_{\perp} \right) : \mathbf{n} \mathbf{n} \\ &= n^{\infty} k_s T_s \left(\hat{\sigma}_{\parallel}^{swim} (\hat{\mathbf{H}} \cdot \mathbf{n})^2 + \hat{\sigma}_{\perp}^{swim} (\hat{\mathbf{H}}_{\perp} \cdot \mathbf{n})^2 \right), \end{aligned} \quad (5.33)$$

where $k_s T_s = \zeta U_0^2 \tau_R / 6$ for 3D swimmers and $\zeta U_0^2 \tau_R / 2$ for 2D swimmers (Takatori *et al.*, 2014). Here, $\hat{\sigma}_{\parallel}^{swim}$ and $\hat{\sigma}_{\perp}^{swim}$ are analytically calculated in the last section.

In the presence of translational diffusivity $D_T = k_B T / \zeta$, the total pressure on the wall also contains the osmotic pressure contribution:

$$\Pi^W = \Pi^{W,swim} + n^{\infty} k_B T. \quad (5.34)$$

From a colloidal perspective as shown by Yan & Brady, (2015b), the pressure applied by swimmers on a wall is due to the formation of a boundary layer on concentration

of swimmers on the microscopic length scale $\delta = \sqrt{D_T \tau_R}$. For hard spheres, the Smoluchowski equation gives

$$\Pi^W = \zeta D_T n^W, \quad (5.35)$$

where n^W is the number density on the wall. In the absence of a bulk polarization field, the boundary layer is such that $n^W/n^\infty = 1 + k_s T_s/k_B T$, and (5.35) is consistent with (5.34).

When $\chi_R = 0$, (5.33) and (5.35) give exactly the same pressure on the wall, and in this section we will show that this is also true for swimmers with nematic order. That is, σ^{swim} is a true tensorial stress.

For simplicity, we consider 2D ABPs between two parallel walls separated by L , and the nematic field direction is applied at an angle φ with the wall normal vector \mathbf{n} , $\cos \varphi = \mathbf{n} \cdot \hat{\mathbf{H}}$. Fluid is assumed to flow freely across the wall, and the wall-particle collision is assumed to be excluded-volume only. The configuration is similar to the sedimentation problem (Yan & Brady, 2015a), except that in this work we consider the dilute limit so swimmer-swimmer interactions are completely ignored to be compatible with the diffusivity calculations in the last section. $L/\ell \rightarrow \infty$ is also imposed to eliminate any confinement effect (Ezhilan *et al.*, 2015; Yan & Brady, 2015b).

In this geometry, the motion of swimmers between the walls is completely determined by the Smoluchowski equation, tracking the probability $P(\mathbf{x}, \mathbf{q}, t)$ of a swimmer appearing at \mathbf{x} with orientation \mathbf{q} at time t . We define the microscopic length $\delta = \sqrt{D_T \tau_R}$, and the run length $\ell = U_0 \tau_R$. All lengths are nondimensionalized with ℓ , and time is scaled with τ_R , and we have:

$$\frac{\partial P}{\partial t} + \nabla \cdot \mathbf{j}_T + \frac{\partial}{\partial \theta} j_R = 0, \quad (5.36)$$

$$\mathbf{j}_T = \cos \theta P - \frac{\delta^2}{\ell^2} \frac{\partial P}{\partial x}, \quad (5.37)$$

$$j_R = \chi_R \sin 2(\theta - \varphi) P - \frac{\partial P}{\partial \theta}. \quad (5.38)$$

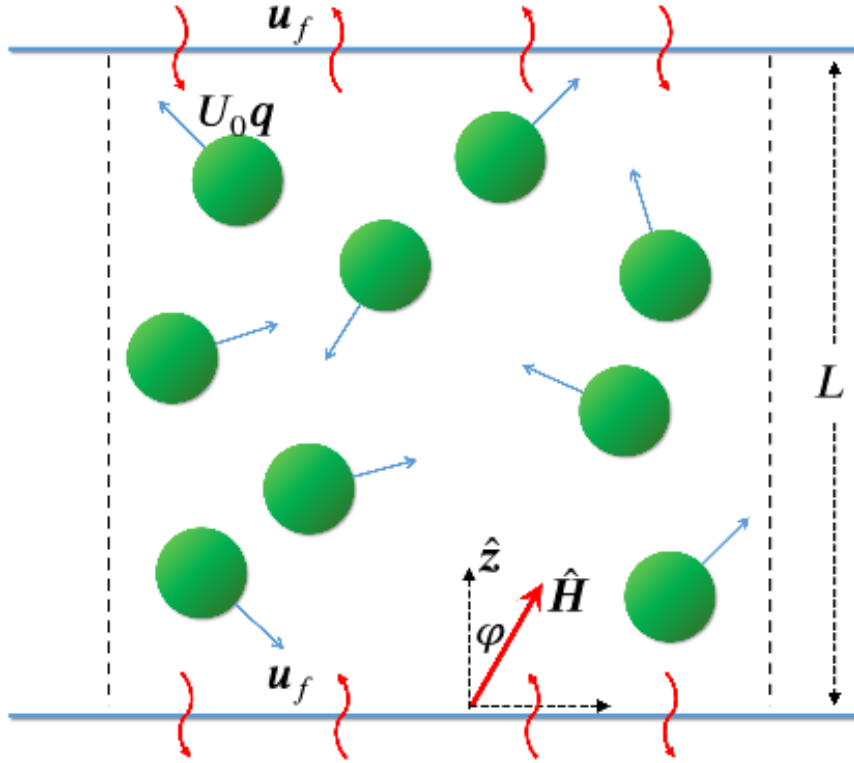


Figure 5.4: \hat{H} is the external field direction, and $U_0 \mathbf{q}$ is the swim velocity of each ABP. $\mathbf{q} \cdot \hat{z} = \cos \theta$, $\hat{H} \cdot \hat{z} = \cos \varphi$. The normal vector of the bottom wall $\mathbf{n} = \hat{z}$.

Those equations can be easily solved with a FEM PDE solver with non-penetrating boundary conditions on the top and bottom walls as illustrated in Fig. 5.4. After steady state is reached, $n^W = \int P(\mathbf{x}^W, \mathbf{q}, t) d\mathbf{q}$, and the pressure on the wall can be calculated from the microscopic colloid perspective (5.35).

From the tensorial perspective (5.33), we can also *analytically* calculate the pressure on the wall:

$$\Pi^{W,swim} = n^\infty k_s T'_s \left(\hat{\sigma}_{\parallel}^{swim} \cos^2 \varphi + \hat{\sigma}_{\perp}^{swim} \sin^2 \varphi \right). \quad (5.39)$$

Here, $k_s T'_s = \zeta U_0^2 \tau_R / 2$ is defined for the 2D geometry with 2D rotations.

Also, Brownian dynamics simulations are performed to compare with both the colloid perspective (5.35) and the tensorial perspective (5.39). In the Brownian Dynamics simulations, the pressure is determined from the force exerted by each

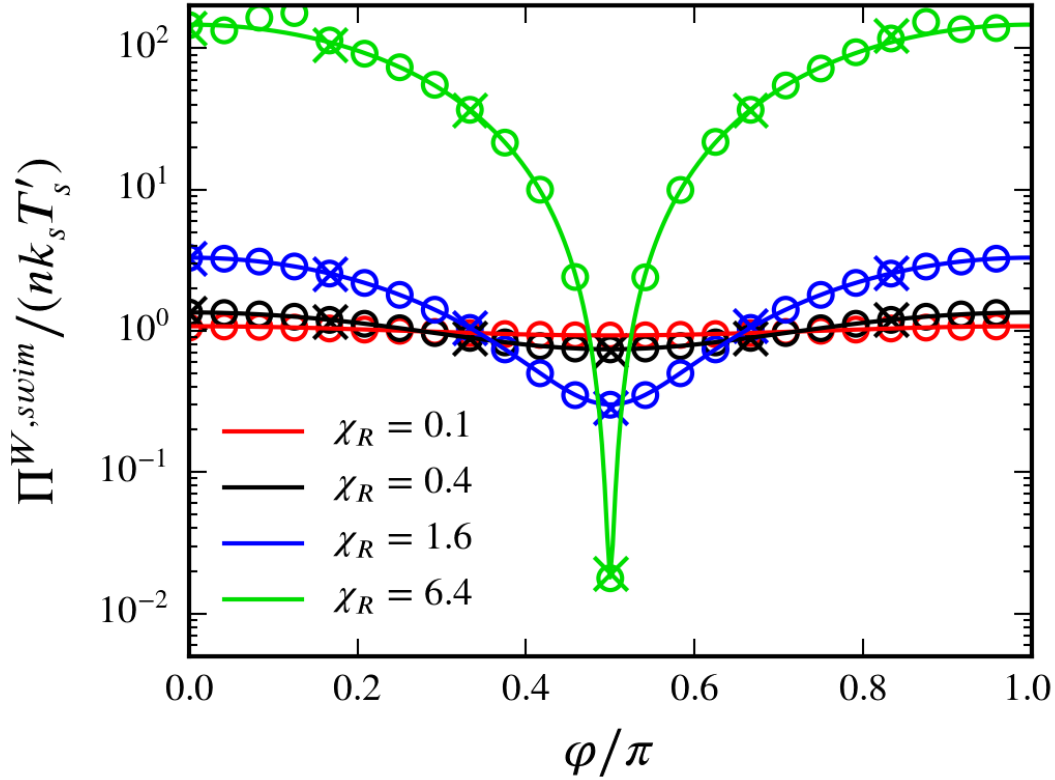


Figure 5.5: Comparison between the colloidal perspective and the continuum mechanics tensorial perspective. The solid lines are calculated analytically from (5.39), the open symbols are calculated from (5.36), solved by FEM solver with $\delta^2/\ell^2 = 0.2$ and $L = 20\ell$. The cross symbols are measured from particle-wall collisions in Brownian dynamics simulations, with $\ell = 4a$ and $\delta = 0$, in a box with $L = 128a = 32\ell$ and periodic in the horizontal direction.

particle-wall collision.

Part 1. The normal component of stress

The comparison between the colloid perspective and the tensorial perspective is shown in Fig. 5.5. The calculation for (5.39) is analytic and is valid for arbitrary ratio of swimming to diffusion, $\ell/\delta \in (0, \infty)$.

The pressure from the colloid perspective is calculated with $\delta^2/\ell^2 = 0.2$ and then the pressure of passive Brownian motion (osmotic pressure) $n^\infty k_B T = n^\infty \zeta D_T$ is subtracted from the result of (5.35). Also $L = 20\ell$ is used to guarantee that there are no confinement effects. The Brownian dynamic simulations are conducted with

$D_T = 0$, and we find that all three methods agree with each other.

The comparison clearly shows that the mechanical swim pressure on a wall can be strongly anisotropic as shown with the case $\chi_R = 6.4$. Actually, based on (5.33) we have that

$$\text{for } \mathbf{n} = \hat{\mathbf{H}}: \Pi^{W,swim} = n^\infty k_s T'_s \hat{\sigma}_\parallel^{swim} \sim n^\infty k_s T'_s \frac{\pi}{2} \frac{e^{\chi_R}}{\chi_R}, \quad (5.40)$$

$$\text{for } \mathbf{n} = \hat{\mathbf{H}}_\perp: \Pi^{W,swim} = n^\infty k_s T'_s \hat{\sigma}_\perp^{swim} \sim n^\infty k_s T'_s \frac{1}{2\chi_R^2}. \quad (5.41)$$

The anisotropy $\hat{\sigma}_\parallel^{swim}/\hat{\sigma}_\perp^{swim} \sim \pi\chi_R e^{\chi_R}$, growing very fast with the field strength χ_R .

Again, it is important that the number density n^∞ in Fig. 5.5 and Fig. 5.6 is the ‘bulk’ value, that is, n at the center between the two walls. It should not be confused with the n^W in (5.35).

Part 2. The tangential component of stress

In continuum mechanics, $\boldsymbol{\sigma}^{swim} \cdot \mathbf{n}$ is the stress on a plane with normal \mathbf{n} , and the tangential component $(\boldsymbol{\sigma}^{swim} \cdot \mathbf{n}) \cdot \mathbf{t}$ is the shear stress applied on that plane, i.e., the friction between the two continuum media. When $\boldsymbol{\sigma}^{swim}$ is isotropic, the shear component is simply always zero for any surface normal \mathbf{n} . For anisotropic $\boldsymbol{\sigma}^{swim}$, however, the tangential component is not necessarily zero. However, there cannot be any shear stress (friction) in the ABP model, because the wall-swimmer interaction is excluded volume only; that is, a force is transmitted only in the normal direction to prevent the swimmer from crossing the wall.

In fact, when a swimmer swims towards a wall, it is trapped on the wall for a period of time until the \mathbf{q} is relaxed to a different direction so it can leave the wall. For the period of time when the particle stays on the wall, the normal component of swim force (Yan & Brady, 2015a) $\mathbf{n} \cdot \zeta U_0 \mathbf{q}$ is transmitted to the wall and contributes to the normal pressure Π^W . The tangent component is not transmitted to the wall and the swimmer is actually ‘sliding’ along the wall. Therefore, the tangential component

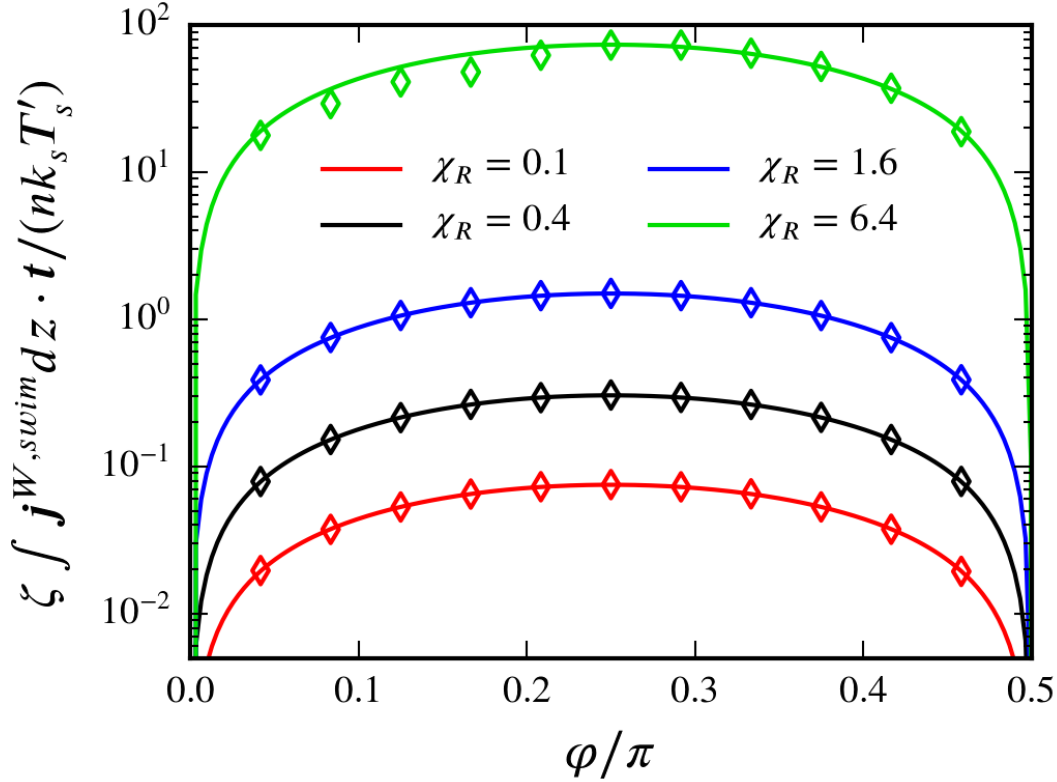


Figure 5.6: Comparison between the colloidal perspective and the continuum mechanics tensorial perspective for the shear component, and the corresponding flux along the wall. The solid lines are calculated analytically from (5.39); the open symbols are data calculated from the same FEM solution as in Fig. 5.5.

of swim stress is a net *flow* of ABPs sliding along the wall in the tangential direction. The direction of the net flux is towards the left on the bottom wall and towards the right on the top wall for the \hat{H} shown in Fig. 5.4. The flux on the bottom and the top walls are of the same magnitude but in the opposite directions. They cancel each other so there is no net overall motion in the domain.

For the 2D geometry shown in Fig. 5.4, the tensorial stress predicts the flow as:

$$\zeta \int \mathbf{j}_T^{W,swim} dz \cdot \mathbf{t} = nk_s T'_s (\hat{\sigma}_{\parallel}^{swim} - \hat{\sigma}_{\perp}^{swim}) \cos \varphi \sin \varphi. \quad (5.42)$$

Here the subscript T represents the ‘translational’ flow along the wall. It is clear that if $\chi_R = 0$, $\hat{\sigma}_{\perp}^{swim} = \hat{\sigma}_{\parallel}^{swim}$ and the flux is always zero; only an anisotropic stress drives a flux. Here, $\int \mathbf{j}_T^{W,swim} dz$ has the dimension of the total flow rate along the

boundary, per unit boundary length (area if in the 3D case), while $\zeta \int j_T^{W,swim} dz \cdot \mathbf{t}$ has the dimension of pressure.

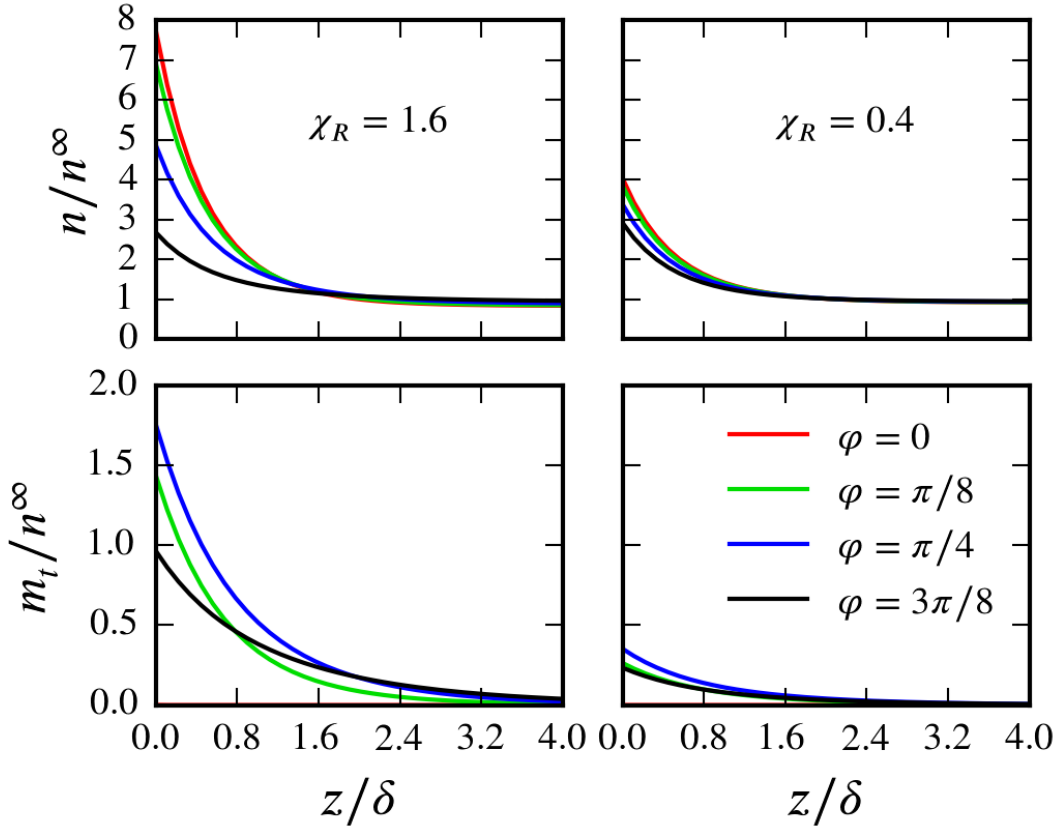


Figure 5.7: The boundary layer structure for the case of $\chi_R = 1.6$ (left column) and $\chi_R = 0.4$ (right column), taken from the same data as shown in Fig. 5.5. Here n^∞ is the number density in the bulk, corresponding to the n in Fig. 5.5 and Fig. 5.6. z represents the height in this boundary layer. $m_t = \mathbf{m} \cdot \mathbf{t}$ is the tangential component of polar order \mathbf{m} . For the $\hat{\mathbf{H}}$ in Fig. 5.4, m_t is towards the left on the bottom wall. For $\varphi = 0$, $m_t = 0$ everywhere as estimated by (5.42) and Fig. 5.6.

From the microscopic colloid perspective, the swimmers now form a kinetic boundary layer (Yan & Brady, 2015b) on the wall, with directed motion as shown in Fig. 5.7. More specifically, on a microscopic scale close to the wall, there is net polar order $\mathbf{m} = \int P \mathbf{q} d\mathbf{q} \neq 0$, even though the nematic orientation field has no polar order in the bulk. By solving the Smoluchowski equation (5.36), the flux is

obtainable by integrating m_t , the component of \mathbf{m} parallel to the wall:

$$\int \dot{\mathbf{j}}_T^{W,swim} dz \cdot \mathbf{t} = \int \mathbf{m} \cdot \mathbf{t} dz. \quad (5.43)$$

Also, here the total stress includes the osmotic pressure $k_B T$ contribution: $\boldsymbol{\sigma}^{tot} = \boldsymbol{\sigma}^{swim} - nk_B T \mathbf{I}$. Since $k_B T \mathbf{I} = \zeta D_T \mathbf{I}$ is always isotropic, it does not contribute to the tangential component:

$$(\boldsymbol{\sigma}^{total} \cdot \mathbf{n}) \cdot \mathbf{t} = (\boldsymbol{\sigma}^{swim} \cdot \mathbf{n}) \cdot \mathbf{t}. \quad (5.44)$$

The comparison between the colloidal perspective and the continuum mechanics tensorial perspective for the shear component, and the corresponding flux along the wall is shown in Fig. 5.6, and the tensorial stress perspective (5.42) agrees very well with the detailed microscopic colloidal perspective (5.43).

5.4 Conclusions & Discussions

In this chapter we discussed an example, designed to extend the notion of the swim pressure to a true tensorial swim stress, for a special case of swimmers in a nematic orientation field.

Swimmers under a nematic orientational potential show significantly enhanced diffusivity parallel to the field direction $\hat{\mathbf{H}}$, and significantly reduced diffusivity in the perpendicular direction. Under a strong field $\chi_R \rightarrow \infty$, the orientation is trapped in the $\pm \hat{\mathbf{H}}$ directions, and only occasionally does a Kramers' hopping event happen. Therefore, the strongly anisotropic diffusivity is induced by a strongly anisotropic orientational fluctuation field \mathbf{B} . This is in contrast to the polarization case (Taketori & Brady, 2014; Yan & Brady, 2015a), where all swimmers are directed towards the same direction and the diffusivity in the $\hat{\mathbf{H}}$ and $\hat{\mathbf{H}}_\perp$ directions both decay algebraically with increasing χ_R .

The anisotropic swim diffusivity gives an anisotropic swim stress $\boldsymbol{\sigma}^{swim} = -n\zeta \mathbf{D}^{swim}$. Using a parallel-wall geometry, we showed that an anisotropic swim stress is truly a

stress in the continuum mechanics sense – the pressure on a boundary with nematic field is $\Pi^W = (\boldsymbol{\sigma}^{swim} \cdot \mathbf{n}) \cdot \mathbf{n}$. The tangential component gives not a shear stress (friction) in the absence of hydrodynamics, but a net flow of ABPs along the wall. This is because the interaction between the ABP and the wall is assumed to be frictionless. In the presence of hydrodynamics, this flux of swimmers along the wall would likely drag some fluid with it, and likely induce a net flow of the suspension parallel to the wall. From a continuum perspective, the swim stress $\boldsymbol{\sigma}^{swim}$ contributes no shear component to the total stress of suspension $\langle \boldsymbol{\sigma} \rangle$. So the flow must be balanced by the viscous shear stress $2\eta \langle \mathbf{e} \rangle$, where $\langle \mathbf{e} \rangle = \frac{1}{2} (\nabla \langle \mathbf{u} \rangle + \nabla \langle \mathbf{u} \rangle^T)$. Further below the continuum scale, if the detailed swimmer-wall hydrodynamic interaction is considered, the net flow of swimmers along the wall may be quantitatively changed. The details in the presence of hydrodynamics is left for a future study.

It is important to realize that the tensorial stress perspective is on the continuum scale $L \gg \ell$, where the detailed interaction structure of swimmers with the wall is ignored, as that happens on the microscopic scale δ as shown in Fig. 5.7. The microscopic colloid perspective (5.35) explained the tensorial stress in the bulk through the formation of a kinetic boundary layer shown in Fig. 5.7. It actually extends the discussion of the kinetic boundary layer of swimmers on the wall (Ezhilan *et al.*, 2015; Yan & Brady, 2015b; Smallenburg & Löwen, 2015) to the case of swimmers with torques.

In this work we discussed the system with nematic order, and it is a special case because nematic order is symmetric and gives no net motion or net swim force $\langle \mathbf{F}^{swim} \rangle$, in contrast to polar ordered swimmers (Takatori & Brady, 2014; Yan & Brady, 2015a). For polar ordered swimmers, however, the notion of a tensorial swim stress is still applicable if we apply a body force to cancel the swim force and therefore to cancel the net motion. In fact, when $\langle \mathbf{F}^{swim} \rangle$ is canceled by a body

force, polarized swimmers exhibit a stress exactly in the form of (5.33). That is, the tensorial perspective makes no assumption of how the anisotropic stress is induced. In fact, it assumes that all information has been contained in the stress itself: n^∞ , $k_s T_s$, $\hat{\sigma}_\perp^{swim}$ and $\hat{\sigma}_\parallel^{swim}$ are sufficient from a continuum mechanics perspective.

For swimmers with *arbitrary* orientational torques, the Smoluchowski equation is:

$$\frac{\partial P}{\partial t} + \nabla \cdot \mathbf{j}_T + \nabla_R \cdot \mathbf{j}_R = 0, \quad (5.45)$$

$$\mathbf{j}_R = \omega(\theta - \varphi)P - \mathbf{D}_R \cdot \nabla_R P, \quad (5.46)$$

$$\mathbf{j}_T = \mathbf{U}_0 P + \mathbf{F}^c P - D_T \nabla P, \quad (5.47)$$

where $\omega(\theta - \varphi)$ is the angular velocity induced by some external torque, as a function of the swimmer's orientation angle θ and the field orientation φ . \mathbf{F}^c is the body force to *cancel* the swim force and any bulk net motion: $\mathbf{F}^c + \mathbf{F}^{swim} = 0$ for each particle to keep the system in a homogeneous state. It is unclear at this stage whether, for arbitrary ω , the stress can still be treated generally as a true tensorial stress. Rigorous mathematical proof requires solution of the boundary layer with arbitrary orientation order and is usually very difficult. The orientation order expansion method (Saintillan & Shelley, 2015; Yan & Brady, 2015b) may be a possible route towards a general proof, but it is subject to proper orientation closure relations. We shall leave it for a future study.

The tensorial view of swimmers has more profound use than simply to estimate the pressure on a flat wall for swimmers without net motion. We showed with Generalized Taylor Dispersion Theory (Frankel & Brenner, 1989) that in a general transport problem such as sedimentation or active micro-rheology, the large scale motion and deformation of swimmers can simply solved with the continuum mechanics flux with tensorial stress, body force, and swim force (Yan & Brady, 2015a):

$$\mathbf{j}_{cm} = \frac{1}{\zeta} \left(\nabla \cdot \boldsymbol{\sigma}^{tot} + \mathbf{F}^g + \langle \mathbf{F}^{swim} \rangle \right). \quad (5.48)$$

The boundary condition for this large-scale transport equation must be properly constructed from the detailed near-wall dynamics on the small scale. This is very similar to the rarefied gas dynamics, where the non-continuum effects must be resolved on the scale of a few mean free paths at the boundary, and then a proper boundary condition for Navier-Stokes equation in the outer region can be constructed from the ‘inner’ solution. Similar outer-inner matching scheme is also true for ABPs, as discussed in [Chapter 4](#).

Chapter 6

A METHOD TO DETERMINE THE BEHAVIOR OF ACTIVE
DIFFUSIOPHORETIC SUSPENSIONS: ACCELERATED
LAPLACIAN DYNAMICS

6.1 Introduction

Active diffusiophoretic suspensions refer to those colloidal particles which are able to convert chemical energy to self-propulsion, usually through patterned surface reactivity (Ebbens *et al.*, 2010). Experimentally, active particles exhibit very interesting behaviors. Howse *et al.*, (2007) showed that the translational diffusion of a single active particle is enhanced by $U_0^2 \tau_R / 6$ on timescales longer than the rotational Brownian motion timescale τ_R , where U_0 is the active velocity. The collective motion is more intriguing. Active particles with attractive interactions were observed to exhibit dynamic clustering and phase behavior in experiments by Theurkauff *et al.*, (2012) and Palacci *et al.*, (2013). Particles with repulsive interaction show transition between uncorrelated motion and an ordered lattice (Soh *et al.*, 2008).

The Active Brownian Particle (ABP) model is proposed to understand the phase separation. In ABPs, the particle's self-propulsion velocity $\mathbf{U}_0 = U_0 \boldsymbol{\xi}$, where U_0 is usually assumed to be a given constant and $\boldsymbol{\xi}$ is subject to rotational Brownian motion. Also, the interaction between ABPs is usually assumed to be collision only (pure repulsive) (Solon *et al.*, 2015a) or a pairwise additive potential (Redner *et al.*, 2013). Under this circumstance, the interaction between ABPs is short-ranged and additive, and therefore can be successfully explained by thermodynamic-type models, such as the ϕ^4 field theory (Wittkowski *et al.*, 2014), density functional theory (Menzel & Löwen, 2013), and motility-induced-phase-separation (Stenhammar *et al.*, 2013; Cates & Tailleur, 2015). For example, the dilute-dense coexistence of active matter can be explained as a first-order gas-liquid phase transition, with the introduction of swim pressure as the equation of state (Takatori *et al.*, 2014; Takatori & Brady, 2015).

However, the applicability of thermodynamics on the active diffusiophoretic suspensions is questionable in the presence of the chemical solute concentration field c . On the single particle level, Brady and Córdova-Figueroa (Córdova-Figueroa &

Brady, 2008; Brady, 2011) showed that a particle's motion can be determined by solving the solute concentration field $c(\mathbf{r})$ around the particle. To leading order, the swim velocity $U_0 \propto c$. They swim faster with more 'fuel' concentration c . In the presence of many particles, the disturbance on $c(\mathbf{r})$ caused by each particle propagates, and causes not only changes of swim velocity, but also particle-particle attraction or repulsion due to diffusiophoresis $\propto \nabla c$. In fact, the self-propulsion and particle-particle interactions are not separable because they come from the same field c . The Damköhler number Da describes how fast the reaction is, and therefore how fast the particle swims (Córdova-Figueroa & Brady, 2008) and how significant the perturbation c' is. As we shall see, the system behavior is controlled by the dimensionless 'fuel concentration' $S_D \propto c^E a^3$, where c^E is the *imposed* solute reactant concentration. At higher S_D , both the swimming $\propto c$ and attraction $\propto \nabla c$ are enhanced and so the system has more chance to form clusters, overcoming the translational Brownian motion randomizing the system towards a homogeneous state.

This 'field-driven' nature results in the fundamentally different system behavior from the ABPs. To probe the system dynamics, the field c must be solved simultaneously with the particles' motion, and it must be done efficiently so that the collective motion of a large amount of particles can be probed. In the continuum limit where solute molecules are much smaller than particles, the governing equation of $c(\mathbf{r})$ can be reduced to Laplace's equation. It is a valid assumption, compared to experiments (Palacci *et al.*, 2013). For a Laplace's equation, it is well known that a source or sink induces a perturbation $c' \propto 1/r$ similar to electrostatics. However, one should not simply impose a fixed $1/r$ interaction between particles, as seen in some simulation work (Palacci *et al.*, 2013; Pohl & Stark, 2014), because the chemical reaction on each particle is proportional to the local concentration c , and should not be treated as a fixed 'charge' in an electrostatic system. Instead, we show in this chapter that the interaction is governed by Brinkman-like chemical screening. It

is a static screening and solely due to the fact that neighbor particles are changing their reactivity $\propto c$ to compensate for every particle's perturbation, and it takes an exponential Yukawa form. However, it is also illegitimate to *prescribe* a Yukawa form pairwise potential, because the screened effect can only be correctly accounted for *after* the full Laplace's equation governing c is solved.

We should determine the motion by solving the Laplace's equation governing $c(\mathbf{r})$, with each particle's reactivity serving as a boundary condition. However, solving a Laplace's equation for N particles is never an easy task because it usually requires $O(N^2)$ or even $O(N^3)$ operations to apply the mesh-based Finite Difference or Finite Volume method. Bonnecaze & Brady, (1990) developed a method to solve the many-body Laplace's equation by a multipole scattering method. Their method achieves significant improvement by avoiding the use of mesh, but still requires $O(N^2)$, $O(N^3)$ explicit matrix construction and inversion. In this work we combine Bonnecaze & Brady's method with the Accelerated Stokesian Dynamics (ASD) by Sierou & Brady, (2001), achieving a matrix-free, $O(N \log N)$ method.

We shall show that our Accelerated Laplacian Dynamics can efficiently track the dynamics of an active diffusiophoretic system. In § 6.2 we formulate the problem, and derive the method in § 6.3. Then in § 6.4 we clarify the concept of chemical screening with both theories and simulations. It is also a verification of our simulation method. Results for attractive particles in a periodic setting and results for attractive Janus particles in a confined monolayer setting are reported in § 6.4. In those parts we analyze the simulation results to address the two fundamental questions of chemically active diffusiophoretic suspensions: when does the clustering process start (the unstable criteria) and when does it stop (the steady state criteria)? We also propose a self-consistent continuum mechanical model based on the concept of swim force (Takatori *et al.*, 2014) and swim force (Yan & Brady, 2015a) as a partial answer.

6.2 Problem formulation

Small colloidal particles can move in response to a concentration gradient of a chemical solute. If the gradient is externally imposed the process is referred to as diffusiophoresis; if the particle generates the gradient itself via, e.g., a surface chemical reaction, it is called self-diffusiophoresis. Following the approach and notation of Brady, (2011) (which has been shown to agree with more conventional approaches (Anderson, 1989)), in both cases the velocity of a spherical colloidal particle of radius a can be written as

$$\mathbf{U} = -\frac{L(\Delta)}{6\pi\eta a} \oint \mathbf{n} k_B T c(\mathbf{x}, t) dS, \quad (6.1)$$

where the dimensionless hydrodynamic mobility function $L(\Delta) = (3/2)\Delta^2(1 + \frac{2}{3}\Delta)/(1 + \Delta)^3$, with $\Delta = \delta/a$, measures the flow of fluid with viscosity η in a layer of thickness δ adjacent to the colloidal particle where the particle-solute interactive force is operative, c.f. Fig. 6.1. Here we have taken the simplest form of interactive force between the solute and the colloidal particle, namely a hard-sphere repulsive force at a distance $r_c = a + \delta$ (and δ need not be small compared to the particle size a , although typically it is so). More general interactive forces will only have a quantitative effect; the work of Brady, (2011) details how to include these (and other) effects. Generalizations to non-spherical particles are also possible (ShklyaeV *et al.*, 2014).

The solute concentration enters the expression for the particle velocity multiplied by the thermal energy $k_B T$, which we recognize as the local osmotic pressure of the solute $\Pi(\mathbf{x}, t) \equiv k_B T c(\mathbf{x}, t)$. This permits the interpretation of the velocity as the result of a force balance between the Stokes drag of the solvent and the osmotic force of the solute: $\mathbf{F}^{drag} + \mathbf{F}^{osmo} = 0$, with $\mathbf{F}^{drag} = -6\pi\eta a \mathbf{U}$ and $\mathbf{F}^{osmo} = -L(\Delta) \oint \mathbf{n} k_B T c(\mathbf{x}, t) dS$. That the osmotic force is a real, measurable, force can be appreciated by realizing that if one wanted to stop the colloidal particle from moving, say by optical tweezers, then the force the tweezers would need to

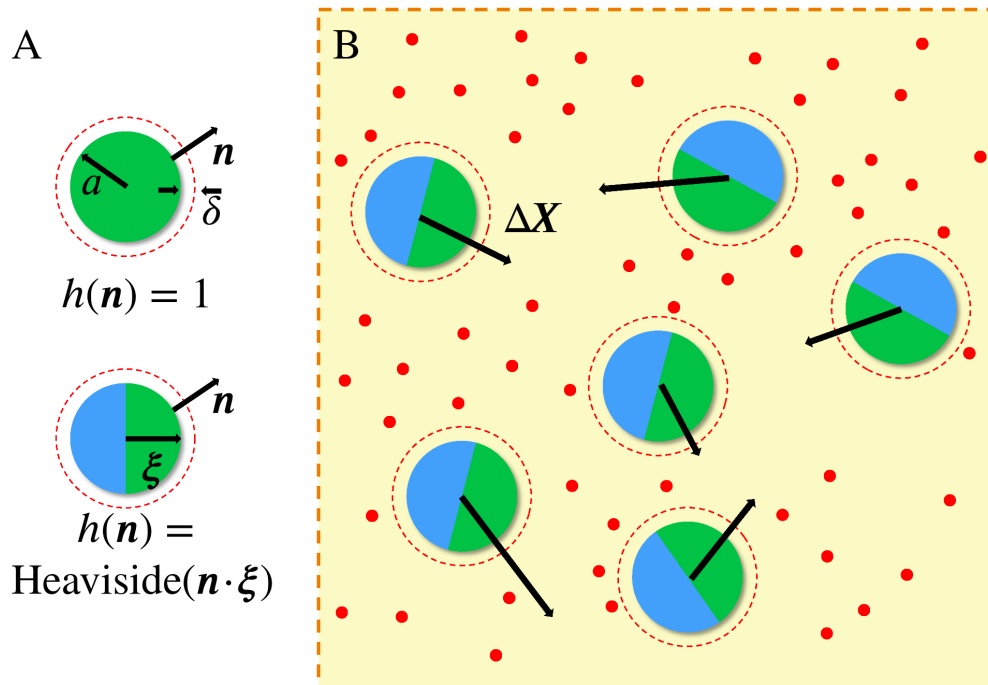


Figure 6.1: (A) The uniformly reactive sink particle and the Janus particle with orientation vector ξ . Both particles have radius a , interaction layer thickness δ and surface normal vector \mathbf{n} . A reactive surface is colored green and a non-reactive surface is blue. Motion ($\Delta\mathbf{X}$) of each Janus particle in a system is governed by the over-damped Langevin equation (6.6). (B) The concentration field c of reactive solute molecules (shown by the red dots) is solved simultaneously with the motion of the active particles.

exert is precisely \mathbf{F}^{osmo} .

For chemically active particles the catalytic reaction at the particle surface can be expressed as $R \rightarrow \theta P$, where R is the reactant, P is the product, and θ is the stoichiometry of the chemical reaction. In general, one needs the osmotic force arising from both the reactants and products, but, as shown by Córdova-Figueroa & Brady, (2008), one only needs to scale (6.1) by the factor $(1 - \theta D_R/D_P)$, where D_R and D_P are the diffusivities of the reactants and products, respectively, to account for both reactants and products.

The reactant concentration satisfies the usual advection-diffusion equation

$$\frac{\partial c}{\partial t} + \nabla \cdot \mathbf{j}_R = 0, \quad (6.2)$$

where the reactant solute flux is given

$$\mathbf{j}_R = \mathbf{u}c - D_R \nabla c, \quad (6.3)$$

and \mathbf{u} is the velocity of the suspending fluid. In this study any fluid motion is the result of the motion of the colloidal particles and thus the relative importance of advection to diffusion is governed by the Péclet number $Pe = Ua/D_R$. Typical phoretic or self-propulsive velocities are of order $1 \mu\text{m}/\text{s}$ for a micron-sized particle, while solute diffusivities are of order $10^3 \mu\text{m}^2/\text{s}$ so that the Péclet number is very small and fluid advection can be neglected. Similarly, the time scale to establish a steady solute concentration profile, a^2/D_R , is much faster than the time scale for the motion of the particle, either due to diffusiophoresis or to its intrinsic Brownian motion, so that the reactant/solute concentration distribution satisfies Laplace's equation

$$\nabla^2 c = 0. \quad (6.4)$$

We model the catalytic reaction at the particle surface as first order and, making use of the stoichiometry/diffusivity factor $(1 - \theta D_R/D_P)$, the reaction can be taken to be irreversible:

$$\mathbf{n} \cdot \mathbf{j}_R = -\kappa_0 h(\mathbf{n})c, \quad (6.5)$$

where κ_0 is the surface reaction rate constant (units of *length/time*) and the nondimensional function $h(\mathbf{n})$ describes the patterned reactivity on the particle surface whose outer normal is \mathbf{n} . For uniformly reactive particles $h(\mathbf{n}) = 1$, while a particle with $h(\mathbf{n}) = \text{Heaviside}(\mathbf{n} \cdot \boldsymbol{\xi})$ describes the pattern of a Janus particle with orientation vector $\boldsymbol{\xi}$: $h = 1$ on the reactive hemisphere and $h = 0$ on the passive hemisphere, see Fig. 6.1. Particles for which $(1 - \theta D_R/D_P) > 0$ reduce the concentration of

reactant near their surface, and will attract a second particle by diffusiophoresis; such particles act as chemical sinks; those with $(1 - \theta D_R/D_P) < 0$ act as sources.

The diffusiophoretic system shares many similarities with electrostatics: both are governed by Laplace's equation with the reactant concentration being the analog of the electrostatic potential, and chemical sink/source particles are analogous to negative/positive charges, etc. There is, however, an important difference. In an electrostatic system the electric field does not disappear if charges are not destroyed. In a diffusiophoretic system, on the other hand, the concentration of reactant is subject to chemical reaction, and when all the reactant (or fuel) is consumed by the particles the concentration goes to zero and all motion (apart from the particles' intrinsic Brownian motion) ceases. Thus, to achieve a steady state with reactive particles, we need to supply reactant (and remove product) at the same rate at which it is consumed (produced) by the particles. In experiments with a monolayer of active particles (Theurkauff *et al.*, 2012), reactant is provided by diffusion from a reservoir above the monolayer.

In this work, we shall consider two types of systems: finite and periodic. For finite systems, we have a finite number of particles moving in an infinite bath of solute (reactant and product), and we specify a boundary condition of a constant reactant concentration c^∞ as the distance goes to infinity. Physically, reactant diffuses from infinity to the particle region to compensate for the consumption by the active particles; no other reactant sources are needed. For a periodic system there is no 'infinity,' and the condition to have a steady state is for a homogeneous generation of reactant at a rate $\langle s \rangle$ that balances the rate of consumption so that the volume average solute concentration $\langle c \rangle$ is a spatial (unit cell average) constant. This makes the system as a whole 'chemically neutral' – the positive uniform chemical source balances the negative reactive sink particles – and ensures that the long-range interactions typical in Laplace systems are convergent. The uniform source of reactant is the counterpart of the constant negative 'electrostatically neutralizing background' in

a one component plasma. Also, similar (but not identical) to electrostatic systems, diffusiophoretic interactions are screened – a phenomenon known as Brinkman screening (Morris & Brady, 1995), which we discuss in § 6.4.

The problem is now the following: for a system of active particles at locations $\mathbf{X}(t)$ we need to solve for the reactant concentration field governed by the steady Laplace's equation (6.4) at all field points \mathbf{r} outside the particles subject to a first order surface reaction boundary condition (6.5) for either (or both) uniform reactive particles ($h(\mathbf{n}) = 1$) or (and) Janus particles ($h(\mathbf{n}) = \text{Heaviside}(\mathbf{n} \cdot \boldsymbol{\xi})$) for either a finite number of active particles or in an infinite periodic system. From the solution for $c(\mathbf{r}; \mathbf{X}(t))$, we determine the phoretic velocity \mathbf{U} of an active particle from (6.1) for a given interactive length $\Delta = \delta/a$ and stoichiometry/diffusivity factor $(1 - \theta D_R/D_P)$. The active particles are then advanced to a new location from the overdamped Langevin equation incorporating Brownian translation (and rotation in the case of Janus particles):

$$\Delta \mathbf{X} = \mathbf{U} \Delta t + \Delta \mathbf{X}^B + \Delta \mathbf{X}^P, \quad (6.6)$$

where the Brownian displacement has zero mean, $\overline{\Delta \mathbf{X}^B} = 0$ and covariance $\overline{\Delta \mathbf{X}^B \Delta \mathbf{X}^B} = 2D \Delta t$, where $D = k_B T / 6\pi\eta a$ is the translation Brownian diffusivity of an active particle. A hard-sphere displacement $\Delta \mathbf{X}^P$ is implemented to prevent particles from overlapping determined from a potential-free algorithm (Foss & Brady, 2000; Heyes & Melrose, 1993). Once the active particles have been advanced to their new location, a new concentration field $c(\mathbf{r}; \mathbf{X}(t))$ must be found and the process repeated until a steady state is reached. For Janus particles, rotational Brownian motion ($D_{rot} = k_B T / 8\pi\eta a^3$) is included as a diffusive reorientation event at each timestep and calculated with the unbiased move method (Beard & Schlick, 2003). Equation (6.6) employs a simple Euler scheme for clarity; higher order schemes such as fifth order Adams-Bashforth multi-step scheme are also used in simulation.

In writing the displacements (6.6) we have neglected any hydrodynamic interactions (HI) among the active particles. HI can be included by combining the method developed in this chapter with Stokesian dynamics (Sierou & Brady, 2001) for hydrodynamically interacting colloidal particles. It should be noted that the hydrodynamic flow field created by a phoretic particle typically corresponds to a force quadrupole with a velocity field decaying as $1/r^3$ or, for Janus particles, as a force dipole or stresslet, decaying as $1/r^2$.

6.3 Method for solution of Laplace's equation

The disturbance to the concentration field caused by a single reactive particle decays as q/r , where q is the net reactant consumption rate, which is the counterpart of the electrostatic charge q_e . Despite the simple form of the potential disturbance the difficulty of solving the Laplace problem for a system of interacting particles is three-fold.

First, the particles have finite size and the concentration or potential field has a distribution on the surface of a particle; thus, the perturbed concentration field induced by an active particle must be considered to a higher order than simply a point sink or source. Second, the $1/r$ interaction is long-ranged and must be properly summed for both finite and periodic systems. Third, to solve for the collective dynamics, the motion of hundreds or thousands of particles must be followed, which requires a highly-efficient solution methodology.

The strategy adopted here is to split the problem into three parts. First, we follow the approach of Bonneau & Brady, (1990) and represent the field induced by each particle by a multipole expansion, including the monopole q (scalar), dipole S

(vector), and quadrupole \mathbf{Q} (second order tensor), defined as:

$$q_\beta = \int_{S_\beta} \mathbf{j}_R \cdot \mathbf{n} \, dS, \quad (6.7)$$

$$\mathbf{S}_\beta = \int_{S_\beta} (\mathbf{x} \mathbf{j}_R + D_{RC} \mathbf{I}) \cdot \mathbf{n} \, dS, \quad (6.8)$$

$$\begin{aligned} \mathbf{Q}_\beta = \int_{S_\beta} & \left([\mathbf{x} \mathbf{x} - \frac{1}{3}(\mathbf{x} \cdot \mathbf{x}) \mathbf{I}] \mathbf{j}_R \cdot \mathbf{n} \right. \\ & \left. + [\mathbf{x} \mathbf{n} + \mathbf{n} \mathbf{x} - \frac{2}{3}(\mathbf{n} \cdot \mathbf{x}) \mathbf{I}] D_{RC} \right) dS, \end{aligned} \quad (6.9)$$

where S_β is the surface of particle β , \mathbf{x} is a vector pointing from the particle center to its surface, and \mathbf{I} is the identity tensor. The quadrupole \mathbf{Q}_β is defined to have zero trace.

Each particle β creates a disturbance concentration field that takes the form:

$$\begin{aligned} c'(\mathbf{r}) &= c(\mathbf{r}) - c^E(\mathbf{r}) \\ &= \frac{1}{4\pi D_R} \left(\frac{q_\beta}{|\mathbf{r} - \mathbf{r}_\beta|} + \mathbf{S}_\beta \cdot \nabla_\beta \frac{1}{|\mathbf{r} - \mathbf{r}_\beta|} \right. \\ & \quad \left. + \frac{1}{2} \mathbf{Q}_\beta : \nabla_\beta \nabla_\beta \frac{1}{|\mathbf{r} - \mathbf{r}_\beta|} + \dots \right), \end{aligned} \quad (6.10)$$

where \mathbf{r} is the field point, \mathbf{r}_β is the center of particle β , and $\nabla_\beta = \partial/\partial \mathbf{r}_\beta$. The gradients ∇c , and $\nabla \nabla c$ can also be constructed in the same fashion. In (6.10) c^E refers to the externally imposed concentration that is either c^∞ in the case of a finite system or the average $\langle c \rangle$ in the case of a periodic system. The expansion (6.10) follows directly from the integral representation for the solution to Laplace's equation and is the same as one would do for the electrostatic potential with the exception that the source strengths, q_β , \mathbf{S}_β and \mathbf{Q}_β , are not given but must be found as a solution to the many-body Laplace problem. (Note that the finite volume of a particle has been included in the definition of the multipoles and thus no longer appears in (6.10).) Although truncated at this level, the multipole description preserves all the important aspects of the problem and also proves to be accurate even when particles are close to one another.

Next, we need to determine the source strengths of a particle in response to the concentration field in which it finds itself. This can be accomplished by so-called Faxen laws, which relate the multipoles q_α , \mathbf{S}_α , \mathbf{Q}_α of particle α to the concentration field $c(\mathbf{r}_\alpha) = c^E + c'$, where $c'(\mathbf{r}_\alpha)$ is the disturbance field caused by all the other particles β . Faxen laws follow from the reciprocal theorem for Laplace's equation and allow one to bypass the detailed solution for the concentration field and proceed directly to the moment strengths. Because the reaction boundary condition at a particle surface is first order and linear, the Faxen laws take a linear form:

$$\begin{pmatrix} q_\alpha \\ \mathbf{S}_\alpha \\ \mathbf{Q}_\alpha \end{pmatrix} = \mathbf{C} \cdot \begin{pmatrix} c(\mathbf{r}_\alpha) \\ \nabla c(\mathbf{r}_\alpha) \\ \nabla \nabla c(\mathbf{r}_\alpha) \end{pmatrix}, \quad (6.11)$$

where the concentration field c is evaluated at the center of particle α and originates from each particle β as given by (6.10). The matrix \mathbf{C} is the analog of the 'capacitance matrix' for electrostatics.

Faxen laws for reactive particles

For a uniform reactive particle, $h(\mathbf{n}) = 1$, the Faxen laws take a rather simple block diagonal form resulting from the particle's symmetry:

$$q_\alpha = -\frac{\text{Da}}{1 + \text{Da}} 4\pi a D_R c(\mathbf{r}_\alpha), \quad (6.12)$$

$$\mathbf{S}_\alpha = -\frac{\text{Da} - 1}{\text{Da} + 2} 4\pi a^3 D_R \nabla c(\mathbf{r}_\alpha), \quad (6.13)$$

$$\mathbf{Q}_\alpha = -\frac{\text{Da} - 2}{3\text{Da} + 9} 4\pi a^5 D_R \nabla \nabla c(\mathbf{r}_\alpha), \quad (6.14)$$

where the Damköhler number $\text{Da} = \kappa_0 a / D_R$ measures the rate of the chemical reaction to diffusion of the reactant. The derivation of the Faxen laws is given in Appendix F. For slow reaction rates or small Damköhler number the sink strength q_α is linear in Da , while the dipole and quadrupole remain finite. At the other extreme of fast reactions, all multipoles are finite as $\text{Da} \rightarrow \infty$. The concentration

field $c(\mathbf{r}_\alpha)$ (which is due to all particles other than α) and its gradients are evaluated at the center of particle α .

It is important to note that even though the dipole and quadrupole do not vanish as $Da \rightarrow 0$, since there is no macroscopically imposed concentration gradient, when the reaction rate goes to zero the monopole of each particle vanishes and there are no gradients induced by the particles. As $Da \rightarrow 0$ the concentration becomes uniform everywhere and all reaction-induced motion ceases.

For Janus particles, $h(\mathbf{n}) = \text{Heaviside}(\mathbf{n} \cdot \boldsymbol{\xi})$, and in this case the Faxen law matrix \mathbf{C} is not diagonal. The asymmetric surface reaction requires all multipoles even when the concentration field is a constant. The relation cannot be expressed in closed analytical form because all multipole moments recursively relate to each other. We use the Boundary Element Method (BEM) to numerically solve for the Faxen laws. The single particle response is truncated at dipole level for simplicity:

$$\begin{pmatrix} q_\alpha \\ \mathbf{S}_\alpha \end{pmatrix} = \mathbf{C}(Da, \boldsymbol{\xi}) \cdot \begin{pmatrix} c(\mathbf{r}_\alpha) \\ \nabla c(\mathbf{r}_\alpha) \end{pmatrix}. \quad (6.15)$$

Here the matrix is not only a function of Da as it was for the uniform reaction case, but is also dependent on the particle orientation vector $\boldsymbol{\xi}$ due to the asymmetry of Janus particles. The BEM formulation and the detailed matrix entries can be found in Appendix G. For a single particle, the solution given by \mathbf{C} at the dipole level matches previous work very well (Córdova-Figueroa & Brady, 2008). The asymptotic dependence of $\mathbf{C}(Da, \boldsymbol{\xi})$ for small and large Da is the same as for the uniform reactive particle.

In addition to the Faxen laws for the sink and dipole strength, for the particle dynamics we need the phoretic velocity of an active particle given by (6.1), which is proportional the integral

$$\mathbf{B}_\alpha = \int_{S_\alpha} \mathbf{n} c \, dS. \quad (6.16)$$

For the uniform reaction case \mathbf{B} is simply related to the dipole moment \mathbf{S} :

$$\mathbf{B}_\alpha = \frac{1}{D_R} \left(\frac{1}{1 - \text{Da}} \right) \mathbf{S}_\alpha = \frac{1}{2 + \text{Da}} 4\pi a^3 \nabla c(\mathbf{r}_\alpha), \quad (6.17)$$

showing that there is no self-motion for a homogeneous reactive particle; reaction-induced motion arises from the concentration gradient created by the other particles, corresponding to normal diffusiophoresis.

Note that from (6.1) the particle velocity is proportional to $-\mathbf{B}_\alpha$ so that the phoretic particle moves down the concentration gradient of solute or reactant and that gradient is provided by the other active particles. The motion is down the concentration gradient because we have assumed repulsive interactions between the solute and the particle at the length δ ; attractive interactions would give motion in the opposite direction. And, in general, it is possible to have a mixture of repulsive and attractive phoretic particles. We consider only repulsive particles in this work. It is a simple matter to extend the method presented here to attractive particles or to mixtures of repulsive and attractive particles.

For a Janus particle there is net motion both due to the nonuniform reaction on the particle surface, i.e. proportional to $c(\mathbf{r}_\alpha)$, and due to phoretic motion down a concentration gradient. Thus, \mathbf{B}_α takes the form

$$\mathbf{B}_\alpha = \mathbf{M}_B(\text{Da}, \boldsymbol{\xi}) \cdot \begin{pmatrix} c(\mathbf{r}_\alpha) \\ \nabla c(\mathbf{r}_\alpha) \end{pmatrix}. \quad (6.18)$$

The phoretic mobility matrix \mathbf{M}_B is related to \mathbf{C} and is given in Appendix G.

The concentration disturbance from other particles: finite and periodic systems

One can find particle α 's multipoles, q_α , \mathbf{S}_α , and \mathbf{Q}_α , from their response to other particles $\beta \neq \alpha$, each of which creates the disturbance (6.10) at the particle α 's center \mathbf{r}_α . In this subsection we describe how to formulate and compute the disturbance field for both finite and periodic systems. In a finite system, the external field $c^E = c^\infty = \text{const.}$ is specified as the boundary condition at infinity. Despite the

long-range nature of particle disturbances, no convergence problem arises because the sum is over a finite number of particles and no cutoff is necessary nor employed. For N particles the many-body concentration disturbances can be written in the matrix form:

$$\begin{pmatrix} c' \\ \nabla c' \\ \nabla \nabla c' \end{pmatrix} = \mathcal{E} \cdot \begin{pmatrix} \mathbf{q} \\ \mathbf{S} \\ \mathbf{Q} \end{pmatrix}, \quad (6.19)$$

where \mathbf{q} is now a vector of sink strengths $\mathbf{q} = \{q_1, q_2, \dots, q_N\}$, as is the concentration disturbance $c' = \{c'(\mathbf{r}_1), c'(\mathbf{r}_2), \dots, c'(\mathbf{r}_n)\}$, and similarly for the dipole and quadrupole. The $(11N \times 11N)$ matrix \mathcal{E} is the counterpart to the ‘potential matrix’ in many-body electrostatic problems (Bonnecaze & Brady, 1990). The entries in \mathcal{E} follow directly from (6.10), and note that the self-terms in \mathcal{E} are zero because the matrix sums over all particles $\beta \neq \alpha$ for each particle α .

In a periodic system $c(\mathbf{r}) = c^E(\mathbf{r}) + c'(\mathbf{r})$ still holds, but there is no boundary condition at infinity. Rather, $c^E = \langle c \rangle$, the volumetric average in the unit cell, as discussed in the previous section. In general, $\langle c \rangle$ can consist of a constant plus a term linear in \mathbf{r} , i.e. $\mathbf{G} \cdot \mathbf{r}$ where \mathbf{G} is a constant gradient. The gradient term is necessary when determining, e.g., the effective conductivity of a distribution of particle inclusions as done by Bonnecaze & Brady, (1991a). Here, we do not impose any macroscopic concentration gradient and shall take $\langle c \rangle$ to be a constant. (Note, there are *microscopic* concentration gradients induced by the active particles.)

For the periodic case, the linear relation (6.19) remains valid, but the explicit construction of the matrix elements is not as straightforward as one now has a periodic sum of long-range multipole interactions, which are computed using the Ewald summation technique. The convergence of the Ewald sum is guaranteed by the homogeneously distributed source $\langle s \rangle$ that provides the ‘chemically neutralizing background.’ Physically, the distributed source must be included in the system. Otherwise the reactant concentration field governed by Laplace’s equation would be

$c = 0$ everywhere – the only periodic solution possible would be the consumption of all reactant.

Bonnecaze & Brady, (1990) have a thorough discussion of the Ewald sum and the convergence in the presence of distributed sources, and their approach can be used here with only a slight modification. In the work of Bonnecaze & Brady, (1990) the neutralizing source was distributed uniformly throughout both the fluid and the particles. Here, however, the source is only in the fluid phase V_f and contributes to the concentration at a point an amount proportional to $\int_{V_f} (\langle s \rangle / r) dV$, which can be rewritten as an integral over all space minus the value within the particles: $\int_{V_f} (\langle s \rangle / r) dV = \int_V (\langle s \rangle / r) dV - \sum_{\beta} \int_{V_{\beta}} (\langle s \rangle / r) dV$. Thus, the ‘charge’ of each particle β can be replaced with an effective charge $q_{\beta}^{eff} = q_{\beta} - V_{\beta} \langle s \rangle$, where V_{β} is the volume of particle β . One can now follow Bonnecaze & Brady, (1990) where it was shown that the concentration field at any point in the fluid (outside the particles) can be written without approximation as

$$\begin{aligned}
 c(\mathbf{r}) - \langle c \rangle &= \frac{a^2 \langle s \rangle}{2D_R} \\
 &+ \frac{1}{4\pi D_R} \sum_{\beta} \left(\frac{q_{\beta}^{eff}}{|\mathbf{r} - \mathbf{r}_{\beta}|} + \mathbf{S}_{\beta} \cdot \nabla_{\beta} \frac{1}{|\mathbf{r} - \mathbf{r}_{\beta}|} + \frac{1}{2} \mathbf{Q}_{\beta} : \nabla_{\beta} \nabla_{\beta} \frac{1}{|\mathbf{r} - \mathbf{r}_{\beta}|} + \dots \right) \\
 &- \frac{1}{4\pi D_R} \int_V \left(\frac{\langle s \rangle}{|\mathbf{r} - \mathbf{r}'|} + n \langle \mathbf{S} \rangle \cdot \nabla' \frac{1}{|\mathbf{r} - \mathbf{r}'|} + n \frac{1}{2} \langle \mathbf{Q} \rangle : \nabla' \nabla' \frac{1}{|\mathbf{r} - \mathbf{r}'|} \right) dV'.
 \end{aligned} \tag{6.20}$$

And, the condition of chemical neutrality relates the average effective charge to the uniform source:

$$n \langle q^{eff} \rangle = \langle s \rangle = n \langle q \rangle / (1 + \phi), \tag{6.21}$$

and particle β 's effective charge is

$$q_{\beta}^{eff} = q_{\beta} + \phi \langle q \rangle / (1 - \phi), \tag{6.22}$$

where n is the number density of particles and $\phi = 4\pi a^3 n/3$ their volume fraction (all particles have been taken to have the same volume).

Equation (6.20) is an absolutely convergent expression for the concentration field for any distribution – periodic or random – of reactive particles. A check on the correctness of this can be seen by ensemble averaging the concentration at \mathbf{r} over all possible realizations of the reactive particles β . The discrete sum $\sum_{\beta} q_{\beta}^{eff} \Rightarrow \int n \langle q^{eff} \rangle$ showing that the sum and the ‘backflow’ integral over $\langle s \rangle$ cancel, as do the dipole and quadrupole terms. Almost cancel that is, because the particles are excluded from being any closer to the field point \mathbf{r} than their radii a and thus there is a contribution from the uniform source in the excluded region from 0 to a : $-(1/4\pi D_R) \int_0^a \langle s \rangle / (|\mathbf{r} - \mathbf{r}'|) dV' = -a^2 \langle s \rangle / 2D_R$, which precisely cancels the constant source term in (6.20). (The dipole and quadrupole contributions from this excluded volume region are zero.)

We now use this convergent formulation for simulation with periodic boundary conditions. Both the particle positions and the concentration field are periodic, and we consider a periodic cubic cell defined by cell vectors $(\mathbf{a}_1, \mathbf{a}_2, \mathbf{a}_3)$ with N particles $(\mathbf{r}_1, \mathbf{r}_2, \dots, \mathbf{r}_N)$ in the primitive cell. The cell volume $V_0 = (\mathbf{a}_1 \times \mathbf{a}_2) \cdot \mathbf{a}_3 = a_1 a_2 a_3$. On the unit cell the Fourier expansion follows the convention:

$$\begin{aligned} f(\mathbf{x}) &= \sum_{\mathbf{k}} \hat{f}(\mathbf{k}) e^{-2\pi i \mathbf{k} \cdot \mathbf{x}}, \\ \hat{f}(\mathbf{k}) &= \frac{1}{V_0} \int_{\text{cell}} f(\mathbf{x}) e^{2\pi i \mathbf{k} \cdot \mathbf{x}} d\mathbf{x}. \end{aligned} \quad (6.23)$$

To calculate the periodic sum efficiently the Ewald summation technique is used (Toukmaji & Board, 1996; Darden *et al.*, 1993). For $\mathbf{r} \neq \mathbf{r}_{\beta}$, i.e., for any spatial point not on a particle position we write:

$$c(\mathbf{r}) = \langle c \rangle + c'_{real}(\mathbf{r}) + c'_{wave}(\mathbf{r}), \quad (6.24)$$

where

$$c'_{real}(\mathbf{r}) = \frac{1}{4\pi D_R} \sum_{\beta} q_{\beta}^{eff} \frac{\text{Erfc}(\sqrt{\pi/\zeta}|\mathbf{r} - \mathbf{r}_{\beta}|)}{|\mathbf{r} - \mathbf{r}_{\beta}|}, \quad (6.25)$$

$$c'_{wave}(\mathbf{r}) = \frac{1}{4\pi D_R V_0} \sum_{\mathbf{k} \neq 0} \sum_{\beta} q_{\beta}^{eff} e^{2\pi i \mathbf{k} \cdot \mathbf{r}_{\beta}} \frac{e^{-\zeta \pi k^2}}{\pi k^2} e^{-2\pi i \mathbf{k} \cdot \mathbf{r}}. \quad (6.26)$$

Here ζ is the splitting parameter that controls the rate of convergence of real- and wave-space sums; the optimal choice of ζ has been thoroughly discussed (Darden *et al.*, 1993). We have only written the ‘charge’ terms in (6.25)-(6.26) to illustrate the procedure. The dipole and quadrupole terms can be found in Appendix H or in Bonnecaze & Brady, (1990). Note that the removal of the $\mathbf{k} = 0$ term in the wave-space sum follows directly from the ‘backflow’ integral over the uniform source distribution $\langle s \rangle$ in (6.20).

Equations (6.25) and (6.26), when added together, give the solution $c(\mathbf{r})$ for any spatial point. From the definition of \mathcal{E} in (6.19) and the formulation of Faxen laws, we need the field that any particular particle responds to, *excluding* the contribution from the particle α itself, and the field is to be evaluated at the particle’s center \mathbf{r}_{α} . Thus, an additional ‘self correction’ must be added to the sum.

The necessity of a self term can also be appreciated by an analogy to the energy calculation in an electrostatic system. In that case, it is well known that the energy contribution from each charge q_i is $q_i \phi_{[i]}/2$, where $\phi_{[i]}$ is the electrostatic potential at the location of q_i excluding the contribution from the charge q_i itself. Therefore, the contribution from particle α must be removed from the Ewald sum. For example, relating q to c' the self term is $-q_{\alpha}^{eff}/2\pi D_R \sqrt{\zeta}$.

To complete the calculation, we need all the elements of the potential matrix \mathcal{E} :

$$\mathcal{E} = \begin{pmatrix} \mathbf{E}_{cq} & \mathbf{E}_{\nabla q} & \mathbf{E}_{\nabla\nabla q} \\ \mathbf{E}_{cS} & \mathbf{E}_{\nabla\nabla S} & \mathbf{E}_{\nabla\nabla S} \\ \mathbf{E}_{cQ} & \mathbf{E}_{\nabla\nabla Q} & \mathbf{E}_{\nabla\nabla Q} \end{pmatrix}. \quad (6.27)$$

Equation (6.25) and (6.26), with the self term $-q_\alpha^{eff}/2\pi D_R\sqrt{\zeta}$ gives the contribution E_{cq} . The other terms can be found in Appendix H.

Problem closure: iterative solver

Combining all particles' response to their environment via the Faxen laws (6.11) we can form a 'grand capacitance' matrix C :

$$\begin{pmatrix} \mathbf{q} \\ \mathbf{S} \\ \mathbf{Q} \end{pmatrix} = C \cdot \left[\begin{pmatrix} c^E \\ \nabla c^E \\ \nabla\nabla c^E \end{pmatrix} + \begin{pmatrix} c' \\ \nabla c' \\ \nabla\nabla c' \end{pmatrix} \right], \quad (6.28)$$

where C depends on the Damköhler number and, in the Janus case, the particle orientation vector ξ . Combining (6.28) with (6.19) we have:

$$(\mathbf{I} - C \cdot \mathcal{E}) \cdot \begin{pmatrix} \mathbf{q} \\ \mathbf{S} \\ \mathbf{Q} \end{pmatrix} = C \cdot \begin{pmatrix} c^E \\ \nabla c^E \\ \nabla\nabla c^E \end{pmatrix}. \quad (6.29)$$

For a given configuration of particles, C and \mathcal{E} are known, as is the 'imposed' concentration field c^E .

A standard GMRES (Generalized minimal residual method) iterative solver can be applied to solve for the unknown multipole moments \mathbf{q} , \mathbf{S} and \mathbf{Q} . In GMRES, the linear system $\mathbf{A}\mathbf{x} = \mathbf{b}$ is solved in such a way that \mathbf{A} appears only as an operator; the operator returns a new vector $\mathbf{A}\mathbf{x}$ for any given vector \mathbf{x} . Such an operator nature allows us to employ iteration without explicitly building the matrix \mathbf{A} . Here, $\mathbf{A} = (\mathbf{I} - C \cdot \mathcal{E})$, $\mathbf{x} = (\mathbf{q}, \mathbf{S}, \mathbf{Q})$, and $\mathbf{b} = C \cdot (c^E, \nabla c^E, \nabla\nabla c^E)$.

After the iterative solver converges, the solution vector $(\mathbf{q}, \mathbf{S}, \mathbf{Q})$ for each particle is known and, from the single particle capacitance matrices C and mobility matrices M_B , the osmotic driving force on each particle is:

$$\mathbf{F}_\beta^{osmo} = -k_B T L(\Delta) M_B \cdot C^{-1} \cdot \begin{pmatrix} q_\beta \\ \mathbf{S}_\beta \\ \mathbf{Q}_\beta \end{pmatrix}. \quad (6.30)$$

Computational cost for computing \mathbf{F}_β^{osmo} is negligible compared with that for computing the moments. The inversion of \mathbf{C} requires $O(11^3)$ (or only 4^3 at the dipole level), and thus computing \mathbf{F}^{osmo} requires $N \times O(11^3)$ operations, not $O((11N)^3)$ operations.

Matrix-free implementation

Computationally, \mathbf{C} is diagonal for homogeneously reactive particles and block diagonal in the Janus case, and only requires $O(N)$ operations. However, \mathcal{E} is dense because of the long-range nature of Laplace's equation. Explicit construction and storage of the matrix \mathcal{E} requires a large amount of memory and slow operations ($O(N^2)$ matrix-vector multiplication). Therefore, the key step to achieving an efficient solver is to eliminate the explicit large matrix operations. Below we briefly describe the implementation utilizing the matrix-free operator nature of a GMRES solver.

For a finite number of particles with an imposed concentration field the strategy is straightforward: $(c'(\mathbf{r}_\alpha), \nabla c'(\mathbf{r}_\alpha), \nabla \nabla c'(\mathbf{r}_\alpha))$ for each particle α in (6.19) is directly summed with the tile algorithm used in the self-gravitating N -body problem utilizing GPU shared memory (Nguyen, 2007). Compared to explicitly building and storing the matrix \mathbf{C} with the CPU (3.1GHz 2nd-gen Intel Core i), the GPU (nVidia GTX 580 & GTX 680, Fermi & Kepler architecture) method used here is able to achieve an increased speed by a factor of 100 and uses about 1% of memory.

For the periodic case of equation (6.19), which includes Ewald summation, the calculations are done on the GPU via the Particle Mesh Ewald (PME hereafter) method (Darden *et al.*, 1993). Successful PME relies on the choice of the splitting parameter ζ such that the real-space sum is convergent within several neighboring particles' contributions. Thus, the real-space sum is reduced from a dense matrix-vector multiplication to a sparse one. GPU performs well in such situations.

The wave-space sum is efficiently calculated with Fast Fourier Transforms (FFT) in

PME (Deserno & Holm, 1998). For future compatibility to include hydrodynamics, we follow the PME convention of the Accelerated Stokesian Dynamics (Sierou & Brady, 2001), which uses $5 \times 5 \times 5$ mesh and $5 \times 5 \times 5$ Lagrangian interpolation for each particle by ensuring for each particle β :

$$\sum_m q_m e^{2\pi i \mathbf{k} \cdot (\mathbf{r}_m - \mathbf{r})} = q_\beta^{eff} e^{2\pi i \mathbf{k} \cdot (\mathbf{r}_\beta - \mathbf{r})}, \quad (6.31)$$

$$\sum_m q_m e^{2\pi i \mathbf{k} \cdot (\mathbf{r}_m - \mathbf{r})} = 2\pi i \mathbf{S}_\beta \cdot \mathbf{k} e^{2\pi i \mathbf{k} \cdot (\mathbf{r}_\beta - \mathbf{r})}, \quad (6.32)$$

$$\sum_m q_m e^{2\pi i \mathbf{k} \cdot (\mathbf{r}_m - \mathbf{r})} = -2\pi^2 \mathbf{Q}_\beta : \mathbf{k} \mathbf{k} e^{2\pi i \mathbf{k} \cdot (\mathbf{r}_\beta - \mathbf{r})}, \quad (6.33)$$

where m refers to point charges on the mesh points. The full Ewald sum given in (H.2), including all q_β^{eff} , \mathbf{S}_β , \mathbf{Q}_β and \mathbf{r}_β terms, is now equal to and can be replaced by a sum of q_m terms on a regular mesh filling the entire periodic simulation box:

$$c'_{wave}(\mathbf{r}) = \frac{1}{4\pi D_R V_0} \sum_{\mathbf{k} \neq 0} \sum_m q_m e^{2\pi i \mathbf{k} \cdot \mathbf{r}_m} \frac{e^{-\zeta \pi k^2}}{\pi k^2} e^{-2\pi i \mathbf{k} \cdot \mathbf{r}}, \quad (6.34)$$

which can be efficiently summed by 3D-FFT with $O(M \log M)$ operations for M mesh points. The $\nabla c'_{wave}(\mathbf{r})$ and $\nabla \nabla c'_{wave}(\mathbf{r})$ terms can be written in the same fashion with an extra $2\pi \mathbf{k}$ factor, and can also be calculated by 3D-FFT. GPU is also used to achieve better performance.

6.4 Results

We demonstrate the methodology and the physics of chemically active particles by two studies. In the first study we give a thorough discussion of the screening that occurs in Laplace problems. Three separate cases are considered: 1) Debye screening of a charged particle in an electrically neutral system, 2) Debye screening in a one component plasma (OCP) in which rapidly moving electrons screen the interactions between the slowly moving positive ions, and 3) systems in which the ‘charge’ on a particle is proportional to the local potential, which results in so-called Brinkman screening. This last case is relevant for chemically active particles.

The second study applies the methodology to systems of chemically interacting phoretic particles where the system's evolution is tracked by simulations, as formulated in the methodology section. In this study we show the onset of instability in a periodic domain when the phoretic velocity of particles is high and show that self-phoresis, as occurs for Janus particles, is necessary ingredient to have a stable distribution. We also study a finite 2D system in which active Janus particles are confined to a monolayer and constrained to lie within a circle of large radius. In this case we show how the distribution of particles can be predicted analytically via a coupled set of continuum-scale conservation equations for the suspensions stress, particle flux and reactant concentration.

Screening in Laplace systems

Screening occurs in Laplace problems when the long-ranged $1/r$ interactions change over to an exponentially screened interaction $e^{-r/L_B}/r$, where the screening length L_B depends on the number density (or concentration) of 'charged' particles. This only occurs in an 'infinite' system; a finite number of charged particles does not (formally) exhibit screening. We first discuss the familiar Debye screening.

There are a number of ways to derive the Debye screening and the approach we take here allows us to discuss all three screening cases from the same perspective and so highlights their similarities and differences. We start from Hinch's averaged-equation method (Hinch, 1977) to describe a dilute electrostatic system consisting of point charges q_α and a uniformly distributed charge density ρ (which is equivalent to $\langle s \rangle$). The ensemble average of any quantity is computed by multiplying by the N -particle configurational probability distribution function $P_N(\mathbf{X}_N)$ and integrating over particle positions \mathbf{X}_N . For a dilute system only the two-body conditional distribution function $P_{\beta|\alpha}$ is required, which gives the probability density for finding particle β relative to α (averaged over all possible configurations for the $N - 2$ other particles). Particle α can be considered as fixed in space because only the relative

configuration is relevant for a statistically homogeneous system. The ensemble averaged Laplace's equation becomes:

$$\lambda \nabla^2 \langle \varphi \rangle_\alpha(\mathbf{r}) = P_{\beta|\alpha}(\mathbf{r}_\beta - \mathbf{r}_\alpha) \langle q_\beta \rangle_\alpha + \langle \rho \rangle, \quad (6.35)$$

where λ stands for the permittivity ϵ for an electrostatic system and the solute diffusivity D_R for a reactive system, and φ denotes the electrostatic potential or the solute concentration. Finally, $\langle \cdot \rangle_\alpha$ denotes the conditional average with the α -particle fixed at \mathbf{r}_α . Equation (6.35) applies outside the particle α .

Debye screening

Debye screening applies to a neutral electrolyte in which there are as many positive as negative charges and therefore $\langle \rho \rangle \equiv 0$. Furthermore, the particle charges are fixed, which for simplicity, we take to be $\pm q$. In (6.35) we must distinguish separately the probability density for finding positive and negative charges outside the particle α (which itself could be either \pm) and thus (6.35) becomes

$$\lambda \nabla^2 \langle \varphi \rangle_\alpha(\mathbf{r}) = [P_{+|\alpha}(\mathbf{r}_\beta - \mathbf{r}_\alpha) - P_{-|\alpha}(\mathbf{r}_\beta - \mathbf{r}_\alpha)] q. \quad (6.36)$$

The charged particles move freely and their distribution is governed by the competition between the electrostatic energy and the thermal energy $k_B T$. At equilibrium the Boltzmann distribution holds with $P_{+|\alpha} \sim n_+ e^{-q\langle \varphi \rangle_\alpha / k_B T}$ and $P_{-|\alpha} \sim n_- e^{+q\langle \varphi \rangle_\alpha / k_B T}$, with $n_+ = n_- = n$. Thus, the RHS of (6.36) becomes

$$[P_{+|\alpha}(\mathbf{r}_\beta - \mathbf{r}_\alpha) - P_{-|\alpha}(\mathbf{r}_\beta - \mathbf{r}_\alpha)] q \quad (6.37)$$

$$= nq [e^{-q\langle \varphi \rangle_\alpha / k_B T} - e^{+q\langle \varphi \rangle_\alpha / k_B T}]$$

$$= -2nq \sinh(q\langle \varphi \rangle_\alpha / k_B T), \quad (6.38)$$

which for small potentials gives,

$$\nabla^2 \langle \varphi \rangle_\alpha(\mathbf{r}) + \langle \varphi \rangle_\alpha / L_D^2 = 0, \quad (6.39)$$

with Debye screening length $L_D = (2nq^2 / \epsilon k_B T)^{-1/2}$. The potential now behaves as $e^{-r/L_D} / r$ outside the particle α .

One Component Plasma (OCP)

A one component plasma typically consists of positive ions surrounded by an equal number of negative electrons. While the system is overall electrically neutral, the electrons move much more quickly than the positive ions and they form a background sea of uniform negative charge. The interest then is in the interaction between the positive ions and how their interaction is modified by the negative background. Equation (6.35) applies to this case, where now all particles α , β , etc. are the positively charged ions and the average charge density $\langle\rho\rangle = -n\langle q\rangle$ corresponds to the uniform sea of negative charge. Again, the ions are distributed according to the Boltzmann distribution and thus (6.35) becomes

$$\lambda\nabla^2\langle\varphi\rangle_\alpha(\mathbf{r}) = nq [e^{-q\langle\varphi\rangle_\alpha/k_B T} - 1], \quad (6.40)$$

where for simplicity we have taken all ions to have the same charge. For small potentials we have again Debye screening with the same screening length as we did for the neutral system.

In both of these systems, electrically neutral and the OCP, the screening is of a dynamic origin – the particles are Boltzmann distributed in response to the conditionally averaged potential. In the case of chemically active particles, a similar screening takes place, but it is static in origin and due to the fact that the ‘charge’ of a reactive particle depends on the concentration field in which it finds itself.

Chemically active particles – Brinkman screening

The screening that takes place for chemically active particles will have the same exponential form as for Debye screening, but its origin is different. First, the screening is present even though the reactive particles can be uniformly distributed in space with a constant number density $P_{\beta|\alpha} = n$. For Debye screening it was essential that the probability for finding a second particle was given by the Boltzmann distribution with an energy that was proportional to the conditionally averaged

potential $P_{\beta|\alpha} \sim e^{-\langle\varphi\rangle_\alpha/k_B T}$. For chemically active particles the screening arises because the reaction rate $\langle r_\beta \rangle_\alpha$ (equivalent to the charge) is proportional to the local concentration. This screening is due to Brinkman who first showed the analogous screening for fluid flow through a dilute fixed bed of particles (Brinkman, 1949).

Brinkman screening in reactive systems has been discussed in detail by Morris & Brady, (1995). Here we briefly show how this comes about. We first rewrite (6.35) in terms of the concentration and reaction rate rather than potential and charge:

$$D_R \nabla^2 \langle c \rangle_\alpha(\mathbf{r}) = P_{\beta|\alpha}(\mathbf{r}_\beta - \mathbf{r}_\alpha) \langle r_\beta \rangle_\alpha - \langle s \rangle. \quad (6.41)$$

If we average (6.41) over all positions of particle α , we have the unconditionally averaged equation – no particles fixed – for the average concentration field $\langle c \rangle$. Since $\nabla^2 \langle c \rangle = 0$ in the statistically homogeneous suspension, the average of (6.41) shows that $n \langle r_\beta \rangle = \langle s \rangle$ – the average reaction rate is equal to the uniform average source of reactant. When particle β is far from particle α in (6.41) the conditionally averaged reaction rate must approach the bulk value, $\langle r_\beta \rangle_\alpha \rightarrow \langle r_\beta \rangle$, and thus the RHS forcing in (6.41) is $n(\langle r_\beta \rangle_\alpha - \langle r_\beta \rangle)$, for a uniform distribution of particles β . For a first order surface chemical reaction (c.f. (6.5)) the reaction rate is proportional to the concentration, and thus to leading order in the number density of reactant particles (6.41) can be written as

$$D_R \nabla^2 \langle c \rangle_\alpha(\mathbf{r}) = -n a^2 \kappa_0 (\langle c \rangle_\alpha(\mathbf{r}) - \langle c \rangle). \quad (6.42)$$

The disturbance concentration $c' = \langle c \rangle_\alpha - \langle c \rangle$ is the relevant quantity and is screened: $c' \sim e^{-r/L_B}/r$, where, as is the case for Debye screening, the Brinkman screening length is proportional to $n^{-1/2}$. Specifically, for uniformly reactive sink particles

$$L_B^S/a = \sqrt{\frac{1 + \text{Da}}{3\phi \text{Da}}}, \quad (6.43)$$

where the Damköhler number $\text{Da} = \kappa_0 a / D_R$. For half reactive Janus particles

$$L_B^J/a = \sqrt{\frac{4\pi}{-3\phi f_c^q}}, \quad (6.44)$$

where f_c^q is the response function given in Appendix G. Here, $\phi = 4\pi a^3 n/3$ is the volume fraction of reactant particles. A more complete derivation of L_B , with corrections for higher volume fractions and including many-body effects, can be found in Morris & Brady, (1995).

In the simulation method described in this work we solve for the concentration field by summing all the long-ranged multipole interactions among particles. Therefore, that we recover Brinkman screening is a validation that our simulation method works properly. To test this, we generate a random but homogeneous configuration of N particles $(\mathbf{r}_1, \mathbf{r}_2, \dots, \mathbf{r}_N)$ in a periodic box, and solve for the particle multipoles with their positions fixed. Then one particle, denoted as particle 0, is randomly chosen and removed from the system, while the other particles are held fixed in space at their original positions. For the $N - 1$ particles remaining after removal, their multipoles $(q_\beta, \mathbf{S}_\beta, \dots)$ change. There is less competition for the reactant, and hence the particle reactivity is higher: $q_{i,\text{after}} < q_{i,\text{before}} < 0$. We calculate the change in monopole strength $\Delta q_i = q_{i,\text{before}} - q_{i,\text{after}}$ of each (not removed) particle i and plot this against the distance of particle i from the removed particle 0. In the case of Janus particles, the orientation of each particle is randomly chosen and also fixed before and after removal.

When a particle is removed, the other particles feel the screened disturbance. According to Faxen laws (6.12) & (6.15), and screening lengths (6.43) & (6.44), q_i changes according to:

$$\text{For Sink: } \Delta q_i = -\frac{\text{Da}}{1 + \text{Da}} q_0 e^{-r_{0,i}/L_B^S} / r_{0,i}, \quad (6.45)$$

$$\text{For Janus: } \Delta q_i = \frac{f_c^q}{4\pi} q_0 e^{-r_{0,i}/L_B^J} / r_{0,i}, \quad (6.46)$$

where $r_{0,i}$ is the distance between particles i and 0. The results are presented in Fig. 6.2 and clearly show Brinkman screening. Outside the Brinkman screening length the particle monopole strength q_i hardly changes no matter whether particle 0 is in the system or not.

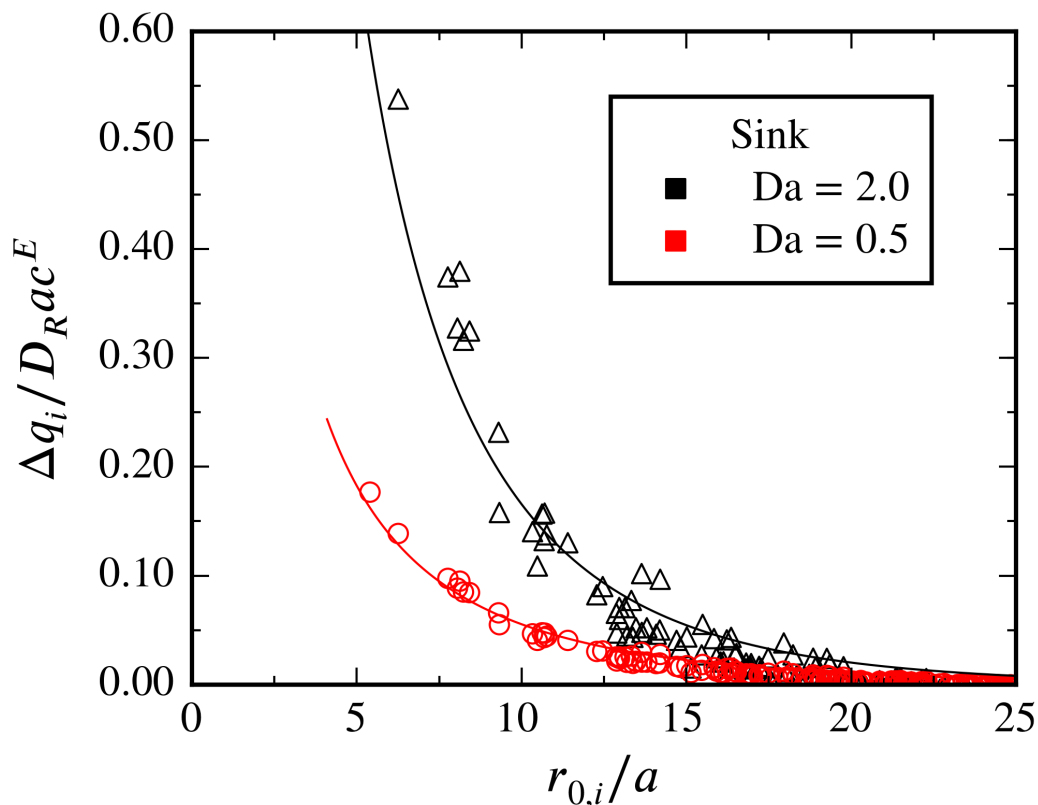


Figure 6.2: Change of particle reactivity Δq_i in the vicinity of the removed test sink particle. Markers are simulation data and solid lines are the theoretical predictions for Brinkman screening (6.45). Simulation data are from a single configuration with $N = 625$, $\phi = 0.01$ (cubic periodic box = $64 \times 64 \times 64 a^3$). Particles are randomly distributed.

Our method thus resolves Brinkman screening properly, but before we proceed to the results for dynamic systems it must be remarked that Brinkman screening arises only *after* the many-body concentration field $c(\mathbf{r})$ is computed properly. This means that one cannot simply prescribe a Yukawa-type interaction potential, $e^{-\alpha r}/r$, between the reactive particles and bypass the solution for the concentration field. By contrast, in an electrostatic system pairwise Yukawa potentials can sometimes be applied when the counter-ions are much smaller and more mobile than the macro-ions, because under these conditions the fast counter-ions are subject to the Boltzmann distribution and are ‘dragged’ along by the macro-ions to screen the electrostatic field between them. Therefore, the electrostatic system can be modeled

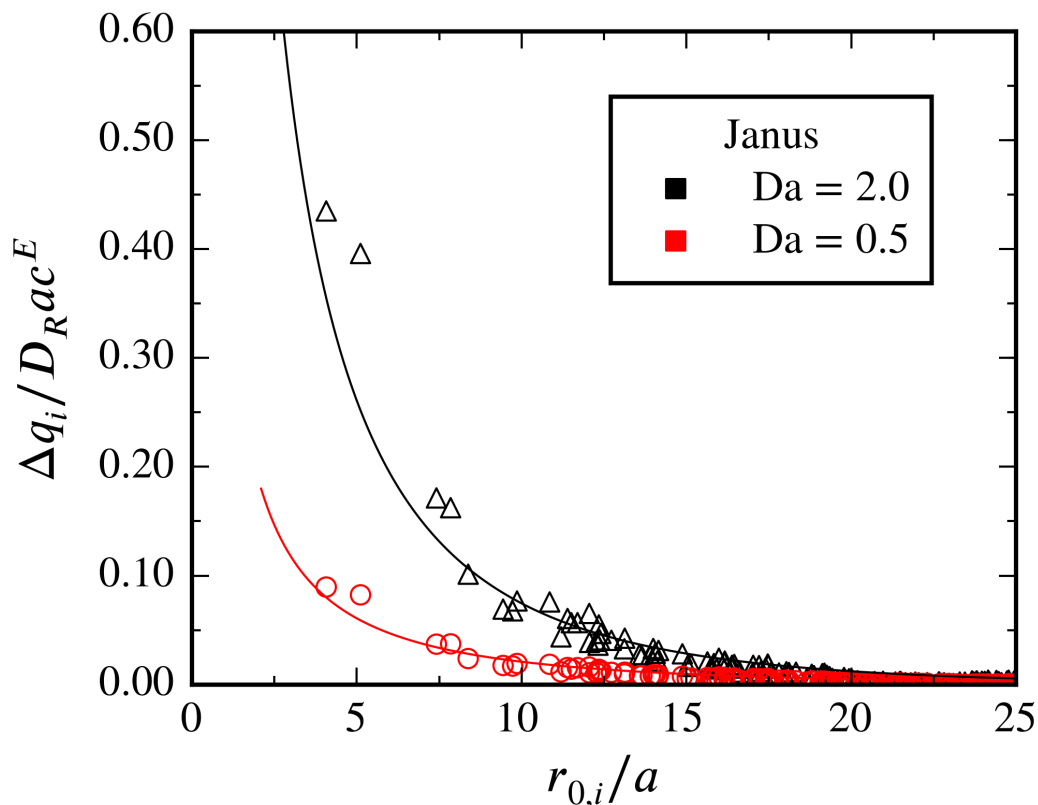


Figure 6.3: Change of particle reactivity Δq_i in the vicinity of the removed test Janus particle. Markers are simulation data and solid lines are the theoretical predictions for Brinkman screening (6.45). Simulation data are from a single configuration with $N = 625$, $\phi = 0.01$ (cubic periodic box = $64 \times 64 \times 64 a^3$). Particles are randomly distributed.

as consisting of only macro-ions with pairwise Yukawa potentials to simplify the calculation of macro-ion motion. This is not possible for for chemically active particles.

Moreover, a dynamic diffusiophoretic system is even more difficult to probe from the one-particle fixed average equation (6.35) point of view. In a dynamic system, not only is q_α (or q_β) changing, but also the distribution $P_{\beta|\alpha}$ is altered by both diffusiophoresis and by Brownian motion (6.6). Although Brownian motion is thermal and by itself obeys the $k_B T$ Boltzmann statistics, the Boltzmann distribution does not apply in general for $P_{\beta|\alpha}$. There is no Hamiltonian or interaction energy

for the the diffusiophoretic problem.

Dynamic evolution of reactive particles

We first discuss the scalings for the diffusiophoretic system to introduce the important nondimensional parameters and the physically realistic parameter space to be explored. We choose the particle radius a as the length scale and the particle translational diffusion time a^2/D as the time scale, where $D = k_B T / 6\pi\eta a$ is the reactive particle's translational diffusivity from the Stokes-Einstein-Sutherland relation. (Not to be confused with the solute reactant diffusivity $D_R \gg D$.) Reactant concentration (expressed as number density) is scaled by c^E , the externally imposed concentration: $c^E = c^\infty$ for the finite case and $c^E = \langle c \rangle$ for the periodic case, respectively. With these chosen scalings the non-dimensional variables follow: particle velocity, $\hat{U} = Ua/D$; concentration, $\hat{c} = c/c^E$; and multipoles: $\hat{q} = q/D_R a c^E$, $\hat{S} = S/D_R a^2 c^E$, and $\hat{Q} = Q/D_R a^3 c^E$. The nondimensional particle velocity due to the osmotic force from equation (6.1) then becomes

$$\hat{U} = -S_D \int_{\hat{S}} \hat{c} \mathbf{n} d\hat{S}, \quad (6.47)$$

where

$$S_D = (1 - \theta D_R / D_P) L(\Delta) c^E a^3, \quad (6.48)$$

which is the ratio of the speed due to phoresis, $U \sim L(\Delta) k_B T c^E a^2 / 6\pi\eta a$, to the characteristic velocity due to Brownian motion, $U^B \sim D/a = k_B T / 6\pi\eta a^2$. We shall refer to S_D as the 'fuel strength.' Recall that $(1 - \theta D_R / D_P)$ is the scaling factor for the reaction $R \rightarrow \theta P$, while $L(\Delta)$ measures hydrodynamic flow in the region of size $\Delta = \delta/a$ adjacent to the particle where the solute-particle interaction is operative. The imposed concentration c^E is taken to be constant in time. Thus, for a given concentration level, stoichiometry and interactive length, S_D is prescribed and fixed. The concentration field \hat{c} is also dependent on the Damköhler number, $\text{Da} = \kappa_0 a / D_R$, which thus indirectly affects a reactant particle's velocity.

The particle displacement from (6.6) in each timestep is:

$$\begin{aligned}\Delta\hat{\mathbf{X}} &= \hat{\mathbf{U}}\Delta\hat{t} + \Delta\hat{\mathbf{X}}^B + \Delta\hat{\mathbf{X}}^{HS} \\ &= -S_D\hat{\mathbf{B}}\Delta\hat{t} + \Delta\hat{\mathbf{X}}^B + \Delta\hat{\mathbf{X}}^{HS},\end{aligned}\tag{6.49}$$

where $\hat{\mathbf{B}}_\alpha = \mathbf{B}_\alpha/a^2c^E$ from (6.16).

As discussed in Section 6.2, for repulsive source particles $(1 - \theta D_R/D_P) < 0$, while for attractive chemical sinks $(1 - \theta D_R/D_P) > 0$. Therefore according to the definition of S_D in (6.48), for $S_D > 0$ we simulate the motion of attractive chemical sinks, while $S_D < 0$ corresponds to repulsive sources. If $S_D = 0$, there is no reaction-induced motion and the system degenerates to Brownian hard spheres as seen from (6.49).

In experiments the particles are typically micron-sized and $(1 - \theta D_R/D_P) \sim O(1)$. In this work we consider the limit where solute or reactants are much smaller than the phoretic particles. For instance, in the experiments of Theurkauff *et al.*, (2012), the solutes are hydrogen peroxide and oxygen molecules, both of which are at the nano-scale. In this limit $L(\Delta)a^3 \sim \delta^2a$, where $\delta \sim O(10^{-9}m)$. Therefore $S_D \sim L(\Delta)a^3c^E \sim O(0.1)$ for $c^E \sim 1mMol/L \sim 10^{23}/m^3$, and $S_D \sim O(100)$ for $c^E \sim 1Mol/L$. We shall focus on the fuel strength range, $0.1 < S_D < 10$, which appears to be sufficient to cover the important system behavior.

For negative $S_D < 0$, the diffusiophoretic particles repel each other and, when the repulsion is strong enough, a crystalline structure may form. Such diffusiophoretic repulsive ‘crystals’ have been observed by Derjaguin & Golovanov, (1984). From the ensemble average equation perspective of (6.35), when repulsion is strong $P_{\beta|\alpha}$ is ‘frozen’ to a fixed point and q_α (and q_β) also approach constants. Therefore, the system becomes similar to an OCP. A detailed discussion of the crystallization behavior for repulsive diffusiophoretic particles will be reported elsewhere.

In an atomic or molecular system with short-range attractive interaction potentials, a gas-liquid phase transition can occur. For Active Brownian Particles (ABPs) a

gas-liquid phase transition can also occur even though the interactions are repulsive (hard-sphere collisions). Each ABP propels itself at a given velocity $U_0\xi$, and the direction ξ is subject to rotational Brownian motion. The translational random walk that results from the rotational Brownian motion generates a unique swim pressure (Takatori *et al.*, 2014), analogous to the osmotic pressure of Brownian solutes. However, unlike the osmotic pressure, the swim pressure is a decreasing function of the active particle concentration, which can destabilize the system. Even though the ABPs are intrinsically non-equilibrium, a ‘thermodynamic’ (Takatori & Brady, 2015) description is possible with the active pressure providing an equation of state.

However, in chemically active particle systems the long-range and non-pairwise additive nature of the phoretic interactions calls into question the notion of a ‘phase.’ We show below that in certain situations the dilute region outside a dense cluster has an inhomogeneous active particle concentration. Thus, ‘thermodynamic-like’ approaches may not be appropriate. Instead, a mechanical approach based on the swim pressure (Takatori *et al.*, 2014) and the swim force (Yan & Brady, 2015a) is shown to apply and to enable predictions of the distribution of active particles in both the dense and dilute regions.

In the following two sections we discuss the system dynamics via a particle-tracking simulation that solves the concentration field $c(\mathbf{r}; \mathbf{X}_N(t))$ at each and every time step and evolves the particle positions according to (6.49).

Attractive sink particles: periodic system

Attractive (non Janus) sink particles show very interesting dynamics. In the limit of $S_D \rightarrow 0$, the system reduces to passive Brownian particles, and remains a random but statistically homogeneous distribution of particles until the freezing density ($\phi \approx 0.5$). At the other extreme of high S_D , the fuel concentration is high and particle-particle attractions are strong and clusters form. In this section we focus

on the range of S_D where the long-time or steady-state structure transitions from homogeneous to clustering.

All simulations start from a random configuration of 2503 particles in a cubic unit cell of $64 \times 64 \times 64 a^3$ with periodic boundary conditions. Results will be presented for a single volume fraction, $\phi = 0.04$, and a single Damköhler number, $Da = 2.0$, but for S_D ranging from 0.3 to 6.0. The multipole moment expansion is truncated at the dipole level. For analysis purposes the particle reactivity q is compared to the isolated single particle reactivity from (6.12): $q_0 = -4\pi D_{RAC}^E Da / (1 + Da)$. The ‘reactivity’ ratio, q/q_0 , shows the effect of particle clustering as a particle in the center of a cluster must compete with its neighbors for the reactant and its reactivity decreases. The clustering behavior is also analyzed by defining a local volume fraction, ϕ_p , which is the ratio of particle volume $4\pi a^3/3$ to the Voronoi cell volume V_{voro} formed by the particle with its surrounding neighbors.

Fig. 6.4 shows the average reactivity $\langle q \rangle / q_0$ as the system evolves in time. At $S_D = 0.3$, the average reactivity $\langle q \rangle / q_0$ is unchanged, showing only small fluctuations. Particles remain randomly distributed, and a snapshot at steady state (A) shows that each particle has almost the same reactivity q . The statistics of ϕ_p in Fig. 6.5 show a narrow distribution around the imposed global volume fraction $\phi = 0.04$. Here $\langle q \rangle / q_0 > 1$ because the average reactivity is increased by many-body effects as ϕ increases for a homogeneous infinite suspension. The dependence $\langle q \rangle \sim \phi$ is discussed in Bonneau & Brady, (1991a).

When S_D is increased to 0.9 clusters form. The reactivity $\langle q \rangle / q_0$ gradually decays and almost reaches a steady state by $t = 300a^2/D$. The simulation was continued to $t = 700a^2/D$ to ensure that the system did reach a steady state. As seen in Fig. 6.4, local fluctuations in volume fraction first form (B1), and the cluster continues to grow until limited by reaction and the size of the periodic unit cell. At steady state (B2) all particles in the box form a single cluster. The particle reactivity is very

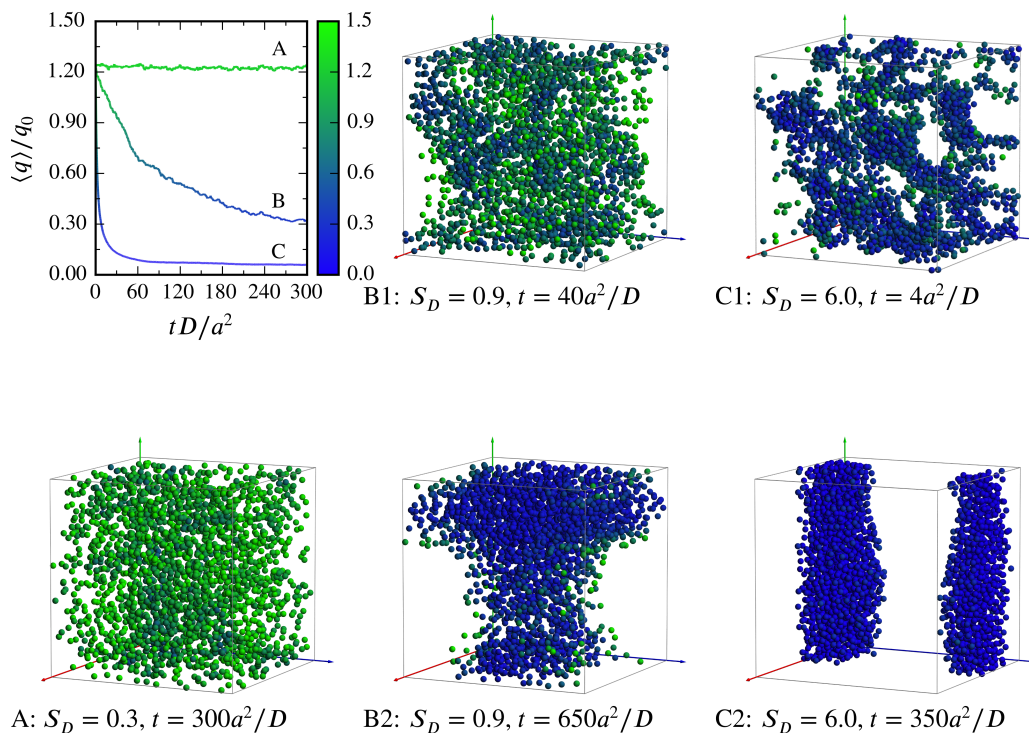


Figure 6.4: Reactivity $\langle q \rangle / q_0$ of the sink system for different values of the fuel strength: (A) $S_D = 0.3$, (B) $S_D = 0.9$, and (C) $S_D = 6.0$ for $\phi = 0.04$, and $Da = 2.0$. There are $N = 2503$ particles in the cubic periodic unit cell. All cases start from a randomly distributed particle configuration. Particles are colored by reactivity $\langle q \rangle / q_0$. (A) is a system snapshot at steady state. (B1) and (C1) are snapshots in transient states and (B2) & (C2) are at the steady states, respectively.

low inside the cluster, although the ϕ_p measurement in Fig. 6.5 shows that the local density is not high, $\phi_p \approx 0.08$. Only a few particles near the cluster surface (the green ones) maintain a significant reactivity near q_0 .

When S_D is increased further to 6.0, the system evolves very quickly. In a very short time, $t \approx 4a^2/D$, a transient gel-like structure (C1) forms, and the average reactivity $\langle q \rangle / q_0$ reaches a very low level. Such a short evolution time means that the particles' diffusive motion, which is on the time scale a^2/D , has almost no effect on the initial evolving transient structure. The clustering process continues and reaches a steady state at about $t = 100a^2/D$. At steady state ($t = 300a^2/D$, C2), all particles collapse

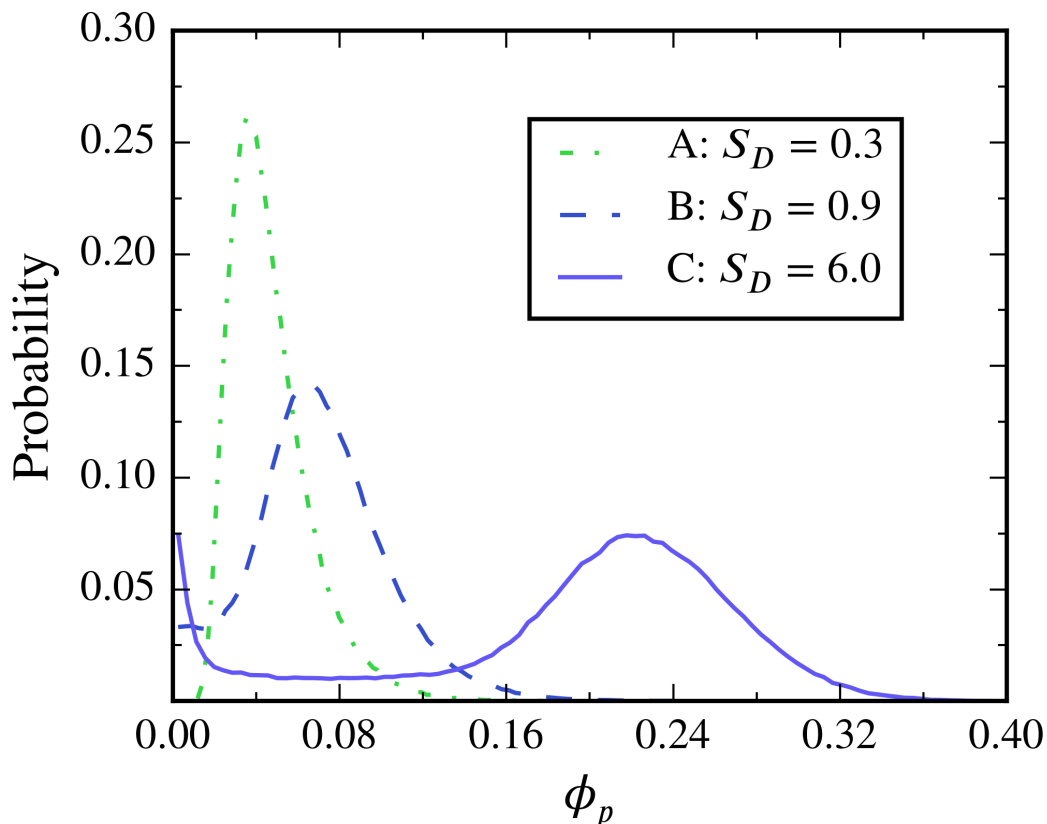


Figure 6.5: Probability distribution of local particle volume fraction ϕ_p at the steady state. Here $\phi = 0.04$, $Da = 2.0$, $N = 2503$ and the periodic box = $64 \times 64 \times 64a^3$. The steady state configurations are A, B2 and C2 in Fig. 6.4.

into a single cluster; there is no coexistence phenomena – no dilute single particles. The statistics of ϕ_p show that the local volume fraction is around 0.2, still very far from the close packing limit where $\phi > 0.5$. It is important to note that the peak close to $\phi_p = 0$ corresponds to those particles on the cluster surface, rather than a dilute phase, as is clear from C2 in Fig. 6.4.

Such a field-driven clustering behavior is quite different from that which occurs in a pairwise short-ranged system, e.g., Lennard-Jones particles. In a Lennard-Jones system (Santos *et al.*, 2010; Lodge & Heyes, 1998), the potential is fixed so that once a cluster starts to form, the clustering process continues until the particle-particle separation reaches the repulsive range of the pairwise potential. In a reactive sink system, however, the attraction, which is due to the reactivity, is neither prescribed

nor fixed but is a solution to the many-particle Laplace equation. Hence, when clusters start to form particles get close to each other and, for not too small Da (fast reaction), the reactant concentration can be locally depleted in a cluster and an individual particle's reactivity can become small, $q_\alpha \sim 0$. Sink particles thus lose their attraction and the clustering process stops, leaving a loosely packed structure. Due to this depletion effect for diffusion-limited (high Da) particles, at intermediate S_D the system may lose its stability and collapse into a cluster, but the cluster is loosely packed because the translational Brownian motion tends to drive the system towards a homogeneous state. The steady structure is always a balance between the translational Brownian motion and the attraction. The higher S_D , the denser the cluster. Recall that S_D measures the fuel strength and is proportional to the reactant concentration $\langle c \rangle$.

The system behavior is quite different from a classical first order gas-liquid phase transition where a dense phase coexists with a dilute phase. In the sink system no coexistence was observed for all cases studied, which were in the range $0.1 < Da < 10$, $\phi < 10\%$ and $S_D < 10$.

Compared to the experiments of Theurkauff *et al.*, (2012) which seem to show phase separation and coexistence, the key difference is that reactive sink particles cannot propel themselves; their motion is due to diffusiophoresis in the concentration gradient of the other particles. We repeated the simulation for Janus particles that undergo self-diffusiophoresis in 3D periodic systems and confirmed that self-propulsion is the vital component for coexistence of chemically active suspensions. However, the 3D simulation is expensive due to the summation of all the long-ranged contributions in the algorithm, and our largest simulations are limited to a box of $128 \times 128 \times 128 a^3$ with about 8000 Janus particles. This is sufficient for qualitative observations but not to carry out a detailed study. Therefore, we shall discuss the steady state structure of Janus particles in a monolayer geometry in the next section. In a monolayer, we can easily extend the system to $512 \times 512 a^2$ and generate reliable

statistics.

Our findings for reactive (non Janus) sink systems suggest that there is a threshold S_D^* , below which the system is stable, while for $S_D > S_D^*$ the system is unstable and collapses into a cluster, which eventually extends to encompass all particles. Linear stability analysis of a similar system can be found in Karpov & Oxtoby, (1997), where they analyzed a system of ‘growing and decaying’ particles and predicted the existence of a threshold. In a more recent work Saha *et al.*, (2014) gave a linear stability analysis of chemically active particles with self-propulsion, phoretic response and chemotaxis based on a Smoluchowski mean-field description, and predicted that an instability threshold exists, which depends on the fuel concentration $\langle c \rangle$, the self-propulsion, Brownian motion, and the attraction due to diffusiophoresis. These predictions have not yet been verified by simulation or experiment. The simulation algorithm presented in this work would allow one to extract the detailed information of the clustering process in various geometries and test the theoretical predictions.

We have also completed a detailed theoretical analysis and found that an instability does exist as predicted in the literature, but the threshold S_D^* is independent of self-propulsion – the instability growth rate becomes positive when attraction overcomes translational Brownian diffusivity, which differs from the prediction by (Saha *et al.*, 2014). In our theory self-propulsion quantitatively reduces the growth rate but has no impact on the threshold, because its effects appear at a higher order in wave number than the competition between diffusiophoretic attraction and Brownian diffusion. We also show that, by properly accounting for the flux of active particles in the presence of the solute concentration gradient (Takatori & Brady, 2015), a simple coarse-grained continuum mechanics theory predicts the instability very well. Our theory is verified by simulations conducted with the method described in this chapter and will be presented in a future work.

Attractive Janus particles: a finite system

In this section we study a second case of Janus particles that both self-propel and attract each other via diffusiophoretic interactions. Similar to the monolayer experiments of Theurkauff *et al.*, (2012) we simulate a finite number of particles confined in a monolayer in 3D space surrounded by a porous circular wall. The porous wall does not allow the Janus particles to escape (hard-sphere collision with the wall), but it has no effect on the reactant concentration field. The simulations are truncated at the dipole level. Further, the Brownian reorientation is assumed to be a 2D in-plane rotation; there is no motion out of the plane.

A snapshot from the steady-state distribution for a system with $N = 2048$, $S_D = 30$, $Da = 5$, $R_{wall} = 128a$ is shown in Fig. 6.6. Here, the non-reactive and reactive hemispheres are colored blue and green, respectively. In contrast to reactive sink particles that all collapse into a single large cluster, the snapshot clearly shows a steady coexistence between a dense cluster and dilute ‘gaseous’ particles. Quantitative statistics are generated with a larger system, $R_{wall} = 256a$, $N = 2048$, $S_D = 60$, $Da = 5$, equilibrated for a very long time $t = 5000a^2/D$.

Fig. 6.7 shows the particle area fraction in the monolayer $\phi_A = n_A \pi a^2$. The most striking feature is that the dilute region is not uniform in concentration; there is a very long decaying tail. The non-homogeneous structure of the dilute part is also evident from Fig. 6.8, which shows the reactant concentration and average swim speed as a function of r . Inside the cluster (approximately $r < 60a$) the reactant is depleted and the particles are not able to propel themselves. The reactive cluster is a large chemical sink that induces a net flux of reactant towards the cluster. Therefore, in the dilute part $1 - c/c^\infty \sim 1/r$. Also, to leading order in the fuel level, $Ua/D \approx (-g_c^z)S_D c/c^\infty$, where g_c^z is the dominant entry in the mobility matrix M_B .

The long tail in ϕ_A , c , and U differs from a ‘thermodynamic’ system in which a phase is a homogeneous component, and thus prohibits the use of a phase-equilibrium

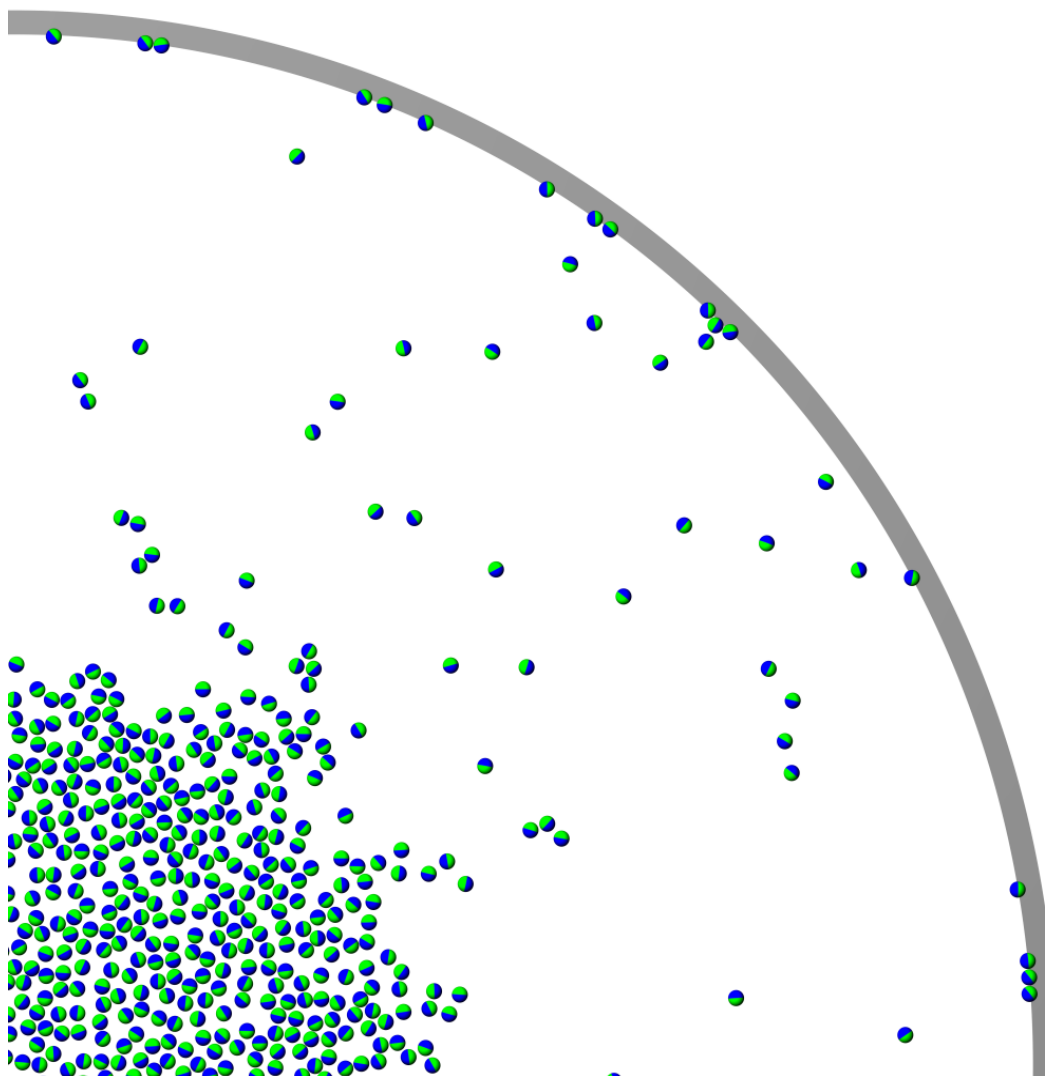


Figure 6.6: Snapshot at steady state of a monolayer of Janus particles. Blue is the non-reactive part and green is the reactive hemisphere. The Janus particles are confined within the circular wall shown in the figure. The wall has no effect on the solute concentration field. $N = 2048$, $S_D = 30$, $Da = 5$, $R_{\text{wall}} = 128a$. Only 1/4 of the simulated system is shown.

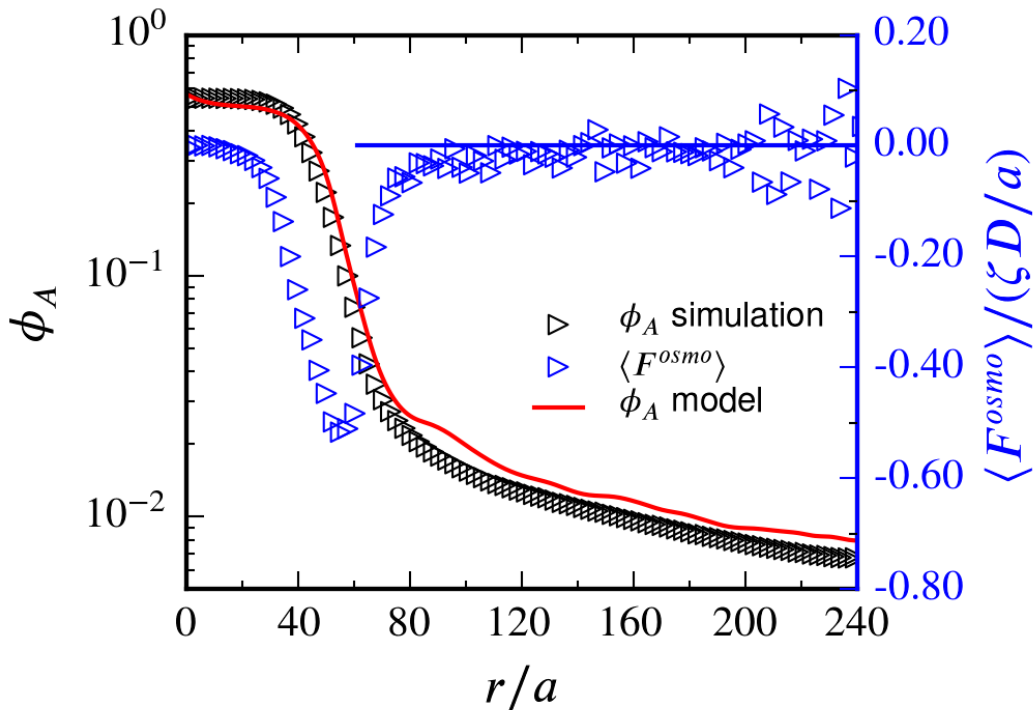


Figure 6.7: The area fraction ϕ_A measured from simulation (black symbols), ϕ_A predicted by the model (red curve), and the average osmotic force $\langle F^{osmo} \rangle$ (blue symbols) as defined in (6.30). Since the orientation distribution is still isotropic, the osmotic force is dominated by the diffusiophoretic force: $\langle F^{osmo} \rangle \approx \langle F^{\nabla c} \rangle$. A negative diffusiophoretic force means a force directed towards the center $r = 0$; the solid blue line is the reference for $n\langle F^{\nabla c} \rangle = 0$. $N = 2048$, $S_D = 60.0$, $Da = 5.0$, $r_{\text{wall}} = 256a$. Data is collected from a steady state period of $t = 5000a^2/D$.

theory to predict this behavior. In principle, this situation can be described from the detailed many-particle Smoluchowski equation, but such a solution is not possible for dense systems where particle-particle collisions are important. Fortunately, however, the recent discovery of the swim pressure (Takatori *et al.*, 2014) as a surface force and the swim force (Yan & Brady, 2015a) as a body force enables a simple approach based on a continuum mechanics description.

At the continuum level, the flux of active particles is driven by stress gradients and ‘body’ forces. The ‘surface’ forces give rise to the total active stress σ^{act} , while the body forces are twofold: (i) the intrinsic self-propulsive velocity $U_0(c)$ is a function of the reactant concentration which varies spatially and this gives rise to an ‘activity-

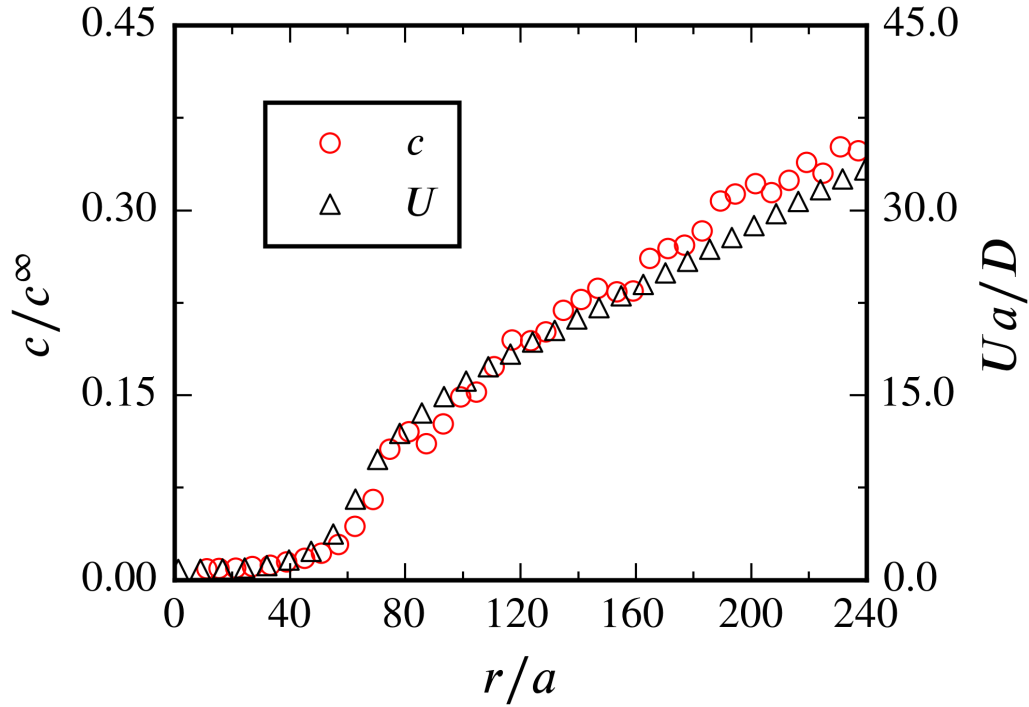


Figure 6.8: Reactant concentration c and velocity $\text{Pe}_p = Ua/D$ along the radial direction. The boundary condition is $c/c^\infty = 1$ as $r \rightarrow \infty$. Data is collected from the same simulation as in Fig. 6.7.

gradient swim force' (Takatori & Brady, 2015): $n\langle \mathbf{F}^{\nabla U_0} \rangle = -\boldsymbol{\sigma}^{swim} \cdot \nabla \ln U_0$, and (ii) the down-gradient diffusiophoretic force arises from the average propulsive force in (6.30): $n\langle \mathbf{F}^{\nabla c} \rangle = -nk_B T L(\Delta) \langle \mathbf{M}_B \cdot \mathbf{C}^{-1} \rangle \cdot \nabla c$. It is important to appreciate that these are two separate and distinct body forces. A non active (non swimming) particle can still be subject to a diffusiophoretic force, and an active non-diffusiophoretic particle can still experience the spatial variation in the fuel concentration and thus have a variable swim speed.

The number density n of active particles is conserved

$$\frac{\partial n}{\partial t} + \nabla \cdot \mathbf{j} = 0, \quad (6.50)$$

where the flux is determined from a momentum balance for the active particles (Yan & Brady, 2015a)

$$0 = -\zeta \mathbf{j} + n\langle \mathbf{F}^{\nabla U_0} \rangle + n\langle \mathbf{F}^{\nabla c} \rangle + \nabla \cdot \boldsymbol{\sigma}^{act}; \quad (6.51)$$

the left-hand-side is zero because the motion is at low Reynolds number. Here, $\zeta = 6\pi\eta a$, is the Stokes drag coefficient (and is not to be confused with the spitting parameter for the Ewald sums). The active stress, σ^{act} , includes the swim stress, the collisional stress, and the Brownian osmotic pressure as discussed below.

At steady state the number density is radially symmetric and since the flux must be finite at $r = 0$, from (6.50) the radial flux is zero everywhere, $j_r = 0$, and the momentum balance (6.51) becomes simply

$$\zeta j_r = \frac{\partial \sigma_{rr}^{act}}{\partial r} + n \langle F^{\nabla U_0} \rangle_r + n \langle F^{\nabla c} \rangle_r = 0, \quad (6.52)$$

where we have neglected the normal stress difference term $(\sigma_{rr}^{act} - \sigma_{\theta\theta}^{act})/r$. The active stress could be anisotropic due to an anisotropic distribution of orientation ξ (Takatori & Brady, 2014). In the system discussed here, however, no significant anisotropy was detected in the simulation data and therefore the normal stress difference is taken to be zero.

In a continuum description one determines both the stress tensor and the body force in a *homogeneous* state and then uses them to *predict* the behavior in an *inhomogeneous* state. For example, to predict the flow of an ideal gas, we have the Navier-Stokes equations, the continuity equation, and the equation of state (EOS) relating the pressure to the density, $p = \rho RT$, from thermodynamics. Chemically active particles can spontaneously separate into dilute and dense regions, as shown in Fig. 6.6, and obtaining the stress as a function of n , S_D and Da for a homogeneous state poses a challenge. A similar challenge arises in classical thermodynamics when phase separation occurs, but at least in this case one can construct the free energy for a homogeneous system via a Monte Carlo method because a conserved energy exists and gives rise to a Boltzmann distribution. No such conserved function exists for active matter and a different approach is needed.

For Active Brownian Particles (ABPs) an accurate EOS has been determined from the micromechanical definition of the stress (Takatori & Brady, 2015), which has

been validated in a sedimentation system (Yan & Brady, 2015a). ABPs do not have phoretic interactions and the swim speed is assumed constant, which corresponds to a uniform fuel concentration or very slow reaction, i.e. $Da \rightarrow 0$. We shall use the model proposed for ABPs, acknowledging that even in a homogeneous state the microstructure with phoretic interactions and for a finite Da may differ from that for ABPs. The dependence on Da will enter through the reactant concentration field and the body forces. As we show below, this model captures the essential physics, is robust and is accurate.

For ABPs in a monolayer with self-propulsion velocity U_0 , drag coefficient ζ , and in-plane diffusive reorientation time τ_R , the dilute Brownian osmotic pressure and swim pressure are:

$$\Pi^B = nk_B T, \quad (6.53)$$

$$\Pi^{swim} = n \langle \mathbf{x} \cdot \mathbf{F}^{swim} \rangle = nk_s T_s \hat{\Pi}^{swim}(\phi_A), \quad (6.54)$$

where the swim force on each particle is $\mathbf{F}^{swim} = \zeta U_0 \boldsymbol{\xi}$, and the ‘activity’ $k_s T_s = \zeta U_0^2 \tau_R / 2$ in 2D. The nondimensional function of area fraction,

$$\hat{\Pi}^{swim}(\phi_A) = (1 - \phi_A - \frac{1}{5} \phi_A^2), \quad (6.55)$$

gives the reduction in the swim pressure due to the hindering effect of other particles (Takatori & Brady, 2015).

The collisional pressure arises from the hard-disk collisions between particles that prevent particle overlap (c.f. Eq.(6.49)) and is given by

$$\Pi^P = n \langle \mathbf{x} \cdot \mathbf{F}^P \rangle = n \left(k_B T + k_s T_s \frac{4}{\pi} Pe_R \right) \phi_A \hat{\Pi}^P(\phi_A), \quad (6.56)$$

where the reorientation Péclet number $Pe_R = a/U_0 \tau_R$. The collisional pressure arises from the ‘collision’ of two particles and thus is $O(n^2)$ in the dilute limit, in contrast to the ‘ideal gas’ Brownian and swim pressures which are both $O(n)$. For Brownian hard disks, the collisional pressure is $nk_B T \phi_A \hat{\Pi}^P(\phi_A)$, and thus the

nondimensional function $\hat{\Pi}^P(\phi_A)$ gives the hard-disk EOS. We take the simplest form for the EOS (Wang, 2010), which gives

$$\hat{\Pi}^P(\phi_A) = \frac{2 - \phi_A}{(1 - \phi_A)^2}. \quad (6.57)$$

In (6.56) we have also supposed that the collisional pressure due to the activity has the same area-fraction dependence as that for Brownian hard-disks and that the two effects are additive. When activity is a small correction to Brownian motion, the additional random walk due to swimming allows one to replace $k_B T$ with $k_B T + k_s T_s$, which is reflected in (6.56). (Note, that the collisional swim stress is transmitted over the particle size a upon collision, not over the run length $\ell = U_0 \tau_R$ as for the swim stress; hence the factor of $4Pe_R/\pi$.) When swimming dominates, the activity is the sole source of particle-particle collisions and the collisional pressure has the same area fraction dependence as for Brownian (or molecular) hard disks (Takatori & Brady, 2015). Thus, (6.56) is correct in the two limits of weak and strong activity and should be a reasonable approximation over the entire range of activity (Takatori & Brady, 2015). (Given the other approximations already made, this is not a critical one.)

Thus, the total active stress is modeled as

$$\boldsymbol{\sigma}^{act} = -\Pi^{act} \mathbf{I} = -(\Pi^B + \Pi^{swim} + \Pi^P) \mathbf{I}, \quad (6.58)$$

and $\sigma_{rr}^{act} = -\Pi^{act}$, which is what is needed in the particle flux balance (6.52).

To check the applicability of (6.58) for diffusiophoretic interacting Janus particles with a reactant concentration-dependent swim velocity, Fig. 6.9 compares the collision pressure Π^P measured from simulation to the estimation given separately by the Brownian and active contributions to the collisional pressure calculated at the corresponding ϕ_A measured at every location r . Inside the cluster $U_0 \approx 0$, and the Brownian collisional pressure dominates and is a good estimation of $\Pi^P \approx \Pi_B^P = nk_B T \phi_A \hat{\Pi}^P$. In the gaseous region, swimming dominates and (6.56)

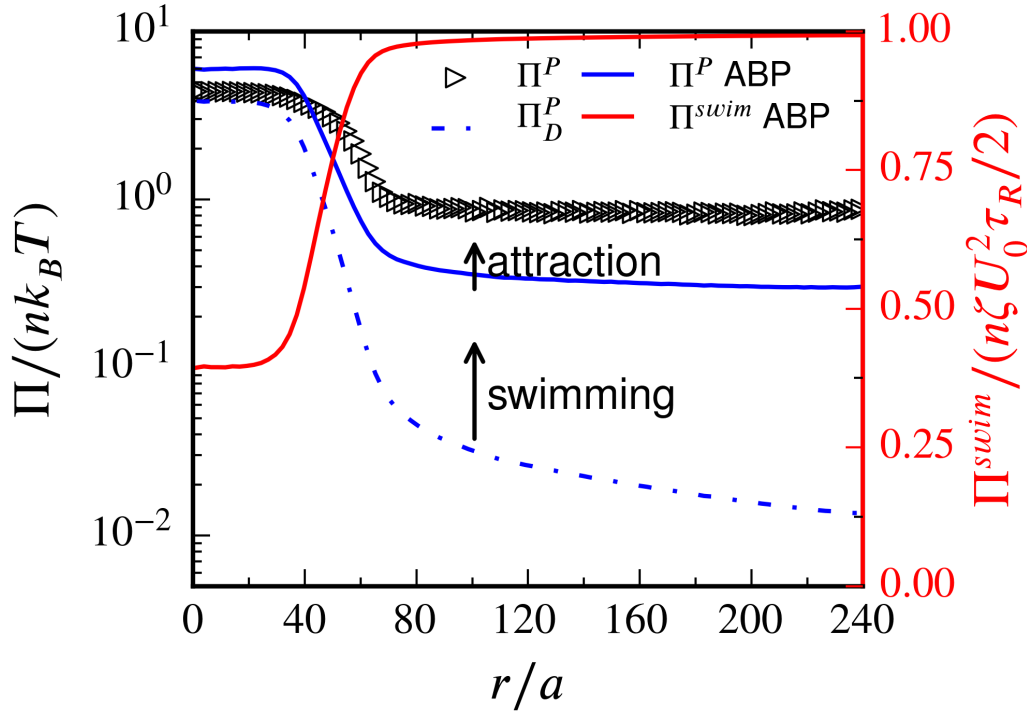


Figure 6.9: The collision pressure Π^P and swim pressure Π^{swim} . Data is collected from the same simulation of Fig. 6.8.

gives $\Pi^P \approx nk_s T_s \phi_A 4Pe_R/\pi$ because the concentration is dilute. However, this estimate is much smaller than Π^P measured in the simulation. The difference in the dilute region can be explained by the diffusiophoretic particle-particle attraction, which causes more collisions among nearby particles. Nevertheless, when dilute, the ‘ideal gas’ swim pressure dominates: $\Pi^{swim} = n\zeta U_0^2 \tau_R/2 \approx 10^2 nk_B T \gg \Pi^P$, and the collisional contribution is not important. In summary, inside the cluster $\Pi^{act} \approx \Pi_B^P$, and outside the cluster $\Pi^{act} \approx \Pi^{swim}$, and the EOS of ABPs can be used as an approximation for diffusiophoretic interacting Janus particles for nonzero Da .

To complete the model for the particle flux, the diffusiophoretic body force $\langle \mathbf{F}^{\nabla c} \rangle$ is needed. For chemically active particles, the diffusiophoretic force arises from the average osmotic propulsive force in (6.30), which includes both the autonomous motion driven by fuel concentration c and diffusiophoresis driven by ∇c . Because the mobility M_B depends on the orientation ξ of the swimmers, the diffusiophoretic

force need not be solely in the direction of ∇c . However, as shown in Fig. 6.7, in the dilute part the slightly negative $\langle F^{\nabla c} \rangle$ is along ∇c (c.f. Fig. 6.8), and we found that the distribution of ξ is unbiased in that region. Thus the orientation-average of M_B can be used, and the diffusiophoretic force is given by

$$n\langle F^{\nabla c} \rangle_r = -nk_B T S_D \frac{1}{2} (g_{cx}^x + g_{cz}^z) \frac{\partial \hat{c}}{\partial r}, \quad (6.59)$$

where we have made the concentration dimensionless and so recover the fuel level S_D from (6.48). The diffusiophoretic force is directed towards the center of the cluster, because $S_D > 0$, $(g_{cx}^x + g_{cz}^z) > 0$ (which are given in Appendix G), and \hat{c} increases with r .

Finally, with the swim pressure, the activity-gradient swim force becomes

$$n\langle F^{\nabla U_0} \rangle_r = \Pi^{swim} \frac{\partial \ln U_0}{\partial r}. \quad (6.60)$$

An examination of the various contributions to the active pressure and the body forces shows that all terms can be scaled with the thermal energy $k_B T$ at which point it drops out, leaving two dimensionless groups: $Pe_R = a/U_0 \tau_R$ and the ratio of activity to thermal energy $k_s T_s / k_B T$. The reorientation time is due to rotary Brownian motion, $\tau_R = 4/3 a^2 / D$, and thus

$$Pe_R = \frac{a}{U_0 \tau_R} = \frac{3 a D}{4 U_0} = \frac{3}{4} \frac{1}{S_D (-g_c^z) \hat{c}}, \quad (6.61)$$

where we have used (6.47) to for the swim speed U_0 in terms of the reactant concentration. Similarly, the activity to thermal energy ratio can be expressed in terms of S_D and \hat{c} :

$$\frac{k_s T_s}{k_B T} = \frac{\zeta U_0^2 \tau_R / 2}{k_B T} = \frac{D^{swim}}{D} = \frac{3}{8} \frac{1}{Pe_R^2} = \frac{2}{3} S_D^2 (-g_c^z)^2 \hat{c}^2, \quad (6.62)$$

where g_c^z is given in Appendix G. Also, the gradient of the swim stress can be combined with the activity-gradient swim force (6.60) to give

$$-\frac{\partial \Pi^{swim}}{\partial r} + \Pi^{swim} \frac{\partial \ln U_0}{\partial r} = -\Pi^{swim} \frac{\partial \ln(\Pi^{swim}/U_0)}{\partial r}. \quad (6.63)$$

We are now in a position to bring all the contributions together into the flux expression for an equation for the area fraction of active particles:

$$\begin{aligned}
0 = & -\frac{\partial}{\partial r} \left(\phi_A + \phi_A^2 \hat{\Pi}^P(\phi_A) \left[1 + \frac{2}{\pi} \beta S_D \hat{c} \right] \right) \\
& - \frac{3}{8} \beta^2 S_D^2 \hat{c} \frac{\partial (\phi_A \hat{\Pi}^{swim} \hat{c})}{\partial r} \\
& - \gamma S_D \phi_A \frac{\partial \hat{c}}{\partial r}, \tag{6.64}
\end{aligned}$$

where $\beta = (-g_c^z)^2$ gives the reactivity-induced self-propulsive motion, while $\gamma = (g_{cx}^x + g_{cz}^z)/2$ gives the diffusiophoretic motion; both are functions of Da and can be found in Appendix G.

Before applying (6.64) to the monolayer, we show that it reduces to the expected behavior in special cases. First, note that S_D and \hat{c} always appear together; the product, $S_D \hat{c}$, is the actual reactant connection at location r . When there is no fuel, $S_D = 0$, (6.64) reduces to

$$\frac{\partial}{\partial r} \left(\phi_A + \phi_A^2 \hat{\Pi}^P(\phi_A) \right) = 0, \tag{6.65}$$

which just says the the total thermodynamic pressure for the passive Brownian particles is a constant. The area fraction is uniform and given by the constraint that all particles are contained within the circle

$$\int_0^R \phi_A(r) r dr = \frac{Na^2}{2}, \tag{6.66}$$

where N is the total number of particles in the circle.

When there is no phoretic attraction, $\gamma = 0$ and the reaction rate is slow ($Da \rightarrow 0$) so that the fuel concentration is approximately uniform, $\hat{c} \approx 1$, (6.64) reduces to the condition that the total active pressure is constant:

$$\frac{\partial}{\partial r} \left(\phi_A + \frac{3}{8} \beta^2 S_D^2 \phi_A \hat{\Pi}^{swim} + \phi_A^2 \hat{\Pi}^P(\phi_A) \left[1 + \frac{2}{\pi} \beta S_D \right] \right) = 0, \tag{6.67}$$

and we recover the behavior of ABPs. Depending on the imposed area fraction from (6.66) and βS_D , the area fraction may remain uniform or the system may phase

separate into dense and dilute regions. When activity dominates, $\beta S_D \gg 1$ the critical point for phase separation in 2D is approximately (Takatori & Brady, 2015) $\phi_A^c \approx 0.58$, $\beta S_D^c \approx 16.3$.

When the particles are not Janus and therefore have no self-propulsion, $\beta = 0$, (6.64) reduces to a balance between the osmotic pressure of the passive Brownian particles and the diffusiophoretic attraction

$$\frac{\partial}{\partial r} \left(\phi_A + \phi_A^2 \hat{\Pi}^P(\phi_A) \right) + \gamma S_D \phi_A \frac{\partial \hat{c}}{\partial r} = 0, \quad (6.68)$$

which, provided ϕ_A is everywhere small so that $\phi_A^2 \hat{\Pi}^P(\phi_A) \ll \phi_A$, gives a Boltzmann-like distribution for the area fraction

$$\phi_A(r) \sim e^{-\gamma S_D \hat{c}(r)}. \quad (6.69)$$

The concentration field \hat{c} is the ‘potential energy’ for the diffusiophoretic force, just like the electrostatic potential for attractive ions. The area fraction is largest where the concentration is smallest – where the ‘energy’ is lowest.

Returning to the full flux balance (6.64) we see that it anticipates the simulation behavior in both the dense cluster and the surrounding dilute region. In the dense region near the center ($r < 40a$ in Figs. 6.7, 6.8, 6.9), the fuel concentration goes to zero, $\hat{c} \approx 0$, and (6.64) reduces the passive Brownian osmotic pressure balance (6.65), which predicts a constant ϕ_A . At the other extreme in the dilute region, since $S_D \gg 1$ and the area fraction is small, (6.64) reduces to

$$\frac{\partial(\phi_A \hat{c})}{\partial r} = 0 \Rightarrow \phi_A \hat{c} = \text{const.} \quad (6.70)$$

Even though there is a concentration gradient the diffusiophoretic force scales as S_D and thus is smaller than the $O(S_D^2)$ swim pressure and variable swim speed. As shown in Fig. 6.10 the prediction from the model matches the simulation data very well. This steady state condition, $\partial(nU_0)/\partial r = 0$ is universal and does not depend on the details of the propulsion mechanism (Takatori & Brady, 2015).

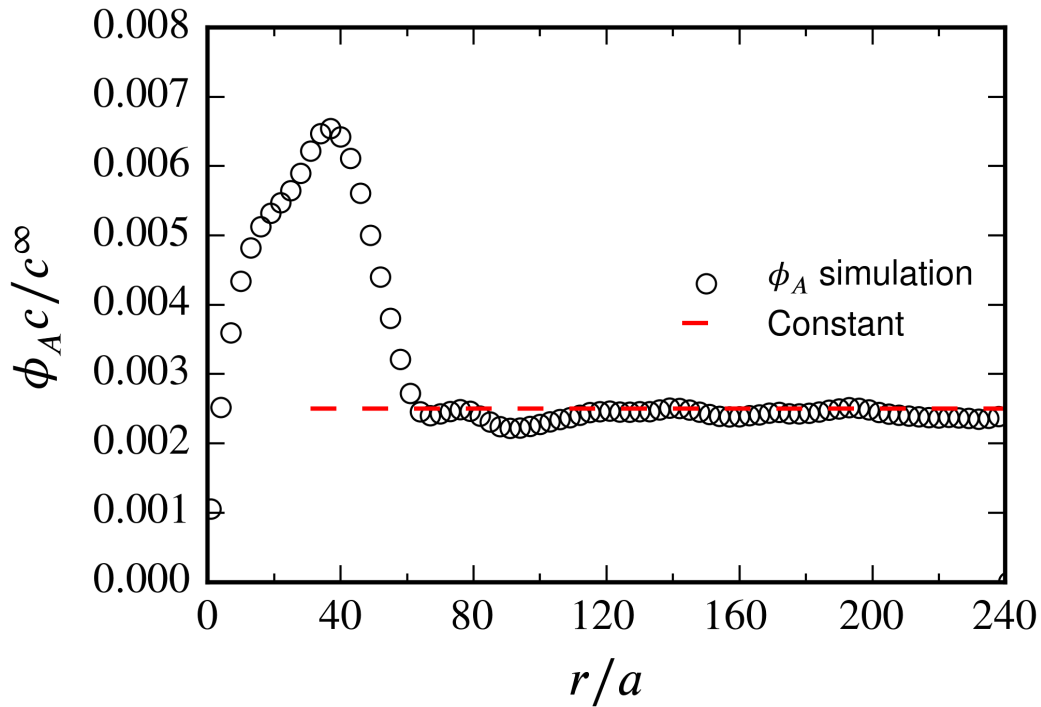


Figure 6.10: The product ϕ_{AC}/c^∞ as a function of r . Data is collected from the same simulation as Fig. 6.8. It is clear that in the dilute region ϕ_{AC}/c^∞ is approximately a constant. The fluctuation is due to the noise in the $c(r)/c^\infty$ measurement in Fig. 6.8.

Up to now we have discussed the behavior of the system without actually knowing much about \hat{c} . However, the concentration distribution is not given, but must be solved for simultaneously with the area fraction field. Further, there is no length scale in the flux balance (6.64); the particle size a only enters through the parameters S_D and Da . The characteristic length scale is set by the concentration distribution, which is governed by the Brinkman equation (6.42), and which for the monolayer can be written as

$$\nabla^2 \hat{c} = f_c^q n_A \kappa_{eff}(\phi_A) \hat{c} \delta(z), \quad (6.71)$$

where $\delta(z)$ means the particles are distributed in a monolayer on the $z = 0$ plane only. In (6.71), f_c^q (c.f. Appendix G) is the nondimensional reaction rate that depends on the Damkholer number, and the nondimensional function $\kappa_{eff}(\phi_A)$ describes the enhancement to the reactivity due to the increased area fraction and is similar to the

3D case discussed by Bonnecaze & Brady, (1991a).

Even though the reactive particles all lie in a 2D plane, the reactant concentration field is fully three dimensional and thus the solution to (6.71) is not a simple exponential as is the case for the fully 3D problem. The concentration field is still screened, but the screening length for the monolayer is not the same as the expression (6.44), $L_B^J = a\sqrt{4\pi/(-3\phi f_c^q)}$, in a 3D system. Thus, we have chosen to compare the predictions of the model for ϕ_A as a function of r/a for easier comparison with the simulation data.

The continuum model is now (almost) complete. The particle area fraction, $\phi_A(r)$, and reactant concentration field, $\hat{c}(r, z)$, must be determined simultaneously from (6.64) and (6.71), along with the conservation of particles (6.66) and a uniform reactant concentration for large distance $\hat{c} \sim 1$ as $|\mathbf{r}| \rightarrow \infty$. The last missing constitutive function is the effective reaction rate $\kappa_{eff}(\phi_A)$. Unfortunately, because the monolayer is neither a strictly 2D nor 3D problem, we cannot simply take the known behavior of κ_{eff} in 3D and use it for the monolayer geometry. Furthermore, even in the dilute limit, the solution to (6.71) is mathematically involved, and thus we proceeded as follows: we take the $\hat{c}(r)$ and $n\langle\mathbf{F}^{\nabla c}\rangle(r)$ measured in the simulation (c.f. Figs. 6.8 and 6.7) as *input* to (6.64) to predict the area fraction profile, ensuring no flux at $r = R$ and for $N = 2048$ in (6.66). As shown in Fig. 6.7, the model matches the simulations very well for all r without any fitting parameters.

As a final remark, it should be appreciated that no ‘surface tension’ term has been added to the above mechanical model, although a peculiar ‘negative surface tension’ has been reported in literature (Bialké *et al.*, 2015). In our model, the diffusiophoretic force, $n\langle\mathbf{F}^{\nabla c}\rangle$, is directed towards the cluster center at the interface and is enough to stabilize the the cluster. Also, at the interface we found a slightly biased distribution of ξ towards the cluster center. The biased ξ may also contribute to $n\langle\mathbf{F}^{\nabla c}\rangle$. For ABPs the autonomous bias of ξ has been discussed at an interface (Redner *et al.*,

2013) and in a force field (Hennes *et al.*, 2014; Enculescu & Stark, 2011). Here, in the presence of the reactant concentration field the details are more complicated but the mechanism is similar. In a strongly biased environment (due to either an interface or a force field), some active particles with favorable orientation (e.g. pointing away from the cluster) can escape from the environment more quickly and thus the particles left behind exhibit a biased distribution of ξ (e.g. pointing towards the cluster). In the model in this work we did not include the effects of an anisotropic swim stress, σ^{swim} , which is a good approximation when the orientational bias is weak (Takatori & Brady, 2014; Yan & Brady, 2015a). However, the normal stress differences that arise from a bias, if localized in a thin region, may act like surface tension. We leave this for a future study.

6.5 Conclusions

In this work an efficient computational method is introduced to explore the chemically active system by particle-tracking simulations. It is based on multipole expansion, with flexibility to deal with both uniformly reactive sink and Janus particles. In fact, particles that have more complicated reactive patterns can be easily simulated, by using the appropriate fitting functions f s and g s in matrices C and M_B . It could be easily done with the same BEM method as used in Appendix G. Our method is also flexible to deal with different geometries, including periodic 3D & monolayer boxes, and finite 3D & monolayer systems. Further, our multipole method can also be extended to simulate the systems on a flat solid boundary which is non-penetrating or absorbs the solutes, as seen in the experiments (Theurkauff *et al.*, 2012). One only need to add the ‘reflected’ multipoles due to the presence of the solid boundary, as the familiar method of image charges in electrostatics or the image method in Stokes flow. The simulations presented in this chapter utilizes only one CPU & GPU, but it can be easily extended to utilize parallel machines, with the help of distributed FFT & sparse matrix libraries. After the field c is solved, other

operations are for each particle only and are independent of each other, so there is no extra barriers to parallelization due to data racing. To further improve our method, the Ewald sum done with FFT may be improved with the Fast Multipole Method, to avoid the large amount of memory required by the FFT on a regular mesh. The multipole method may also be combined with the immersed boundary method (Bhalla *et al.*, 2013) to offer the flexibility to accommodate simulations in domains of complex geometry.

With the simulation method, we clarified the notion of chemical screening. It is a static self-screening, which is fundamentally different from Debye screening. The screening means a shortened range of perturbation propagation instead of an interaction potential. Also, it is the result *after* the correct full solution of the Laplace's equation, and should not be *prescribed* as seen in some previous work (Pohl & Stark, 2014). Besides, this screening is fundamentally different from the Keller-Segel model in which the chemical solutes are assumed to be absorbed by the medium (fluid). Experimentally (Theurkauff *et al.*, 2012), the chemical solutes such as H_2O_2 , O_2 are not absorbed by the medium. Therefore, in our model the chemical screening is solely due to the fact that the chemical reaction rate on a particle's surface is proportional to the local solute concentration. This screening has a key role in the determination of the instability threshold S_D^* , because without the screening, the absolutely long-ranged interaction $\sim q/r$ is well-known to result in the collapse of all particles into a big single cluster. Mathematically, it corresponds to the finite time blow-up discussed in some variations of the Keller-Segel model (Horstmann, 2001; Horstmann & Winkler, 2005). S_D^* has been briefly discussed in the work by Saha *et al.*, (2014), and shall be discussed in detail in our future work. Further, we demonstrated examples of simulation to address the two most important questions, when the clustering process starts and when the process stops.

For sink particles we showed that the system is stable and remains random at small

S_D but forms a cluster at higher S_D . The particles compete for reactant so when they get close to each other their reactivities q are reduced and thus exert less attraction to each other. Therefore at the intermediate range of S_D where the system loses stability and collapses to a cluster, the structure remains loosely packed. More importantly, no coexistence behavior is observed for the sink system. We always observe a large cluster occupying the entire simulation box. It can be understood by diffusiophoresis. When a cluster forms, it acts as a large sink and forces a net flux of solutes into the cluster. This flux induces a gradient ∇c , which is long-ranged and every particle is pushed toward the cluster by diffusiophoresis ∇c . Then at steady state, the system shows a balance between translational Brownian motion and diffusiophoresis attraction.

For Janus particles we observed similar coexistence behavior as observation in experiments (Theurkauff *et al.*, 2012). Inside the cluster, reactant is also depleted: $U_0 \propto c \rightarrow 0$, and therefore the behavior is close to a pure Brownian hard disk system: $\Pi^P \approx \Pi_D^P$. Outside the cluster, the particle distribution is not homogeneous: $\phi_A(r)$ exhibits a long decaying tail, and $U_0 \propto c$ remains true. In the gaseous part, we showed that collision pressure Π^P is increased by both self-propulsion and diffusiophoretic attraction. The inhomogeneity of the dilute part forbids a thermodynamic equilibrium description of the steady state, because thermodynamic argument is based upon the equilibrium of two homogeneous phases. In fact, the dense and the dilute parts seen in our simulations should not be termed as phases. Instead, we proposed a mechanical model which is built upon swim pressure and swim force, which are counterparts of ideal gas pressure and gravity in classical Navier-Stokes equations. Our self-consistent mechanical model successfully explained the steady state coexistence structure without any fitting parameters. The model can be improved to be a *predictive* model, with proper extensions to solve (i) the $c(r)$ distribution from many-body reactions and (ii) the $\langle \mathbf{F}^{swim} \rangle$ of the interface.

In this chapter, we focused on the most fundamental aspects of chemically active

suspensions, and a lot of interesting systems can be investigated with proper extensions. For example, under some conditions the solutes may also apply a torque \mathbf{L} on the particles, and it can be easily implemented by an equation $\mathbf{L} \sim (c, \nabla c)$, similar to (6.30). Some interesting results of dumbbell-shaped (sphere-dimer) active particles have also been discussed (Thakur & Kapral, 2012). In our algorithm, two or more particles can be either rigidly or flexibly connected to create such swimmers, with some minor modifications of the Faxen Laws and a proper treatment of the binding force (Swan *et al.*, 2011).

Hydrodynamics is a more important component, and can be added to this simulation with the method of Accelerated Stokesian Dynamics (ASD) (Sierou & Brady, 2001). With the assumption that solutes diffuse very fast, $D_R \gg D$, the Stokes flow has no effect on the c field. So the calculation of c equation is mostly decoupled from the Stokes flow. In a rough approximation, the boundary condition for the Stokes flow is still no-slip, and in this case the Stokes flow and solutes transport are completely decoupled. All we need to do in this case is to replace the Stokes drag $6\pi\eta a$ in (6.1) by the full resistance matrix \mathbf{R}_{FU} . A more satisfactory approximation is that the boundary condition for the Stokes flow should be determined by the local concentration field c , in the presence of a surface slip velocity (Anderson, 1989; Brady, 2011). In this case, the Stokes flow can be solved after the solution of the solute field c . This is one-way coupling and still solvable by the method of ASD, with some minor modifications due to slip velocity on the lubrication correction and the Faxen laws relating Stokes flow multipoles (force \mathbf{F} , torque \mathbf{L} , and stresslet \mathbf{S}) to the surrounding flow. At this stage, the role of hydrodynamics in the clustering process and the steady state structure is unclear. In principle it increases the drag when clustering happens and slows down both translational and rotational motion. A particle-tracking simulation is necessary to probe the systems and it is one of our future topics.

Acknowledgments Wen Yan thanks Mu Wang, Charles Slominski and James Swan

for the documents and discussions on Accelerated Stokesian Dynamics. This work is supported by NSF CBET-1437570.

*Chapter 7***CLUSTERING OF CHEMICALLY ACTIVE PARTICLES:
STABILITY ANALYSIS WITH THE MATRIX PERTURBATION
METHOD**

Active matter refers to a system made of many objects, each of which achieves self-propulsion by converting energy into motion, like swimming bacteria suspensions (Rusconi *et al.*, 2014). Active diffusiophoretic suspensions are a common artificial realization, referring to those colloidal particles which are able to convert chemical energy to self-propulsion, usually through patterned surface reactivity. They are synthesized to be reactive on one half while non-reactive on the other, and such asymmetric pattern allows them to achieve self-diffusiophoresis by creating a solute concentration gradient (Theurkauff *et al.*, 2012; Palacci *et al.*, 2013; Howse *et al.*, 2007). They are termed *Janus* particles in literature because of the asymmetric surface reactivity pattern.

Active matter displays interesting collective behavior, such as a glass transition (Berthier & Kurchan, 2013), Casimir effect (Ray *et al.*, 2014), and bacteria turbulence (Wensink *et al.*, 2012). One of the most notable features of active matter is that it may show coexistence of dilute and dense components in a single system. In the experiment by Theurkauff *et al.*, (2012), Janus particles are confined on a surface with a large reservoir above evolved to a non-uniform steady state under a tilted gravity acting as a sedimentation force. At steady state the system separates into dense and dilute regions. In another experiment by Palacci *et al.*, (2013), the system shows a similar coexistence behavior.

Many models have been proposed to explain the coexistence. A minimal model is called the Active Brownian Particle (ABP) model, in which each particle takes a fixed swim velocity U_0 while the direction ξ is subject to run-and-tumble or rotational Brownian diffusion. The particle-particle interaction is assumed to be hard-sphere collisions in the simplest case. For this model, the swim pressure defined by Takatori *et al.*, (2014), gives an Equation of State, and Takatori & Brady, (2015) proposed a successful thermodynamic-like theory to describe the coexistence as a classical first order gas-liquid phase transition. Simulations and models are also proposed for particles with short-ranged pairwise additive interactions, *e.g.*, the Lennard-Jones

potential (Redner *et al.*, 2013; Buttinoni *et al.*, 2013). Generally, in active matter showing coexistence under short-ranged interactions, the effect of the interface is limited to the short range of a pair-wise potential and therefore both dense and dilute regions are identifiable as a ‘pure substance’ in contact with one another, which allows a thermodynamic phase-equilibrium approach (Solon *et al.*, 2015a; Wittkowski *et al.*, 2014; Menzel & Löwen, 2013).

Despite its success, the thermodynamic approach may not be applicable in a realistic system where the objects interact with each other by a continuous field rather than via a short-ranged pairwise potential. To appreciate the ‘field-drive’ nature of a realistic model, one can consider that in the continuum limit where the solute molecules are much smaller than the moving particle, the active particle’s propulsion velocity is given by Brady, (2011):

$$U_0 = -\frac{L(\Delta)k_B T}{6\pi\eta a} \oint c(\mathbf{x}, t) \mathbf{n} dS, \quad (7.1)$$

where $L(\Delta) = (3/2)\Delta^2(1 + \frac{2}{3}\Delta)/(1 + \Delta)^3$, with $\Delta = \delta/a$ measuring the flow of fluid with viscosity η in a layer of thickness δ adjacent to the colloidal particle where a particle-solute interactive force is operative. Here, we have taken the simplest form of interactive force between the solute and the colloidal particle, namely a hard-sphere repulsive force at a distance $r_c = a + \delta$ (and δ need not be small compared to the particle size a , although typically it is so). More general interactive forces will only have a quantitative effect, as detailed in Brady, (2011). Generalizations to non-spherical particles are also possible as shown by Shklyaev *et al.*, (2014).

Thus, to determine the particle’s velocity we need to solve for the solute concentration field $c(\mathbf{x}, t)$ field that enters Equation (7.1). Typical phoretic or self-propulsive velocities are of order $1\mu\text{m}/\text{s}$ for a micron-sized particle, while nano-sized solute diffusivities are of order $10^3\mu\text{m}^2/\text{s}$ so that the Péclet number $\text{Pe} = U_0 a / D_R \ll 1$ and advection can be neglected. Similarly, the time scale to establish a steady solute concentration profile a^2/D_R is much faster than the time scale for the motion of

the colloidal particles, either due to diffusiophoresis or to their intrinsic Brownian motion, so that the solute concentration distribution satisfies Laplace's equation:

$$\nabla^2 c = 0. \quad (7.2)$$

In this realistic model, the particles' swim velocity U_0 is proportional to c , while c is governed by Laplace's equation and each particle acts as a sink on the solute field. It is similar to the famous chemotaxis model (Keller & Segel, 1971) but more complicated because the dynamics in the swim orientation space must also be resolved. At steady state particles show coexistence between a dilute and a dense part. However, in this case, due to the long-range nature of Laplace's equation, neither part can be identified as a homogeneous 'pure substance' and the thermodynamic approach is called into question.

In this work, linear stability analysis is applied to a dilute homogeneous state, to find when and how particles cluster. To match existing experiments (Theurkauff *et al.*, 2012; Palacci *et al.*, 2013) we shall consider mainly particles moving in a monolayer geometry. Our model describes both the particles and solute molecules as a continuum, and we shall treat the particles as in the dilute limit $\phi \rightarrow 0$.

The major difficulty of the stability analysis comes from the swimming orientation space. A common approach utilized in the literature is to attain a linear dynamical system by expanding the orientation space in a hierarchy of moments (Saintillan & Shelley, 2015), truncated at some finite level. Then the eigensystem can be numerically solved (Ezhilan *et al.*, 2013; Saintillan & Shelley, 2008). But with this approach it is difficult to probe the entire parameter space. The analytical approach common in literature is to close the hierarchy expansion with a hypothetical closure relation, usually at the dipole or quadrupole level due to algebraic complexity (Saha *et al.*, 2014). Such a moment hierarchy method usually involves tedious algebra and assumes the moments relax to isotropy fast enough. However, with this assumption

information about the orientation during the development of instability is lost, which is actually an interesting behavior of chemical swimmers, as shown in §7.2 and §7.3.

In this work we follow a similar orientation moments approach to formulate the growth of a perturbation \mathbf{b} in an infinite dimensional linear dynamical system $\dot{\mathbf{b}} = \mathbf{M}_{ins}^\infty \mathbf{b}$. However, we take the matrix perturbation method to find the eigensystem of \mathbf{M}_{ins}^∞ , without any assumption of a closure. This approach is a systematic and straightforward technique, as detailed in Appendix K. Analytical results are also verified by simulation in which the field $c(\mathbf{x}, t)$ is solved in detail and each particle motion is tracked over time.

After the detailed analysis, we propose a simple coarse-grained model to reproduce the detailed solution in the limit of fast rotational relaxation $D_{rot} \rightarrow \infty$. In this model, we consider the large-scale dynamics via a continuum mechanics description of the active particles. Yan & Brady, (2015a,b) have discussed the continuum mechanics of active Brownian particles by defining the swim pressure (Takatori *et al.*, 2014) as a surface force and the swim force as a body force, for particles with constant swim velocity U_0 . In this work, by analyzing the detailed solution, we extend the continuum mechanics to system where the intrinsic swim velocity U_0 is dependent on $c(\mathbf{x}, t)$, and therefore varies from place to place.

We formulate the model and describe the analytical and simulation methods in §7.1. In §(7.1) we introduce the linear stability analysis for monolayer geometry, and we briefly describe the simulation method to verify our theory. The solutions are given in §7.2 for homogeneously reactive particles, and in §7.3 for Janus particles with the matrix perturbation analysis. The detailed solution gives a general result about the ‘active flux’ in active matter and is discussed in §7.4. Based on the detailed solution and active flux, coarse-grained models are also discussed in §7.2 and §7.4. Calculation details can be found in Appendix K and L.

7.1 Problem formulation & methodology

The solute field $c(\boldsymbol{x}, t)$

The reaction of solutes on particles' surfaces is assumed to be first order $R \rightarrow \theta P$, where R is the reactant, P is the product, and θ is the stoichiometry of the chemical reaction. In general, one needs to solve for both the reactant and product concentrations, but as shown by Córdova-Figueroa & Brady, (2008), one only needs to scale the governing equations by the factor $(1 - \theta D_R/D_P)$, where D_R and D_P are the diffusivities of the reactants and products, respectively. After the scaling, one only needs to solve for the reactant concentration field. Therefore, we consider the reactant field only and denote its concentration field by $c(\boldsymbol{x}, t)$ and its diffusivity by D_R .

The reactivity on the particle surface serves as a boundary condition for $c(\boldsymbol{x}, t)$:

$$\boldsymbol{j}_R = -D_R \nabla c, \quad (7.3)$$

$$\boldsymbol{n} \cdot \boldsymbol{j}_R = -\kappa_0 h(\boldsymbol{n}) c, \quad (7.4)$$

where $h(\boldsymbol{n})$ is a function to describe the reactivity pattern on the particle surface, and κ_0 is the reaction rate constant. The Damköhler number $\text{Da} = \kappa_0 a/D_R$ compares the reaction rate to diffusion of reactant. $\text{Da} \rightarrow \infty$ is diffusion limited and $\text{Da} \rightarrow 0$ is reaction limited. For uniformly reactive particles $h(\boldsymbol{n}) = 1$, while a particle with $h(\boldsymbol{n}) = \text{Heaviside}(\boldsymbol{n} \cdot \boldsymbol{\xi})$ describes the pattern of a Janus particle with orientation vector $\boldsymbol{\xi}$: $h = 1$ on the reactive hemisphere and $h = 0$ on the passive hemisphere. Particles always decrease the reactant concentration and increase the product concentration near their surfaces, and the prefactor $\theta D_R/D_P$ describes the relative effect of reactant and product. When $\theta D_R/D_P > 1$, the products push the particles more effectively than the reactants do and the particles can be considered as sources releasing the products, and therefore they repel each other, according to (7.1). Therefore, when $(1 - \theta D_R/D_P) < 0$ particles repel each other and do not show clustering behavior. They are discussed in Chapter 8. Sinks with $(1 - \theta D_R/D_P) > 0$ show a

clustering process when attraction wins. In the following sections we focus on sinks and seek to understand the initial stage of their clustering process through a stability analysis.

Each active particle disturbs the solute field $c(\mathbf{x})$, which can be represented by a multipole expansion $(q, \mathbf{S}, \mathbf{Q}, \dots)$. Here q denotes the monopole (scalar), \mathbf{S} represents the dipole (vector), and \mathbf{Q} represents the quadrupole (2nd order tensor). Physically, the monopole q represents the net consumption of reactants on a particle, and higher order moments describing the non-uniform consumption of solute reactants on the particle surface.

Due to the first order surface reaction, all the moments are linearly dependent on c , such as $q = -\kappa c$, etc. Here κ is the reactivity of the entire particle, which depends on Da . The detailed derivations can be found in Chapter 6. Thus to leading order we can write the equation for c as:

$$D_R \nabla^2 c = S - \kappa n c, \quad (7.5)$$

where n is the number density of particles, and S is the source of solutes to compensate for the consumption and keep the system evolving.

In this many-body problem, each particle's disturbance shall be properly summed to achieve a solution $c(\mathbf{x}, t)$. The sum depends on the particles' configuration, and is not straightforward because c is governed by Laplace's equation and the particles' multipoles induce long-ranged disturbances such as $1/r, 1/r^2, \dots$. In this work, we shall consider mainly a monolayer geometry and also a full 3D one. In the monolayer case, we consider a statistically uniform infinite monolayer of particles moving in an infinite 3D bath of reactive solutes, and we specify a boundary condition of a constant reactant concentration $c(\mathbf{x}, t) \rightarrow c^\infty$ as $z \rightarrow \pm\infty$, where z is the distance to the monolayer. Particles are free to move on the $z = 0$ plane, and 2D in-plane Brownian reorientation of $\boldsymbol{\xi}$ is to be considered. c^∞ is imposed as the 'propulsion fuel

concentration'. Physically, reactant diffuses from infinity to the particle region to compensate for the consumption by the active particles.

There is a subtlety, which comes from the 'infinite monolayer' and Laplace's equation. The particles consume reactants (as sinks), and there a statistically uniform monolayer applies a uniform flux of reactants $\langle j_c \rangle \propto \nabla c \neq 0$ on large scale toward the $z = 0$ plane. When the monolayer is finite, Laplace's equation $\nabla^2 c = 0$ is well-posed. However when the monolayer is infinitely large, it would demand a constant flux boundary condition to the entire half space, and it is well-known that in this case the Laplace equation allows only the trivial solution $c = 0$ everywhere, where particles consume all solutes and all dynamics stop.

To mathematically allow for a non-trivial solution $c(\mathbf{x}, t)$ and to physically keep the system evolving, the large scale boundary condition must be fixed to $\langle j_c \rangle = 0$, which requires a homogeneous generation of reactant at a rate S in the monolayer that balances the consumption so that the average solute consumption rate on the monolayer is zero. The result is that the large scale averaged solute concentration $\langle c \rangle(x, y, z)$ is a spatial constant not only along x, y direction in the $z = 0$ plane, but also a constant at any z . Similarly, in the 3D case a homogeneous generation of solute is also required. This makes the system 'chemically neutral' – the positive uniform chemical source balances the consumption of reactants on reactive sink particles – and ensures that the long-ranged interactions in Laplace systems are convergent (Bonnecaze & Brady, 1990). By analogy, the uniform source of reactant S is the counterpart of the constant negative 'electrostatically neutralizing background' in one component plasma.

Motion of active Janus particles

After the solute field $c(\mathbf{x}, t)$ is appropriately solved, we need to determine each particle's propulsion velocity according to (7.1). The propulsion velocity of particle

α is given by

$$U_{0,\alpha} = - (1 - \theta D_R/D_P) L(\Delta) \langle c \rangle a^3 \mathbf{B}_\alpha \frac{D_T}{a}, \quad (7.6)$$

$$\text{with } \mathbf{B}_\alpha = \int_{S_\alpha} \mathbf{n} c dS. \quad (7.7)$$

Here $D_T = k_B T / (6\pi\eta a)$ is the particle Brownian translational diffusivity. As discussed in Chapter 6, \mathbf{B}_α can also be linearly related to the environment of the particle α :

$$\mathbf{B}_\alpha = M_B(\text{Da}_\alpha, \boldsymbol{\xi}_\alpha) \cdot \begin{pmatrix} c(\mathbf{r}_\alpha) \\ \nabla c(\mathbf{r}_\alpha) \end{pmatrix}. \quad (7.8)$$

For uniformly reactive particles the linear relation is simple:

$$\mathbf{B}_\alpha = \frac{1}{D_R} \left(\frac{1}{1 - \text{Da}} \right) \mathbf{S}_\alpha = \frac{1}{\text{Da} + 2} 4\pi a^3 \nabla c(\mathbf{r}_\alpha), \quad (7.9)$$

where the concentration gradient is evaluated at the center of particle α . This is classical diffusiophoresis.

For Janus particles an accurate representation would require all gradients of the c field and that is both physically unnecessary and computationally intractable. Therefore the matrix M_B is numerically solved by BEM and truncated at dipole level, which is the minimum set to capture the self-propulsion and many-body attraction features. M_B is linearly dependent on the orientation $\boldsymbol{\xi} = (\xi_x, \xi_y, \xi_z)$ and the reaction pattern functions $g_c^z, g_{c_z}^z, g_{c_x}^x$. Details about the g functions and detailed derivations can be found in Chapter 6. Combining (7.1) and (7.8), the velocity of a single particle is given by:

$$\mathbf{U}_0 = P \boldsymbol{\xi} c - (M \mathbf{I} + A \boldsymbol{\xi} \boldsymbol{\xi}) \cdot \nabla c, \quad (7.10)$$

where P, M, A are proportionality constants describing the self-propulsion, migration down ∇c , and asymmetric migration. In dimensionless form:

$$\frac{\mathbf{U}_0}{D_T/a} = S_D \hat{P} \boldsymbol{\xi} \frac{c}{\langle c \rangle} - S_D (\hat{M} \mathbf{I} + \hat{A} \boldsymbol{\xi} \boldsymbol{\xi}) \cdot \frac{\nabla c}{\langle c \rangle/a}, \quad (7.11)$$

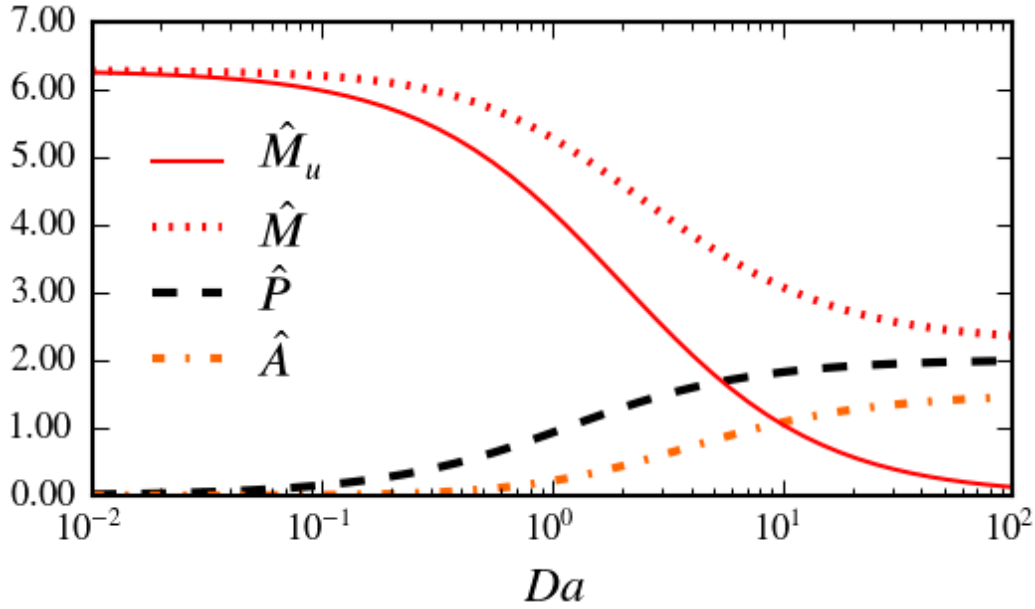


Figure 7.1: Motion functions of a Janus particle \hat{P} , \hat{M} , \hat{A} and a uniformly reactive particle \hat{M}_u .

where $\langle c \rangle$ is the average solute concentration (the ‘fuel’) in the system, and $S_D = (1 - \theta D_R/D_P)L(\Delta)a^3\langle c \rangle$, is the non-dimensionalized ‘fuel concentration’. $\hat{P} = g_{c_z}^z$, $\hat{M} = g_{c_x}^x$, and $\hat{A} = g_{c_z}^z - g_{c_x}^x$ are shown in Fig. 7.1. Also for a uniformly reactive particle, $\hat{P} = \hat{A} = 0$ and $\hat{M}_u = 4\pi/(Da + 2)$, analytically calculated with the first order reaction constants.. When $Da \rightarrow 0$, the reaction is so slow that both Janus and uniform particles approach the passive (no reaction) limit, where $\hat{M} \rightarrow \hat{M}_u \rightarrow 2\pi$.

Active particles are also subject to translational and rotational Brownian diffusivity characterized by D_T and D_{rot} , respectively. For a single free particle in 3D space $D_{rot} = (3/4)D_T/a^2$. In this work we consider the general case where D_{rot} and D_T are free to change, though they should be on the same order due to their same physical origin. For a single particle with constant propulsion velocity U_0 , and for times longer than the reorientation time $\tau_R = 1/D_{rot}$, the motion is diffusive; the long time diffusivity D_l is enhanced by self-propulsion. For free motion in 3D space, $D_l = D_T + U_0^2/6D_{rot}$, while for 2D in plane rotation $D_l = D_T + U_0^2/2D_{rot}$.

Instability in a monolayer geometry: governing equations

In this section we establish the governing equations for a chemically active system in a monolayer geometry, and we assume that the diffusive reorientation process is in the xy -plane. The orientation vector $\xi = (\cos \theta, \sin \theta)$ is set by the orientation angle θ . We also consider the dilute limit where a one-particle Smoluchowski equation for phase space density $\mathcal{P}(x, y, \theta)$ describes the particles' motion well. The solute field $c(\mathbf{x})$ is governed by Laplace's equation as discussed before, while the $c(\mathbf{x})$ field extends to the entire space $c(x, y, z)$. The concentration is altered by the reactive particles, each serving as a sink, and the $\mathcal{P}(x, y, \theta)$ field feels a 'feed-back' from the $c(\mathbf{x})$ equation. With this model we try to describe the experimental geometry where a layer of particles are immersed in a large reservoir of solutes, and to analytically capture the linear stability.

As discussed by Morris & Brady, (1995) and in Chapter 6, a key feature in such systems is Brinkman screening. That is, the long-ranged perturbation is screened to short range Brinkman length L_B , because the particles can compensate for the perturbation caused by one particle. It is a many-body effect. In 3D space the screening takes an explicit exponential form $c' \sim e^{-r/L_B}$. For the monolayer geometry the physics is the same. In fact, the chemical screening information is contained in the 'feedback factor' F_c and F_c^{3D} , which describes the response of solute concentration to perturbations in particle number density. F_c and F_c^{3D} are expressed in the wave-space depending on q and are derived later. The screening length L_B also sets an intrinsic length scale to the Laplace's equation. Outside this length, the particles cannot feel the perturbations, as shown in Chapter 6. So when individual particles move closer and induce a perturbation on the n field, those particles outside the screening length L_B do not feel the attraction coming from the cluster, while translational Brownian motion now has a chance to bring the system back to equilibrium. This competition gives a stability threshold, which will be thoroughly discussed in this work. Without screening, particles always feel attraction no matter how far they

are from the cluster and the system is unconditionally unstable.

We define the probability density in phase space as $\mathcal{P}(x, y, \theta)$, and the particle volume fraction (area fraction in monolayer) in the xy plane $\phi_A(x, y) = \pi a^2 n_A(x, y) = \pi a^2 \int_0^{2\pi} \mathcal{P}(x, y, \theta) d\theta$. $n_A(x, y)$ is the number density (per unit area) in xy plane.

Utilizing (7.10), the governing equations are:

$$-D_R(\nabla_{xy}^2 + \frac{\partial^2}{\partial z^2})c = \left(S - \kappa c(z=0) \int_0^{2\pi} \mathcal{P}(x, y, \theta) d\theta \right) \delta(z), \quad (7.12)$$

$$\frac{\partial \mathcal{P}}{\partial t} + \nabla \cdot (\mathbf{U}_0 \mathcal{P}) - D_T \nabla_{xy}^2 \mathcal{P} - D_{rot} \frac{\partial^2}{\partial \theta^2} \mathcal{P} = 0. \quad (7.13)$$

Here D_R is the solute diffusivity, $\nabla_{xy}^2 = \partial^2/\partial x^2 + \partial^2/\partial y^2$. S is the strength of the distributed source, which should satisfy $\int S dx dy = \int (\kappa c(z=0) \int_0^{2\pi} \mathcal{P}(x, y, \theta) d\theta) dx dy$ to balance the consumption of the solute by particles. κ represents a single particle's consumption rate, and depends on Da . A delta function $\delta(z)$ appears because the sources S and particles are restricted on the monolayer $z = 0$ only. \mathbf{U}_0 is the propulsion velocity in (7.10), and its components in phase space (x, y, θ) are $(U_0 \cos \theta, U_0 \sin \theta, 0)$.

Generally, each particle's effect on the $c(\mathbf{x})$ field is not only a reactive monopole κc , but also includes a dipole, quadrupole, etc., as discussed in §7.1. However here the higher moments are all ignored in the analytical analysis as their effects are weak. This is validated by the simulation results which include the dipoles.

Also, in the n equation (7.13), a single particle's propulsion \mathbf{U}_0 is used to represent the collective motion of a continuum field $\mathcal{P}(x, y, \theta)$, where we neglected any inter-particle collisions at finite ϕ and any possible many-body effects on particles' mobility. Hydrodynamic interactions are also completely ignored. The above two-equation system is the minimum form for the active particles' stability problem. Nevertheless, it preserves all the interesting aspects of the problem and also allows an elegant analytical solution with the matrix perturbation method.

Equations (7.12) and (7.13) permit a homogeneous steady state: $\mathcal{P} = \mathcal{P}_0$ and $c = c_0$ everywhere. Linear stability analysis will be considered based on this homogeneous steady state: $\mathcal{P} = \mathcal{P}_0 + \mathcal{P}'(x, y, \theta, t)$ and $c(x, y, z) = c_0 + c'(x, y, z, t)$, where $\mathcal{P}' \ll \mathcal{P}_0$ and $c' \ll c_0$. Without losing generality, a plane wave perturbation in the x direction $\mathbf{q} = (q, 0, 0)$ in the monolayer will be considered, which is then decomposed into Fourier modes in θ space:

$$\mathcal{P}' = \sum_{q,m} b_{q,m}(t) \exp(-im\theta) \exp(-iqx), \quad (7.14)$$

where m takes integer values: $m = 0, 1, 2, \dots$. By definition of the Fourier series, $b_{q,0}(t) = \frac{1}{2\pi} n_{A,q}(t)$.

At $t = 0$ the initial perturbation is $b_{q,m}(0)$, and the development of these $b_{q,m}$ modes to $t \rightarrow \infty$ will determine the stability of the system. Physically, an initial perturbation in n field will cause a change in c field, then through $U_0 \sim (c, \nabla c)$ a ‘feedback’ from c field controls the future development of the \mathcal{P}' perturbation.

The ‘feedback’ of the solute field can be determined from Equation (7.12) by Fourier transform in the z direction combined with a Fourier expansion in the x direction. The process is detailed in Appendix I. The result is:

$$c'(x, y, z = 0) = \sum_q \left(-\frac{c_0 \kappa \pi}{\mathcal{P}_0 \kappa \pi + D_R q} \right) b_{q,0}(t) e^{-iqx} = \sum_q F_c b_{q,0}(t) e^{-iqx}, \quad (7.15)$$

where we define $F_c = -c_0 \kappa \pi / (\mathcal{P}_0 \kappa \pi + D_R q) < 0$ as the ‘ c -feedback factor’, which determines the perturbation in c induced by a perturbation in \mathcal{P} .

Equation (7.13) is then linearized for \mathcal{P}' and c' :

$$\begin{aligned} & \frac{\partial \mathcal{P}'}{\partial t} + \mathcal{P}_0 \left(P \sin \theta \frac{\partial c'}{\partial y} - (M + A \sin^2 \theta) \frac{\partial^2 c'}{\partial y^2} - A \cos \theta \sin \theta \frac{\partial^2 c'}{\partial x \partial y} \right) \\ & + \mathcal{P}_0 \left(P \cos \theta \frac{\partial c'}{\partial x} - (M + A \cos^2 \theta) \frac{\partial^2 c'}{\partial x^2} - A \cos \theta \sin \theta \frac{\partial^2 c'}{\partial x \partial y} \right) \\ & + \frac{\partial \mathcal{P}'}{\partial x} (P c_0 \cos \theta) + \frac{\partial \mathcal{P}'}{\partial y} (P c_0 \sin \theta) \\ & - D_T \nabla_r^2 \mathcal{P}' - D_{rot} \frac{\partial^2}{\partial \theta^2} \mathcal{P}' = 0. \end{aligned} \quad (7.16)$$

Then we convert $\cos \theta$ and $\sin \theta$ to exponential form (equivalent to taking a Fourier series again), and substitute (7.14) and (7.15). The development of all \mathbf{b} modes is described by a linear dynamical system:

$$\frac{d}{dt}\mathbf{b}(t) = \mathbf{M}_{ins}^{\infty}\mathbf{b}(t), \quad (7.17)$$

where $\mathbf{b}(t) = (\dots, b_{q,-1}, b_{q,0}, b_{q,1} \dots)$ is an infinite dimensional vector consisting of all the Fourier modes in (7.14), whose initial condition will be denoted as $\mathbf{b}^0 = \mathbf{b}(t = 0)$. $\mathbf{M}_{ins}^{\infty}$ is also of infinite dimension and the entries are known from (7.16). By the general theory briefly described in Appendix J, the eigenvalues of matrix $\mathbf{M}_{ins}^{\infty}$ control the growth rate and each corresponding eigenvector governs a eigenmode of the instability. When all eigenvalues are negative, the homogeneous \mathcal{P}_0, c_0 state is stable.

$\mathbf{M}_{ins}^{\infty}$ can be decomposed into three parts: $\mathbf{M}_{ins}^{\infty} = \mathbf{M}_P^{\infty} + \mathbf{M}_{MA}^{\infty} + \mathbf{M}_D^{\infty}$, where they represent contributions from propulsion, migration, and diffusion respectively. \mathbf{M}_{MA}^{∞} is the simplest one with only three non-zero entries: $-\frac{1}{2}\mathcal{P}_0 F_c (A + 2M)q^2$ at $(0, 0)$ and $-\frac{1}{4}\mathcal{P}_0 F_c Aq^2$ at $(0, \pm 2)$. \mathbf{M}_D^{∞} occupies the major diagonal entries, with the (m, m) entry being $-m^2 D_{rot} - D_T q^2$. \mathbf{M}_P^{∞} puts $\frac{1}{2}ic_0 Pq$ at each sub-diagonal and super-diagonal entry.

When $P = M = A = 0$ from (7.10), the particles achieve no motion from the c field and are merely passive Brownian particles in this case. $\mathbf{M}_{ins}^{\infty} = \mathbf{M}_D^{\infty}$, which is diagonal, and all entries are negative. The solution for each mode is decoupled: $b_{q,m}(t) \propto \exp(\sigma_{q,m}t)$ and $\sigma_{q,m} = -m^2 D_{rot} - D_T q^2$. The passive Brownian system is thus unconditionally stable, as expected.

When $P = 0$ but $M, A \neq 0$, $\mathbf{M}_{ins}^{\infty} = \mathbf{M}_{MA}^{\infty} + \mathbf{M}_D^{\infty}$. In this case the only off-diagonal entry appears at $(0, \pm 2)$ and depends on A . It forms the basis for the matrix perturbation analysis, and is solved in §7.2.

When $P \neq 0$, the system becomes complicated because the subdiagonal entries

imply coupling between those θ -modes and make the eigensystem not analytically solvable.

In this work we shall analytically calculate the eigensystem of M_{ins}^∞ by matrix perturbation technique, based on the results for $P = 0$ case in §7.2. The eigenvalues and eigenvectors for the general case $\lambda_m(P)$ and $\mathbf{v}_m(P)$ are then represented by

$$\lambda_m(q; P) = \lambda_m^{(P0)} + P\lambda_m^{(P1)} + P^2\lambda_m^{(P2)} + \dots, \quad (7.18)$$

$$\mathbf{v}_m(q; P) = \mathbf{v}_m^{(P0)} + P\mathbf{v}_m^{(P1)} + P^2\mathbf{v}_m^{(P2)} + \dots, \quad (7.19)$$

where for clarity \mathbf{v}_m will be represented as sum of basis vectors $\mathbf{e}_i = (\dots, 0, 0, 1, 0 \dots)$, with 1 at the i th position. A similar expansion on powers of q in the long-wave length limit $q \rightarrow 0$ is also calculated for verification and greater insight.

Simulation: accelerated Laplacian dynamics

To verify the analytical results, a Brownian dynamics simulation is utilized to track the system's evolution. We consider N particles in an L -by- L square periodic box and L is guaranteed to be much larger than the wavelength corresponding to the maximum growth rate.

The problem is now the following: for a system of active particles at locations $\mathbf{X}(t)$, we need to solve the propulsion velocity U_0 according to orientation $\boldsymbol{\xi}$, which by equation (7.1) requires a solution of the reactant concentration field governed by the steady Laplace's equation at all field points \mathbf{x} outside the particles, subject to a first order surface reaction boundary condition for either (or both) uniformly reactive particles and Janus particles. The active particles are then advanced to a new location from the overdamped Langevin equation incorporating Brownian translation and rotation:

$$\Delta \mathbf{X} = U \Delta t + \Delta \mathbf{X}^B + \Delta \mathbf{X}^{HS}, \quad (7.20)$$

$$\Delta \theta = \Delta \theta^B, \quad (7.21)$$

where the Brownian displacement has zero mean, $\langle \Delta \mathbf{X}^B \rangle = 0$ and covariance $\langle \Delta \mathbf{X}^B \Delta \mathbf{X}^B \rangle = 2D_T \Delta t$. $\Delta \mathbf{X}^{HS}$ is a hard-sphere displacement to prevent particles from overlapping, determined by a potential-free algorithm (Foss & Brady, 2000; Heyes & Melrose, 1993). $\Delta \theta^B$ is the rotational Brownian motion in xy plane, satisfying $\langle \Delta \theta^B \rangle = 0$, and $\langle \Delta \theta^B \Delta \theta^B \rangle = 2D_{rot} \Delta t$. Once the active particles have been advanced to their new locations and orientations, a new concentration field $c(\mathbf{x})$ must be found and the process is repeated until a steady state is reached. $\Delta \theta$ is a diffusive reorient event at each timestep and is calculated with the unbiased move method (Beard & Schlick, 2003). Equation (7.21) employs a simple Euler scheme, for clarity. Higher order schemes such as the Adams-Bashforth multi-step scheme are also easy to include in the simulation. In our tests, using an Euler scheme has no impact on the system dynamics.

The difficulty lies in the accurate & efficient solution of $c(\mathbf{x})$ at each timestep. The method originates from Bonnecaze & Brady, (1990) and is detailed as the Accelerated Laplace's Dynamics (ALD) in Chapter 6. Each particle's velocity \mathbf{U} is calculated at each timestep with ALD, as driven by the solute concentration field $c(\mathbf{r})$.

Instability dispersion relation $\sigma(q)$ is then extracted from the wave-space number density profile $\hat{n}_A(\mathbf{k})$, by an ensemble average of simulations. In each ensemble, a large number (usually 1200) of systems are simulated starting from the same homogeneous but random positions of particles. However, the orientation of each particle is differently randomized from system to system. In this way, the ensemble average of initial perturbation is only on the isotropic mode $m = 0$, and no average orientation distribution is perturbed. Mathematically it means $\langle \hat{n}_A(\mathbf{k}, t = 0) \rangle \neq 0$ and $\langle b_{m \neq 0}^0 \rangle = 0$. Also, the random number seeds to calculate the Brownian translation and rotation are different from system to system. In this way, the ensemble explores different trajectories starting from the same initial configuration. The large number of systems allows us to average out the tremendous noise resulting from

Brownian motion. Also importantly, the simulations track the system for a short time (about $10a^2/D_T$) to make sure we are capturing the linear stability regime. In fact, when the simulation is stopped the particles barely move so perturbation \mathcal{P}' is guaranteed to be small.

The number density in (x, y) space $n_A(x, y)$ is transformed to wave space $\hat{n}_A(\mathbf{k}, t)$, where $\mathbf{k} = (k_x, k_y)$ is the discretized wave space vector. From Hansen & McDonald, (2013), $\hat{n}_A(\mathbf{k}, t) = \sum_{\beta} \mathbf{r}_{\beta}(t) \cdot \mathbf{k}$, for each particle β . Then $\langle \hat{n}_A(\mathbf{k}, t) \rangle \propto \exp(\sigma(\mathbf{k})t)$ is fitted from simulation data for each discrete \mathbf{k} to get $\sigma(\mathbf{k})$. We observed that $\sigma(\mathbf{k})$ is isotropic in all our simulations, i.e., σ is a function of $|\mathbf{k}|$ only, independent of the direction of \mathbf{k} . Therefore an isotropic dispersion relation $\sigma(q = |\mathbf{k}|)$ is averaged for each ensemble, and is compared with analytical solution.

With this method, we are able to extract the developing perturbation $n'_A(x, y, t)$, which corresponds to the development of $m = 0$ mode $b_{q,0}(t)$ in the analytic result.

7.2 The base case: $P = 0$

In this case $M_{ins}^{\infty} = M_{MA}^{\infty} + M_D^{\infty}$ allows an analytical solution of the eigensystem, and the parameters $(M, A, D_R, \kappa, D_T, D_{rot}, c_0, \mathcal{P}_0)$ are arbitrary and none of them is required to be small. The eigensystem solution for $m \neq 0$ is:

$$\lambda_m = -m^2 D_{rot} - q^2 D_T, \quad (7.22)$$

$$\mathbf{v}_m = \mathbf{e}_m, \quad (7.23)$$

where $\mathbf{e}_m = (\dots, 0, 0, 1, 0, \dots)$ is the basis vector in the linear space and 1 appears on the m th position. For $m = 0$:

$$\lambda_0 = -q^2 D_T - q^2 \left(M + \frac{1}{2} A \right) \mathcal{P}_0 F_c, \quad (7.24)$$

$$\mathbf{v}_0 = \mathbf{e}_0 + \frac{\pi A c_0 \kappa \mathcal{P}_0 q^2}{2 (\pi c_0 \kappa \mathcal{P}_0 q^2 (A + 2M) + 8 D_{rot} (D_R q + \pi \kappa \mathcal{P}_0))} (\mathbf{e}_2 + \mathbf{e}_{-2}). \quad (7.25)$$

It is clear from the eigenvector \mathbf{v}_0 that the only coupling should appear at $m = 0$ and $m = \pm 2$ because \mathbf{v}_0 and $\mathbf{v}_{\pm 2}$ are linearly dependent, and it is induced by asymmetric

down-gradient diffusiophoresis represented by A .

The general solution for $\mathbf{b}(t)$ is straightforward for $m \neq \pm 2$:

$$b_{q,m}(t) = \exp(\lambda_m t) b_{q,m}^0. \quad (7.26)$$

The coupling between $m = 0$ and $m = \pm 2$ appears at $b_{q,\pm 2}$:

$$\begin{aligned} b_{q,\pm 2}(t) &= \exp(\lambda_{\pm 2} t) b_{q,\pm 2}^0 + \frac{\exp(\lambda_0 t) - \exp(\lambda_{\pm 2} t)}{2 + \frac{4M}{A} - \frac{16D_{rot}}{Aq^2\mathcal{P}_0F_c}} b_{q,0}^0 \\ &= \exp(\lambda_{\pm 2} t) b_{q,\pm 2}^0 + \mathbf{v}_0 \cdot \mathbf{e}_{\pm 2} (\exp(\lambda_0 t) - \exp(\lambda_{\pm 2} t)) b_{q,0}^0. \end{aligned} \quad (7.27)$$

For uniformly reactive particles, $A = 0$, $\mathbf{v}_0 = \mathbf{e}_0$ and the θ modes are completely decoupled. Note that λ_m is symmetric for positive and negative m . One can appreciate the symmetry in $\pm m$ by realizing that the $\exp(\pm im\theta)$ modes can be rearranged into $\cos m\theta$ and $\sin m\theta$, which are equivalent with only a phase shift $\pi/2$. Based on the above exact solution, we can discuss the instability and orientational order.

The instability threshold and growth rate $\sigma(q)$

When $\lambda_m < 0$ for any m, q , the system is stable. By (7.22) and (7.24), $\lambda_{m \neq 0}$ is always negative, and $\lambda_0 < 0$ is guaranteed when $D_T > (M + \frac{1}{2}A)\mathcal{P}_0F_c$ for any q . Note that by definition (7.15) F_c also depends on q . The dispersion relation of growth rate $\sigma(q)$ is given by λ_0 :

$$\sigma = \lambda_0 = \frac{-2D_R D_T q^3 - 2(D_T - c_0(M + A/2))\kappa\mathcal{P}_0\pi q^2}{\kappa\mathcal{P}_0\pi + D_R q}, \quad (7.28)$$

where one should remember that $2\pi\mathcal{P}_0 = n_{A0} = \phi_0/\pi a^2$. The instability threshold is very simple. Realizing that by definition all parameters in (7.28) are positive, $\sigma < 0$ is guaranteed by ensuring:

$$\frac{(M + \frac{1}{2}A)c_0}{D_T} < 1. \quad (7.29)$$

We can define dimensionless $M_C = (M + \frac{1}{2}A)c_0/D_T$ as the strength of phoretic migration relative to Brownian diffusion, and the instability threshold is $M_C^* = 1$.

When phoretic migration wins, $M_C > 1$ and the system is unstable. In a particular system, M and A are determined by Da , and therefore M_C is controlled by solute concentration c_0 . From this perspective, M_C is the scaled ‘fuel’ concentration.

When the system is unstable, the growth rate consists of a positive q^2 term and a negative q^3 term. Thus there is a maximum growth rate σ_{max} with corresponding q_{max} :

$$q_{max} = \frac{\pi \kappa \mathcal{P}_0}{4D_R} \left(M_C + \sqrt{M_C(M_C + 8)} - 4 \right), \quad (7.30)$$

$$\sigma_{max} = \frac{\pi^2 D_T \kappa^2 \mathcal{P}_0^2 \left(-\sqrt{M_C(M_C + 8)} + 3M_C \right) \left(M_C + \sqrt{M_C(M_C + 8)} - 4 \right)^2}{8D_R^2 \left(M_C + \sqrt{M_C(M_C + 8)} \right)}. \quad (7.31)$$

Both q_{max} and σ_{max} are monotonically increasing with M_C . Around the stability boundary $M_C^* = 1$, we can calculate the leading order dependence on the ‘instability driving force’ $M_C - 1$:

$$q_{max} \approx \frac{2\pi \kappa \mathcal{P}_0}{3D_R} (M_C - 1) + O(M_C - 1)^2, \quad (7.32)$$

$$\sigma_{max} \approx \frac{8\pi^2 D_T \kappa^2 \mathcal{P}_0^2}{27D_R^2} (M_C - 1)^3 + O(M_C - 1)^4. \quad (7.33)$$

As the system approaches the stability boundary ($M_C \rightarrow 1$), both q_{max} and σ_{max} are asymptotically zero.

Uniformly reactive particles ($P = 0$, $A = 0$) are used in simulation to check the validity of the growth rate (7.28). Also the L -by- L square periodic simulation box is guaranteed to be large enough: $L \gg 2\pi/q_{max}$. The comparison is shown in Fig. 7.2.

Orientation-order induced by the particle asymmetry A

Equation (7.27) shows that when the initial perturbation is isotropic, i.e., the perturbation $b_{q,m}^0 = 0$ for all $m \neq 0$, the development $b_{q,\pm 2}(t > 0)$ can be non-zero. Beyond that simple coupling, (7.27) also shows that nematic order is induced.

Remember that $\lambda_{\pm 2} < 0$ is always true and λ_0 depends on M_C . Therefore, when $M_C > 1$, λ_0 can be positive for some q , and then $b_{q,\pm 2}$ will be exponentially

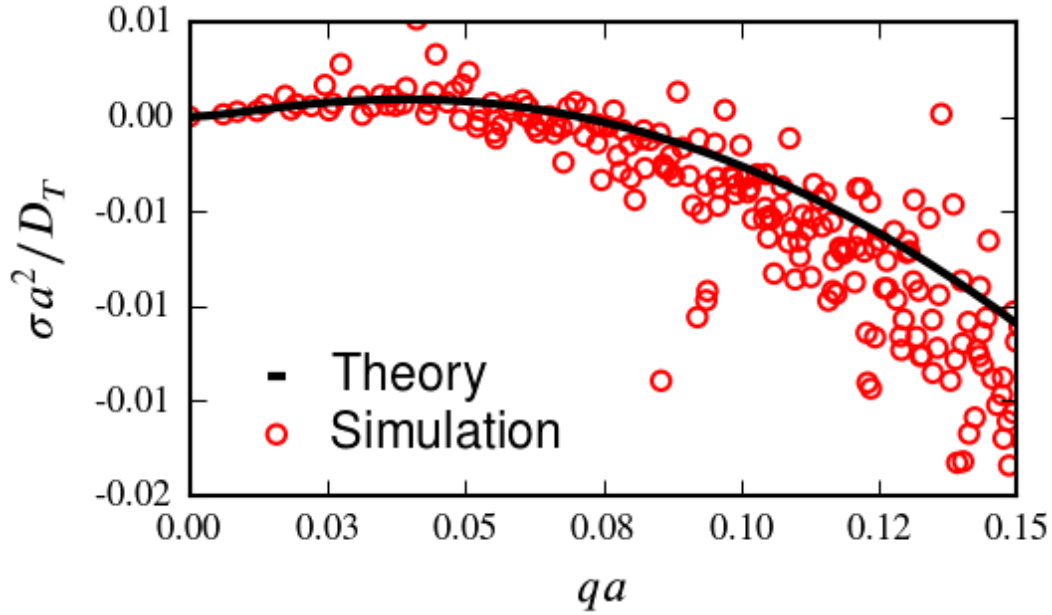


Figure 7.2: The instability dispersion relation $\sigma(q)$ for uniformly reactive particles $P = A = 0$ at $Da = 2$. The theory is given by (7.28), and the simulation is extracted from an ensemble of 1200 systems with $N = 1668$ particles in a periodic box size $L = 512a$. $\phi = 0.02$ and $M_{c_0}/D_T = 2$.

increasing until the perturbation develops beyond the linear stability regime. When $M_C < 1$, λ_0 is always negative, but we can show that $|\lambda_0| < |\lambda_{\pm 2}|$ is guaranteed. Therefore when the system approaches the homogeneous steady state, $b_{q,\pm 2}$ first grows to non-zero and eventually decays to zero by rotational Brownian motion.

By the definition (7.14) of the Fourier expansion, $b_{q,\pm 2}$ represents quadrupolar order $\sin 2\theta, \cos 2\theta$ in the diffusiophoresis front of the particles. It is also clear from (7.27) that this θ -order is proportional to A , the asymmetric diffusiophoretic migration. This originates from $A\xi\xi\nabla c$ in the equation (7.10) which is nematic ordered. When a gradient ∇c is imposed, some particles with favorable orientation ($\xi = \pm\nabla c/|\nabla c|$) will move faster than other particles, so in the moving front the nematic order emerges. If $A = 0$, particles are symmetric and there is no such effect.

This θ -order is one of the distinguishing features of asymmetric self-propulsion particles, and we shall see it again when we solve the general case $P \neq 0$ in §7.3.

Coarse-grained model & chemical screening

In this part we briefly discuss a coarse-grained model and discuss the connection between the instability and chemical screening.

We assume that the rotational diffusivity D_{rot} is large enough so that the particles are isotropic in θ -space. In this regime we directly work with the number density field $n_A(x, y) = \int_0^{2\pi} \mathcal{P}(x, y, \theta) d\theta$:

$$\frac{\partial n_A}{\partial t} - D_T \nabla_{xy}^2 n_A = -\nabla_{xy} \cdot (\langle \mathbf{U}_0 \rangle_{\xi} n_A), \quad (7.34)$$

without invoking the full Smoluchowski equation (7.13) of $\mathcal{P}(x, y, \theta)$. Here $\langle \mathbf{U}_0 \rangle_{\xi}$ is the coarse-grained velocity of particles under the chemical field c . The $c(x, y, z)$ field equation is the same as (7.12). Here, because we have assumed $P = 0$, according to (7.10) we must have $\langle \mathbf{U}_0 \rangle_{\xi} \propto \nabla c$. The linear stability analysis of the density field $n_A(x, y)$ follows the similar route as for $\mathcal{P}(x, y, \theta)$:

$$\sigma(q) = -D_T q^2 + q^2 F_c \left(-\langle \mathbf{U}_0 \rangle_{\xi} / \nabla c \right). \quad (7.35)$$

$\langle \mathbf{U}_0 \rangle_{\xi}$ can be calculated by an isotropic average of (7.10), setting $P = 0$:

$$\langle \mathbf{U}_0 \rangle_{\xi} = \frac{\int - (M \mathbf{I} + A \xi \xi) \cdot \nabla c d\xi}{\int 1 d\xi} = -(M + \frac{1}{2}A) \nabla c, \quad (7.36)$$

which shows a simple down-gradient diffusiophoresis. Substituting this into (7.35), the coarse-grained approach gives exactly the same solution as the exact approach, (7.28), with \mathcal{P}_0 replaced by $n_{A0} = 2\pi \mathcal{P}_0$.

With this coarsened-grained model, we can easily extend our discussion from a monolayer to a full 3D system, without solving the detailed rotational diffusion in 3D orientation space. In this case $n(x, y, z)$ and $c(x, y, z)$ both extend to the entire 3D space and are governed by:

$$\frac{\partial n}{\partial t} - D_T \nabla^2 n = -\nabla \cdot (\langle \mathbf{U}_0 \rangle_{\xi} n), \quad (7.37)$$

$$-D_R \nabla^2 c = S - \kappa c n. \quad (7.38)$$

In this case, the linear perturbation analysis proceeds with $n = n_0 + n'$, and can be solved with the same method. n' induces a change c' to the homogeneous c_0 field, and c' is solvable as the counterpart of (7.15) in the 3D case:

$$c'(x, y, z) = \sum_q \left(-\frac{\kappa c_0}{\kappa n_0 + D_R q^2} \right) n'_q(t) e^{-iqx} = \sum_q F_c^{3D} n'_q(t) e^{-iqx}, \quad (7.39)$$

The instability growth rate is the same as (7.35), with only F_c and $\langle U \rangle_\xi$ replaced by their 3D counterparts:

$$\sigma^{3D} = \frac{-D_T q^4 + \kappa n_0 \left(c_0 \left(-\langle U_0 \rangle_\xi^{3D} / \nabla c \right) - D_T \right) q^2}{D_R q^2 + \kappa n_0}. \quad (7.40)$$

For 3D rotational diffusivity, $\langle U_0 \rangle_\xi^{3D} = -(M + \frac{1}{3}A)\nabla c$, averaged on the spherical space of ξ . In this case, the instability threshold for the 3D system is $M_C^{3D*} = c_0(M + \frac{1}{3}A)/D_T = 1$, the same as the monolayer case. As discussed in § 7.1, the existence of a threshold is due to chemical Brinkman screening. Here, the chemical screening information is contained in the feedback factor F_c and F_c^{3D} , expressed in the wavenumber depending on q . $F_c^{3D} = -\kappa c_0 / (\kappa n_0 + D_R q^2) = -c_0/n_0(1 + L_B^2 q^2)$, which is the wavenumber form of the exponentially screened attraction $\exp(-r/L_B)$. In wavenumber, the competition between screened diffusio-phoretic attraction and the translation Brownian $-D_T q^2$ gives an stability threshold $M_C = c_0 \left(-\langle U_0 \rangle_\xi / \nabla c \right) / D_T$.

For Janus particles with $P \neq 0$, which will be discussed in §7.3, chemically screening is still applicable and to the leading order the screening length for $P = 0$ particles is still applicable, as shown in Chapter 6. As a result, we shall see that the solution structure of instability growth rate $\sigma(q)$ and the instability threshold M_C^* are very similar to the $P = 0$ case.

7.3 The general case with propulsion: $P \neq 0$

When $P \neq 0$, M_p^∞ introduces nonzero entries $ic_0 P q/2$ on sub- and super-diagonals of the instability matrix M_{ins}^∞ , so the eigenvalues are modified and the eigenvectors

are no longer perpendicular to each other. Physically, M_p^∞ induces an $O(c_0P)$ coupling between those θ -modes, and may change the dispersion relation $\sigma(q)$. Also by (7.10), one can appreciate that the coupling just scales as the swim velocity $U_0 = c_0P$ in the initial homogeneous state (\mathcal{P}_0, c_0) .

Due to the coupling the m modes in θ space no longer behave as $b_{q,m}(t) \propto \exp(\sigma_{q,m}t)$. Instead, they form ‘eigenmodes’, where several $b_{q,m}$ modes may develop together and this ‘eigenmode’ is given by the eigenvectors of M_{ins}^∞ . The coupling is determined by the entry $\frac{1}{2}ic_0Pq$. When we perturb the system with some monochromatic perturbation where $b_{q,m}^0 = 0$ except for some $m = m_s$, all m modes will be excited by this m_s initial perturbation in the developing fluctuation \mathcal{P}' . Qualitatively in $M_{ins}^\infty = \frac{1}{2}ic_0Pq$, the imaginary unit i means a phase shift of $\pi/2$ in wave form and c_0Pq governs the magnitude of the excited modes.

In this case M_{ins}^∞ becomes an infinite dimensional matrix and the analytical solution for eigenvalues and eigenvectors is not possible. Since we are interested in the role of propulsion on the stability threshold M_C^* and the dispersion relation, we can expand the eigensystem of M_{ins}^∞ as the perturbation series of this propulsion parameter P .

Mathematically, this can be done by matrix perturbation theory, with P a perturbing variable. Note that choosing P as the perturbation parameter is equivalent to choosing c_0P or c_0Pq since they always appear together in M_p^∞ . Nevertheless by choosing P we can utilize the exact solution for the $P = 0$ case in (7.24). The eigenvalue $\lambda_0(q; P)$ and eigenvector $v_0(q; P)$ can be expanded as series of P . The dispersion relation $\sigma(q; P)$ is still governed by the 0 mode eigenvalue $\lambda_0(q; P)$, because those $m \neq 0$ modes are all governed by $-m^2 D_{rot} q^2$ and are almost always negative. By calculating $v_0(q; P)$ we can work out the coupling of θ modes due to propulsion.

The detailed procedures are described in Appendix K, and the full solutions are complicated and included in Appendix L for reference. In this section we focus

on the physical effects and compare the analytical solution $\sigma(q; P)$ with simulation results.

Eigensystem expansion for small P

At small P , the $O(P)$ and $O(P^3)$ corrections to instability λ_0 are both zero:

$$\lambda_0(q; P) \approx \lambda_0 - O\left(\frac{c_0^2 P^2 q^3 D_R}{D_{rot} \kappa \mathcal{P}_0}\right) - O\left(\frac{c_0^3 A P^2 q^4}{D_{rot}^2}\right) + O(P^4), \quad (7.41)$$

where the two terms represent effect of self-propulsion P and effect of the coupling between propulsion and asymmetric migration A . Note that the effect of coupling occurs at q^4 , which is one order higher than the propulsion's q^3 dependence. The full solution can be found in Appendix L. Also we shall see that this coincides with the long wavelength limit $q \rightarrow 0$ result in §7.3 and implies important physics for active matter, which shall be addressed later in §7.4 when we build a coarse-grained model.

The expansion of eigenvector $\mathbf{v}_0(P)$ at small P , starting from (7.22) can also be calculated. The full analytic expression can also be found in Appendix L. Here, we discuss the leading order perturbation $\mathbf{v}_0(q; P) = \mathbf{v}_0^{(P0)} + P\mathbf{v}_0^{(P1)} + P^2\mathbf{v}_0^{(P2)} + \dots$:

$$\mathbf{v}_0^{(P1)} = O\left(\frac{ic_0 D_R q^2}{D_{rot} \kappa \mathcal{P}_0}\right) (\mathbf{e}_1 + \mathbf{e}_{-1}) + O\left(\frac{iAc_0^2 q^3}{D_{rot}^2}\right) (\mathbf{e}_3 + \mathbf{e}_{-3}), \quad (7.42a)$$

$$\mathbf{v}_0^{(P2)} = -O\left(\frac{q^3 c_0^2 D_R}{D_{rot}^2 \kappa \mathcal{P}_0}\right) (\mathbf{e}_2 + \mathbf{e}_{-2}) - O\left(\frac{q^4 A c_0^3}{D_{rot}^3}\right) (\mathbf{e}_4 + \mathbf{e}_{-4}). \quad (7.42b)$$

According to the general theory detailed in Appendix J, an arbitrary initial perturbation $\mathbf{b}(t=0)$ develops as follows:

$$\mathbf{b}(t) = C_0 \exp(\lambda_0(P)t) \mathbf{v}_0 + C_{-1} \exp(\lambda_{-1}(P)t) \mathbf{v}_{-1} + C_1 \exp(\lambda_1(P)t) \mathbf{v}_1 + \dots, \quad (7.43)$$

where C_i s are constants determined by initial condition $t=0$ in the above equation.

Similarly, the other eigenvalues and eigenvectors are all perturbed: $\lambda_m(q; P) \sim \lambda_m + O(P^2) + \dots \sim -D_T q^2 - D_{rot} m^2 + O(P^2) < 0$, and $\mathbf{v}_m(q; P) \sim \mathbf{v}_m + O(iP) + \dots =$

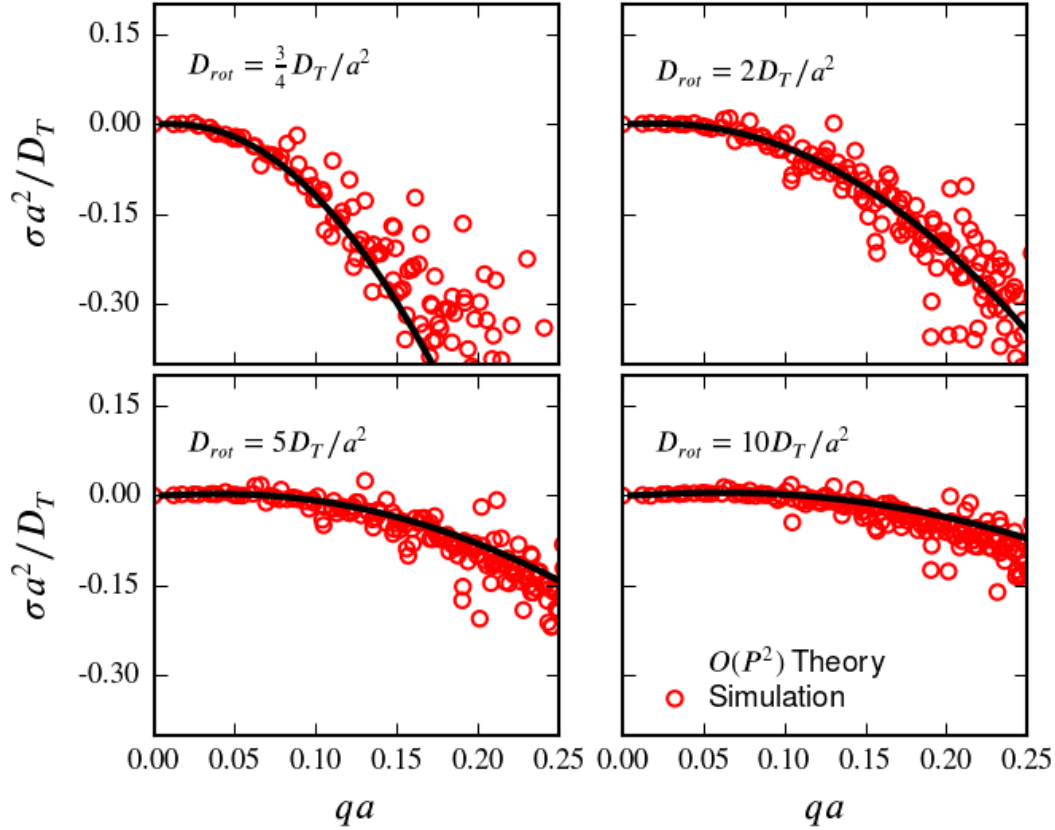


Figure 7.3: The instability dispersion relation $\sigma(q)$ for $Da = 5$ Janus particles. The theory is (7.28) with the first correction of $O(P^2)$, and the simulations are averaged over an ensemble of 1200 systems. $N = 1668$ particles are simulated with periodic box size $L = 512a$. $\phi = 0.02$. $M_C = (M + A/2)c_0/D_T = 12 \gg M_C^* = 1$ to ensure that instability is significant for quantitative measurement, but not too large to go beyond the linear instability regime.

$e_m + O(iP) + \dots$. Thus in the vicinity of $P = 0$ these $m \neq 0$ modes are controlled by rotational diffusivity $m^2 D_{rot}$, and thus for all $m \neq 0$ modes $C_m \exp(\lambda_m(P)t) \mathbf{v}_m$ quickly disappears and only the $C_0 \exp(\lambda_0(P)t) \mathbf{v}_0$ governs the growth of $\mathbf{b}(t)$. So the dispersion relation $\sigma(q; P)$ can be described by $\lambda_0(q; P)$. $\sigma(q; P)$ with the leading order $O(P^2)$ correction agrees well with the simulation measured dispersion relation $\sigma(q; P)$, as shown in Fig. 7.3.

The growth of the leading mode $C_0 \exp(\lambda_0(P)t) \mathbf{v}_0$ also shows the coupling between the m -modes. We shall briefly discuss the role of propulsion P in the coupling by setting $A = 0$, as the $A \neq 0$ case has been discussed in §7.2. In this case, to leading

order:

$$v_0(q; P) = e_0 + O\left(\frac{ic_0 P q^2 D_R}{D_{rot} \kappa \mathcal{P}_0}\right)(e_1 + e_{-1}) - O\left(\frac{c_0^2 P^2 q^3 D_R}{D_{rot}^2 \kappa \mathcal{P}_0}\right)(e_2 + e_{-2}), \quad (7.44)$$

where by definition e_0 represents an isotropic distribution in θ -space, $e_{\pm 1}$ means polar order and $e_{\pm 2}$ means quadrupolar order. Such coupling means an isotropic perturbation will develop together at growth rate $\sigma(q; P)$ with θ -order perturbation.

Such θ -order coupling comes solely from the propulsion P . It can be understood by considering the simplest model with only two points r_1 and r_2 , where particles isotropically swim at velocity $Pc_1 \neq Pc_2$. When $n_1 = n_2 = n$, the flux of particles from r_1 to r_2 will be $j_{12} \propto nPc_1$ and $j_{21} \propto nPc_2$. At next instant of time, particles with orientation $r_1 \rightarrow r_2$ move to r_2 and vice versa. Because the flux $j_{12} \neq j_{21}$ since $Pc_1 \neq Pc_2$, the θ distribution at both points is no longer isotropic, except when rotational diffusivity is infinitely fast ($D_{rot} \rightarrow \infty$) to retain the isotropic distribution. Faster swimming and slower rotational diffusivity means more θ order emerges in the form of coupling between the orders, and this explains the scaling in (7.44).

Eigenvalue solution for arbitrary P : the long wavelength limit $q \rightarrow 0$

When P is not close to zero, the above perturbation solution for small P is no longer valid. Nevertheless, we can proceed analytically for arbitrary P but small q , by realizing that M_p^∞ is also linearly dependent on wavenumber q , and the instability, as a collective behavior, usually happens at the long wavelength limit where the length scale of collective motion is far larger than single particle radius. In fact, since translational Brownian motion is a stabilizing effect as $-D_T q^2 < 0$, for large q the system is always stable. Thus the small q limit gives enough relevant information about the system stability in $\sigma(q)$.

Starting from (7.19), it is straightforward to solve the equation such that $\lambda_0^{(q0)} = 0$, and the perturbation series for arbitrary P, M, A is:

$$\lambda_0(q) = \lambda_0^{(q0)} + q\lambda_0^{(q1)} + q^2\lambda_0^{(q2)} + \dots, \quad (7.45)$$

where $\lambda_0^{(q0)} = 0$ and

$$\lambda_0^{(q1)} = 0, \quad (7.46a)$$

$$\lambda_0^{(q2)} = -D_T + c_0 \left(M + \frac{A}{2} \right), \quad (7.46b)$$

$$\lambda_0^{(q3)} = -\frac{c_0 D_R (A + 2M)}{2\pi\kappa\mathcal{P}_0} - \frac{c_0^2 D_R P^2}{2\pi D_{rot}\kappa\mathcal{P}_0}, \quad (7.46c)$$

$$\lambda_0^{(q4)} = -\frac{Ac_0^3 P^2}{32D_{rot}^2} + \frac{c_0 D_R^2 (A + 2M)}{2\kappa^2 \mathcal{P}_0^2 \pi^2} + \frac{c_0^2 D_R^2 P^2}{2D_{rot}\kappa^2 \mathcal{P}_0^2 \pi^2}. \quad (7.46d)$$

At leading order, $\sigma(q) \sim O\left(-D_T + c_0\left(M + \frac{A}{2}\right)\right)q^2$, while the first correction given by propulsion P is negative and at a higher order of q : $O(-P^2 q^3)$. This is exactly the same result as given by the P perturbation we showed in (7.41): self-propulsion P stabilizes the system, but it appears at a higher order of wave number $O(q^3)$.

More importantly, the above expansion in q allows us to locate the instability threshold in the parameter space. In fact, the instability threshold depends only on the sign of the second order correction $\lambda_0^{(q2)}$. When $\lambda_0^{(q2)} > 0$, no matter how $\lambda_0^{(q3)}$ and higher order terms change, the growth rate $\lambda_0(q)$ must be positive around the $q \rightarrow 0$ limit. The boundary is thus located at $M_C^* = c_0(M + A/2)/D_T = 1$, the same value we have seen in the $P = 0$, non-swimming case (7.29), as shown in Fig. 7.4. As we increase M_C and $P(\text{Da})$, the particles swim faster but the boundary is unchanged. D_{rot} is irrelevant in the diagram because rotational Brownian motion appears together with self-propulsion, which is on a higher order of wave number and has no impact on the stability threshold. Physically, it means that the isotropic diffusiophoretic attraction and Brownian motion governs the threshold. The number density \mathcal{P}_0 also does not matter. If we extend our analysis to finite number density, many-body effects on the reactivity κ , the swim velocity (7.10), and particle-particle collisions must be properly included, which is beyond the scope of the current work. Nevertheless, those effects can usually be written as a series as $a_0 + a_1\phi + a_2\phi^2 + \dots$ and thus can be included in principle with the current matrix-perturbation framework, by writing $M_{ins}^\infty(\phi)$ as series of ϕ .

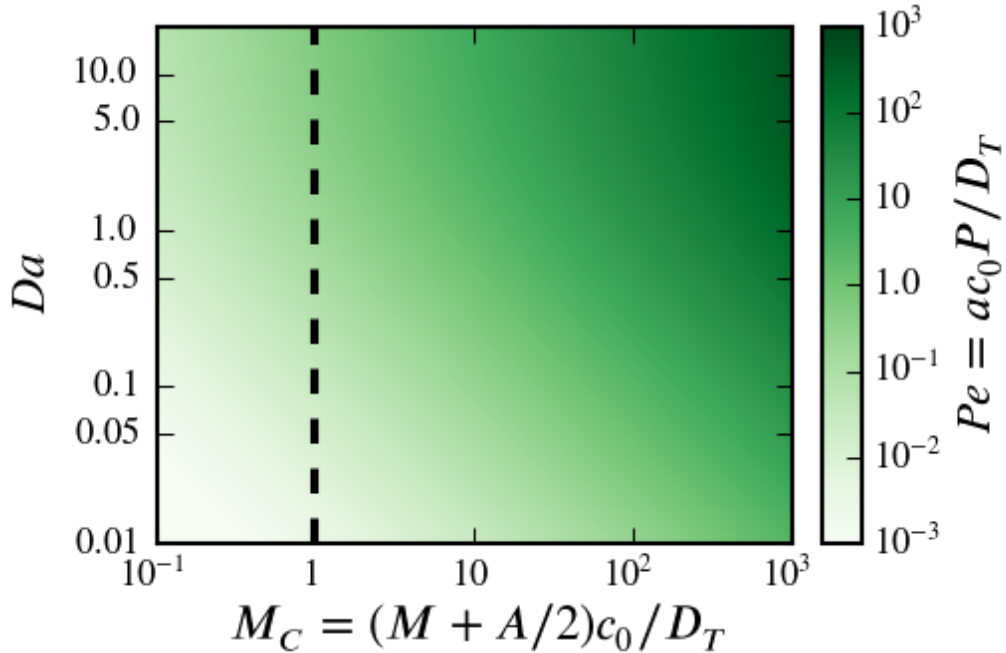


Figure 7.4: The parameter space (M_C, Da) and the instability threshold $M_C^* = 1$. The threshold is the same for arbitrary D_{rot} and arbitrary number density as long as it is dilute $\mathcal{P}_0 \rightarrow 0$. The colormap is for a single particle's non-dimensionalized swim velocity $c_0P/(D_T/a)$. Faster chemical reaction (larger Da) and more 'fuel' (higher c_0) gives higher swim velocity.

Effect of propulsion P : fast and slow reactions

In §7.3, the stability dispersion relation $\sigma(q)$ is given as series of both P and q . The effect of self-propulsion P , as well as rotation D_{rot} , appears at $\lambda_0^{(q^3)}$, while the instability threshold is determined by $\lambda_0^{(q^2)}$. At q^3 , propulsion P does not change the boundary $M_C^* = 1$, but it does strongly affect the shape of the dispersion relation $\sigma(q; P)$. As shown in Fig. 7.1, P, M, A are all controlled by chemical reaction rate Da .

When $Da \rightarrow 0$, the reaction is so slow that particles cannot generate significant propulsion, and so $P \rightarrow 0$. In this case, the third order correction is asymptotically zero as P^2 , also physically the particles behave very similarly to those passive particles ($P = 0$): σ_{max} and q_{max} are monotonically increasing as M_C increases. In the other limit where $Da \rightarrow \infty$, self-propulsion approaches its diffusion-limited

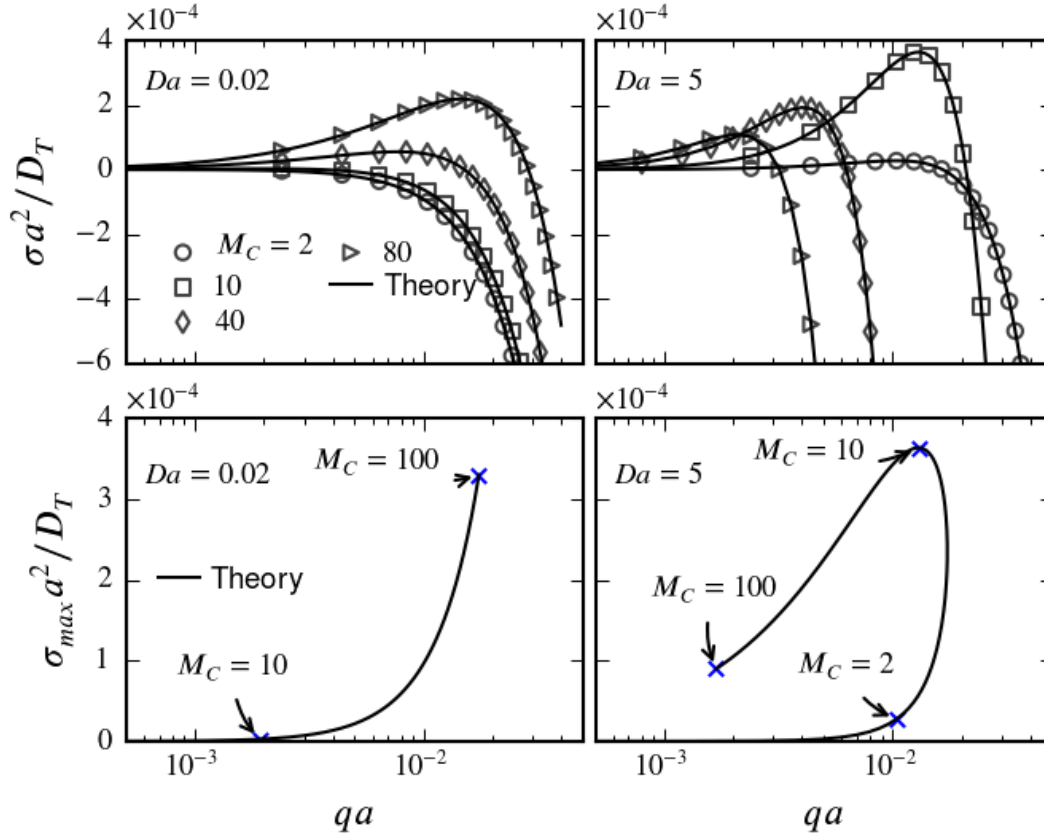


Figure 7.5: The instability dispersion relation $\sigma(q)$ for $Da = 0.02$ and $Da = 5$ Janus particles. The symbols are numerical results for M_{ins}^∞ truncated at 15×15 . The solid lines $\sigma(q)$ and the σ_{max} are calculated with the $O(P^3)$ full solution in Appendix (L). $a^2 D_{rot} = D_T$ and $\phi_0 = 0.02$ is fixed.

value $P \sim Da/(1 + Da) \sim O(1)$. In this case the negative $O(q^3)$ term shows significant effect: $\sigma(q)$ is stabilized by this negative $O(q^3)$ term, meanwhile the σ_{max} and q_{max} are no longer monotonically increasing. They show a peak at some M_C and then are quickly suppressed towards zero by self-propulsion. In fact we can show that they both approach zero when $M_C \rightarrow \infty$, in the limit $Da \rightarrow \infty$.

A comparison of $\sigma(q; P)$ for $Da = 0.02$ and $Da = 5$ is shown in Fig. 7.5. The $\sigma(q)$ and σ_{max} are calculated based on the full solution (L.3), up to P^2 , and thus are not limited to the small q limit. The behavior shows clearly what we have estimated. Finite self-propulsion P does not change the boundary $M_C^* = 1$ as $\sigma_{max} > 0$ is guaranteed for $M_C > 1$ no matter what P . Meanwhile σ_{max} can be suppressed by

self-propulsion. It can be understood that Janus particles with $P > 0$ can escape the attraction by self-propulsion, if the orientation is different from the ∇c direction.

We also compared the result given by the above perturbation method and the numerical solution, in which the eigenvalues of M_{ins}^∞ are calculated numerically by an eigensystem solver for a truncated finite dimensional M_{ins}^∞ . We used a 15×15 truncation, which is tested and guaranteed to be large enough. The comparison result is also shown in Fig. 7.5.

7.4 Active flux and continuum mechanics

In last section we solved the detailed model for M_{ins}^∞ . In sum, we calculated the $\sigma(q)$ up to $O(P^3)$ and $O(q^4)$, and the two different expansion series agree with each other. We showed the coupling between different θ -modes by calculating $v_0(P)$ up to $O(P^2)$. The instability threshold is found at $M_C^* = 1$. Also we discussed the stabilization effect of propulsion P on σ_{max} . In this section, we seek a simpler solution based on the continuum mechanics of active matter (Takatori *et al.*, 2014; Yan & Brady, 2015a) without invoking the full M_{ins}^∞ including all θ -modes.

We shall start from the coarse-grained $P = 0$ case described in §7.2, and proceed in the $D_{rot} \rightarrow \infty$ limit. We assume that the rotational diffusion is fast enough so that the θ distribution is always homogeneous.

Coarse-grained model for $P \neq 0$

In this regime, there are two timescales: rotational diffusion scale $1/D_{rot}$ and the instability growth timescale $1/\sigma_{max}$, and we have showed that the latter is on the same scale as translational diffusivity a^2/D_T . It is well known that for self-propulsion particles with velocity U_0 and rotational diffusivity D_{rot} , on timescale $\tau \gg 1/D_{rot}$, the motion becomes diffusive and the effective translational diffusivity is enhanced by $U_0^2/2D_{rot}$ for 2D rotation and $U^2/6D_{rot}$ for 3D rotation. Therefore in the current limit, $1/D_{rot} \ll a^2/D_T$, we can ignore the detailed θ -modes and simply replace the

translational diffusivity D_T in § 7.2 by the effective diffusivity $D_T + U_0^2/2D_{rot}$.

By (7.10), $U_0 \sim Pc$. Therefore the governing equations for a monolayer system with 2D rotation is similar to (7.34):

$$-D_R(\nabla_{xy}^2 + \frac{\partial^2}{\partial z^2})c = (S - \kappa n_A c(z=0))\delta(z), \quad (7.47)$$

$$\frac{\partial n_A}{\partial t} - (D_T + \frac{P^2 c^2}{2D_{rot}})\nabla_{xy}^2 n_A = -\nabla_{xy} \cdot (n_A \langle \mathbf{U} \rangle_{\xi}). \quad (7.48)$$

To finish the coarse-graining process we also need a governing relation for $\langle \mathbf{U} \rangle_{\xi}$. We have showed in § 7.2 that when $P = 0$ the averaged $\langle \mathbf{U} \rangle_{\xi} = (M + A/2)\nabla c$. To include the effect of $P \neq 0$, physically we are searching for the flux of Janus particles in a homogeneous $n(x, y) = n_{A0}$ density field, in the presence of ∇c . Here we first heuristically derive the expression of \mathbf{j} based on the exact solution in last section, then we discuss the physical implications.

Assume that $\mathbf{j} = n \langle \mathbf{U} \rangle_{\xi} = n (F_P + M + A/2) \nabla c$, where F_P is a function of P to be determined. Combined with (7.47), we can solve for the dispersion relation $\sigma(q)$:

$$\sigma(q) = -\left(D_T + \frac{c_0^2 P^2}{2D_{rot}}\right)q^2 + \left(F_P + M + \frac{A}{2}\right)\left(\frac{c_0 \kappa n_{A0} q^2}{n_{A0} \kappa + 2qD_R}\right). \quad (7.49)$$

Remember that by definition $n(x, y) = \int_0^{2\pi} \mathcal{P}(x, y, \theta) d\theta$, so $n_{A0} = 2\pi \mathcal{P}_0$. Here we have an $O(q^2)$ dependence in the diffusion term. However we know from the last section that the leading order contribution of P to $\sigma(q)$ is $O(q^3)$. Therefore the only allowed solution is that F_P cancels exactly with the $c_0^2 P^2 / 2D_{rot}$ term.

Thus, we reach the full expression of $\mathbf{j} = n_A \langle \mathbf{U} \rangle_{\xi}$, for a monolayer system:

$$\mathbf{j} = n_A \langle \mathbf{U} \rangle_{\xi} = n \left(-\frac{P^2 c}{2D_{rot}} + M + \frac{A}{2} \right) \nabla c. \quad (7.50)$$

The coarse-grained $\sigma(q)$ is therefore easy to calculate:

$$\sigma_{cg}(q) = \left(\frac{A}{2} + M \right) \frac{c_0 \kappa n_{A0}^2 q^2}{2qD_R + \kappa n_{A0}} - \frac{c_0^2 P^2 q^3 D_R}{D_{rot} (2qD_R + \kappa n_{A0})} - q^2 D_T, \quad (7.51)$$

where the three terms are the diffusiophoresis down ∇c , the negative self-propulsion term, and the translational diffusion term.

We can compare this coarse-grained simple theory with the analytic solution in Appendix L up to P^2 order. Due to the ‘fast rotation’ assumption, $\sigma_{cg}(q)$ is expected to show some difference from the exact solution when P and σ are both significant, and D_{rot} is small. We specifically choose $Da = 5$ to achieve fast propulsion and $M_C = 10$ so that the growth rate is around its maximum as shown in Fig. 7.5. We find that σ_{cg} works very well in tracking the maximum growth rate as shown in Fig. 7.6, even for D_{rot} as small as 0.02.

Further, we show that the full 3D simulation can also be solved easily by this coarse-grained procedure. We have the governing equation for a full 3D case, with the effective translational diffusivity $D_T + P^2 c^2 / 6D_{rot}$. Also the coarse-grained flux is slightly modified:

$$-D_R \nabla^2 c = S - \kappa n c, \quad (7.52)$$

$$\frac{\partial n}{\partial t} - \left(D_T + \frac{P^2 c^2}{6D_{rot}} \right) \nabla^2 n = -\nabla \cdot \left(n \langle \mathbf{U} \rangle_{\xi, 3D} \right), \quad (7.53)$$

$$n \langle \mathbf{U} \rangle_{\xi, 3D} = n \left(-\frac{P^2 c}{6D_{rot}} + M + \frac{A}{3} \right) \nabla c. \quad (7.54)$$

Following the route similar to §7.2, we get $\sigma_{cg}^{3D}(q)$:

$$\sigma_{cg}^{3D}(q) = \left(\frac{A}{3} + M \right) \frac{c_0 \kappa n_{A0} q^2}{q^2 D_R + \kappa n_{A0}} - \frac{c_0^2 P^2 q^4 D_R}{6D_{rot} (q^2 D_R + \kappa n_{A0})} - q^2 D_T, \quad (7.55)$$

where the three terms are respectively diffusiophoresis, self-propulsion, and translational diffusivity. Simple calculation reveals an instability threshold at $M_C^{3D*} = c_0(M + A/3)/D_T = 1$. Here the leading order contribution of propulsion is $O(-P^2 q^4 / 6D_{rot})$, still on a higher order of diffusiophoresis, so is expected to have no effect on the instability threshold.

σ_{cg} and σ_{cg}^{3D} are rather general results. When $P = 0$ and $A = 0$, where particles are uniformly reactive, the system degenerates to the ‘growing and decaying particles’

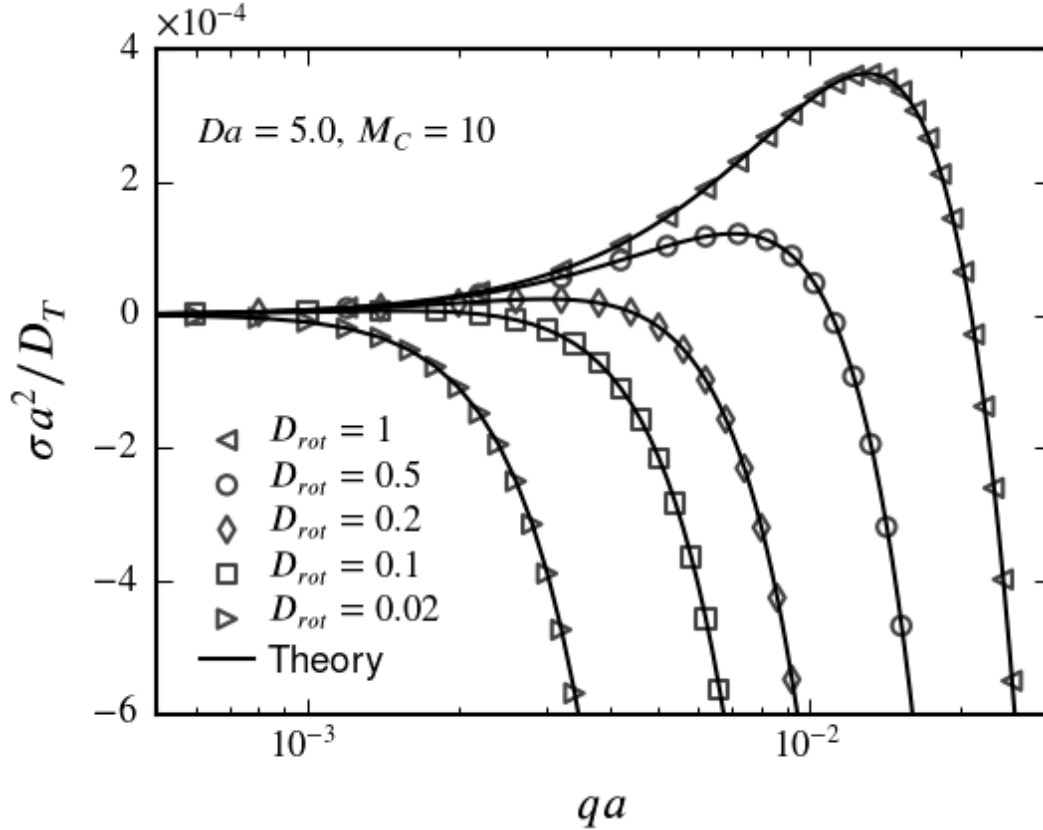


Figure 7.6: Comparison between the coarse-grained monolayer solution $\sigma_{cg}(q)$ with the exact solution. The symbols are calculated from the coarse-grained model and the solid lines are the analytical solutions up to $O(P^2)$ solved in §7.3, corresponding to different value of D_{rot} . $Da = 5$, $M_C = 10$, $\phi_A = \pi a^2 n = 0.02$ are fixed.

discussed by Karpov & Oxtoby, (1997). When $A = 0$, it agrees with the result given by Saha *et al.*, (2014), derived by the traditional moment hierarchy method of Smoluchowski equations. However we should point out that here $\sigma_{cg}^{3D}(q) \sim O(-P^2 q^4 / 6D_{rot})$ while in Saha *et al.*, (2014) the authors ignored the Brinkman screening length $\sim q^2$ too early so their result scales as $O(-P^2 q^2 / 6D_{rot})$.

Active flux j^{act}

In this subsection we briefly extend our discussion from chemically active particles to general active matter, with the important knowledge $\mathbf{j} = n\langle \mathbf{U} \rangle_\xi$ in the presence of ∇c derived from a stability analysis. In general, a ∇c means simply a gradient of swim velocity ∇U_0 , by (7.10). We shall discuss the simplest Active Brownian

Particle (ABP) system, governed by the following Langevin equations, in the absence of translational Brownian motion and any external forces or torques:

$$\dot{\mathbf{X}} = U_0 \boldsymbol{\xi} + \frac{1}{\zeta} \mathbf{F}^P, \quad (7.56)$$

where U_0 is the intrinsic self-propulsion velocity, ζ is an isotropic drag, and \mathbf{F}^P is the particle-particle collision force. \mathbf{F}^P can be ignored in the dilute limit. For simplicity D_T is ignored here and in the following flux analysis. In the dilute limit discussed in this work, $\mathbf{F}^P \rightarrow 0$ and can be ignored in discussing the flux. $\boldsymbol{\xi}$ is subject to rotational Brownian motion.

The flux due to self-propulsion under ‘fuel gradient’ $c, \nabla c$ is $\mathbf{j} = -nP^2 c \nabla c / dD_{rot}$, where $d = 2$ for 2D system and $d = 6$ for a 3D system. By (7.10) $\mathbf{U} = \boldsymbol{\xi} P c$, so we can relate \mathbf{j} directly to the self-propulsion velocity of general active matter. It is important that this flux is for a homogeneous density field n and comes solely from ∇U_0 , the ‘activity’ gradient. Therefore we shall denote it as the ‘active flux’:

$$\mathbf{j}^{act} = -nU_0 \nabla U_0 / dD_{rot}, \quad (7.57)$$

which allows us to discuss the steady state distribution $\phi(\mathbf{x})$ of active matter, under a propulsion velocity gradient ∇U_0 . This \mathbf{j}^{act} corresponds to the ‘drift velocity’ in Cates & Tailleur, (2015).

Consider an initially homogeneous system with swimming U_0 and gradient of activity ∇U_0 , there will generally be a volume fraction gradient $\nabla \phi$ at steady state in response to ∇U_0 . The flux must be zero at steady state: $\mathbf{j}^{act} + \mathbf{j}^{\nabla \phi} = 0$, where \mathbf{j}^{act} is calculated as (7.57) and $\mathbf{j}^{\nabla \phi} = -U_0^2 / dD_{rot} \nabla \phi$ is the diffusion flux down the ϕ gradient, where $-U_0^2 / dD_{rot}$ is the effective translational diffusivity due to swimming at timescale $\tau \gg 1/D_{rot}$. $\mathbf{j}^{act} + \mathbf{j}^{\nabla \phi} = 0$ requires that $\nabla(\phi U_0) = 0$ and therefore $\phi \propto 1/U_0$. This is confirmed by 2D simulations of ABPs, as shown in Fig. 7.7.

Importantly, \mathbf{j}^{act} and $\mathbf{j}^{\nabla \phi}$ are both established in the dilute limit $\phi \rightarrow 0$ and fast rotational diffusion limit $D_{rot} \rightarrow \infty$. At finite ϕ , \mathbf{F}^P must be included and the fluxes

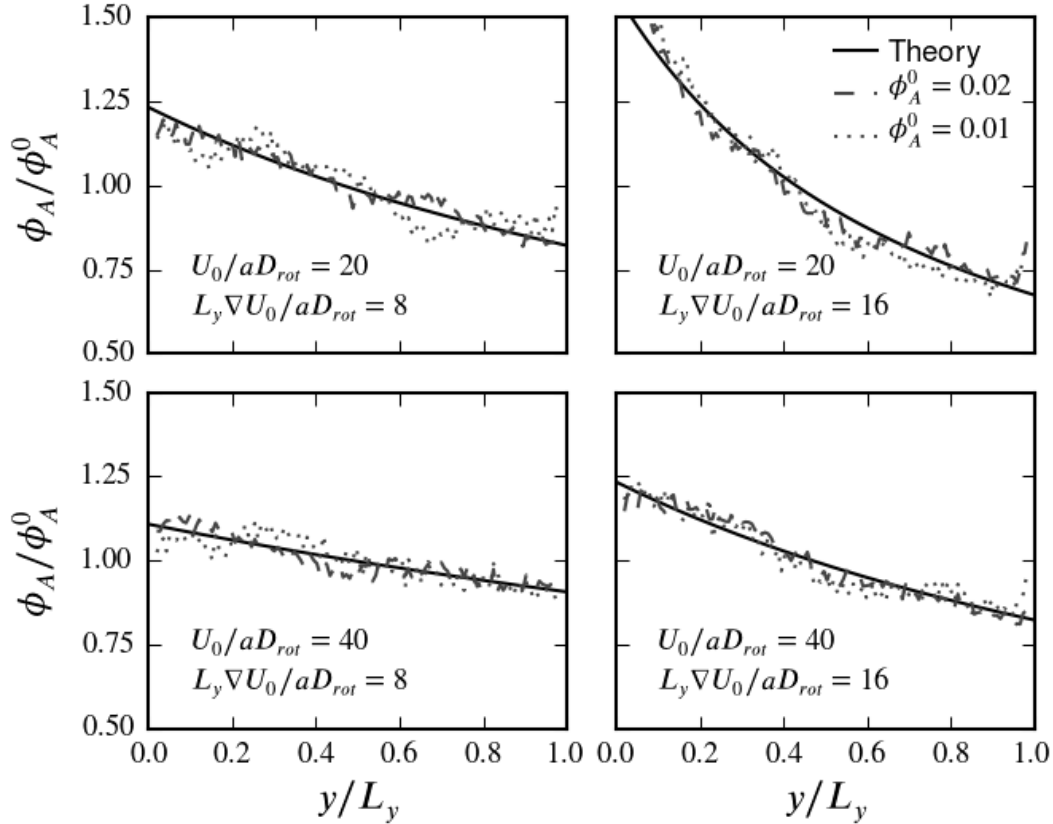


Figure 7.7: Comparison between the $\phi \propto 1/U_0$ theory and the simulation measurement. ∇U_0 is applied in the y direction. $N = 1000$ ABPs are simulated in a periodic box $L_x = L_y = 250a$. $\phi_A^0 = 0.02$. Local ϕ_A is extracted by building Voronoi cells of each particle and is averaged for 500 snapshots of the steady state. $D_T = 0$.

must be modified accordingly. If D_{rot} is not fast enough, the distribution is no longer isotropic everywhere and the detailed calculation in §7.3 must be considered.

A continuum mechanics view on the coarse-grained model

In the last subsections we *deduced* the form of ‘active flux’ in the coarse-grained model (7.48) and (7.54), to reproduce the full analytical solution. In fact, if we consider the active particles as a continuum, Yan & Brady, (2015a) have shown that the flux of ABPs with constant swimming velocity U_0 can be written as:

$$\mathbf{j}_{cm} = \frac{1}{\zeta} \nabla \cdot \boldsymbol{\sigma}^{act} + \frac{1}{\zeta} n \langle F^{swim} \rangle, \quad (7.58)$$

where σ^{act} is the active pressure defined as $\sigma^{act} = n\zeta D^{act}$ (Takatori *et al.*, 2014). In the dilute limit $D^{act} = D_T + \frac{1}{2}U_0^2/D_{rot}$ for 2D rotation. $\langle F^{swim} \rangle$ is the average swim force, with the definition $F^{swim} = \zeta U_0$ per particle. ζ is the drag coefficient, and is assumed to be $\frac{1}{6\pi\eta a}$ in this work. For dilute chemically active particles, to leading order $U_0 = Pc$ so $\sigma^{act} = n\zeta D^{act} = n\zeta(D_T + \frac{1}{2}P^2c^2/D_{rot})$. The swim force is simply an orientation average of (7.10): $\langle F^{swim} \rangle = -\zeta(M + \frac{1}{2}A)\nabla c$. Since we considered the fast rotation case $D_{rot} \rightarrow \infty$, $\langle F^{swim} \rangle = 0$ due to isotropic orientation distribution.

Also, the perturbed $c(\mathbf{x})$ field gives non-constant U_0 , and there is an extra piece of flux due to a varying U_0 (Takatori & Brady, 2015):

$$\mathbf{j}_{cm} = \frac{1}{\zeta} \left(\nabla \cdot \sigma^{act} - \sigma^{swim} \cdot \nabla \ln U_0 + n \langle \mathbf{F}^{swim} \rangle \right) \quad (7.59)$$

In the dilute limit, $\sigma^{swim} = \sigma^{act} = n\zeta(D_T + \frac{1}{2}U_0^2/D_{rot})$. Combining all the components, the particle phase equation is:

$$\frac{\partial n}{\partial t} + \nabla \cdot \mathbf{j}_{cm} = 0. \quad (7.60)$$

It reproduces exactly the same result as (7.48). For the full 3D system, we can simply replace $\frac{1}{2}U_0^2/D_{rot}$ by $\frac{1}{6}U_0^2/D_{rot}$ and replace $M + \frac{1}{2}A$ by $M + \frac{1}{3}A$, and again we reproduce exactly the same result as (7.54).

The continuum mechanics view seems trivial in this dilute system because the diffusion-convection equations (7.48) and (7.54) work very well. However, the continuum mechanics view is a more fundamental perspective to describe the motion and deformation of active matter, and its application is far beyond the dilute limit. It works well in predicting the equilibrium dense-dilute coexistence system, for both chemically active particles and ABPs with hard-sphere collision only (Takatori & Brady, 2015; Yan & Brady, 2015a).

7.5 Discussion & Conclusions

When active matters separate from a homogeneous state is one of the most fundamental questions in this area. In this work we found an analytical solution for chemically active particles by linear stability analysis. We calculated the stability dispersion relation $\sigma(q; P)$ for both non-propulsion $P = 0$ and self-propulsion $P \neq 0$ cases, and the results match the simulation very well. In the $P = 0$ case, instability is governed by $M_C = c_0(M + A/2)/D_T$ and $M_C^{3D} = c_0(M + A/3)/D_T$, which is the ‘scaled fuel concentration’ depending on diffusiophoresis parameters M, A and translational diffusivity D_T . We showed that for Janus particles the asymmetric diffusiophoresis down ∇c induces quadrupolar orders in the developing or decaying instability modes. In the $P > 0$ case, we show that self-propulsion P suppresses the growth rate $\sigma(q)$, but this ‘stabilizing’ effect is on a higher order ($\sim O(q^3)$ in monolayer and $\sim O(q^4)$ in 3D) of the governing order of M_C ($\sim O(q^2)$), so the stability threshold $M_C^* = 1$ is not changed. We also demonstrated that for Janus particles with weak reaction $Da \rightarrow 0$, the swimming velocity is almost zero and σ_{max} monotonically increases with M_C as in the $P = 0$ case, while for diffusion-limited reactions $Da \rightarrow \infty$, the instability is strongly suppressed by propulsion so when $M_C \rightarrow \infty$, $\sigma_{max} \rightarrow 0$.

We explained the instability by chemical screening, where the long-ranged $1/r$ perturbation governed by Laplace’s equation $\nabla^2 c = 0$ is screened to a short-ranged potential on length scale L_B and therefore an instability threshold comparing chemical attraction and diffusion $M_C^* = 1$ exists, for both $P = 0$ and $P \neq 0$ cases.

We deduced the active flux $j^{act} = -nU_0 \nabla U_0 / dD_{rot}$, where d is a constant depending on dimension, by comparing the analytic results with the coarse-graining procedures in the fast rotation regime $D_{rot} \rightarrow \infty$, and we showed that with j^{act} the coarse-grained results $\sigma_{cg}(q)$ works very well, compared to the exact solution $\sigma(q; P)$. We also showed that it is actually governed by the continuum mechanics of active

matter, and built upon surface forces (the swim pressure) and body forces (the swim force). The continuum mechanics perspective is also valid at finite number density, where the particle-particle collisions are not negligible. We leave this case for a future study.

Last, we also demonstrated matrix perturbation as a systematic method to calculate the eigensystem of a matrix, which may be very difficult to analytically calculate with old methods. This method applies to arbitrarily large matrices, and can overcome the complex coupling between different orientational θ -modes. Also the results are calculated in block-matrix fashion and therefore do not require a finite truncation at some particular dimension $N \times N$ of an infinite linear instability dynamic system; any N will give the same results. This method can be used to calculate a lot more cases and to extract more information of the chemically active system. For example, beyond the dilute limit of particles, the many body effect would make the reactivity κ in (7.13) a function $\kappa(n)$, whose effect on the eigensystem can be expanded as $O(n=0) + O(n) + O(n^2) + \dots$, and all orders can be calculated systematically with the matrix perturbation method.

*Chapter 8***ANTI-SWARMING: STRUCTURE AND DYNAMICS OF
REPULSIVE CHEMICALLY ACTIVE PARTICLES**

8.1 Introduction

Chemically active particles suspended in fluids may achieve self-propulsion by surface catalytic reactions of chemical solutes (Ebbens & Howse, 2010). One common mechanism is self-diffusiophoresis, whereby the motion of a particle is due to the asymmetric solute concentration field $c(\boldsymbol{x}, t)$ it creates. Usually reactants are consumed on the surface of a chemically active particle, and when a second particle appears in the vicinity, it is attracted by a diffusiophoretic velocity $U \sim -\nabla c$. Active particles with attractive interactions are observed to exhibit dynamic clustering and gas-liquid phase transition (Theurkauff *et al.*, 2012; Palacci *et al.*, 2013; Buttinoni *et al.*, 2013). Thermodynamic-like theories (Takatori & Brady, 2015) utilizing the swim pressure (Takatori *et al.*, 2014) as an equation of state, and some other theories based on similar thermodynamic-like models (Stenhammar *et al.*, 2013; Cates & Tailleur, 2015; Solon *et al.*, 2015b) work well in describing the phase separation phenomena.

However, few studies have investigated active particles with repulsive interactions. In fact, if the surface chemical reactions release solutes instead of consuming them, the solute concentration $c(\boldsymbol{x}, t)$ is increased in the vicinity of each particle, and the diffusiophoretic velocity is now repulsive between particles. Repulsive particles, if confined in a constant volume container, may overcome the randomizing thermal Brownian motion and form a crystal lattice (Soh *et al.*, 2008). Derjaguin & Golevanov, (1984) observed the formation of periodic crystal-like structures in living cells and suggested that it is due to the repulsive diffusiophoretic interaction.

A classical example of repulsive particles that show a liquid-crystal transition is the so-called One Component Plasma (OCP). In an OCP, moving positive charges are immersed in a uniform, rigid, and neutralizing background sea of negative electrons, and the system behavior is governed by the coupling parameter Γ_e , which measures the electrostatic energy relative to thermal energy (Brush *et al.*, 1966). It is well

known that the liquid-like structure at small Γ_e transforms to BCC (body-centered cubic) for $\Gamma_e \gtrsim 175$ (Gillan, 1974; Rogers, 1974; Stroud & Ashcroft, 1976; Itoh & Ichimaru, 1977; Bernu, 1979; Baus & Hansen, 1980; Tan *et al.*, 1995; DeWitt *et al.*, 2001; Chugunov *et al.*, 2003; Daligault, 2006).

In this chapter we explore the collective motion of repulsive active particles by simulations, with a full solution of the diffusiophoretic interactions as described in Chapter 6. We show that repulsive chemically active particles exhibits a ‘liquid-crystal’ phase transition, similar to an OCP. Quantitatively, we define a coupling parameter Γ_c for the chemically active system by mapping it to Γ_e in an OCP by a simple analogy.

8.2 Problem formulation

First order surface catalytic reaction $R \rightarrow \theta P$ is assumed to occur homogeneously on the particle surface. Making use of the stoichiometry/diffusivity factor $(1 - \theta D_R/D_P)$, the reaction can be taken to be irreversible: $\mathbf{j}_R \cdot \mathbf{n} = -\kappa c(\mathbf{n})$ on the boundary, where c is the reactant concentration, κ is the reaction rate constant and \mathbf{n} is the surface normal vector pointing outward. The Damkhöler number $Da = a\kappa/D_R$ governs the reaction rate, where D_R is the reactant diffusivity: $Da \rightarrow \infty$ is diffusion limited due to fast reaction, and $Da \rightarrow 0$ is the slow reaction limit.

When the chemical solutes are much smaller in size compared to the particles, each chemically active particle is driven by the osmotic pressure of the reactant solute concentration $k_B T c(\mathbf{x}, t)$ integrated over the particle’s surface (Córdova-Figueroa & Brady, 2008; Brady, 2011):

$$\mathbf{U}_0 = -(1 - \theta D_R/D_P) \frac{L(\Delta)}{6\pi\eta a} \oint \mathbf{n} k_B T c(\mathbf{x}, t) dS, \quad (8.1)$$

where a is the particle radius, η is the solution viscosity, D_R, D_P are diffusivity of reactants and products, and the nondimensional hydrodynamic mobility function $L(\Delta) = (3/2)\Delta^2(1 + \frac{2}{3}\Delta)/(1 + \Delta)^3$, with $\Delta = \delta/a$, measures the flow of fluid with

viscosity η in a layer of thickness δ adjacent to the colloidal particle where the particle-solute interactive force is operative. Here we have taken the simplest form of interactive force between the solute and the colloidal particle, namely a hard-sphere repulsive force at a distance $r_c = a + \delta$ (and δ need not be small compared to the particle size a , although typically it is so). More general interactive forces will only have a quantitative effect and the details are discussed in Brady, (2011). The prefactor $(1 - \theta D_R/D_P)$ scales the solution of reactant concentration $c(\mathbf{x}, t)$ to the total solute concentration of both reactant and products. When $\theta D_R/D_P > 1$, the products push the particles more effectively than the reactants do and the particles can be considered sources releasing the products and therefore they repel each other.

The governing equation for $c(\mathbf{x}, t)$ is the classic convection-reaction-diffusion equation. The convection is controlled by particle Peclet number $Pe = U_0 a/D_R$. In diffusiophoresis, the particle velocity U_0 is usually so small that $Pe \ll 1$ (Córdova-Figueroa & Brady, 2008), and therefore the convection of c can be ignored. Diffusion of c is fast enough for c to achieve a steady state, instantaneously following the particle motion. In this case, the governing equation for the reactant can be reduced to Laplace's equation, $\nabla^2 c = 0$, similar to an electrostatic field. To leading order, the disturbance to the solute concentration field induced by one reactive particle is $c' \sim q/r$, where q is the particle reactivity; that is, how many molecules are consumed on the particle surface in unit time, which is an analogy to the electrostatic charge Ze .

The active particles are assumed to be confined in a constant volume three dimensional space, and the reactant is assumed to be released by distributed sources throughout the space to maintain the system as 'chemically neutral'. Therefore the volume average reactant concentration is maintained at constant $\langle c \rangle$. Without the chemically neutralizing condition, the particles eventually consume all the reactant and no steady state can be achieved. Experimentally, Theurkauff *et al.*, (2012) has demonstrated a 2D implementation of a chemically neutral suspension, in which

the solutes diffuse to the colloid monolayer reaction zone from a large reservoir and the system is kept evolving for many hours to reach a steady state. The chemically neutral assumption is also common for 3D reactive suspension system (Bonnecaze & Brady, 1991b).

An analogy to an OCP can be made. The repulsive active particles resemble the positive ions in an OCP, and the chemically neutralizing sources are similar to the electrostatically neutralizing background. By analogy, active particles should be liquid-like when the repulsion is weak, and be solid-like when the repulsion is strong enough to align the particles into a periodic lattice.

A key difference, however, is that moving ions in an OCP are point charges and the charges are fixed at Ze , while the reactivity q of a chemically active particle changes in response to the local concentration of reactant, due to the chemical reaction on the particle's surface. Also, the reactivity shows some distribution on the particles' spherical surface: the particle is more than merely a 'point charge'. The changing reactivity results in changing interactions, which is fundamentally different from the additive pairwise potential assumption employed in previous simulation work on attractive active particles (Redner *et al.*, 2013; Palacci *et al.*, 2013). The changing reactivity also poses a great difficulty in thermodynamic-like treatments. Even if we define a mean-field effective pairwise potential, it is state-dependent, and it is known that some thermodynamic inconsistencies and peculiarities may appear for density-dependent pairwise interactions (Louis, 2002; Tejero & Baus, 2003).

In this work, we simulate the system with the Accelerated Laplacian Dynamics method described in Chapter 6. All computational details can be found in Chapter 6, and we only briefly describe the approach without mathematical details. The reaction on each particle is represented by a multipole expansion: the monopole q and the dipole \mathcal{S} , similar to electrostatics. Here q is the net consumption rate of reactant and \mathcal{S} is the asymmetry of the consumption on the particle surface. Second,

the perturbation c' of each particle to the average $\langle c \rangle$ field is calculated from q , which propagates as $1/r$, and S , which propagates as $1/r^2$. Third, With the first order reaction condition, the monopole and dipole strength of particle α follow a Faxen-type law $q_\alpha \propto \langle c \rangle + c'(\mathbf{x}_\alpha)$, $S_\alpha \propto \nabla \langle c \rangle + c'(\mathbf{x}_\alpha)$, where $c'(\mathbf{x}_\alpha)$, $\nabla c'(\mathbf{x}_\alpha)$ are perturbations due to all particles $\beta \neq \alpha$ and are evaluated at the center of α . In this way, the equations for the c field are closed and can be solved iteratively at each timestep for different configurations of particles.

The diffusiophoretic velocity is then determined with the solution of solute concentration field c at each timestep. The velocity \mathbf{U}_0 in (8.1) can be calculated analytically utilizing the first order reaction boundary condition $\mathbf{j}_R \cdot \mathbf{n} = -\kappa c(\mathbf{n})$:

$$\frac{\mathbf{U}_{0,\alpha}}{D/a} = -(1 - \theta D_R/D_P) L(\Delta) \langle c \rangle a^3 \frac{4\pi a \nabla c(\mathbf{x}_\alpha)}{(Da + 2) \langle c \rangle}. \quad (8.2)$$

The system dynamics is integrated by overdamped Brownian dynamics: $\Delta X = \mathbf{U}_0 \Delta t + \Delta X^B + \Delta X^{HS}$, where ΔX^B is the translational Brownian motion satisfying $\langle \Delta X^B \rangle = 0$, $\langle \Delta X^B \Delta X^B \rangle = 2D\Delta t$, and ΔX^{HS} is the non-overlapping collision displacement calculated with the potential free algorithm (Foss & Brady, 2000).

We nondimensionalize the system with particle radius a , particle diffusion time $\tau_D = a^2/D = a^2/(k_B T/6\pi\eta a)$ and the imposed reactant concentration $\langle c \rangle$. Then $\mathbf{U}_0 \propto -S_D \nabla (c/\langle c \rangle)$, where $S_D = (1 - \theta D_R/D_P) L(\Delta) \langle c \rangle a^3$ is the nondimensional concentration, i.e., the ‘fuel concentration’. Increasing $|S_D|$ is equivalent to increasing hydrogen peroxide concentration in the experiments (Theurkauff *et al.*, 2012; Howse *et al.*, 2007). In this chapter, we report only the result of the repulsive case $S_D < 0$. The attractive case is discussed in Chapter 6 and Chapter 7.

8.3 The weak repulsion regime: fluctuating interaction

In simulations covering a wide range of volume fraction and Damköhler $0.001 < \phi < 0.15, 0.1 < Da < 10$, we found that under weak repulsion (small $|S_D|$), the system remains randomly distributed due to the Brownian motion. Voronoi cells

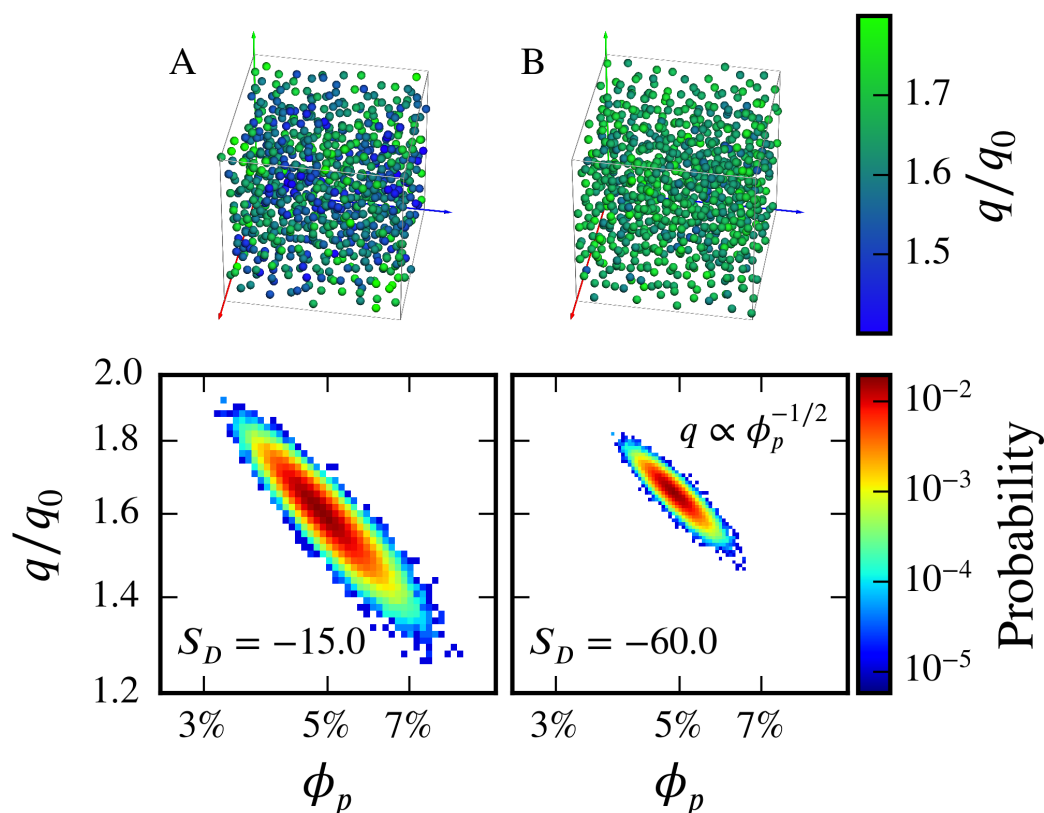


Figure 8.1: The distribution of particle reaction q and local volume fraction ϕ_p , and their correlation. A: The snapshot of the equilibrium structure of system in a periodic box of $42a \times 42a \times 42a$, with $\phi = 4.88\%$, $Da = 2.0$, $N = 864$, $S_D = -15.0$, $\Gamma_c \approx 20$. Each particle is colored by q/q_0 . B: The same system, but equilibrated with stronger repulsion $S_D = -60.0$, $\Gamma_c \approx 80$.

are built with all particles to analyze the structure, and each particle's local volume fraction is defined as $\phi_p = \frac{4}{3}\pi a^3/V_p$, where V_p is the volume of the Voronoi cell occupied by that particle.

The first order reaction $R \rightarrow \theta P$ gives that reactivity $q_0 = -4\pi D_R a \langle c \rangle Da / (1 + Da)$ in an infinitely dilute system $\phi \rightarrow 0$. At a finite ϕ , it is well known that the many-body effect of reactive particles increases the average reactivity $\langle q \rangle / q_0 > 1$ (Bonnicaze & Brady, 1991b), as shown in Fig. 8.1. We also found that although in principle $\langle q \rangle / q_0$ should also be related to whether the specific structure is random or some crystal, the dependence is very weak (Lebenhaft & Kapral, 1979), especially in the

regime where ϕ is far from the closed-packing limit $\phi_{RCP} \approx 0.64$. We have found that with $B = 1.62$, in the following equation, it is a universal fit to $\langle q \rangle / q_0$ for all structures and all (Da, ϕ) ranges we investigated in this chapter.

$$\frac{\langle q \rangle}{q_0} = \frac{1}{1 - B\phi^{1/3}\text{Da}/(1 + \text{Da})}. \quad (8.3)$$

Fig. 8.1 shows the statistics between q and ϕ_p for an example system of $\text{Da} = 2$, $\phi = 0.0488$, at different repulsion strengths. The correlation shows that $q \propto \phi_p^{-1/2}$, because when particles get closer they compete for reactant so their reactivity decreases with local volume density. Also under strong repulsion the particle reactivity q is narrowly distributed around $\langle q \rangle$, because the strong repulsion keeps the structure almost always homogeneously distributed.

Therefore, in the strong repulsion case, we can ignore the fluctuations of q and define a parameter based on $\langle q \rangle$ to quantify the leading order effect of repulsion vs Brownian motion, again by an analogy to an OCP. In an OCP, the controlling parameter is $\Gamma_e = (Ze)^2 / (4\pi\epsilon_0 L k_B T)$, where Ze is the ion charge, ϵ_0 is the electrostatic conductivity, and L is a length scale determined by ion number density n : $L = (3/4\pi n)^{1/3}$. Γ_e actually measures the electrostatic potential energy of two ions separated at L to the thermal kinetic energy $k_B T$. Similarly, we can define Γ_c as the ratio of repulsion to Brownian motion, where subscript c denotes chemically active particles. To leading order, the repulsive diffusiophoretic velocity $U_0 \sim -S_D \nabla c$, as shown in equation (8.2), and in the overdamped limit $\mathbf{F} \propto 6\pi\eta a U_0 \sim \nabla 1/r$. Then, we can define an ‘average potential’ Φ according to $\mathbf{F} = -\nabla \Phi$. We use the same length scale $L = (3/4\pi n)^{1/3}$ as in an OCP, but replace the number density n with particle volume fraction ϕ , since particles are not point charges. We also scale $\langle q \rangle$ with q_0 , as the scaling in (8.3). Therefore, we have $\Phi_L = S_D k_B T \langle q \rangle / [(Da + 2)\langle c \rangle D_R L]$. Then Γ_c can be defined in the nondimensionalized form:

$$\Gamma_c = -4\pi \frac{\text{Da}}{1 + \text{Da}} \frac{S_D}{\text{Da} + 2} \phi^{1/3} \frac{\langle q \rangle}{q_0}. \quad (8.4)$$

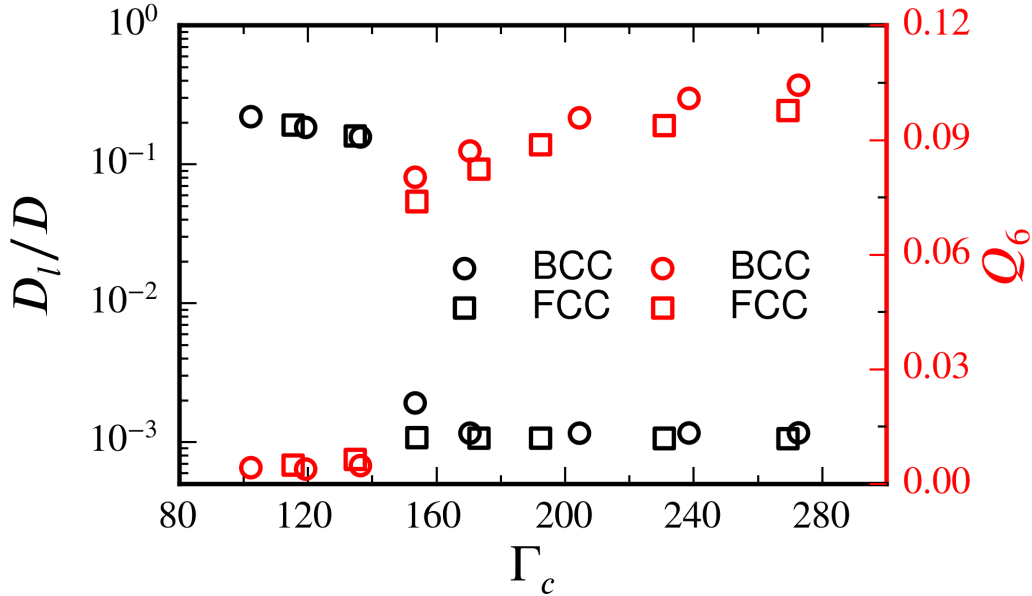


Figure 8.2: The measurement of structural change of BCC and FCC crystals, both for $Da = 2.0$. $\phi = 3.88\%$ for BCC system and $\phi = 4.88\%$ for FCC system.

The thermal energy $k_B T$ does not appear in Γ_c because both the repulsive force (in equation (8.1)) and thermal motion scale linearly as $k_B T$.

8.4 The strong repulsion regime: ‘liquid-crystal’ phase transition

The analogy to an OCP and the similar definition of Γ_c implies the existence of a liquid-crystal phase transition, which is confirmed by our simulations. In an OCP, BCC is considered the stable crystal structure. However, the free energy difference between BCC and FCC is very small, and FCC can also maintain its structure, similar to diamond and graphite. The melting point of both FCC and BCC are reported (Dubin, 1990; Stringfellow *et al.*, 1990) to be: $\Gamma_e^{BCC} \approx 175$ and $\Gamma_e^{FCC} \approx 185$.

For chemical active particles, we conducted the simulation in 3D cubic periodic boxes with approximately $N = 1000$ particles, with very large S_D ($\Gamma_c \sim 800$), starting from a random particle distribution, and track the structure evolution for a very long time $\sim 1000\tau_D$. The simulation process is equivalent to suddenly cooling a liquid to very low temperature, and allowing it to relax to equilibrium. BCC

crystals formed in all “cooling” simulations, with inevitable distortion and defects. The formation of a BCC lattice is similar to the experiments (Tan *et al.*, 1995) and simulations (Daligault, 2006) of an OCP.

In order to accurately locate the transition, i.e., the “melting point” of the repulsive active particle crystal, “melting simulations” are conducted. Melting, instead of cooling, is chosen because in the liquid-solid phase transition the cooling process usually requires a large amount of sub-cooling to provide the crystallization with enough ‘driving force’, while the melting usually occurs immediately at the melting point. From the definition of Γ_c , increasing the “temperature” is equivalent to decreasing Γ_c . We start from 3D periodic systems of perfect crystal structures and run simulation cases covering a wide range of Γ_c , for sufficiently long time $\sim 1000\tau_D$.

We use both the dynamic criterion D_l/D (Löwen *et al.*, 1993) and the static criterion Q_6 to quantify the structure, and they give consistent results for the melting point. D_l is the long time diffusivity of particles, and Q_6 is the order parameter to measure the structure order of a particle’s neighbors (ten Wolde *et al.*, 1995) As shown in Fig. 8.2, Q_6 and D_l/D give consistent results in quantifying the system ‘melting point’, for both BCC and FCC structures. However, the calculation of D_l/D requires significantly more computational power because we must track the system for a very long time to calculate D_l . Limited by computing resource, we calculate Q_6 only when mapping the entire phase diagram for the range of $0.001 < \phi < 0.15, 0.1 < \text{Da} < 10, N \approx 1000$. When calculating Q_6 (ten Wolde *et al.*, 1995) we include approximately the second shell of neighbors in a lattice. If we include only the first shell of neighbors, value of Q_6 would change due to smaller number of neighbors, but the measured transition point does not change. Test runs show that a simple cubic lattice spontaneously transforms to a distorted BCC lattice. Therefore we search for the melting point of BCC and FCC lattices only. As shown in Fig. 8.3 and Fig.8.4 all the melting simulation shows the same sharp jump of Q_6 , and the

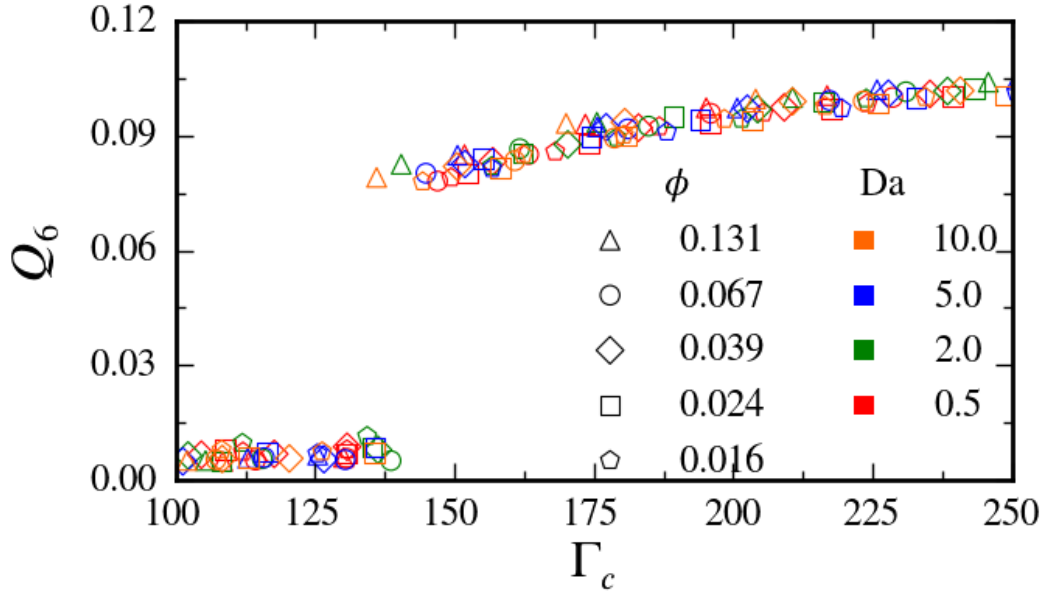


Figure 8.3: The measurement Q_6 of BCC. For each combination of ϕ (shape) and Da (color), simulations of different S_D are conducted so that a range of $100 < \Gamma_c < 250$ is covered. The melting point $\Gamma_c^{BCC} \approx 140$.

transition point for both BCC and FCC is $\Gamma_c^{BCC,FCC} \approx 140$.

8.5 Conclusions & Discussion

We explored repulsive chemically active particles with simulations, and showed that the system behavior can be determined by a single parameter Γ_c . The ‘liquid-crystal’ phase transition is located at $\Gamma_c^{BCC,FCC} \approx 140$, which differs from the OCP results $\Gamma_e^{BCC} \approx 175, \Gamma_e^{FCC} \approx 185$. The difference may come from three effects. First, although for repulsive chemically active particles the almost homogeneous local structure allows us to define Γ_c based on $\langle q \rangle$, all fluctuations are ignored, which is greatly different from an OCP system with fixed point charges. More importantly, the changing reactivity leads to Brinkman screening (Morris & Brady, 1995), which changes the long-ranged $1/r$ interaction to a screened $\exp(r/L_B)/r$, where L_B is the screening length. The role of screening in repulsive active matter is a complicated issue and it is unclear whether it causes the differences in the melting point of Γ_c compared to Γ_e . Second, limited by computing resources, in simulations we

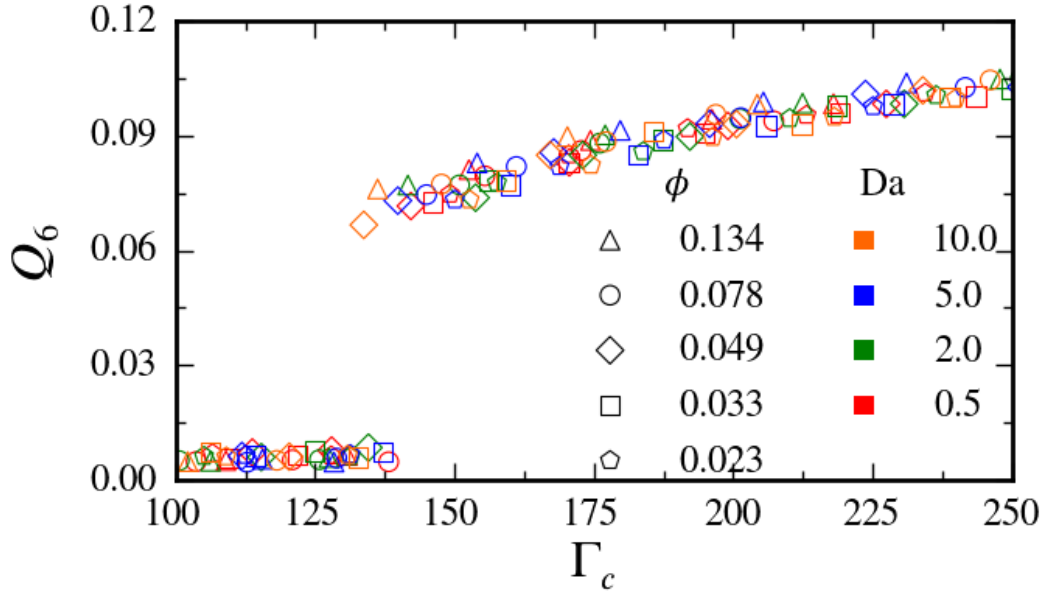


Figure 8.4: The measurement Q_6 of FCC. For each combination of ϕ (shape) and Da (color), simulations of different S_D are conducted so that a range of $100 < \Gamma_c < 250$ is covered. The melting point $\Gamma_c^{FCC} \approx 140$.

truncate the particle multipole expansion at the dipole level limited by computing resources, so some inaccuracy is inevitable. Third, the transition point of an OCP system is solved in literature by searching for the free energy cross-over calculated with Monte-Carlo methods. However, thermodynamics for repulsive active particles are not yet defined, and so we have to search for a transition point with dynamic simulations, which may give $\sim 10\%$ error depending on the system property and methodology (Hoffmann & Löwen, 2001).

Further, as regards the common experiment realizations with giving hydrogen peroxide and oxygen molecules as the fuel, both are at the nano-scale, and in this limit $L(\Delta)a^3 \sim \delta^2 a$, where $\delta \sim 10^{-9}m$. Therefore, $S_D \sim O(100)$ for $\langle c \rangle \sim 1Mol/L$, and $\Gamma_c \sim O(100)$. So the estimated phase-transition at $\Gamma_c^{BCC,FCC} \sim 140$ is within the reach of experiments. If the particles are confined on a monolayer by gravity and geometry, similar repulsive crystals should form, which should be hexagonal because the repulsion to leading order is isotropic.

In this chapter we investigated homogeneously reactive particles. In addition to particle-particle interaction, active Janus particle with a reactive hemisphere also achieve self-propulsion given by (8.1). For Janus particles no repulsive crystal formation is observed in simulations, because Janus particles can achieve a much larger velocity, U_0 , so the long-ranged repulsion due to diffusiophoresis is not strong enough to trap them in a lattice. Also, it is not legitimate to define a Γ_c^J by simply replacing the diffusivity $D_T = k_B T / \zeta$ with the swim-diffusivity D^{swim} for Janus particles and then determine the system dynamics with Γ_c^J , because D^{swim} only appears at a time longer than the reorient time τ_R , and the short time dynamics is also important in many cases, such as the crystal formation. In fact, it is not clear that whether a meaningful parameter Γ_c^J could be defined similar to Γ_c for Janus particles. Moreover, swimming pressure and thermodynamic-like theories (Takatori *et al.*, 2014; Takatori & Brady, 2015) describe the attractive active swimmers very well, but it is also not clear whether a similar non-equilibrium thermodynamic argument can be conducted to estimate the melting point $\Gamma_c^{BCC,FCC}$. A discussion for repulsive Janus particles is left for a future study.

Acknowledgment Wen Yan thanks Prof. Zhen-Gang Wang for bringing his attention to the repulsive system. This work is supported by NSF CBET-1437570.

Chapter 9

CONCLUSIONS AND OUTLOOK

In this thesis the dynamics of chemically active suspensions is discussed. The solute reactant is consumed at the particles' surface, and each particle generates a perturbation to the reactant concentration field $c(\mathbf{r})$. The active particles are modeled as osmotic motors (Córdova-Figueroa & Brady, 2008) and achieve self-propulsion and particle-particle interactions from the solute field $c(\mathbf{r})$. This is an example of a 'field-driven' system. Understandings of the behavior of this system can also be applied to other systems because the concentration field obeys a reaction-advection-diffusion equation, the same equation as for other fields, such as electrostatic, temperature, and so on (Bonnecaze & Brady, 1990). In 'field-driven' problems, the particle-particle interactions are generally not described by additive potentials and thermodynamics may not be valid. However, a mechanical perspective offers a sound framework for analysis.

A detailed theoretical continuum mechanics foundation for active matter is examined in Chapters 2 to 5, focusing on the ABP model as a general model for active matter. With the surface force defined as the swim pressure (or stress) in the work of Takatori *et al.*, (2014), the swim force is defined in Chapter 2, and is explained as a body force in the continuum mechanics formulation. The microscopic mechanism of *mechanical* swim pressure (or stress) is explained in Chapter 3 as an extension from the traditional passive Brownian particles colliding with a passive macroscopic body. The microscopic theory is extended to a general curved body in Chapter 4 and the resulting boundary layer is analogous to the Knudsen layer seen in rarefied gas-dynamics. When the mean-free-path is small but non-zero, far from the macroscopic body the Navier-Stokes equations can be solved in the bulk, with a boundary condition modified from the Knudsen layer. For active matter, it is shown in Chapter 4 that the kinetic accumulation boundary layer plays the same pivoting role as a Knudsen layer, connecting the sub-continuum and continuum scales. Based on microscopic understandings, Chapter 5 extends the notion of the swim stress to the anisotropic and tensorial cases, incorporating the manipulation of swimming

orientation \mathbf{q} in the continuum mechanics framework of active matter.

With the mechanical understandings for the minimal ABP model, the dynamics of the ‘field-driven’ chemically active suspensions is discussed from Chapters 6 to 8.

In Chapter 6 an algorithm – Accelerated Laplacian Dynamics – is introduced as a tool to probe the detailed system dynamics. The notion of chemical screening is clarified by simulation and analysis, and the steady-state structure of the coexistence between dense and dilute regions is explained from a continuum mechanics model. More importantly, the steady state structure does not show a *homogeneous* dilute region. Instead, the properties of the dilute regions vary as a function of the distance to the dense cluster. This is because the cluster consumes reactants and induces a net flux proportional to the reactant concentration gradient ∇c towards the cluster center. Thus the reactant gradient does not vanish, even if the simulation zone is extended to infinitely large, to maintain the continuity of the solute flux. This is a key difference between a coexistence in a *field driven* system and a *short-ranged pairwise additive potential* system. In the latter, outside some length *prescribed* by the short-ranged attraction potential, the swimmers do not feel the existence of the cluster, and remain in a *homogeneous* state, and therefore a thermodynamic equilibrium theory between two phases is possible.

The steady state of the clustering is explained in Chapter 6 with an approximation to ABP continuum mechanics. The stress induced by particle-particle diffusiophoretic attraction is found to be weak and small compared to the swim pressure (or stress) induced by self-propulsion. Based on that, the equilibrium structure is explained with a mean-field assumption, where the stress is fully described by the ABP model, and chemical concentration appears indirectly as $U_0 \propto c$, and a diffusiophoretic $\langle \mathbf{F}^{swim} \rangle \propto \nabla c$. Also, the ‘activity-gradient swim force’ $-\boldsymbol{\sigma}^{swim} \cdot \nabla \ln U_0$ plays an important role in the presence of a self-propulsion velocity gradient $\nabla U_0 \propto \nabla c$. In fact, for fast swimmers in the dilute region where the collisional pressure and the

osmotic pressure $nk_B T$ are negligible compared to σ^{swim} , at steady state $nU_0 = const$ is satisfied. For chemical swimmers $\phi_A c = const$ because $U_0 \propto c$.

The onset of the clustering behavior is found from a linear stability analysis on the chemical concentration field c and the swimmer probability density $\mathcal{P}(\mathbf{x}, \mathbf{q}, t)$. The instability threshold is found to give $M_C^* = M c_0 / D_T$ as a competition between attraction and translational diffusion, independent of self propulsion. The effect of self propulsion is found to be a stabilizing effect, appearing at a higher order wave number. The threshold is universal for either a monolayer or a periodic 3D system, and is consistent with a coarse-grained, continuum mechanical description which neglects the detailed orientational coupling by assuming that rotational diffusivity is always strong enough such that the instability growth happens on a timescale longer than τ_R , as required by the continuum mechanical theory so that there is a *separation-of-scales*. The matrix-perturbation technique is applied to solve the detailed instability dynamics. It is a systematic method, and beyond the cases discussed in this work, can also probe the effect of many-body reactivity, many-body collisions, many-body transport coefficients, etc, as a series expansion of volume fraction ϕ or the reactivity.

This thesis constitutes a quantitative research on chemically active suspensions, as an example system of *field-driven* active matter systems. Also, substantial attention is paid to continuum mechanics as a tool to explain the dynamics of chemically active particles. However, this work is by no means comprehensive nor complete.

First, the role of hydrodynamic interactions (HI) is not included in this discussion. Including HI requires more than a integration of the algorithm in Chapter 6 with Accelerated Stokesian Dynamics (Sierou & Brady, 2001). Since in self-diffusiophoresis the particles achieve self-propulsion with a surface slip velocity that fundamentally changes the boundary condition and near-field lubrication in HI, they must be *jointly* solved. That coupling increases the complexity of including

HI, and a thorough examination is required to avoid exponentially increasing the complexity of the algorithm.

Also, the simulation method in this work solves the chemical field efficiently with a multipole expansion method to avoid the use of mesh, but the drawback is that the multipoles are *analytically* coded in the algorithm. That strategy limits the capability of this algorithm to model simple geometries, including periodic, monolayer, and possibly confinement between parallel walls. To enable explorations in flexible geometries, the algorithm discussed here may be extended in an immersed boundary method fashion (Hoppensteadt & Peskin, 2002), which may also be combined with the HI effects.

On the physical side, the research on the continuum mechanics for active matter is still in its infancy. One of the key properties in continuum mechanics, the (shear and bulk) viscosity, is missing from the current formulation, because only dilute or sedimentation systems have been examined. In the dilute limit, the swimmer-swimmer interaction is absent, so the viscosity (with hydrodynamic interactions) is missing. In a sedimentation system, there is no shearing motion and the viscosity is not important. To build a consistent and useful continuum mechanics, the viscosity must be properly included in a fashion compatible with the thermodynamic constructions built for active matter (Takatori & Brady, 2015). To achieve that, the complete framework from Liouville equations to Boltzmann equation and Chapman-Enskog expansion in classical kinetic theory may be a viable route.

Beyond fundamental theories for simple model systems, many physical problems in the real world can be understood in the framework of active matter. For example, recently, Shelley, (2016) summarized the application of active matter theories to the understanding of the dynamics of micro-tubule/motor-protein assemblies. With a deeper understanding of the mechanics of active matter and a more powerful computational framework, many similar biological and synthetic systems can be

addressed.

Appendix A

THE SWIM FORCE OF ACTIVE MATTER

There is a recurring discussion in the literature about the nature and origin of the force causing self-propelled bodies to move at low Reynolds number. The discussion revolves about the notion that since self-propulsion is a ‘force-free’ motion, one cannot say that a self-propelled body experiences a Stokes drag. Or that the propulsive force can be written as a swim force $\mathbf{F}^{swim} = \zeta \mathbf{U}_0$. And if it is, this swim force is not a ‘true’ force. However, this is a misunderstanding about what is force-free motion and the nature of hydrodynamics at low Reynolds numbers.

The steady, non-accelerating motion of any body is force-free. At low Reynolds numbers $Re = \rho U a / \eta \ll 1$, where ρ is the density of the fluid, η is its viscosity, and U and a are the characteristic velocity and length scales of the motion, respectively, the acceleration of the fluid is negligible compared to the viscous and pressure forces and *all* motion is thus force-free. (We also specify that the inertia of the particle is negligible, which is characterized by the Stokes number $St = \rho_p / \rho \times Re \ll 1$, with ρ_p the particle density.) What is meant when one says that self-propulsion at low Reynolds number is force-free is that there is no *external* force causing the body to move. There are, however, *internal* forces that cause it to move.

In the simplest description of self propulsion, consider a body of fixed overall shape but whose surface can deform – a ‘squirmers.’ A paramecium is the classic biological example and phoretic colloidal particles can also be modeled as being propelled by a local slip velocity at their surface (Anderson, 1989; Blake, 1971). At a point \mathbf{x} on the surface of a the body, the fluid velocity $\mathbf{u}(\mathbf{x}) = \mathbf{U} + \mathbf{\Omega} \times (\mathbf{x} - \mathbf{X}) + \mathbf{u}^s(\mathbf{x})$, where \mathbf{u}^s is the ‘slip’ velocity, \mathbf{X} is the body center, and \mathbf{U} and $\mathbf{\Omega}$ are the rigid-body translational and rotational motion of the body about its center. The slip velocity

can be expanded in moments $\mathbf{u}^s(\mathbf{x}') = \mathbf{E}^s \cdot \mathbf{x}' + \mathbf{B}^s : (\mathbf{x}'\mathbf{x}' - \mathbf{I}(x')^2) + \dots$, where $\mathbf{x}' = \mathbf{x} - \mathbf{X}$, and the tensors $\mathbf{E}^s(t)$, $\mathbf{B}^s(t)$, etc. are, in general, functions of time and are determined by the swimming gait. Here \mathbf{x}' is the point in the swimmer's surface. The linearity of low-Reynolds number or Stokes flow allows a familiar moment expansion (Kim & Karrila, 2005) of the total hydrodynamic force/torque \mathcal{F}^H on the swimmer

$$\mathcal{F}^H = -\mathbf{R}_{\mathcal{F}\mathcal{U}} \cdot \mathcal{U} - \mathbf{R}_{\mathcal{F}E} : \mathbf{E}^S - \mathbf{R}_{\mathcal{F}B} \odot \mathbf{B}^S - \dots, \quad (\text{A.1})$$

where we have grouped the force/torque together as a single vector in the same fashion as in Stokesian dynamics (Durlafsky *et al.*, 1987), $\mathcal{F}^H = (\mathbf{F}^H, \mathbf{L}^H)$, and similarly for the translational/rotational velocities: $\mathcal{U} = (\mathbf{U}, \mathbf{\Omega})$. The hydrodynamic resistance tensors $\mathbf{R}_{\mathcal{F}\mathcal{U}}$, $\mathbf{R}_{\mathcal{F}E}$, etc. are functions of the body geometry only and couple the force to the velocity, to the 'squirming set' $\mathbf{E}^s(t)$, $\mathbf{B}^s(t)$, etc.

In the Stokes flow regime, the rigid body's motion is overdamped and thus force-free: $\mathcal{F}^H + \mathcal{F}^{ext} = 0$, where \mathcal{F}^{ext} is any external force such as gravity or an external torque. For a passive (i.e. non-swimming or non-active) body when $\mathcal{F}^{ext} = 0$, $\mathcal{F}^H = 0$ and there is no motion. For a swimmer when $\mathcal{F}^{ext} = 0$, $\mathcal{F}^H = 0$ is still true, but $\mathcal{U} \neq 0$ in (A.1); the drag, $-\mathbf{R}_{\mathcal{F}\mathcal{U}} \cdot \mathcal{U}$, cancels the swimming part, $-\mathbf{R}_{\mathcal{F}E} : \mathbf{E}^S - \mathbf{R}_{\mathcal{F}B} \odot \mathbf{B}^S - \dots$. Indeed, we can define

$$\mathcal{F}^{swim} = -\mathbf{R}_{\mathcal{F}E} : \mathbf{E}^S - \mathbf{R}_{\mathcal{F}B} \odot \mathbf{B}^S - \dots, \quad (\text{A.2})$$

and

$$\mathcal{F}^{drag} = -\mathbf{R}_{\mathcal{F}\mathcal{U}} \cdot \mathcal{U}, \quad (\text{A.3})$$

and then the required force-free motion $\mathcal{F}^H = \mathcal{F}^{drag} + \mathcal{F}^{swim} = 0$ gives

$$\mathcal{U} = \mathbf{R}_{\mathcal{F}\mathcal{U}}^{-1} \cdot \mathcal{F}^{swim}. \quad (\text{A.4})$$

Equation (A.2) is the *definition* of the swim force (and torque). The reorientation of a nonBrownian swimmer that gives rise to its random walk arises from the squirming

set $\mathbf{E}^s(t)$, etc. changing direction (relative to the body fixed coordinate system). That the swim force is a real measurable force can be appreciated by recognizing that if one wanted to keep the swimmer from moving, the force required is \mathbf{F}^{swim} .

We have considered the simplest model for self-propulsion, namely a squirmer. However, as shown by Swan *et al.*, (2011) the exact same structure applies for swimmers that propel by large deformations of their body shape – the hydrodynamic resistance tensors are now also functions of time but the definitions, (A.1) - (A.3), apply at each instant.

It is important to note that a nonzero swim force does not imply that the fluid velocity disturbance caused by the swimmer decays as $1/r$ as it would for a body with a nonzero hydrodynamic force. This is most clearly seen from the integral representation for the solution to the Stokes equations. The velocity field outside a particle in Stokes flow can be expanded in force moments to give

$$\begin{aligned} u_i(\mathbf{x}) = & -J_{ij}F_j^H - \frac{1}{2}\epsilon_{ijk}\nabla_k J_{il}L_j^H \\ & - \frac{1}{2}(\nabla_k J_{ij} + \nabla_j J_{ik})S_{jk}^H \\ & - \frac{1}{2}\nabla_j\nabla_k J_{il}Q_{jkl}^H - \dots, \end{aligned} \quad (\text{A.5})$$

where the Stokeslet, $8\pi\eta J_{ij}(\mathbf{x}) = \delta_{ij}/r + x_i x_j/r^3$, is evaluated at the particle center. The hydrodynamic force and torque are given by their usual expressions: $\mathbf{F}^H = \int \boldsymbol{\sigma} \cdot \mathbf{n} dS$, $\mathbf{L}^H = \int \mathbf{x}' \times \boldsymbol{\sigma} \cdot \mathbf{n} dS$, and the stresslet is given by $\mathbf{S}^H = \frac{1}{2} \int [\mathbf{x}' \boldsymbol{\sigma} \cdot \mathbf{n} + \boldsymbol{\sigma} \cdot \mathbf{n} \mathbf{x}' - 2\eta(\mathbf{u}^s \mathbf{n} + \mathbf{n} \mathbf{u}^s)] dS$, with $\boldsymbol{\sigma}$ the fluid stress tensor; there is a corresponding expression for the hydrodynamic quadrupole \mathbf{Q}^H , etc.

Since the drag force \mathcal{F}^{drag} balances the swim force there is *no* hydrodynamic force or torque on the swimmer: $\mathcal{F}^H = 0$ ($\mathbf{F}^H = 0$, $\mathbf{L}^H = 0$), and the velocity disturbance decays at leading order as $1/r^2$ coming from the stresslet \mathbf{S}^H . If the slip velocity does not generate a stresslet, then the leading order velocity disturbance decays as $1/r^3$ corresponding to the quadrupole \mathbf{Q}^H . And so on depending on the nature of the propulsive mechanism and the body geometry. There is no difficulty (or

ambiguity) in speaking about a swim force and a drag force for a self-propelled body and the velocity disturbance generated by the swimming body decaying faster than $1/r$. In fact, Blake, (1971) and Ishikawa *et al.*, (2006) expanded the hydrodynamic interactions between two squirmers in a series of surface radial and tangential velocity modes. These modes may cancel such that the velocity disturbance decays as $1/r^n$, which can be very fast for large n .

Even for a single particle, hydrodynamics can also generate a single particle contribution to the active stress $\sigma_h \sim n\zeta U_0 a \langle \mathbf{q}\mathbf{q} \rangle$, which scales as $n\zeta U_0 a$, as opposed to the swim stress that scales as $n\zeta U_0^2 \tau_R$. As discussed by Takatori *et al.*, (2014) for fast swimmers ($\text{Pe}_R \rightarrow 0$), $\sigma_h / \sigma^{swim} \sim U_0 a / (U_0^2 \tau_R) = a / (U_0 \tau_R) = \text{Pe}_R \rightarrow 0$.

Considering other forces that affect the motion of active particles, the overdamped Langevin equation of a set of swimmers can be written as,

$$0 = \mathcal{F}^{drag} + \mathcal{F}^{swim} + \mathcal{F}^B + \mathcal{F}^{ext} + \mathcal{F}^P, \quad (\text{A.6})$$

where $\mathcal{F}^B = 2k_B T \mathbf{R}_{\mathcal{F}\mathcal{U}} \delta(t)$ is a Brownian force with zero mean, \mathcal{F}^{ext} is any external force, and \mathcal{F}^P is a particle-particle interactive or collision force. The resistance tensors are now functions of both the individual swimmer body shape and the relative separation and orientation of all the swimmers, as is standard in Stokesian dynamics.

In the simplest case where the hydrodynamic interactions among the swimmers are neglected and only translational swimming is relevant, the hydrodynamic resistance tensor $\mathbf{R}_{\mathcal{F}\mathcal{U}}$ can be simplified to an isotropic drag tensor $\zeta \mathbf{I}$, so that $\mathbf{F}^{drag} = -\zeta \mathbf{U}$, $\mathbf{F}^{swim} = \zeta U_0 \mathbf{q}$, and we have the ‘Active Brownian Particle’ (ABP) model in the main text. Here, $\mathbf{q}(t)$ is the orientation vector for the swimming direction and is subject to run-and-tumble motion or rotational Brownian diffusion, which are equivalent (Cates & Tailleur, 2013), and comes from the torque balance in (A.6). For a spherical swimmer, $\zeta = 6\pi\eta a$ and the swim force arises from the quadrupole squirming set $\mathbf{B}^s(t)$.

In this work we focus on this ABP model, with both translational (D_T) and rotational (D_R) diffusivity. In this case the time scale is set by $1/D_R (= \tau_R)$, and the reorientation Péclet number (Takatori *et al.*, 2014) $\text{Pe}_R = aD_R/U_0 = a/\ell$ controls how far the swimmer travels in one reorientation time – its run length $\ell = U_0\tau_R$ – compared to its size a . The ratio $D_T/(a^2D_R)$ controls the relative strength of translational Brownian diffusion and reorientational diffusion.

With \mathcal{F}^{swim} defined in (A.2), the suspension stress (Brady, 1993; Batchelor, 1970) in the absence of macroscopic shearing and external torques is:

$$\langle \boldsymbol{\sigma} \rangle = -\langle p_f \rangle \mathbf{I} + \langle \boldsymbol{\sigma}^{swim} \rangle + \langle \boldsymbol{\sigma}^B \rangle + \langle \boldsymbol{\sigma}^P \rangle, \quad (\text{A.7})$$

where $-\langle p_f \rangle \mathbf{I}$ is the isotropic (incompressible) fluid pressure, $\langle \boldsymbol{\sigma}^{swim} \rangle$ is the swim stress, $\langle \boldsymbol{\sigma}^B \rangle = -nk_B T \mathbf{I}$ is the Brownian stress (Brady, 1993), and $\langle \boldsymbol{\sigma}^P \rangle$ is the particle collision stress. The swim stress $\langle \boldsymbol{\sigma}^{swim} \rangle$ can be anisotropic if the swimmers' reorienting process is biased by, for example, an external torque. For the ABP model, $\langle \boldsymbol{\sigma}^{swim} \rangle$ has been thoroughly discussed in both the isotropic (Takatori *et al.*, 2014) and anisotropic (Takatori & Brady, 2014; Yan & Brady, 2015a) cases. In the text, we have written the 'particle stress' $\langle \boldsymbol{\sigma}^{(p)} \rangle = \langle \boldsymbol{\sigma}^{swim} \rangle + \langle \boldsymbol{\sigma}^B \rangle + \langle \boldsymbol{\sigma}^P \rangle$ as is customary in colloidal dynamics.

Appendix B

ANISOTROPIC STRESS UNDER \hat{H} FIELD

In this section we follow the convention by Frankel & Brenner, (1989) to derive the anisotropic swim diffusivity D^{swim} and ideal gas swim stress $\sigma^{swim} = -n\zeta D^{swim}$. Similar methods have also been used in Zia & Brady, (2010) and Takatori & Brady, (2014). In the theory by Frankel & Brenner, (1989), \mathbf{q} is a local degree of freedom. For the swimmers considered here, \mathbf{q} is the orientation vector of each swimmer. The steady state distribution, $P_0^\infty(\mathbf{q})$, is analytically solvable from the Langevin equation for \mathbf{q} :

$$\frac{d\mathbf{q}}{dt} = \Omega_c \mathbf{q} \times \hat{\mathbf{H}} + \dot{\eta}, \quad (\text{B.1})$$

where $\hat{\mathbf{H}}$ is the unit vector in the direction of the orienting field, Ω_c is its magnitude, and $\dot{\eta}$ is the rotational Brownian motion characterized by D_R .

The orientation-average velocity is defined as:

$$\langle \mathbf{U} \rangle = \int_{\mathbf{q}} P_0^\infty(\mathbf{q}) \mathbf{U}(\mathbf{q}) d\mathbf{q}. \quad (\text{B.2})$$

By decomposing $\Delta \mathbf{U}(\mathbf{q}) = \mathbf{U}(\mathbf{q}) - \langle \mathbf{U} \rangle$, the effective diffusivity is given by

$$D^{swim} = \int_{\mathbf{q}} P_0^\infty(\mathbf{q}) \mathbf{B}(\mathbf{q}) \Delta \mathbf{U}(\mathbf{q}) d\mathbf{q}, \quad (\text{B.3})$$

where the \mathbf{B} field is the solution to

$$\nabla_{\mathbf{q}} \cdot [\mathbf{u} P_0^\infty \mathbf{B} - \mathbf{d} \cdot \nabla_{\mathbf{q}} (P_0^\infty \mathbf{B})] = \Delta \mathbf{U} P_0^\infty, \quad (\text{B.4})$$

$$\int_{\mathbf{q}} P_0^\infty \mathbf{B} d\mathbf{q} = 0, \quad (\text{B.5})$$

with appropriate BC in \mathbf{q} space. Here \mathbf{u} and \mathbf{d} are velocity and (intrinsic) diffusivity in \mathbf{q} space, respectively. For swimmers in this work, \mathbf{u} is the torque applied by the $\hat{\mathbf{H}}$ field, and $\mathbf{d} = D_R \mathbf{I}$ is the rotational diffusivity.

In a 2D system, $\mathbf{q} = (\cos \theta, \sin \theta)$, and we define $\hat{\mathbf{H}} = (0, 1)$. The steady probability distribution $P_0^\infty(\theta)$ is:

$$P_0^\infty(\theta) = \frac{\exp(-\chi_R \cos \theta)}{\pi I_0(\chi_R)}, \quad (\text{B.6})$$

and the average orientation is

$$\langle q_z \rangle = \frac{I_1(\chi_R)}{I_0(\chi_R)}, \quad (\text{B.7})$$

where $\chi_R = \Omega_c \tau_R = \Omega_c / D_R$, and I_0, I_1, I_n, \dots are Bessel functions.

With the mathematical expansion

$$\exp(z \cos \theta) = I_0(z) + 2 \sum_{n=1}^{\infty} I_n(z) \cos(n\theta), \quad (\text{B.8})$$

we have

$$D_{\perp}^{swim} = 2 \sum_{n=1}^{\infty} \frac{I_n(\chi_R)}{n \chi_R I_0(\chi_R)} \times \int_{-\pi}^{\pi} \frac{\exp(-\chi_R \cos \theta) \sin \theta \sin(n\theta)}{2\pi I_0(\chi_R)} d\theta. \quad (\text{B.9})$$

The parallel diffusivity, D_{\parallel}^{swim} , is more complicated. First define

$$\begin{aligned} f(p) = & -(p + \pi)I_1(\chi_R) - \sin p I_0(\chi_R) + \\ & I_1(\chi_R) \left(p + \pi + 2 \frac{I_1(\chi_R) \sin p}{I_0(\chi_R)} + \cos p \sin p \right) \\ & + \sum_{n=2}^{\infty} I_n(-\chi_R) \left(- \frac{I_1(\chi_R) \sin(np)}{n I_0(\chi_R)} \right. \\ & \left. + \frac{\cos(np) \sin p - n \cos p \sin(np)}{n^2 - 1} \right) \end{aligned} \quad (\text{B.10})$$

and

$$B_{\parallel}(\theta) = \int_{-\pi}^{\theta} \exp(\chi_R \cos p) f(p) dp. \quad (\text{B.11})$$

Finally,

$$D_{\parallel}^{swim} = \int_{-\pi}^{\pi} \left(\cos \theta + \frac{I_1(\chi_R)}{I_0(\chi_R)} \right) \times \frac{\exp(-\chi_R \cos \theta)}{2\pi I_0(\chi_R)} B_{\parallel}(\theta) d\theta. \quad (\text{B.12})$$

These expressions are used for the anisotropic swim stress in the text.

Appendix C

CLOSURE OF THE SMOLUCHOWSKI EQUATION

The moment expansion of the Smoluchowski equation for the probability density for finding a swimmer at \mathbf{x} with orientation \mathbf{q} is:

$$\frac{\partial n}{\partial t} + \nabla \cdot \mathbf{j}_n = 0 \quad , \quad \mathbf{j}_n = U_0 \mathbf{m} - D_T \nabla n, \quad (\text{C.1})$$

$$\frac{\partial \mathbf{m}}{\partial t} + \nabla \cdot \mathbf{j}_m + 2D_R \mathbf{m} = 0 \quad , \quad \mathbf{j}_m = U_0 \tilde{\mathbf{Q}} - D_T \nabla \mathbf{m}, \quad (\text{C.2})$$

$$\frac{\partial \tilde{\mathbf{Q}}}{\partial t} + \nabla \cdot \mathbf{j}_{\tilde{\mathbf{Q}}} + 6D_R [\tilde{\mathbf{Q}} - \frac{1}{3}n\mathbf{I}] = 0 \quad , \quad \mathbf{j}_{\tilde{\mathbf{Q}}} = U_0 \tilde{\mathbf{B}} - D_T \nabla \tilde{\mathbf{Q}}. \quad (\text{C.3})$$

Here, we have written the second moment as $\tilde{\mathbf{Q}}(\mathbf{x}, t) = \int \mathbf{q}\mathbf{q}P(\mathbf{x}, \mathbf{q}, t)d\mathbf{q}$, and $\tilde{\mathbf{B}} = \int \mathbf{q}\mathbf{q}\mathbf{q}P d\mathbf{q}$ is the third moment.

In the simplest situation of no temporal or spatial variation, a uniform concentration n and no polar order $\mathbf{m} = 0$ are solutions of (C.1)-(C.2), and the second moment has solution $\tilde{\mathbf{Q}} = \frac{1}{3}n\mathbf{I}$. This leads to the natural definition of the nematic order field $\tilde{\mathbf{Q}} = \mathbf{Q} + \frac{1}{3}n\mathbf{I}$, or $\mathbf{Q}(\mathbf{x}, t) = \int (\mathbf{q}\mathbf{q} - \frac{1}{3}\mathbf{I})P(\mathbf{x}, \mathbf{q}, t)d\mathbf{q}$. The conservation equation for \mathbf{Q} is

$$\frac{\partial \mathbf{Q}}{\partial t} + \nabla \cdot \mathbf{j}_{\mathbf{Q}} + 6D_R \mathbf{Q} = 0, \quad (\text{C.4})$$

which now does have the solution of no nematic order $\mathbf{Q} = 0$ in the uniform case. The flux expressions now become: $\mathbf{j}_n = U_0 \mathbf{m} - D_T \nabla n$, $\mathbf{j}_m = U_0 \mathbf{Q} + \frac{1}{3}U_0 n \mathbf{I} - D_T \nabla \mathbf{m}$ and $\mathbf{j}_{\tilde{\mathbf{Q}}} = U_0 \tilde{\mathbf{B}} - \frac{1}{3}U_0 \mathbf{m} \mathbf{I} - D_T \nabla \mathbf{Q}$.

We shall discuss the $\tilde{\mathbf{B}}$ -field and its closure in a moment, but we can already appreciate why closing the equations with $\mathbf{Q} = 0$ leads to a very good approximation as demonstrated by the results presented in the main text. First, we are not setting the second moment to zero; we are approximating the second moment with the ‘isotropic’ distribution $\tilde{\mathbf{Q}} \approx \frac{1}{3}n\mathbf{I}$. Second, (C.4) shows that the \mathbf{Q} -field

is screened like the \mathbf{m} -field, but with a temporal decay that is 3-times faster and a screening length that is $\sqrt{3}$ shorter. Third, as we show below, when variations are slow, like the \mathbf{m} -field where $\mathbf{m} \sim -\frac{1}{6}(U_0/D_R)\nabla n$, the nematic order goes as $\mathbf{Q} \sim -(U_0/D_R)\nabla\mathbf{m} \sim (U_0/D_R)^2\nabla\nabla n$, and thus $\mathbf{Q} \sim O(\ell/L)^2 n$ which is small. Finally, for the 1D flat wall problem, the value of the concentration at the surface, $n^\infty(1 + \frac{1}{6}(\ell/\delta)^2)$, follows directly from the full Smoluchowski equation and is *independent* of the closure. Thus, it is perhaps not surprising that the simple closure $\mathbf{Q} = 0$ works very well except when the body curvature is on the order of the microscopic length $\delta = \sqrt{D_T\tau_R}$.

The equation for the third moment is

$$\frac{\partial \tilde{\mathbf{B}}}{\partial t} + \nabla \cdot \mathbf{j}_{\tilde{\mathbf{B}}} + 12D_R[\tilde{\mathbf{B}} - \frac{1}{6}\boldsymbol{\alpha} \cdot \mathbf{m}] = 0 \quad , \quad \mathbf{j}_{\tilde{\mathbf{B}}} = U_0\tilde{\mathbf{C}} - D_T\nabla\tilde{\mathbf{B}}, \quad (\text{C.5})$$

where $\alpha_{ijkl} = \delta_{ij}\delta_{kl} + \delta_{ik}\delta_{jl} + \delta_{il}\delta_{jk}$ is the fourth order isotropic tensor and $\tilde{\mathbf{C}} = \int \mathbf{q}\mathbf{q}\mathbf{q}\mathbf{q}P(\mathbf{x}, \mathbf{q})d\mathbf{q}$ is the fourth moment.

The proper ‘isotropic’ $\tilde{\mathbf{B}}$ field is $\tilde{\mathbf{B}} = \mathbf{B} + \frac{1}{5}\boldsymbol{\alpha} \cdot \mathbf{m}$, and the equation for \mathbf{B} becomes

$$\frac{\partial \mathbf{B}}{\partial t} + \nabla \cdot \mathbf{j}_{\mathbf{B}} + 12D_R\mathbf{B} = 0 \quad , \quad \mathbf{j}_{\mathbf{B}} = U_0\tilde{\mathbf{C}} - \frac{1}{5}U_0\boldsymbol{\alpha} \cdot [\mathbf{Q} + \frac{1}{3}n\mathbf{I}] - D_T\nabla\mathbf{B}. \quad (\text{C.6})$$

In the examples where we included the nematic field \mathbf{Q} , we closed the equations by setting $\mathbf{B} = 0$, which follows the same reasons as for setting $\mathbf{Q} = 0$. With this closure the \mathbf{Q} -field flux is

$$\mathbf{j}_{\mathbf{Q}} = \frac{1}{5}U_0[\boldsymbol{\alpha} - \frac{5}{3}\mathbf{I}\mathbf{I}] \cdot \mathbf{m} - D_T\nabla\mathbf{Q}, \quad (\text{C.7})$$

which was used in the examples presented in the main text. With this constitutive equation for the flux, for slow variations we see that $\mathbf{Q} \sim (\ell^2/135)(\nabla\nabla - \frac{1}{3}\mathbf{I}\nabla^2)n$.

Appendix D

PRINCIPAL CURVATURES

For a curve on a 2D plane, described by a parametrized curve $(x(t), y(t))$, the curvature is well-known:

$$\kappa = -\frac{|x'y'' - x''y'|}{(x'^2 + y'^2)^{3/2}}. \quad (\text{D.1})$$

For a smooth surface in 3D space, at any point the planes of two principal curvatures and the tangent plane are perpendicular to each other (Edwards *et al.*, 2013). The mean curvature non-dimensionalized by L is simply determined by the surface normal vector \mathbf{n} :

$$H = \frac{\hat{\kappa}_1 + \hat{\kappa}_2}{2} = -\frac{1}{2}\hat{\nabla} \cdot \mathbf{n}. \quad (\text{D.2})$$

The details about how to build a curvilinear coordinate system and all the expansion of operators can be found in the Appendix of the work by Edwards *et al.*, (2013). Without going to the tedious algebraic details, here we only include the relevant leading order expansion of operators:

$$\hat{\nabla}_* f = \frac{\partial f}{\partial q_\perp} \mathbf{n} + O\left(\frac{\delta}{|R|}\right)^2, \quad (\text{D.3a})$$

$$\hat{\nabla}_* \cdot f = -(J_S)f + \frac{\partial f}{\partial q_\perp} + O\left(\frac{\delta}{|R|}\right)^2, \quad (\text{D.3b})$$

$$\hat{\nabla}_*^2 f = -(J_S)\frac{\partial f}{\partial q_\perp} + \frac{\partial^2 f}{\partial q_\perp^2} + O\left(\frac{\delta}{|R|}\right)^2, \quad (\text{D.3c})$$

where $J_S = 2H$, and $\hat{\nabla}_*$ is the nabla operator in the (orthogonal) curvilinear coordinate system q_1, q_2, q_\perp , defined on the curved surface shown in Fig. 4.2. q_\perp follows the direction of the surface normal vector \mathbf{n} . q_1 and q_2 are on the curved surface, and are located in the two planes associated with the two principal vectors, respectively. It is clear that to leading order $O(\delta/|R|)$, there is no need to deal with

the gradients on q_1, q_2 directions. The formulation of (D.3) is consistent with the work in literature (Cox, 1997; Yariv, 2009) in solving the curved boundary layers.

The expansion of operator $\hat{\nabla}_*$ beyond the leading order relies on a rigorous algebra of the full curvilinear space. Mathematically, the second order expansion relies not only on the mean curvature H , but also on the *variations* of curvatures. The full expansion may include up to 21 curvature coefficients (Panaras, 1987), and probably forbids any analytical work.

Appendix E

THE NOTATION FOR ROTATIONAL FLUX IN 3D SPACE

Rotation is mathematically challenging to describe. In this work we follow the convention of Brenner & Condiff, (1972), by defining a nabla operator in orientation space ∇_R . The evolution of a spherical ABP with orientation \mathbf{q} by torque and Brownian motion can be described in a spherical coordinate system ($0 < \theta < \pi, 0 < \phi < 2\pi$):

$$\mathbf{q} = \sin \theta \cos \phi \mathbf{e}_x + \sin \theta \sin \phi \mathbf{e}_y + \cos \theta \mathbf{e}_z. \quad (\text{E.1})$$

The rotational gradient operator $\nabla_R = \mathbf{q} \times \frac{\partial}{\partial \mathbf{q}}$. Here we have:

$$\frac{\partial f(\theta, \phi)}{\partial \mathbf{q}} = \mathbf{e}_\theta \frac{\partial f}{\partial \theta} + \frac{1}{\sin \theta} \mathbf{e}_\phi \frac{\partial f}{\partial \phi}, \quad (\text{E.2})$$

$$\nabla_R = \mathbf{q} \times \frac{\partial f}{\partial \mathbf{q}} = \mathbf{e}_\phi \frac{\partial f}{\partial \theta} - \frac{1}{\sin \theta} \mathbf{e}_\theta \frac{\partial f}{\partial \phi}. \quad (\text{E.3})$$

Also, the operators are usually used with its derivatives:

$$\frac{\partial}{\partial \mathbf{q}} \mathbf{q} = \mathbf{I} - \mathbf{q}\mathbf{q}, \quad (\text{E.4})$$

$$\mathbf{q} \cdot \frac{\partial}{\partial \mathbf{q}} = \frac{\partial}{\partial \mathbf{q}} \cdot \mathbf{q} = 0, \quad \frac{\partial}{\partial \mathbf{q}} \times \mathbf{q} = 0, \quad (\text{E.5})$$

$$\left(\mathbf{q} \times \frac{\partial}{\partial \mathbf{q}} \right) \times \mathbf{q} = -2\mathbf{q}, \quad (\text{E.6})$$

$$\mathbf{q} \times \left(\mathbf{q} \times \frac{\partial}{\partial \mathbf{q}} \right) = -\frac{\partial}{\partial \mathbf{q}}, \quad (\text{E.7})$$

$$\nabla_R \cdot \nabla_R = \frac{1}{\sin \theta} \left(\frac{\partial}{\partial \theta} \sin \theta \frac{\partial}{\partial \theta} \right) + \frac{1}{\sin^2 \theta} \frac{\partial^2}{\partial \phi^2}. \quad (\text{E.8})$$

For a orientational potential energy $U(\mathbf{q})$, the torque and angular velocity are:

$$\mathbf{L} = -\nabla_R U, \quad \boldsymbol{\omega} = \frac{1}{\zeta_R} \mathbf{L}, \quad (\text{E.9})$$

where we assumed the isotropic orientational drag ζ_R . The general case comes from linearity of stokes flow: $\boldsymbol{\omega} = \mathbf{M}_{\Omega L} \cdot \mathbf{L}$. The angular velocity is interpreted as:

$$\dot{\mathbf{q}} = -\mathbf{q} \times \boldsymbol{\omega}. \quad (\text{E.10})$$

Appendix F

FAXEN LAWS FOR A HOMOGENEOUSLY REACTIVE PARTICLE

Consider uniform reaction everywhere on the particle surface, $h(\mathbf{n}) = 1$. With the first order reactive boundary condition (6.5) for $\mathbf{n} \cdot \mathbf{j}_R$, the multipoles of particle α become:

$$q_\alpha = -\kappa \int_S c dS, \quad (\text{F.1})$$

$$\mathbf{S}_\alpha = (D_R - \kappa a_R) \int_S \mathbf{n} c dS, \quad (\text{F.2})$$

$$\mathbf{Q}_\alpha = (2a_R D_R - \kappa a_R^2) \left(\int_S \mathbf{n} \mathbf{n} c dS - \frac{1}{3} \int_S \mathbf{I} c dS \right). \quad (\text{F.3})$$

Thus, we need 3 surface integrals of c : $\int_S c dS$, $\int_S \mathbf{n} c dS$ and $\int_S \mathbf{n} \mathbf{n} c dS$.

For any point \mathbf{x} on the surface S of some particle α , the integral (Bonnetcaze & Brady, 1990) that represents the solution to Laplace's equation can be written as:

$$c(\mathbf{x}) - c'(\mathbf{x}) - c^E(\mathbf{x}) \quad (\text{F.4})$$

$$= \frac{1}{4\pi} \int_{S_y} \left(\mathbf{j}_R(\mathbf{y}) \frac{1}{D_R |\mathbf{x} - \mathbf{y}|} + c(\mathbf{y}) \frac{\mathbf{x} - \mathbf{y}}{|\mathbf{x} - \mathbf{y}|^3} \right) \cdot \mathbf{n}_y dS_y. \quad (\text{F.5})$$

Here c denotes the actual field value, c' and c^E refer to other particles' perturbation and the imposed external field respectively, and \mathbf{y} is a vector on the particle surface.

Take integral $\int_{S_x} dS$ of both sides. For the left side we have

$$\int_{S_x} [c(\mathbf{x}) - c'(\mathbf{x}) - c^E(\mathbf{x})] dS \quad (\text{F.6})$$

$$= \int_S c dS - 4\pi a^2 (c' + c^E)|_{r_\alpha}, \quad (\text{F.7})$$

where $(c' + c^E)|_{r_\alpha}$ means that the value of c' and c^E are evaluated at the center of particle α , \mathbf{r}_α . The right side becomes a double integral over both \mathbf{x} and \mathbf{y} on the

surface. By exchanging the order of integration, we have:

$$\int_S c dS - 4\pi a^2 (c' + c^E)|_{r_\alpha} \quad (\text{F.8})$$

$$= \frac{a}{D_R} \int_S \mathbf{j}_R \cdot \mathbf{n} dS = \frac{a}{D_R} q, \quad (\text{F.9})$$

from which we get the Faxen laws for monopole q . One can easily check that if we put only one particle in infinite field with condition c^∞ , the Faxen laws give $q = -[4\pi\text{Da}/(1 + \text{Da})] D_R a c^\infty$, which is the consumption rate of reactant on the particle surface and coincides with solution given by traditional methods, e.g., separation of variables.

The S_α and Q_α relations can also be derived in the same way, but require some lengthy math. We shall not repeat the process here. Also, the factor $\text{Da}/(1 + \text{Da})$ covers both reaction-limited and diffusion-limited cases. In the diffusion-limited case ($\text{Da} \rightarrow \infty$), $\text{Da}/(1 + \text{Da}) \rightarrow 1$ and the Faxen laws reduces to the relations given by Bonnecaze & Brady, (1990). In the reaction-limited case $\text{Da} \rightarrow 0$ and therefore $\text{Da}/(1 + \text{Da}) \rightarrow \text{Da}$, so that $q_\alpha \propto \text{Da}$.

Appendix G

FAXEN LAWS FOR A JANUS REACTIVE PARTICLE

For Janus particles, the Boundary Element Method (BEM hereafter) is used to calculate the Faxen laws matrix. We follow the standard BEM convention, and the problem of a singularity on the boundary, which often occurs in the BEM method, is appropriately handled (Pozrikidis, 2002).

The numerical solution is conducted for a Janus particle with its orientation vector $\boldsymbol{\xi} = \hat{z}$. Due to symmetry, \mathbf{C} (truncated at dipole level) takes the following form:

$$\begin{pmatrix} q \\ S_x \\ S_y \\ S_z \end{pmatrix} = \begin{pmatrix} f_c^q & 0 & 0 & f_{cz}^q \\ 0 & f_{cx}^{sx} & 0 & 0 \\ 0 & 0 & f_{cy}^{sy} & 0 \\ f_c^{sz} & 0 & 0 & f_{cz}^{sz} \end{pmatrix} \begin{pmatrix} c \\ (\nabla c)_x \\ (\nabla c)_y \\ (\nabla c)_z \end{pmatrix}, \quad (\text{G.1})$$

where S_x , S_y and S_z are components of vector \mathbf{S} . $(\nabla c)_x$, $(\nabla c)_y$ and $(\nabla c)_z$ are components of ∇c . The five response functions, f_c^q , f_{cz}^q , f_{cx}^{sx} , f_c^{sz} , f_{cz}^{sz} , are functions of Da only. The BEM solution is done for Da in the range (0.01, 100.0), covering both reaction-limited ($\text{Da} \rightarrow 0$) and diffusion-limited ($\text{Da} \rightarrow \infty$) cases. The reactivity f functions are fitted by an interpolation form to allow each f to be evaluated for arbitrary Da :

$$f_c^q = - \frac{4\pi\text{Da}}{1 + \text{Da}} \frac{0.72\text{Da}^2 + 1.98\text{Da} + 1}{\text{Da}^2 + 3.26\text{Da} + 2}, \quad (\text{G.2})$$

$$f_{cz}^q = - \frac{4\pi\text{Da}}{1 + \text{Da}} \frac{0.46\text{Da}^2 + 0.36\text{Da} + 0.38}{\text{Da}^2 + 0.82\text{Da} + 1}, \quad (\text{G.3})$$

$$f_{cx}^{sx} = - 2\pi \frac{\text{Da} - 2.76}{\text{Da} + 2.76}, \quad (\text{G.4})$$

$$f_c^{sz} = - \frac{4\pi\text{Da}}{1 + \text{Da}} \frac{0.46\text{Da}^2 + 0.39\text{Da} + 0.38}{\text{Da}^2 + 0.87\text{Da} + 1}, \quad (\text{G.5})$$

$$f_{cz}^{sz} = - 2\pi \frac{\text{Da} - 7.77}{4.50\text{Da} + 7.70}. \quad (\text{G.6})$$

The typical error of these fitting functions is around 2%. Here, we do not pursue the absolute accuracy because our interest is in the correct scaling of the response and the correct features of propulsion and interaction.

For particles with $\xi \neq \hat{z}$, rotation can be applied to the matrices C :

$$C = \begin{pmatrix} f_c^q & f_{cz}^q \xi^T \\ f_c^{sz} \xi & f_{cx}^{sx} \mathbf{I} + (f_{cz}^{sz} - f_{cx}^{sx}) \xi \xi \end{pmatrix}, \quad (\text{G.7})$$

where ξ is a 3×1 column vector.

Similarly, M_B is calculated from the orientation ξ and the fitted functions g_c^z , g_{cz}^z and g_{cx}^x :

$$M_B = \begin{pmatrix} g_c^z \xi & g_{cx}^x \mathbf{I} + (g_{cz}^z - g_{cx}^x) \xi \xi \end{pmatrix}, \quad (\text{G.8})$$

where

$$g_{cx}^x = 2\pi \frac{0.36\text{Da}^2 + 2.55\text{Da} + 1}{\text{Da}^2 + 2.65\text{Da} + 1}, \quad (\text{G.9})$$

$$g_c^z = -\frac{4\pi\text{Da}}{1 + \text{Da}} \frac{0.16\text{Da}^2 + 0.094\text{Da} + 0.13}{\text{Da}^2 + 0.60\text{Da} + 1}, \quad (\text{G.10})$$

$$g_{cz}^z = 4\pi \frac{0.30\text{Da}^2 + 0.95\text{Da} + 0.5}{\text{Da}^2 + 2.05\text{Da} + 1}. \quad (\text{G.11})$$

Appendix H

ALL CONTRIBUTIONS OF \mathcal{E} IN THE EWALD SUM

For compactness of the equations, we define:

$$f(r) = \frac{\text{Erfc}\left(\sqrt{\pi/\zeta}r\right)}{r}, \quad (\text{H.1})$$

and $\mathbf{r} = \mathbf{x} - \mathbf{y}$. Suppose that \mathbf{x} is at the location of particle 1, $\mathbf{x} = \mathbf{y}_1$. In the summation, \mathbf{y}_{other} means all other particles in space. $\mathbf{r} = \mathbf{x} - \mathbf{y}_\beta = \mathbf{y}_1 - \mathbf{y}_\beta$, and β denotes the other particles. In this context, $\nabla = \nabla_1 = \partial/\partial\mathbf{y}_1$, $\nabla_2 = \nabla_\beta = \partial/\partial\mathbf{y}_\beta$.

The realspace sum, wavenumber sum, and the self-correction terms are:

$$c(\mathbf{y}_1) = \langle c \rangle \quad (\text{H.2a})$$

$$+ \frac{1}{4\pi D_R} \sum_{\beta \neq 1} (q_\beta^{eff} - \mathbf{S}_\beta \cdot \nabla_1 + \frac{1}{2} \mathbf{Q}_\beta : \nabla_1^{(2)}) f(r) \quad (\text{H.2b})$$

$$+ \frac{1}{4\pi D_R V_0} \sum_{\mathbf{k} \neq 0} \sum_{\beta} (q_\beta^{eff} - \mathbf{S}_\beta \cdot \nabla_1 + \frac{1}{2} \mathbf{Q}_\beta : \nabla_1^{(2)}) e^{2\pi i \mathbf{k} \cdot (\mathbf{y}_\beta - \mathbf{y}_1)} \frac{e^{-\zeta \pi k^2}}{\pi k^2} \quad (\text{H.2c})$$

$$+ \left(-\frac{1}{2\pi D_R \sqrt{\zeta}}\right) q_1^{eff} + \frac{1}{6 D_R \zeta^{3/2}} \text{Tr} \mathbf{Q}_1, \quad (\text{H.2d})$$

$$\nabla c(\mathbf{y}_1) = \frac{1}{4\pi D_R} \sum_{\beta \neq 1} (q_\beta^{eff} \nabla_1 - \mathbf{S}_\beta \cdot \nabla_1^{(2)} + \frac{1}{2} \mathbf{Q}_\beta : \nabla_1^{(3)}) f(r) \quad (\text{H.2e})$$

$$+ \frac{1}{4\pi D_R V_0} \sum_{\mathbf{k} \neq 0} \sum_{\beta} (q_\beta^{eff} \nabla_1 - \mathbf{S}_\beta \cdot \nabla_1^{(2)} + \frac{1}{2} \mathbf{Q}_\beta : \nabla_1^{(3)}) e^{2\pi i \mathbf{k} \cdot (\mathbf{y}_\beta - \mathbf{y}_1)} \frac{e^{-\zeta \pi k^2}}{\pi k^2} \quad (\text{H.2f})$$

$$+ \left(-\frac{1}{3 D_R \zeta^{3/2}}\right) \mathbf{S}_1, \quad (\text{H.2g})$$

$$\text{and } \nabla \nabla c(\mathbf{y}_1) = \frac{1}{4\pi D_R} \sum_{\beta \neq 1} (q_\beta^{eff} \nabla_1^{(2)} - \mathbf{S}_\beta \cdot \nabla_1^{(3)} + \frac{1}{2} \mathbf{Q}_\beta : \nabla_1^{(4)}) f(r) \quad (\text{H.2h})$$

$$+ \frac{1}{4\pi D_R V_0} \sum_{\mathbf{k} \neq 0} \sum_{\beta} (q_\beta^{eff} \nabla_1^{(2)} - \mathbf{S}_\beta \cdot \nabla_1^{(3)} + \frac{1}{2} \mathbf{Q}_\beta : \nabla_1^{(4)}) \\ e^{2\pi i \mathbf{k} \cdot (\mathbf{y}_\beta - \mathbf{y}_1)} \frac{e^{-\zeta \pi k^2}}{\pi k^2} \quad (\text{H.2i})$$

$$+ \left(\frac{1}{3D_R \zeta^{3/2}} \mathbf{I} q_1^{eff} \right) + \left(-\frac{\pi}{5D_R \zeta^{5/2}} \right) \mathbf{T} : \mathbf{Q}_1. \quad (\text{H.2j})$$

Here $\nabla^{(i)}$ means to take ∇ operator i times, which gives the correct tensor structure.

Tr is the trace operator, and \mathbf{T} is the 4th order isotropic tensor: $\mathbf{T}_{ijkl} = (\delta_{ij}\delta_{kl} + \delta_{ik}\delta_{jl} + \delta_{il}\delta_{jk})$.

Appendix I

FEEDBACK FACTOR F_C

In this part, the ‘feedback factor’ F_C from c is derived. It is, the perturbation c' as a function of the perturbation in number density \mathcal{P}' , controlled by the c equation (7.12):

$$-D_R(\nabla_{xy}^2 + \frac{\partial^2}{\partial z^2})c = \left(S - \kappa c(z=0) \int_0^{2\pi} \mathcal{P}(x, y, \theta) d\theta \right) \delta(z). \quad (\text{I.1})$$

The perturbation in number density in phase space is (7.14). Here because only $\int n d\theta$ appears in the above equation, only the $m = 0$ mode matters: $b_{q,0} = \frac{1}{2\pi} \int \mathcal{P} d\theta$. Also for the simplicity of notion, here we take an arbitrary mode q :

$$\mathcal{P}' = b_{q,0}(t) \exp(-iqx), \quad (\text{I.2})$$

and the response of c' is assumed to be:

$$c'(x, y, z, t) = A(z)b_{q,0}(t) \exp(-iqx). \quad (\text{I.3})$$

In the following, the Fourier transform in the z axis and in the xy plane will be considered independently, to overcome the difficulty due to the monolayer geometry. In short, $A(z=0)$ is solved.

Substitute c' into (7.12), and the perturbation around the steady state c_0, \mathcal{P}_0 satisfies:

$$\begin{aligned} & -D_R \left(-q^2 A(z) e^{-iqx} + A''(z) e^{-iqx} \right) \\ & = -\delta(z) \left(\kappa 2\pi \mathcal{P}_0 A(z) e^{-iqx} + 2\pi \kappa b_{q,0}(t) c_0 e^{-iqx} \right), \end{aligned} \quad (\text{I.4})$$

where we used the fact that in linear perturbation, change in S is on second order, thus negligible.

Take Fourier transform of $A(z)$ in above equation, follow the convention:

$$\hat{f}(\omega) = \int f(z) e^{-2\pi i \omega z} dz, \quad (\text{I.5})$$

$$f(z) = \int \hat{f}(\omega) e^{2\pi i \omega z} d\omega. \quad (\text{I.6})$$

We get:

$$D_R \left(q^2 \hat{A}(\omega) + 4\pi^2 \omega^2 \hat{A}(\omega) \right) = -2\pi \mathcal{P}_0 \kappa A(z=0) - \kappa c_0 2\pi b_{q,0}(t), \quad (\text{I.7})$$

with solution:

$$\hat{A}(\omega) = -\frac{2\pi \kappa \mathcal{P}_0 A(z=0) + b_{q,0}(t) c_0}{D_R \left(q^2 + 4\pi^2 \omega^2 \right)}. \quad (\text{I.8})$$

Transform back to real space with $\omega \rightarrow z$:

$$A(z) = -\frac{2\pi \kappa}{D_R} \left(\mathcal{P}_0 A(z=0) + b_{q,0}(t) c_0 \right) \frac{e^{-qz}}{2q}, \quad (\text{I.9})$$

which means, high frequency (large q) components decay faster away from the $z = 0$ plane.

Let $z = 0$, we get:

$$A(z=0) = -\frac{\kappa c_0 \pi}{D_R q + \pi \kappa \mathcal{P}_0} b_{q,0}(t) = F_c b_{q,0}(t), \quad (\text{I.10})$$

where $F_c = -\frac{\kappa c_0 \pi}{D_R q + \pi \kappa \mathcal{P}_0}$ is the ‘feedback factor’ defined in the main text.

Appendix J

LINEAR DYNAMIC SYSTEM

The general theory of linear dynamic systems (Guckenheimer & Holmes, 2013, ch. 1) is briefly reviewed here for reference. A linear dynamical system is a group of first order ODEs which can be represented by a linear algebraic form:

$$\frac{d}{dt}\mathbf{x}(t) = \mathbf{A}\mathbf{x}(t), \quad (\text{J.1})$$

where $\mathbf{x}(t)$ is an N -dimensional vectorial function of time t and \mathbf{A} is a constant $N \times N$ matrix. The initial condition is $\mathbf{x}(t = 0) = \mathbf{x}_0$. The matrix \mathbf{A} is also called the operator of that dynamical system. In this work ‘matrix’ and ‘operator’ are used interchangeably.

When \mathbf{A} has N eigenvalues $(\lambda_1, \lambda_2, \dots, \lambda_N)$ and N linear independent eigenvectors $(\mathbf{v}_1, \mathbf{v}_2, \dots, \mathbf{v}_N)$, a general solution to (J.1) exists:

$$\mathbf{x}(t) = \sum_{i=1}^N C_i \exp(\lambda_i t) \mathbf{v}_i, \quad (\text{J.2})$$

where C_i s are constants and should satisfy the initial condition:

$$\mathbf{x}_0 = \sum_{i=1}^N C_i \mathbf{v}_i. \quad (\text{J.3})$$

C_i s can be uniquely determined because eigenvectors $(\mathbf{v}_1, \mathbf{v}_2, \dots, \mathbf{v}_N)$ are assumed to be linearly independent.

When all eigenvalues $(\lambda_1, \lambda_2, \dots, \lambda_N)$ have negative-valued real part, $\mathbf{x}(t) \rightarrow \mathbf{0}$ as $t \rightarrow \infty$. Therefore the stability of the system (J.1) is completely determined by the sign of the real part of the eigenvalues.

Appendix K

**PERTURBATION OF EIGENVALUES & EIGENVECTORS OF A
COMPLEX MATRIX: GENERAL THEORY.**

In this section the general theory developed by Kato, (1995) is briefly described here, following Kato's notations. The detailed theory can also be found in Baumgärtel, (1985).

Definitions

Resolvent

If λ is not an eigenvalue of \mathbf{A} , then $\lambda\mathbf{I} - \mathbf{A}$ is invertible. In this case, λ is called a regular point. The set of all regular points is called the *resolvent set* and is denoted by $\text{res}\mathbf{A}$. One writes

$$\mathbf{R}(\lambda) = \mathbf{R}(\lambda, \mathbf{A}) = (\mathbf{A} - \lambda\mathbf{I})^{-1}. \quad (\text{K.1})$$

For $\lambda_1 \neq \lambda_2$, \mathbf{R} commutes: $\mathbf{R}(\lambda_1)\mathbf{R}(\lambda_2) = \mathbf{R}(\lambda_2)\mathbf{R}(\lambda_1)$. Also $\mathbf{R}(\lambda)$ is an operator-valued, differentiable function of λ .

Eigenprojection

For an eigenvalue λ_j of matrix \mathbf{A} , we define the eigenprojection corresponding to λ_j :

$$\mathbf{P}_j = -\frac{1}{2\pi i} \int_{C_j} \mathbf{R}(\lambda, \mathbf{A}) d\lambda, \quad (\text{K.2})$$

where C_j is a positively oriented sphere with center λ_j , which consists of regular points and is such that no other eigenvalue lies inside C_j .

Eigennilpotent

For an eigenvalue λ_j of matrix A , we define the eigennilpotent:

$$D_j = (A - \lambda_j I)P_j. \quad (\text{K.3})$$

D_j has only one eigenvalue: 0. The number m satisfying $D_j^m = 0$, $D_j^{m-1} \neq 0$ is called the *index* of the eigenvalue λ_j .

Canonical form

A matrix A can be represented by $A = S + D$, where $S = \sum_h \lambda_h P_h$ and $D = \sum_h D_h$.

Perturbation

This part is adapted from Kato's work (Kato, 1995, ch. 2).

Assume $T(x) = T + xT_1 + x^2T_2 + \dots$. We may suppose that a matrix-valued function $T(x)$ is given, which is holomorphic in a given domain D_0 of the complex x -plane. x is the perturbation variable. The unperturbed symbols are denoted as T, λ , etc. The perturbed ones are denoted as a function of x as $T(x), \lambda(x)$, etc.

It can be proved that the number of eigenvalues of $T(x)$ is a constant s independent of x , with the exception of some special values of x . There are only a finite number of such *exceptional points* x in each compact subset of D_0 . This number s is equal to dimension N if these analytic functions (if there are more than one) are all distinct; in this case $T(x)$ is simple and therefore diagonalizable for all non-exceptional x . If, on the other hand, there happen to be identical ones among these analytic functions, then we have $s < N$; in this case $T(x)$ is said to be *permanently degenerate*.

It can be proved that each eigenvalue function $\lambda_j(x), j \in [1, s]$ is a continuous function of x .

In general there are several cycles with the same center. All the eigenvalues belonging to cycles with center λ are said to depart from the unperturbed eigenvalue λ by

splitting at $x = 0$. The set of these eigenvalues will be called the λ -group, since they cluster around λ for small x .

Let λ be one of the eigenvalues of T , with algebraic multiplicity m . Let Γ be a closed positively-oriented curve, say a circle, in the resolvent set $P(T)$ enclosing λ but no other eigenvalues of T . Define

$$P = -\frac{1}{2\pi i} \int_{C_j} R(\lambda, A) d\lambda, \quad (\text{K.4})$$

which is a projection and is equal to the sum of the eigenprojections for all the eigenvalues of $T(x)$ lying inside Γ . It follows that the eigenvalues of $T(x)$ lying inside Γ form exactly the λ -group. For brevity we call $P(m)$ the *total projection*, for the λ -group.

The foregoing general results are somewhat simplified in the case in which $T(x)$ is linear in x . Then $T(x)$ is defined in the whole complex plane, which will be taken as the domain D_0 . The algebraic functions $\lambda_j(x)$ (perturbed eigenvalues) have no pole at a finite value of x . At $x = \infty$ they have at most a pole of order 1.

The eigenvalue λ will in general split into several eigenvalues of $T(x)$ for small $x \neq 0$ (the λ -group). The total projection $P(x)$ for this λ -group is holomorphic at $x = 0$:

$$P(x) = \sum_0^{\infty} P^{(n)}(x), \quad P^{(0)} = P, \quad (\text{K.5})$$

where

$$P^{(n)} = -\frac{1}{2\pi i} \int_{\Gamma} R^{(n)}(\lambda, A) d\lambda. \quad (\text{K.6})$$

It follows that, the weighted mean $\hat{\lambda}(x)$ of the λ -group eigenvalues of $T(x)$:

$$\hat{\lambda}(x) = m \operatorname{Tr}(T(x)P(x)) = \lambda + m \operatorname{Tr}((T(x) - \lambda I)P(x)). \quad (\text{K.7})$$

If there is no splitting of λ so that the λ -group consists of a single eigenvalue $\lambda(x)$ with multiplicity m , we have $\hat{\lambda} = \lambda$, which is always true for $m = 1$

These series give a complete solution to the eigenvalue problem for the λ -group in the case of no splitting, $\lambda(x)$, $P(x)$ and $D(x)$ being all holomorphic at $x = 0$.

If in particular λ is a semisimple eigenvalue of $T(x)$, we have $D = 0$ and the first terms of series expansion can be explicitly given:

$$P^{(1)} = -PT^{(1)}S - ST^{(1)}P, \quad (\text{K.8})$$

$$\begin{aligned} P^{(2)} = & -PT^{(2)}S - ST^{(2)}P + PT^{(1)}ST^{(1)}S + ST^{(1)}PT^{(1)}S \\ & + ST^{(1)}ST^{(1)}P - PT^{(1)}PT^{(1)}S^2 - PT^{(1)}S^2T^{(1)}P - S^2T^{(1)}PT^{(1)}P, \end{aligned} \quad (\text{K.9})$$

$$P^{(3)} = \dots . \quad (\text{K.10})$$

Under the same semisimple condition, with algebraic multiplicity m , the equations for

$$\hat{\lambda} = \lambda + x\hat{\lambda}^{(1)} + x^2\hat{\lambda}^{(2)} + x^3\hat{\lambda}^{(3)} + x^4\hat{\lambda}^{(4)} + \dots, \quad (\text{K.11})$$

are:

$$\hat{\lambda}^{(1)} = \frac{1}{m} \text{Tr} T^{(1)}P, \quad (\text{K.12})$$

$$\hat{\lambda}^{(2)} = \frac{1}{m} \text{Tr} [T^{(2)}P - T^{(1)}ST^{(1)}P], \quad (\text{K.13})$$

$$\begin{aligned} \hat{\lambda}^{(3)} = & \frac{1}{m} \text{Tr} [T^{(3)}P - T^{(1)}ST^{(2)}P - T^{(2)}ST^{(1)}P \\ & + T^{(1)}ST^{(1)}ST^{(1)}P - T^{(1)}S^2T^{(1)}PT^{(1)}P], \end{aligned} \quad (\text{K.14})$$

$$\begin{aligned} \hat{\lambda}^{(4)} = & \frac{1}{m} \text{Tr} [T^{(4)}P - T^{(1)}ST^{(3)}P - T^{(2)}ST^{(2)}P - T^{(3)}ST^{(1)}P \\ & + T^{(1)}ST^{(1)}ST^{(2)}P + T^{(1)}ST^{(2)}ST^{(1)}P + T^{(2)}ST^{(1)}ST^{(1)}P \\ & - T^{(1)}S^2T^{(1)}PT^{(2)}P - T^{(1)}S^2T^{(2)}PT^{(1)}P - T^{(2)}S^2T^{(1)}PT^{(1)}P \\ & - T^{(1)}ST^{(1)}ST^{(1)}ST^{(1)}P + T^{(1)}S^2T^{(1)}ST^{(1)}PT^{(1)}P \\ & + T^{(1)}ST^{(1)}S^2T^{(1)}PT^{(1)}P + T^{(1)}S^2T^{(1)}PT^{(1)}ST^{(1)}P \\ & - T^{(1)}S^3T^{(1)}PT^{(1)}PT^{(1)}P], \end{aligned} \quad (\text{K.15})$$

Here S refers to the *reduced resolvent* of T , with respect to the eigenvalue λ . We denote it by $S(\zeta)$, which is the holomorphic part of resolvent $R(\zeta)$ in the neighborhood of the considered eigenvalue λ :

$$R(\zeta) = -\frac{P}{\zeta - \lambda} - \sum_{k=2}^{\nu(\lambda)} \frac{D_{\lambda}^{k-1}}{(\zeta - \lambda)^k} + S(\zeta). \quad (\text{K.16})$$

Perturbation of eigenvectors

Kato points out that (Kato, 1995, p. 92) ‘Since the eigenvectors are not uniquely determined, however, there are no definite formulas for the eigenvectors $v(x)$ of $T(x)$ as functions of x ’. However a special case is enough for the instability problem considered in this work. When multiplicity $m = 1$ and $T(x)$ is linear in x (see Kato, 1995, p. 93),

$$v(x) = v - xST^{(1)}v + x^2S(T^{(1)} - \lambda^{(1)})ST^{(1)}v + \dots . \quad (\text{K.17})$$

Appendix L

PERTURBATION SERIES: FULL SOLUTION

The expansion series for small P is presented here.

$$\lambda_0(P) = \lambda_0^{(P0)} + P\lambda_0^{(P1)} + P^2\lambda_0^{(P2)} + \dots, \quad (\text{L.1})$$

$$\mathbf{v}_0(P) = \mathbf{v}_0^{(P0)} + P\mathbf{v}_0^{(P1)} + P^2\mathbf{v}_0^{(P2)} + \dots. \quad (\text{L.2})$$

Here $\lambda_0^{(P0)}$ and $\mathbf{v}_0^{(P0)}$ are solved in (7.28) and (7.24). The series for $\lambda_0(P)$ are:

$$\lambda_0^{(P1)} = 0, \quad (\text{L.3a})$$

$$\lambda_0^{(P2)} = - \frac{c_0^2 D_R q^3}{\pi c_0 \kappa \mathcal{P}_0 q^2 (A + 2M) + 2D_{rot} (D_R q + \pi \kappa \mathcal{P}_0)} - \frac{\pi A c_0^3 \kappa \mathcal{P}_0 q^4}{(D_R q + \pi \kappa \mathcal{P}_0) \left(\frac{\pi c_0 \kappa \mathcal{P}_0 q^2 (A+2M)}{D_R q + \pi \kappa \mathcal{P}_0} + 2D_{rot} \right) \left(\frac{2\pi c_0 \kappa \mathcal{P}_0 q^2 (A+2M)}{D_R q + \pi \kappa \mathcal{P}_0} + 16D_{rot} \right)}, \quad (\text{L.3b})$$

$$\lambda_0^{(P3)} = 0. \quad (\text{L.3c})$$

The full analytical expression of $\lambda_0^{(P4)}$ is too complicated to be listed here. In the special case of $M = A = 0$:

$$\lambda_0^{(P4)} = - \frac{c_0^2 q^4 (7c_0^2 + 15c_0 F_c \mathcal{P}_0 + 8F_c^2 \mathcal{P}_0^2)}{32D_{rot}^3} = \frac{c_0^4 D_R q^5 (\pi \kappa \mathcal{P}_0 - 7D_R q)}{32D_{rot}^3 (D_R q + \pi \kappa \mathcal{P}_0)^2}. \quad (\text{L.4})$$

The leading order contributions of M and A are on $O(q^6)$ and $O(q^7)$:

$$\begin{aligned} \lambda_0^{(P4)} \approx & O \left(\frac{17c_0^4 D_R^3 q^7}{32\pi^3 D_{rot}^3 \kappa^3 \mathcal{P}_0^3} - \frac{9c_0^4 D_R^2 q^6}{32\pi^2 D_{rot}^3 \kappa^2 \mathcal{P}_0^2} + \frac{c_0^4 D_R q^5}{32\pi D_{rot}^3 \kappa \mathcal{P}_0} \right) \\ & + O \left(\left(\frac{5c_0^5 q^6}{2304 D_{rot}^4} - \frac{167c_0^5 D_R q^7}{2304\pi D_{rot}^4 \kappa \mathcal{P}_0} \right) A \right) \\ & + O \left(- \frac{9c_0^5 D_R q^7}{128\pi D_{rot}^4 \kappa \mathcal{P}_0} M \right). \end{aligned} \quad (\text{L.5})$$

The series for the eigenvector $\mathbf{v}_0(P)$ are:

$$\mathbf{v}_0^{(P1)} = f_1(\mathbf{e}_1 + \mathbf{e}_{-1}) + g_1(\mathbf{e}_3 + \mathbf{e}_{-3}), \quad (\text{L.6a})$$

$$\mathbf{v}_0^{(P2)} = f_2(\mathbf{e}_2 + \mathbf{e}_{-2}) + g_2(\mathbf{e}_4 + \mathbf{e}_{-4}), \quad (\text{L.6b})$$

where

$$f_1 \sim O(ic_0 D_R q^2 / D_{rot} \kappa \mathcal{P}_0 \pi), \quad f_2 \sim O(-c_0^2 D_R q^3 / D_{rot}^2 \kappa \mathcal{P}_0), \quad (\text{L.7a})$$

$$g_1 \sim O(iAc_0^2 q^3 / D_{rot}^2), \quad g_2 \sim O(Ac_0^3 q^4 / D_{rot}^3).$$

The full solution is:

$$f_1 = \frac{ic_0 q^2 \left(\pi D_R \kappa \mathcal{P}_0 \left(c_0 q^2 (3A + 4M) + 16 D_{rot} \right) + \pi^2 A c_0 \kappa^2 \mathcal{P}_0^2 q + 16 D_R^2 D_{rot} q \right)}{2 \left(\pi c_0 \kappa \mathcal{P}_0 q^2 (A + 2M) + 2 D_{rot} (D_R q + \pi \kappa \mathcal{P}_0) \right)} \times \frac{1}{\pi c_0 \kappa \mathcal{P}_0 q^2 (A + 2M) + 8 D_{rot} (D_R q + \pi \kappa \mathcal{P}_0)}, \quad (\text{L.8a})$$

$$g_1 = \frac{i \pi A c_0^2 \kappa \mathcal{P}_0 q^3 (D_R q + \pi \kappa \mathcal{P}_0)}{2 \left(\pi c_0 \kappa \mathcal{P}_0 q^2 (A + 2M) + 8 D_{rot} (D_R q + \pi \kappa \mathcal{P}_0) \right)} \times \frac{1}{\pi c_0 \kappa \mathcal{P}_0 q^2 (A + 2M) + 18 D_{rot} (D_R q + \pi \kappa \mathcal{P}_0)}, \quad (\text{L.8b})$$

and

$$\begin{aligned}
f_2 = & - \frac{1}{(\pi c_0 \kappa \mathcal{P}_0 q^2 (A + 2M) + 2D_{rot} (D_R q + \pi \kappa \mathcal{P}_0))} \\
& \times \frac{1}{(\pi c_0 \kappa \mathcal{P}_0 q^2 (A + 2M) + 18D_{rot} (D_R q + \pi \kappa \mathcal{P}_0))} \\
& \times \frac{1}{(\pi c_0 \kappa \mathcal{P}_0 q^2 (A + 2M) + 8D_{rot} (D_R q + \pi \kappa \mathcal{P}_0))^3} \\
& \times \left(1152\pi^4 q^3 c_0^2 D_R D_{rot}^3 \kappa^4 \mathcal{P}_0^4 \right. \\
& + 16\pi^3 c_0^2 D_{rot}^2 \kappa^3 \mathcal{P}_0^3 q^4 (5\pi^2 A c_0 \kappa^2 \mathcal{P}_0^2 + 288D_R^2 D_{rot}) \\
& + 16\pi^2 c_0^2 D_R D_{rot}^2 \kappa^2 \mathcal{P}_0^2 q^5 (11\pi^2 c_0 \kappa^2 \mathcal{P}_0^2 (3A + 4M) + 432D_R^2 D_{rot}) \\
& + 3\pi c_0^2 D_{rot} \kappa \mathcal{P}_0 q^6 (3\pi^4 A c_0^2 \kappa^4 \mathcal{P}_0^4 (A + 4M) \\
& + 16\pi^2 c_0 D_R^2 D_{rot} \kappa^2 \mathcal{P}_0^2 (23A + 44M) + 1536D_R^4 D_{rot}^2) \\
& + c_0^2 D_R D_{rot} q^7 (\pi^4 c_0^2 \kappa^4 \mathcal{P}_0^4 (35A^2 + 192AM + 136M^2) \\
& + 16\pi^2 c_0 D_R^2 D_{rot} \kappa^2 \mathcal{P}_0^2 (59A + 132M) + 1152D_R^4 D_{rot}^2) \\
& + \frac{1}{2} \pi c_0^3 \kappa \mathcal{P}_0 q^8 (2\pi^2 c_0 D_R^2 D_{rot} \kappa^2 \mathcal{P}_0^2 (43A^2 + 276AM + 272M^2) \\
& + \pi^4 A c_0^2 \kappa^4 \mathcal{P}_0^4 (A + 2M)(A + 4M) + 64D_R^4 D_{rot}^2 (9A + 22M)) \\
& + \pi^2 c_0^4 D_R \kappa^2 \mathcal{P}_0^2 q^9 (\pi^2 c_0 \kappa^2 \mathcal{P}_0^2 (A + 2M) (A^2 + 6AM + 4M^2) \\
& + D_R^2 D_{rot} (17A^2 + 120AM + 136M^2)) \\
& \left. + \frac{1}{2} \pi^3 c_0^5 D_R^2 \kappa^3 \mathcal{P}_0^3 (A + 2M) q^{10} (A^2 + 8AM + 8M^2) \right), \tag{L.9a}
\end{aligned}$$

$$\begin{aligned}
g_2 = & - \frac{\pi A c_0^3 \kappa \mathcal{P}_0 q^4 (D_R q + \pi \kappa \mathcal{P}_0)^2}{2 (\pi c_0 \kappa \mathcal{P}_0 q^2 (A + 2M) + 8D_{rot} (D_R q + \pi \kappa \mathcal{P}_0))} \\
& \times \frac{1}{(\pi c_0 \kappa \mathcal{P}_0 q^2 (A + 2M) + 18D_{rot} (D_R q + \pi \kappa \mathcal{P}_0))} \tag{L.9b} \\
& \times \frac{1}{\pi c_0 \kappa \mathcal{P}_0 q^2 (A + 2M) + 32D_{rot} (D_R q + \pi \kappa \mathcal{P}_0)}.
\end{aligned}$$

BIBLIOGRAPHY

1. Solon, A. P., Stenhammar, J., Wittkowski, R., Kardar, M., Kafri, Y., Cates, M. E. & Tailleur, J. Pressure and Phase Equilibria in Interacting Active Brownian Spheres. *Phys. Rev. Lett.* **114**, 198301 (2015).
2. Redner, G. S., Baskaran, A. & Hagan, M. F. Reentrant phase behavior in active colloids with attraction. *Phys. Rev. E* **88**, 012305 (1 2013).
3. Takatori, S. C., Yan, W. & Brady, J. F. Swim Pressure: Stress Generation in Active Matter. *Phys. Rev. Lett.* **113**, 028103 (2014).
4. Takatori, S. C. & Brady, J. F. Towards a thermodynamics of active matter. *Phys. Rev. E* **91**, 032117 (2015).
5. Morris, J. F. & Brady, J. F. Bulk Reaction-Rate in a Heterogeneous Reaction System. *Ind. Eng. Chem. Res.* **34**, 3514–3523 (1995).
6. Theurkauff, I., Cottin-Bizonne, C., Palacci, J., Ybert, C. & Bocquet, L. Dynamic clustering in active colloidal suspensions with chemical signaling. *Phys. Rev. Lett.* **108**, 268303 (2012).
7. Palacci, J., Sacanna, S., Steinberg, A. P., Pine, D. J. & Chaikin, P. M. Living Crystals of Light-Activated Colloidal Surfers. *Science* **339**, 936–940 (2013).
8. Paxton, W. F., Sundararajan, S., Mallouk, T. E. & Sen, A. Chemical locomotion. *Angew. Chem. Int. Ed. Engl.* **45**, 5420–5429 (2006).
9. Ebbens, S., Jones, R. A. L., Ryan, A. J., Golestanian, R. & Howse, J. R. Self-assembled autonomous runners and tumblers. *Phys. Rev. E* **82**, 015304 (2010).
10. Manjare, M., Yang, B. & Zhao, Y.-P. Bubble Driven Quasioscillatory Translational Motion of Catalytic Micromotors. *Phys. Rev. Lett.* **109**, 128305 (2012).
11. Baraban, L., Streubel, R., Makarov, D., Han, L., Karnaushenko, D., Schmidt, O. G. & Cuniberti, G. Fuel-free locomotion of Janus motors: magnetically induced thermophoresis. *ACS Nano* **7**, 1360–1367 (2013).
12. Würger, A. Self-Diffusiophoresis of Janus Particles in Near-Critical Mixtures. *Phys. Rev. Lett.* **115**, 188304 (2015).
13. Samin, S. & van Roij, R. Self-Propulsion Mechanism of Active Janus Particles in Near-Critical Binary Mixtures. *Phys. Rev. Lett.* **115**, 188305 (2015).
14. Kitahata, H., Iida, K. & Nagayama, M. Spontaneous motion of an elliptic camphor particle. *Phys. Rev. E* **87**, 010901 (2013).
15. Sengupta, S., Patra, D., Ortiz-Rivera, I., Agrawal, A., Shklyaev, S., Dey, K. K., Córdova-Figueroa, U., Mallouk, T. E. & Sen, A. Self-powered enzyme micropumps. *Nat Chem* **6**, 415–422 (2014).

16. Soh, S., Bishop, K. J. M. & Grzybowski, B. A. Dynamic Self-Assembly in Ensembles of Camphor Boats. *J. Phys. Chem. B* **112**, 10848–10853 (2008).
17. Dey, K. K., Pong, F. Y., Breffke, J., Pavlick, R., Hatzakis, E., Pacheco, C. & Sen, A. Dynamic Coupling at the Ångström Scale. en. *Angew. Chem. Int. Ed.* **55**, 1113–1117 (2016).
18. Howse, J. R., Jones, R. A., Ryan, A. J., Gough, T., Vafabakhsh, R. & Golestanian, R. Self-motile colloidal particles: from directed propulsion to random walk. *Phys. Rev. Lett.* **99**, 048102 (2007).
19. Berthier, L. & Kurchan, J. Non-equilibrium glass transitions in driven and active matter. *Nat. Phys.* **9**, 310–314 (2013).
20. Ni, R., Cohen Stuart, M. A. & Dijkstra, M. Pushing the glass transition towards random close packing using self-propelled hard spheres. *Nat. Commun.* **4**, 2704 (2013).
21. Rusconi, R., Guasto, J. S. & Stocker, R. Bacterial transport suppressed by fluid shear. *Nat. Phys.* **10**, 212–217 (2014).
22. Uspal, W. E., Popescu, M. N., Dietrich, S. & Tasinkevych, M. Rheotaxis of spherical active particles near a planar wall. *Soft Matter* **11**, 6613–6632 (2015).
23. Kaya, T. & Koser, H. Direct Upstream Motility in Escherichia coli. *Biophys. J.* **102**, 1514–1523 (2012).
24. Durham, W. M., Climent, E. & Stocker, R. Gyrotaxis in a Steady Vortical Flow. *Phys. Rev. Lett.* **106**, 238102 (2011).
25. ten Hagen, B., Kümmel, F., Wittkowski, R., Takagi, D., Löwen, H. & Bechinger, C. Gravitaxis of asymmetric self-propelled colloidal particles. *Nat. Commun.* **5**, 4829 (2014).
26. Miño, G., Mallouk, T. E., Darnige, T., Hoyos, M., Dauchet, J., Dunstan, J., Soto, R., Wang, Y., Rousselet, A. & Clément, E. Enhanced Diffusion due to Active Swimmers at a Solid Surface. *Phys. Rev. Lett.* **106**, 048102 (2011).
27. Cohen, J. A. & Golestanian, R. Emergent Cometlike Swarming of Optically Driven Thermally Active Colloids. *Phys. Rev. Lett.* **112**, 068302 (2014).
28. Delmotte, B., Keaveny, E. E., Plourabouè, F. & Climent, E. Large-scale simulation of steady and time-dependent active suspensions with the force-coupling method. *J. Comput. Phys.* **302**, 524–547 (2015).
29. Saintillan, D. & Shelley, M. J. Emergence of coherent structures and large-scale flows in motile suspensions. *J. R. Soc. Interface* **9**, 571–585 (2011).
30. Wioland, H., Woodhouse, F. G., Dunkel, J., Kessler, J. O. & Goldstein, R. E. Confinement Stabilizes a Bacterial Suspension into a Spiral Vortex. *Phys. Rev. Lett.* **110**, 268102 (2013).

31. Ray, D., Reichhardt, C. & Reichhardt, C. J. O. Casimir effect in active matter systems. *Phys. Rev. E* **90**, 013019 (2014).
32. Wensink, H. H., Dunkel, J., Heidenreich, S., Drescher, K., Goldstein, R. E., Lowen, H. & Yeomans, J. M. Meso-scale turbulence in living fluids. *Proc. Natl. Acad. Sci. U. S. A.* **109**, 14308–14313 (2012).
33. Dunkel, J., Heidenreich, S., Drescher, K., Wensink, H. H., Bär, M. & Goldstein, R. E. Fluid Dynamics of Bacterial Turbulence. *Phys. Rev. Lett.* **110**, 228102 (2013).
34. Patteson, A. E., Gopinath, A., Purohit, P. K. & Arratia, P. E. Particle diffusion in active fluids is non-monotonic in size. en. *Soft Matter* **12**, 2365–2372 (2016).
35. Peng, Y., Lai, L., Tai, Y.-S., Zhang, K., Xu, X. & Cheng, X. Diffusion of Ellipsoids in Bacterial Suspensions. *Phys. Rev. Lett.* **116**, 068303 (2016).
36. Baraban, L., Tasinkevych, M., Popescu, M. N., Sanchez, S., Dietrich, S. & Schmidt, O. G. Transport of cargo by catalytic Janus micro-motors. *Soft Matter* **8**, 48–52 (2012).
37. Burdick, J., Laocharoensuk, R., Wheat, P. M., Posner, J. D. & Wang, J. Synthetic nanomotors in microchannel networks: directional microchip motion and controlled manipulation of cargo. *J. Am. Chem. Soc.* **130**, 8164–8165 (2008).
38. Felderhof, B. U. Collinear swimmer propelling a cargo sphere at low Reynolds number. *Phys. Rev. E* **90**, 053013 (2014).
39. Popescu, M. N., Tasinkevych, M. & Dietrich, S. Pulling and pushing a cargo with a catalytically active carrier. English. *Epl* **95**, 28004 (2011).
40. Sasaki, Y., Takikawa, Y., Jampani, V. S. R., Hoshikawa, H., Seto, T., Bahr, C., Herminghaus, S., Hidaka, Y. & Orihara, H. Colloidal Caterpillars for Cargo Transportation. en. *Soft Matter* **10**, 8813–8820 (2014).
41. Gao, W. & Wang, J. Synthetic micro/nanomotors in drug delivery. *Nanoscale* **6**, 10486 (2014).
42. Michelin, S., Montenegro-Johnson, T. D., Canio, G. D., Lobato-Dauzier, N. & Lauga, E. Geometric pumping in autophoretic channels. *Soft Matter* **11**, 5804–5811 (2015).
43. Zhang, J., Yao, Y., Sheng, L. & Liu, J. Self-Fueled Biomimetic Liquid Metal Mollusk. *Adv. Mater.* **27**, 2648–2655 (2015).
44. Kaiser, A., Peshkov, A., Sokolov, A., ten Hagen, B., Löwen, H. & Aranson, I. S. Transport Powered by Bacterial Turbulence. *Phys. Rev. Lett.* **112**, 158101 (2014).

45. Saintillan, D. & Shelley, M. J. in *Complex Fluids in Biological Systems* (ed Spagnolie, S. E.) 319–355 (Springer New York, 2015). ISBN: 978-1-4939-2065-5. doi:[10.1007/978-1-4939-2065-5_9](https://doi.org/10.1007/978-1-4939-2065-5_9).
46. Wittkowski, R., Tiribocchi, A., Stenhammar, J., Allen, R. J., Marenduzzo, D. & Cates, M. E. Scalar ϕ^4 field theory for active-particle phase separation. *Nat. Commun.* **5**, 4351 (2014).
47. Menzel, A. M. & Löwen, H. Traveling and resting crystals in active systems. *Phys. Rev. Lett.* **110**, 055702 (2013).
48. Stenhammar, J., Tiribocchi, A., Allen, R. J., Marenduzzo, D. & Cates, M. E. Continuum Theory of Phase Separation Kinetics for Active Brownian Particles. *Phys. Rev. Lett.* **111**, 145702 (2013).
49. Cates, M. E. & Tailleur, J. Motility Induced Phase Separation. *Annu. Rev. Condens. Matter Phys.* **6**, 219–244 (2015).
50. Anderson, J. L. Colloid Transport by Interfacial Forces. *Annu. Rev. Fluid Mech.* **21**, 61–99 (1989).
51. Wei, H. H. & Jan, J. S. Self-propulsion and dispersion of reactive colloids due to entropic anisotropy. *J. Fluid Mech.* **657**, 64–88 (2010).
52. Ebbens, S. J. & Howse, J. R. Direct observation of the direction of motion for spherical catalytic swimmers. *Langmuir* **27**, 12293–6 (2011).
53. Córdova-Figueroa, U. M. & Brady, J. F. Osmotic propulsion: the osmotic motor. *Phys. Rev. Lett.* **100**, 158303 (2008).
54. Brady, J. F. Particle motion driven by solute gradients with application to autonomous motion: continuum and colloidal perspectives. *J. Fluid Mech.* **667**, 216–259 (2011).
55. Berke, A. P., Turner, L., Berg, H. C. & Lauga, E. Hydrodynamic Attraction of Swimming Microorganisms by Surfaces. *Phys. Rev. Lett.* **101**, 038102 (2008).
56. Derjaguin, B. & Golovanov, M. On long-range forces of repulsion between biological cells. *Colloids and Surfaces* **10**, 77–84 (1984).
57. Bonnecaze, R. T. & Brady, J. F. A Method for Determining the Effective Conductivity of Dispersions of Particles. *P. Roy. Soc. Lond. A Mat.* **430**, 285–313 (1990).
58. Bonnecaze, R. T. & Brady, J. F. Rate of Diffusion-Limited Reactions in Dispersions of Spherical Traps Via Multipole Scattering. *J. Chem. Phys.* **94**, 537–540 (1991).
59. Bonnecaze, R. T. & Brady, J. F. The Effective Conductivity of Random Suspensions of Spherical-Particles. *P. Roy. Soc. Lond. A Mat.* **432**, 445–465 (1991).

60. Sierou, A. & Brady, J. F. Accelerated Stokesian Dynamics simulations. *J. Fluid Mech.* **448**, 115–146 (2001).
61. Hennes, M., Wolff, K. & Stark, H. Self-Induced Polar Order of Active Brownian Particles in a Harmonic Trap. *Phys. Rev. Lett.* **112**, 238104 (2014).
62. Takatori, S. C. & Brady, J. F. Swim Stress, Motion, and Deformation of Active Matter: Effect of an External Field. *Soft Matter* **10**, 9433–9445 (2014).
63. Tailleur, J. & Cates, M. E. Sedimentation, trapping, and rectification of dilute bacteria. *Europhys. Lett.* **86**, 60002 (2009).
64. Lushi, E., Goldstein, R. E. & Shelley, M. J. Collective chemotactic dynamics in the presence of self-generated fluid flows. *Phys. Rev. E* **86**, 040902 (2012).
65. Stenhammar, J., Marenduzzo, D., Allen, R. J. & Cates, M. E. Phase behaviour of active Brownian particles: the role of dimensionality. *Soft Matter* **10**, 1489–1499 (2014).
66. Lefauve, A. & Saintillan, D. Globally aligned states and hydrodynamic traffic jams in confined suspensions of active asymmetric particles. *Phys. Rev. E* **89**, 021002 (2014).
67. Li, S., Jiang, H. & Hou, Z. Effects of Hydrodynamic Interactions on Crystallization of Passive and Active Colloidal Systems. *Soft Matter* **11**, 5712–5718 (2015).
68. Yang, X., Manning, M. L. & Marchetti, M. C. Aggregation and segregation of confined active particles. *Soft Matter* **10**, 6477–6484 (2014).
69. Mallory, S. A., Šarič, A., Valeriani, C. & Cacciuto, A. Anomalous thermo-mechanical properties of a self-propelled colloidal fluid. *Phys. Rev. E* **89**, 052303 (2014).
70. Fily, Y., Baskaran, A. & Hagan, M. F. Dynamics of self-propelled particles under strong confinement. *Soft Matter* **10**, 5609–5617 (2014).
71. Solon, A. P., Fily, Y., Baskaran, A., Cates, M. E., Kafri, Y., Kardar, M. & Tailleur, J. Pressure is not a state function for generic active fluids. *Nat. Phys.* **11**, 673–678 (2015).
72. Cates, M. E. & Tailleur, J. When are active Brownian particles and run-and-tumble particles equivalent? Consequences for motility-induced phase separation. *Europhys. Lett.* **101**, 20010 (2013).
73. Enculescu, M. & Stark, H. Active Colloidal Suspensions Exhibit Polar Order under Gravity. *Phys. Rev. Lett.* **107**, 058301 (2011).
74. Lauga, E. & Powers, T. R. The hydrodynamics of swimming microorganisms. *Rep. Prog. Phys.* **72**, 096601 (2009).
75. Toner, J., Tu, Y. & Ramaswamy, S. Hydrodynamics and phases of flocks. *Ann. Phys.* **318**, 170–244 (2005).

76. Cates, M. E., Marenduzzo, D., Pagonabarraga, I. & Tailleur, J. Arrested phase separation in reproducing bacteria creates a generic route to pattern formation. *Proc. Natl. Acad. Sci. U. S. A.* **107**, 11715–11720 (2010).
77. Bialké, J., Löwen, H. & Speck, T. Microscopic theory for the phase separation of self-propelled repulsive disks. *Europhys. Lett.* **103**, 30008 (2013).
78. Buttinoni, I., Bialké, J., Kümmel, F., Löwen, H., Bechinger, C. & Speck, T. Dynamical Clustering and Phase Separation in Suspensions of Self Propelled Colloidal Particles. *Phys. Rev. Lett.* **110**, 238301 (2013).
79. Wysocki, A., Winkler, R. G. & Gompper, G. Cooperative motion of active Brownian spheres in three-dimensional dense suspensions. *Europhys. Lett.* **105**, 48004 (2014).
80. Fily, Y. & Marchetti, M. C. Athermal Phase Separation of Self-Propelled Particles with No Alignment. *Phys. Rev. Lett.* **108**, 235702 (2012).
81. Fily, Y., Henkes, S. & Marchetti, M. C. Freezing and phase separation of self-propelled disks. *Soft Matter* **10**, 2132 (2014).
82. Yan, W. & Brady, J. F. The swim force as a body force. *Soft Matter* **11**, 6235–6244 (2015).
83. Ezhilan, B., Alonso-Matilla, R. & Saintillan, D. On the distribution and swim pressure of run-and-tumble particles in confinement. *J. Fluid Mech.* **781**, R4 (2015).
84. Brady, J. F. Brownian-Motion, Hydrodynamics, and the Osmotic-Pressure. *J. Chem. Phys.* **98**, 3335–3341 (1993).
85. Squires, T. M. & Brady, J. F. A simple paradigm for active and nonlinear microrheology. *Phys. Fluids* **17**, 73101 (2005).
86. Brady, J. F. & Morris, J. Microstructure of strongly sheared suspensions and its impact on rheology and diffusion. *J. Fluid Mech.* **348**, 103–139 (1997).
87. Foss, D. R. & Brady, J. F. Brownian dynamics simulation of hard-sphere colloidal dispersions. *J. Rheol.* **44**, 629–651 (2000).
88. Asakura, S. & Ooswa, F. On the interaction of two bodies immersed in a solution of macromolecules. *J. Chem. Phys.* **22**, 1255 (1954).
89. Shklyaev, S., Brady, J. F. & Córdova-Figueroa, U. M. Non-spherical osmotic motor: chemical sailing. *J. Fluid Mech.* **748**, 2488–520 (2014).
90. Li, G. & Tang, J. X. Accumulation of Microswimmers near a Surface Mediated by Collision and Rotational Brownian Motion. *Phys. Rev. Lett.* **103**, 078101 (2009).
91. Li, G., Besson, J., Nisimova, L., Munger, D., Mahautmr, P., Tang, J. X., Maxey, M. R. & Brun, Y. V. Accumulation of swimming bacteria near a solid surface. *Phys. Rev. E* **84**, 041932 (2011).

92. Lauga, E., DiLuzio, W. R., Whitesides, G. M. & Stone, H. A. Swimming in Circles: Motion of Bacteria near Solid Boundaries. *Biophys. J.* **90**, 400–412 (2006).
93. Yan, W. & Brady, J. F. The force on a boundary in active matter. *J. Fluid Mech.* **785**, R1 (2015).
94. Smallenburg, F. & Löwen, H. Swim pressure on walls with curves and corners. *Phys. Rev. E* **92**, 032304 (2015).
95. Brenner, H. & Condiff, D. W. Transport mechanics in systems of orientable particles. III. Arbitrary particles. *J. Colloid Interface Sci.* **41**, 228–274 (1972).
96. Sullivan, J. M. Curvatures of Smooth and Discrete Surfaces. *arXiv:0710.4497*. arXiv: 0710.4497 (2007).
97. Panaras, A. G. *Boundary-layer equations in generalized curvilinear coordinates* tech. rep. NASA-TM-100003, A-87272, NAS 1.15:100003 (NASA, 1987).
98. Coffey, W. T. & Kalmykov, Y. P. Thermal fluctuations of magnetic nanoparticles: Fifty years after Brown. *J. Appl. Phys.* **112**, 121301 (2012).
99. Frankel, I. & Brenner, H. On the foundations of generalized Taylor dispersion theory. *J. Fluid Mech.* **204**, 97–119 (1989).
100. Kramers, H. A. Brownian motion in a field of force and the diffusion model of chemical reactions. *Physica* **7**, 284–304 (1940).
101. Coffey, W. T., Crothers, D. S. F. & Titov, S. V. Escape times for rigid Brownian rotators in a bistable potential from the time evolution of the Green function and the characteristic time of the probability evolution. *Physica A* **298**, 330–350 (2001).
102. Pohl, O. & Stark, H. Dynamic Clustering and Chemotactic Collapse of Self-Phoretic Active Particles. *Phys. Rev. Lett.* **112**, 238303 (2014).
103. Heyes, D. M. & Melrose, J. R. Brownian dynamics simulations of model hard-sphere suspensions. *J. Non-Newtonian Fluid Mech.* **46**, 1–28 (1993).
104. Beard, D. A. & Schlick, T. Unbiased rotational moves for rigid-body dynamics. *Biophys. J.* **85**, 2973–2976 (2003).
105. Toukmaji, A. Y. & Board, J. A. Ewald summation techniques in perspective: a survey. *Comput. Phys. Commun.* **95**, 73–92 (1996).
106. Darden, T., York, D. & Pedersen, L. Particle mesh Ewald: An $N \log(N)$ method for Ewald sums in large systems. *J. Chem. Phys.* **98**, 10089 (1993).
107. Nguyen, H. *GPU Gems 3* (Addison-Wesley Professional, 2007).
108. Deserno, M. & Holm, C. How to mesh up Ewald sums. I. A theoretical and numerical comparison of various particle mesh routines. *J. Chem. Phys.* **109**, 7678–7693 (1998).

109. Hinch, E. J. An averaged-equation approach to particle interactions in a fluid suspension. *J. Fluid Mech.* **83**, 695–720 (04 1977).
110. Brinkman, H. C. A calculation of the viscous force exerted by a flowing fluid on a dense swarm of particles. *Appl. Sci. Res.* **1**, 27–34 (1949).
111. Santos, P. H. S., Campanella, O. H. & Carignano, M. A. Brownian Dynamics Study of Gel-Forming Colloidal Particles. *J. Phys. Chem. B* **114**, 13052–13058 (2010).
112. Lodge, J. F. M. & Heyes, D. M. Structural evolution of phase-separating model colloidal liquids by Brownian dynamics computer simulation. *J. Chem. Phys.* **109**, 7567–7577 (1998).
113. Karpov, V. G. & Oxtoby, D. W. Self-organization of growing and decaying particles. *Phys. Rev. E* **55**, 7253–7259 (1997).
114. Saha, S., Golestanian, R. & Ramaswamy, S. Clusters, asters, and collective oscillations in chemotactic colloids. *Phys. Rev. E* **89**, 062316 (2014).
115. Wang, X.-Z. A simple and accurate equation of state for hard-disk fluids. *Physica A* **389**, 3048–3052 (2010).
116. Bialké, J., Siebert, J. T., Löwen, H. & Speck, T. Negative Interfacial Tension in Phase-Separated Active Brownian Particles. *Phys. Rev. Lett.* **115**, 098301 (2015).
117. Bhalla, A. P. S., Griffith, B. E., Patankar, N. A. & Donev, A. A minimally-resolved immersed boundary model for reaction-diffusion problems. *J. Chem. Phys.* **139**, 214112 (2013).
118. Horstmann, D. The nonsymmetric case of the Keller-Segel model in chemotaxis: some recent results. *Nonlinear. Diff.* **8**, 399–423 (2001).
119. Horstmann, D. & Winkler, M. Boundedness vs. blow-up in a chemotaxis system. *J. Differ. Equations* **215**, 52–107 (2005).
120. Thakur, S. & Kapral, R. Collective dynamics of self-propelled sphere-dimer motors. *Phys. Rev. E* **85**, 26121 (2012).
121. Swan, J. W., Brady, J. F., Moore, R. S. & Ch. E. 174. Modeling hydrodynamic self-propulsion with Stokesian Dynamics. Or teaching Stokesian Dynamics to swim. *Phys. Fluids* **23**, 71901 (2011).
122. Keller, E. F. & Segel, L. A. Model for chemotaxis. *J. Theor. Biol.* **30**, 225–234 (1971).
123. Ezhilan, B., Shelley, M. J. & Saintillan, D. Instabilities and nonlinear dynamics of concentrated active suspensions. *Phys. Fluids* **25**, 70607 (2013).
124. Saintillan, D. & Shelley, M. J. Instabilities and pattern formation in active particle suspensions: kinetic theory and continuum simulations. *Phys. Rev. Lett.* **100**, 178103 (2008).

125. Hansen, J. & McDonald, I. *Theory of Simple Liquids: with Applications to Soft Matter* ISBN: 9780123870339 (Elsevier Science, 2013).
126. Ebbens, S. J. & Howse, J. R. In pursuit of propulsion at the nanoscale. *Soft Matter* **6**, 726–738 (4 2010).
127. Brush, S. G., Sahlin, H. L. & Teller, E. Monte Carlo Study of a One-Component Plasma. I. *J. Chem. Phys.* **45**, 2102–2118 (1966).
128. Gillan, M. J. A simple model for the classical one-component plasma. *J. Phys. C* **7**, L1–L4 (1974).
129. Rogers, F. J. Statistical-Mechanics of Coulomb Gases of Arbitrary Charge. *Phys. Rev. A* **10**, 2441–2456 (1974).
130. Stroud, D. & Ashcroft, N. Comment on the thermodynamics of a classical one-component plasma. *Phys. Rev. A* **13**, 1660–1663 (1976).
131. Itoh, N. & Ichimaru, S. Lattice model for the screening potential of the classical one-component plasma. *Phys. Rev. A* **16**, 2178–2180 (1977).
132. Bernu, B. Single-Particle Motion in the Strongly Coupled One-Component Plasma. *J. Stat. Phys.* **21**, 447–464 (1979).
133. Baus, M. & Hansen, J. P. Statistical-Mechanics of Simple Coulomb-Systems. *Phys. Rep.* **59**, 1–94 (1980).
134. Tan, J. N., Bollinger, J. J., Jelenkovic, B. & Wineland, D. J. Long-Range Order in Laser-Cooled, Atomic-Ion Wigner Crystals Observed by Bragg Scattering. *Phys. Rev. Lett.* **75**, 4198–4201 (23 1995).
135. DeWitt, H., Slattery, W., Baiko, D. & Yakovlev, D. Harmonic lattice theory of Coulomb solids and comparison with Monte Carlo simulations. *Contrib. Plasma Phys.* **41**, 251–254 (2001).
136. Chugunov, A. I., Baiko, D. A., Yakovlev, D. G., De Witt, H. E. & Slattery, W. L. Pair distribution of ions in Coulomb crystals. *Physica A* **323**, 413–427 (2003).
137. Daligault, J. Crystal nucleation in the one-component plasma. *Phys. Rev. E* **73**, 056407 (2006).
138. Louis, A. A. Beware of density dependent pair potentials. *J. Phys. Condens. Matter* **14**, 9187 (2002).
139. Tejero, C. F. & Baus, M. On the relation between the compressibility and the static structure factor of a fluid with a state-dependent pair-potential. *J. Chem. Phys.* **118**, 892–896 (2003).
140. Lebenhaft, J. R. & Kapral, R. Diffusion-controlled processes among partially absorbing stationary sinks. *J. Stat. Phys.* **20**, 25–56 (1979).

141. Dubin, D. H. First-order anharmonic correction to the free energy of a Coulomb crystal in periodic boundary conditions. *Phys. Rev. A* **42**, 4972–4982 (1990).
142. Stringfellow, G. S., DeWitt, H. E. & Slattery, W. L. Equation of state of the one-component plasma derived from precision Monte Carlo calculations. *Phys. Rev. A* **41**, 1105–1111 (1990).
143. Löwen, H., Palberg, T. & Simon, R. Dynamic Criterion for Freezing of Colloidal Liquids. *Phys. Rev. Lett.* **70**, 1557–1560 (1993).
144. ten Wolde, P., Ruiz-Montero, M. & Frenkel, D. Numerical Evidence for bcc Ordering at the Surface of a Critical fcc Nucleus. *Phys. Rev. Lett.* **75**, 2714–2717 (1995).
145. Hoffmann, G. P. & Löwen, H. Freezing and melting criteria in non-equilibrium. *J. Phys. Condens. Matter* **13**, 9197–9206 (2001).
146. Hoppensteadt, F. C. & Peskin, C. S. *Modeling and Simulation in Medicine and the Life Sciences* ISBN: 978-0-387-21571-6 (Springer New York, New York, NY, 2002).
147. Shelley, M. J. The Dynamics of Microtubule/Motor-Protein Assemblies in Biology and Physics. *Annu. Rev. Fluid Mech.* **48**, 487–506 (2016).
148. Blake, J. R. A spherical envelope approach to ciliary propulsion. *J. Fluid Mech.* **46**, 199–208 (1971).
149. Kim, S. & Karrila, S. J. *Microhydrodynamics: Principles and Selected Applications* 978-0486442198 (Courier Corporation, 2005).
150. Durlofsky, L., Brady, J. F. & Bossis, G. Dynamic Simulation of Hydrodynamically Interacting Particles. *J. Fluid Mech.* **180**, 21–49 (1987).
151. Ishikawa, T., Simmonds, M. P. & Pedley, T. J. Hydrodynamic interaction of two swimming model micro-organisms. English. *J. Fluid Mech.* **568**, 119–160 (2006).
152. Batchelor, G. K. The stress system in a suspension of force-free particles. *J. Fluid Mech.* **41**, 545 (1970).
153. Zia, R. N. & Brady, J. F. Single-particle motion in colloids: force-induced diffusion. *J. Fluid Mech.* **658**, 188–210 (2010).
154. Edwards, D. A., Brenner, H. & Wasan, D. T. *Interfacial Transport Processes and Rheology* ISBN: 9781483292274 (Butterworth-Heinemann, 2013).
155. Cox, R. G. Electroviscous forces on a charged particle suspended in a flowing liquid. *J. Fluid Mech.* **338**, 1–34 (1997).
156. Yariv, E. An Asymptotic Derivation of the Thin-Debye-Layer Limit for Electrokinetic Phenomena. *Chem. Eng. Commun.* **197**, 3–17 (2009).

157. Pozrikidis, C. *A Practical Guide to Boundary Element Methods with the Software Library BEMLIB* ISBN: 9781420035254 (CRC Press, 2002).
158. Guckenheimer, J. & Holmes, P. *Nonlinear Oscillations, Dynamical Systems, and Bifurcations of Vector Fields* ISBN: 9781461270201 (Springer New York, 2013).
159. Kato, T. *Perturbation Theory for Linear Operators* ISBN: 9783540586616 (Springer Science & Business Media, 1995).
160. Baumgärtel, H. *Analytic perturbation theory for matrices and operators* ISBN: 9783764316648 (Birkhäuser Verlag, 1985).

Appendix M

CONSENT FORM